DNA-TEMPLATED NANOWIRES FOR SENSING VOLATILE ORGANIC COMPOUNDS

By

Oshido, Barnabas Atsinafe

School of Natural and Environmental Sciences
Newcastle University
Newcastle Upon Tyne, UK.

A thesis submitted for the degree of
Doctor of Philosophy

June, 2019.

Abstract

The fabrication of gas sensors with semi-conducting nanowires has attracted considerable interest in recent times because of their potential of selective and fast detection of low quantities of gaseous analyte when incorporated into miniature and low-power consumer electronics. DNA templating is a relatively new process for fabrication of nanowires at room temperature without the requirement for vacuum technology. This thesis describes the synthesis, characterization and gas sensing application of DNA templated metal sulfides and carbon nanotube nanowires.

DNA templated CdS, $CdZnS_2$ and ZnS were synthesized in solution to form smooth and continuous nanowires.The reaction involves initial coordination of the metal ion(s) with DNA and subsequent co-precipitation with sulfide ions upon addition of Na_2S.The nanowires were deposited on the substrate via molecular combing to form a well-aligned network for electrical characterisation and gas sensing experiments. The structure, chemical composition and morphology of the nanowires were characterised by atomic force microscopy (AFM), powder X-ray diffraction (XRD), Fourier transform infrared (FTIR) spectroscopy, UV-vis spectroscopy, photoluminescence (PL), fluorescence microscopy, transmission electron microscopy, X-ray photoelectron spectroscopy and Raman spectroscopy. These techniques showed that the metal sulfides interact with the DNA template to form microcrystalline nanowires of typical diameter < 10 nm and controllable Cd:Zn ratio. The current-voltage (I-V) properties as a function of temperature were measured using micro-band electrodes on a probe station, Impedance spectroscopy and current transients were used to estimate contact resistances. The nanowires showed weak conductivity with I-V curves typical of metal-semiconductor-metal systems and described by the space charge limited conduction model. The temperature dependent properties of the nanowires showed simple Arrhenius behaviour. The room temperature sensing properties of the nanowires to volatile organic compounds (VOCs) such as ethanol, acetone, chloroform and hexane were also determined. They demonstrated good and reversible sensing response to the VOCs but with a higher sensitivity towards ethanol. The result also suggests that the room temperature sensing mechanism of the VOCs molecules on CdS/DNA, ZnS/DNA and $CdZnS_2$/DNA nanowire sensor is essentially driven by their direct adsorption on the surface and interaction with charges in the nanowires.

Multi-walled carbon nanotubes (MWCNT) - deoxyribonucleic acid (DNA) nanocomposite based gas sensor were also fabricated using different MWCNT/DNA ratios to design a resistive sensor. The gas sensor was used for sensing various volatile organic vapours (VOCs) such as methanol, ethanol, chloroform and acetone. These sensors exhibited excellent selectivity and sensitivity towards methanol vapour at room temperature even when exposed to low concentrations. The effect of increase in temperature on the sensitivity of the various MWCNT/DNA ratio gas sensor was extensively investigated. The sensors also showed good reversibility with most of the analyte especially acetone.

Dedication

To my parent who thought it wise to get me educated and support my dreams.

Acknowledgements

It is with immense gratitude that I acknowledge the support, guidance, meticulous observations and suggestions made by my supervisors Dr. Benjamin Horrocks and Prof. Andrew Houlton during the course of this research. Their continuous assistance in the use of laboratory equipment and softwares did not only made my research easier but also made me a better scientist. Their continuous regular meetings and feedback during the course of this research culminated into this well documented thesis. I will remain eternally grateful for all your effort in ensuring the completion of this work.

I wish to specially express my gratitude to Andres Aldana who supported me during the early part of my laboratory synthesis and some of preliminary characterisation processes. Special gratitude to Dr. Osama El-zubir for introducing and assisting me during AFM imaging and XPS data fitting. His immense support and valuable advice throughout the course of this research made life easier. Special thanks to Dr. Maggie White for the XRD data acquisition and Dr. Kathryn White of the Newcastle medical school for training on the use of TEM.

I am indebted to all the members of the chemical nanoscience research group especially those I share the same supervisor (Dr. Steve Nomor, Dr. Hector Oyems, Dr Mansur I. Yahaya, Dr. Shams Ali and Luke Saunders) whose companion I have enjoyed during the cause of this programme. To all my office mates Dr. Collete Whitfield, Dr. Samantha Lunn, Glenn Lamming, Tom Bamford and Rachel Little who made the office quite lively and supported with many other assistance I requested.

To my mentor and former head of Chemistry department Prof. Simon T. Ubwa and other colleagues at Benue State University, Makurdi. Thank you all for encouragement and support to embark on this programme. The Vice Chancellor Prof. Msugh Kembe is not left out for approving my study leave and making sure my remunerations are promptly paid. My deepest appreciation also goes to TETFUND for financial support to undertake this studies.

To my beloved parent Mr. and Mrs David Oshido who have supported my education right from childhood to this stage. To my siblings especially my elder brother Pharm. Samuel Oshido and the rest, thank you all for standing by me. My wonderful friends Dr. Egena Ode and Dr. Aamo Iorliam, Doreen Torhile and Vivian Ofubu thank you all for the valuable advice and motivation during the difficult moments.

Table of contents

List of figures

List of schemes

List of tables

CHAPTER ONE

Introduction

This chapter gives a general overview of nanoscience and nanowires, synthesis of nanowires using DNA as template, the mechanism of nanowire growth and alignment of the nanowires on electrodes to form gas sensors. It also provides a literature review on semiconductor metal sulfides, metal sulfide gas sensors and mechanism of sensing using metal sulfide gas sensors.

1.1 Nanoscience

Nanoscience is an area of science concerned with the study of phenomena or organisation of objects with characteristic dimensions on the order of nanometres. The materials that are investigated are commonly called nanomaterials and their typical size spans the range of 1-100 nm[1–3]. Nanomaterials have drawn much attention because of their novel properties due to quantum confinement and their high surface to volume ratio. The bulk of research in this area is been channelled into size and property optimisation[4]. In order to fully understand the properties of nanomaterials, it is very important to know the different types of nanomaterials. They can be categorised into zero- dimensional (0-D), One- dimensional (1-D), two dimensional (2-D) and three dimensional (3-D) nanomaterials depending on the number of macroscopic dimensions[5]. A schematic representation of the different dimensions of nanomaterial is presented in figure 1.1.

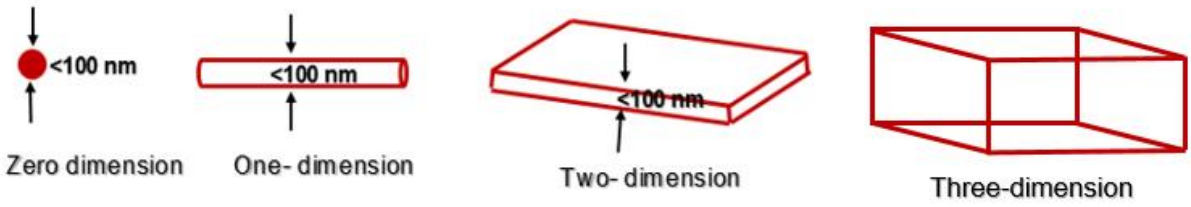

Figure 1.1 The schematic diagram showing the different dimensions of nanomaterials.

The 0-D materials are material which have all the three dimension in the nanometre region, i.e., have no macroscopic dimensions. They therefore exhibit quantum confinement in all three dimensions. The most common examples of 0-D materials are nanoparticles and quantum dots. The distinction between these two types depends on the ratio of the particle radius *R* to the Bohr radius of the exciton, *a*.

$$a = \epsilon_r \frac{m_e}{\mu} a_0 \quad (1.1)$$

Where ε_r is the relative permittivity (dielectric constant) of the material, m_e is the rest mass of the electron and μ is the reduced mass of the electron in the conduction band and the hole in the valence band. Equation (1.1) is based on the analogy between the electron orbiting the proton of a hydrogen atom in the 1s state (reduced mass ~ m_e) and the electron in the conduction band of the particle orbiting a hole in the valence band. The reduced mass of electron and hole is typically about 0.1 m_e and the relative permittivity of many semiconductors is of order 10 therefore a ~ 100 a_0 where a_0 is the Bohr radius of the hydrogen atom, 0.0529 nm. When the particle radius R approaches the typical value of a ~ 5 nm, the electron and hole experience energy changes due to confinement of their wave functions. This effect is called quantum confinement and distinguishes a quantum dot from a nanoparticle. The result is a change in the energy level structure of the particle, discussed below.

The 1-D materials are long, thin objects with one macroscopic dimension and may exhibit size quantisation in two dimensions. The most typical examples of 1-D materials are nanowires, nanorods and nanotubes[6]. The 2-D materials have two sides that are outside the nanoscale region and therefore may exhibit size confinement in only one dimension. The materials that exhibit such properties are nanolayers and nanofilms[7,8]. The 3-D materials are those that do not exhibit size confinement and therefore represent bulk materials[9]. However, nanomaterials are sometimes arranged using size confined components into microstructures that exhibit special and novel properties such as in DNA origami.

The quantum confinement of these nanomaterials are usually explained using the electronic band structure of materials. Solid materials are generally classified based on their electronic structures as insulators, semi-conductors and metals. All crystalline solid materials are made up of electronic bands of which the most important are the filled valence band and an empty conduction band[10]. The separation between the valence and conduction band of a material is commonly called the bandgap (E_g) of the material. The band gap energy is defined as the energy required to move an electron from the top of the occupied valence band to the bottom of the conduction band. In bulk metal, the valence (VB) and conduction bands (CB) overlap and there is no band gap for electrons. In general, completely filled and completely empty bands do not contribute to electronic conduction. In a metal, there is at least one partially filled band

and the electrons flow freely, subject only to scattering from atomic lattice vibrations. In semiconductors, the VB and CB are filled and empty at 0 K because there is a small gap between the valence and the conduction band. As the temperature is raised, electrons may be excited to the conduction band; this occurs to an appreciable extent only when thermal energy RT is a significant fraction of the bandgap energy[11,12]. Alternately, electrons may reach the conduction band by thermal ionization of impurity levels (doping) or by absorption of light of photon energy greater than the bandgap. Different types of bulk semiconductors have different band gaps depending on the separation between the valence band and the conduction band. If the gap is sufficiently high such that even when it acquires a large amount of energy, the electron cannot reach the CB, then the material can be termed an insulator or non-conductor[13]. There is no definite threshold that distinguishes semiconductors from insulators, but a bandgap of 4 eV means that electrons would require an energy much larger than available from thermal energy at ambient temperature or than available by absorption of visible light. The energy diagram showing the different classes of solid materials classified based on their electronic structure is shown in figure 1.2.

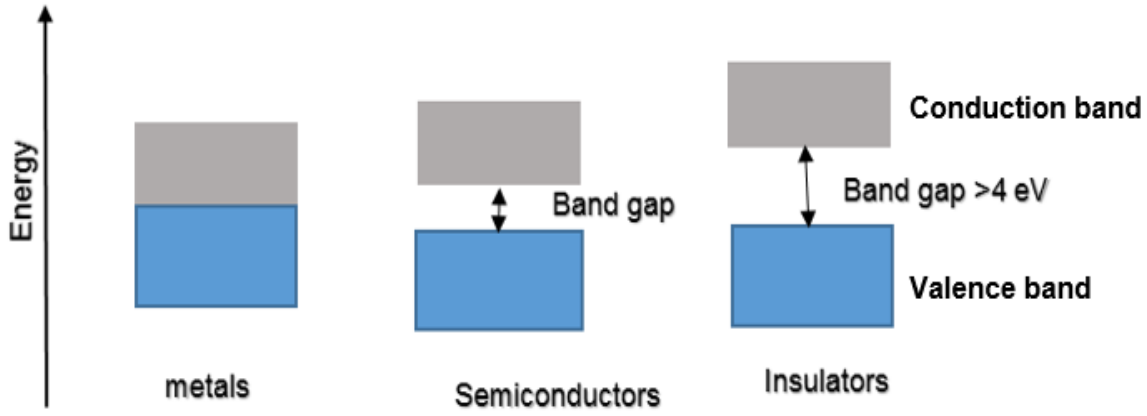

Figure 1.2 Energy band diagram of the different types of materials classified based on their electronic structure.

In a regular semiconductor crystal, the band gap is fixed owing to the continuous energy states. In a quantum confined semiconductor crystal, the band gap is size dependent and can be altered to produce a range of energies between the valence and conduction band. A schematic illustration of the change in the band structure of a typical semiconductor from bulk solid to nanoscale in comparison with an isolated atom is shown in figure 1.3.

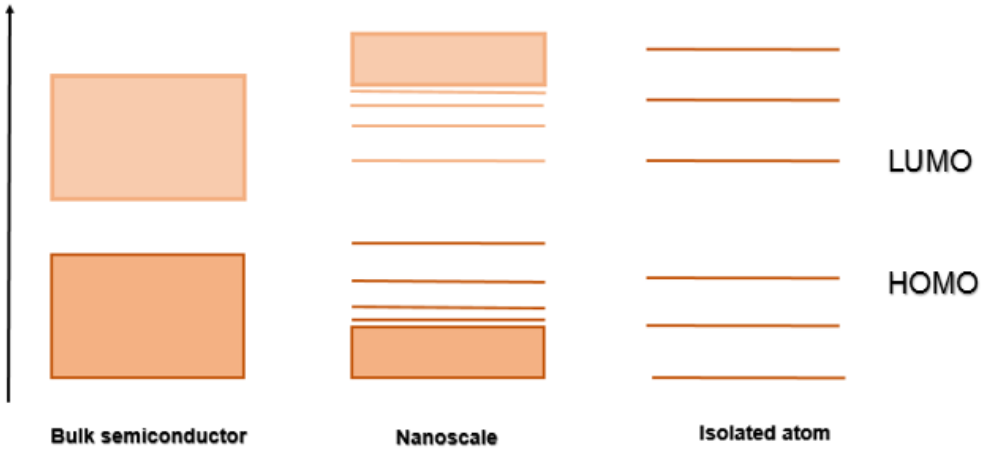

Figure 1.3 Schematic illustration of the change in the band structure of a typical semiconductor from bulk solids to nanoscale in comparison with an isolated atom. The formation of discrete energy levels as the bulk solids is scaled down to nanoscale is an evidence of quantisation.

In the bulk semiconductor, the VB and CB are continuous bands of energy levels and in a small molecular cluster or isolated atom, the energy levels form a discrete ladder (figure 1.3 right). At the nanoscale, when one or more material dimensions approach the Bohr radius of the exciton, the gap between the topmost filled level (HOMO or top of the VB) and the lowest lying empty level (LUMO or bottom of CB) starts to increase. The energy level spectrum also starts to transform from the continuous spectrum of the bulk solid to the discrete spectrum of an isolated atom. There are several consequences: the lowest photon energy at which the material absorbs and emits light shifts to the blue and further the spectrum may begin to show peaks instead of a threshold as in the bulk solid. However, the precise details of the spectra are also dependent on the dimensionality.

In metals, electronic properties change very little with manipulation of size due to the absence of band gap and as such quantum confinement is not very conspicuous or absent. Semiconductors' electronic structure in the other hand can easily be manipulated through the tuning of band gap by size adjustment. This leads to many interesting electronic, optical and chemical properties. The size, type, symmetry and strength of bonding orbitals of individual atoms determines the electronic structure in a semiconductor[13]. This makes studies of semiconducting material very important as they can be manipulated depending on the kind of application and environment where it will be used. As well as quantum confinement effects, the material properties also depend on surface tension effects. In a molecular view, the atoms at the surface of a

material have a higher free energy than those in the bulk because they lack at least one neighbour – they have “dangling bonds” or “unsatisfied valences”. Nanomaterials have a greater fraction of atoms at their surface and therefore a larger free energy. This may make them chemically more reactive; it certainly results in a much greater influence of surface chemical events on the physical properties of the material. A simple calculation shows the number of atoms throughout the volume of an object is proportional to L^3 where L is its characteristic radius. The number of surface atoms varies with L^2 and therefore the surface S to volume V ratio is simply:

$$\frac{S}{V} \sim \frac{1}{L} \tag{1.2}$$

As the size L decreases, the influence of the surface increases in proportion. In the case of nanowires, the result is a greater influence of the surface atoms on the conductivity. These properties make nanowires particularly suitable for the gas sensing applications. In this thesis, we synthesize semiconducting nanomaterials and prepare gas sensors using the sensitivity of their conductivity to chemical events (gas adsorption) on their surfaces.

1.2 Nanowires

One dimensional nanostructures have attracted intensive research owing to their different applications in fabrication of nanoscale devices and in mesoscopic physics[14]. These 1D nanostructures are important because they have discrete molecular states, show density of states singularities and exhibit special phenomena such as spin - charge separation[15]. Among the different types of 1D nanostructures, nanowires are the most interesting and widely studied.

Nanowires are particularly interesting in the investigation of charge transport at the nanoscale and have been studied for their applications as transducers in gas sensors[16–18] or as interconnects in nanoelectronic devices[19–21]. They can be synthesised using different methods including solution-phase techniques which allows high quality and large scale production[22].

The amount of published articles about nanowires has increased tremendously over the last few years, indicating the widespread and growing applications for these nanostructures. Most of the literatures are focused on the optimisation of the synthesis

and characterisation process, with the incorporation and controlled assembly of these nanostructures in devices still emerging. A histogram showing the number of publications citation per year as obtained in Scopus is shown in figure 1.4.

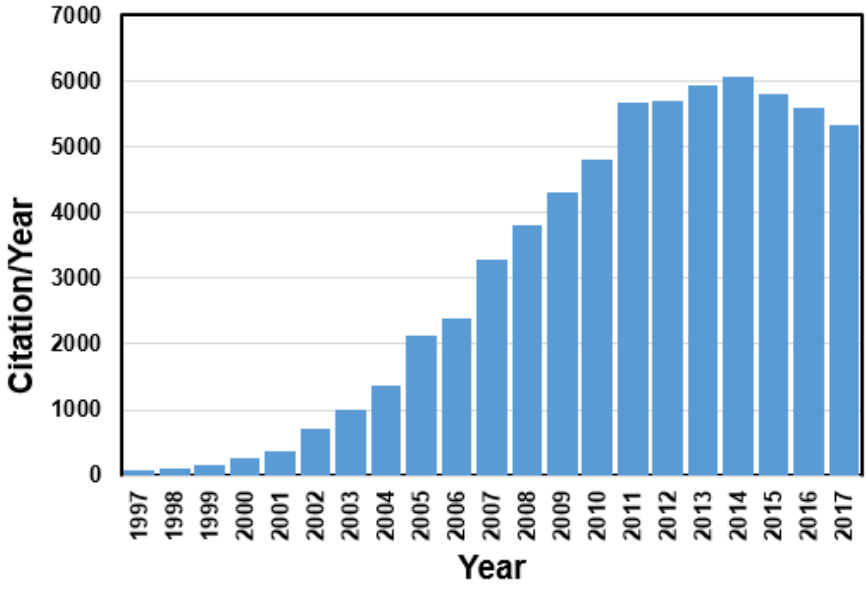

Figure 1. 4 Histogram of citations per year to '' Nanowires'' - related publications on Scopus. (Search done on 24/07/2018).

1.3 Synthesis of Nanowires

Different physical and chemical methods have been employed for synthesis of metal sulfide nanowires such as thermal evaporation[23], hydrothermal growth[24–26], physical vapour deposition (PVD)[27,28], chemical vapour deposition (CVD)[29–33] high pressure autoclave processes and templating routes. The template route is one of the most convenient methods of nanowire synthesis[34]. Apart from the use of conventional templates such as anodized alumina membrane[35] and porous polycarbonate membranes[36], biomolecules have also been successfully used because they have shown capabilities in self-assembling nanoscale materials[37]. Different biomolecules have shown potentials to act as templating materials such as viruses[38] and proteins[39]. DNA can also be used because of its superior and robust properties such as long length (few microns) and chemical stability.

The synthesis of DNA templated nanowires by co-precipitation in solution is very advantageous because it can be faster and cheaper as well as convenient for large scale printing and deposition. The nanowires can be uniform with equal grain size along their length because the strand is uniform with a diameter of 2 nm[40]. It has been

previously proven that is possible to incorporate inorganic material into DNA via base pairing, electrostatic interaction and covalent linkage[41]. These properties can be very useful for synthesising nanowires that are to be used for making gas sensors with reversible properties. First we review some basic aspects of DNA structure.

1.4 DNA structure

DNA is a biopolymer that comprises monomeric units called nucleotides[42–44].The nucleotides consist of three basic components; a nitrogenous heterocyclic base, a pentose sugar and a phosphate residue. The heterocyclic bases are monocyclic pyrimidines or bicyclic purines. The main pyrimidines are thymine (T), cytosine (C) and Uracil (U) while the purines are guanine (G) and adenine (A). These bases are joined to form four nucleosides which includes deoxy-guanosine, deoxy-adenosine, deoxy-thymidine and deoxy-cytidine. The pentose sugar in DNA is 2-deoxy-D-ribose. The sugar is attached to the nitrogenous bases through glycosidic bonds. DNA is a biopolymer with quite a complex structure that is composed of a skeleton with alternating phosphate and sugar groups[45–48]. The phosphate esters of these nucleosides are commonly referred to as nucleotides. The structures of the major pyrimidine and purine bases of DNA are shown in figure 1.5.

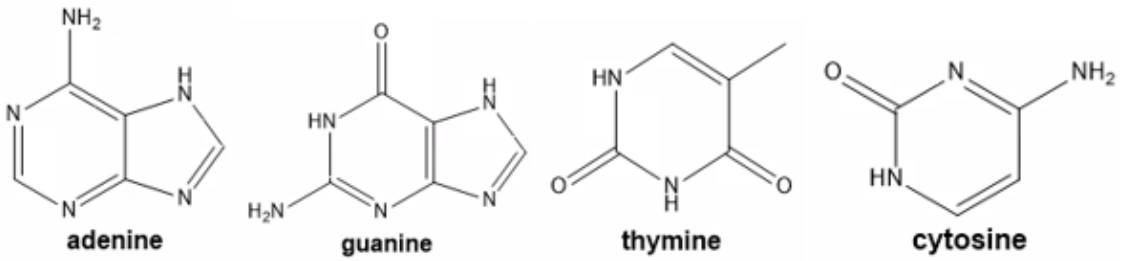

Figure 1. 5 Structure of the major pyrimidines and purine bases of DNA.

These pyrimidines and purine bases bind to the 2-deoxy-D-ribose to form deoxy-ribonucleosides with loss of an oxygen atom. The structure of the four main deoxy-ribonucleosides found in DNA are presented in figure 1.6.

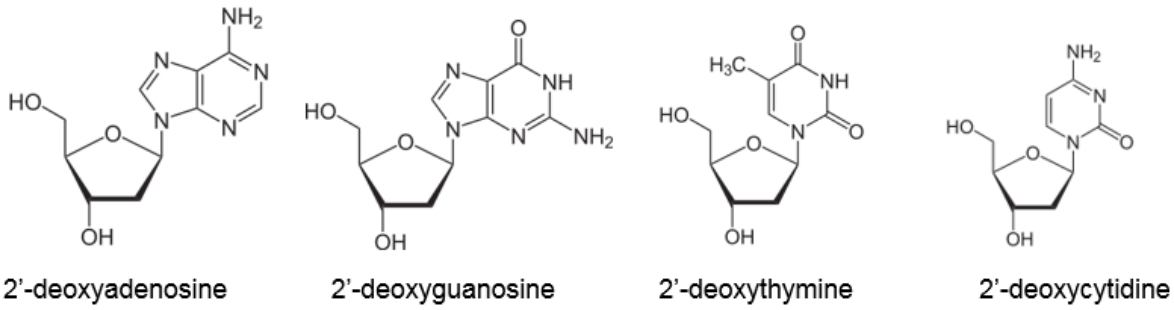

Figure 1.6 Structure of the four main deoxy-ribonucleosides found in DNA.

1.5 DNA as template for nanowire fabrication.

There are many features both chemical and structural that make DNA an important scaffold for self-assembly of various 1-dimensional nanostructures. DNA can be found in various lengths ranging from nanometres to micrometres and with a high surface to volume ratio with a diameter of about 2 nm. This makes it suitable for controlled material growth since the length can be adjusted by increasing or decreasing the number of base pairs. It has many bonding sites at which materials can adhere. Such sites include the polyanionic phosphate backbone and the heteroatoms (N, O) of the aromatic bases[49–52]. Some possible binding sites are shown in the diagram (figure 1.7) below;

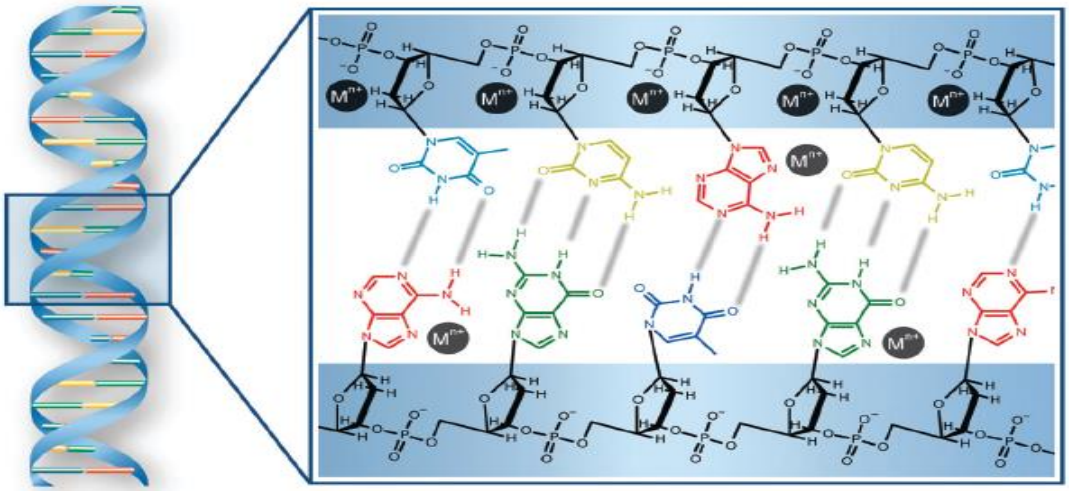

Figure1.7 Diagrammatic illustration of DNA duplex showing the feasible binding sites of metal ions during synthesis of semi-conducting DNA nanowires[51].

There are many commercial sources of DNA that can be used as templates for the synthesis of nanostructures without any additional purification or modifications. The commonly used are bacteriophage T4 DNA[53], genomic DNA from Salmon testes, calf

thymus[54], Escherichia. coli B genomic DNA[55], herrings testes DNA and lambda DNA[56–59]. The most widely used DNA template for synthesis of one dimensional nanowires is the double stranded linear bacteriophage lambda (λ) DNA which is 16.7 μm in length when fully extended and has 48,502 base pairs[60,61]. An important aspect of the DNA structure for templating reactions considered below is the stiffness of the double helix. The persistence length of DNA is about 50 nm, in other words it is a stiff polymer which tends to exhibit a more extended conformation than most synthetic polymers, which form random coils. Templating on a random coil would likely produce nanoparticles rather than nanowires.

1.6 Templating reactions on DNA

The ability of metal ions to interact and stick to DNA molecules has given rise to the synthesis of different kinds of 1-dimensional semi-conducting nanostructures such as nanowires, nanoropes and nanotubes. These involve the treatment of the DNA molecules with the appropriate metal ion leading to the doping of the DNA strand with the metal and subsequently reaction with the appropriate source of chalcogenide (anion) to precipitate on the metal leading to the formation of continuous coated 1-D nanostructures. This process makes use of the stiffness and metal-binding properties of DNA and is not dependent on the sequence information on the DNA.

The templating process of the metal chalcogenides on DNA involves three main stages: (i) the activation stage, which involves the creating of an active metal sites on the DNA when metal cations bind to the aromatic bases or polyanionic phosphate backbone. (ii) the nucleation stage, in which the added sulfide anion reacts with the active metal sites to form metal sulfide precipitates or nanoclusters on the DNA.(iii) the growth stage, in which the metal sulfide nanoclusters acts as the nucleation site for growth of the metal sulfide nanostructures during a process called Oswald ripening (the process of dissolution of the metal sulfide and re-precipitation that occurs in order to re-distribute material from regions of high surface energy to low surface energy) leading to smoothening of the nanowire surface[61,62] .The diagrammatic representation of the whole process has been illustrated below in figure 1.8.

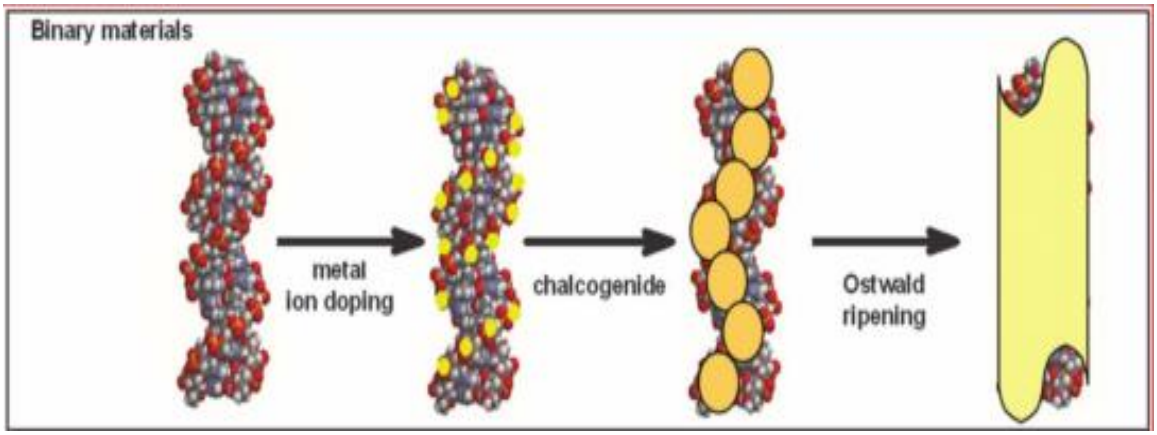

Figure 1.8 Schematic representation of the steps involved in the synthesis of DNA templated semiconducting nanowire[50].

For a ternary metal sulfide, the DNA molecule is first doped with the two metals ions before treatment with the anion (sulfide) to avoid the formation of two different metal anions in solution. Different research groups have reported on the synthesis of various metal sulfides such as Zinc Sulfide (ZnS)[55], Cadmium sulfide (CdS)[63], Copper sulfide (CuS)[64], Lead sulfides (PbS)[65], Molybdenum Sulfide (MoS_2)[66].

An attempt to template PbS nanoparticles on DNA molecules was carried out by Sargent and his co-researchers[65]. They reported a novel route for synthesis of efficient photoluminescent PbS quantum dots on DNA template. It was prepared by dropwise addition of $Pb(NO_3)_2$ to DNA, followed by treatment with Na_2S at temperatures ranging from 20 ℃ to 100℃. It was established that the nanoparticles prepared had intensive living tissue penetration and low auto-fluorescence (fluorescence of the cells in the presence of UV light) because they emit light in the infrared wavelength region. This shows that efficient light emitting PbS nanoparticles can be synthesised by templating reaction on DNA molecules. Gao et al [55] have also explored the fabrication of ZnS nanoparticles on DNA template from Escherichia coli. In that research, the templating reaction was done by reacting aqueous DNA solution with an aqueous solution of $Zn(Ac)_2$ and incubating for 24 hours at 4℃. This was later followed by addition of $Na_2S_2O_3$ aqueous solution and increasing the temperature from 48℃ to 80℃ within 0.5 to 3 hours. The DNA templated ZnS nanowires prepared had zinc blende structure with diameter range of 20 – 30 nm.

Another metal sulfide previously studied for its ability to bind to DNA template was CuS[64]. In this particular case, CuS which is an indirect bandgap metal sulfide was templated on the DNA by initially treating the DNA with $CuCl_2$ so as to produce DNA

copper complex which is further treated with Na_2S to form DNA templated copper sulfide nanowires. The DNA templated CuS nanowires was prepared both in solution and by a surface immobilised method. AFM studies showed that the solution based approach gave smoother and more continuous nanowires while surface immobilised method showed beads of the nanoparticles along the DNA strands with heights as high as 10 nm. The crystal structure of the nanowires were determined using TEM, which showed the covallite crystal lattice. Electrical properties of the nanowires were however not measured. Recently, Goswani et al [66] reported the ability of MoS_2 nanocrystals to be confined on a DNA matrix by wet chemical synthesis through the regulation of reaction conditions such as pH. The reaction process involved two stages. The first step was the reaction of an aqueous solution of DNA from salmon testes with $MoCl_5$ at room temperature with vigorous stirring, which was then followed by addition of NaOH solution to reduce the pH to ~9. The second step involves the addition of NaS_2 to the already synthesized DNA/Mo complex, followed by addition of HCl to reduce the pH to ~6 and stirring. The nanocrystals of DNA/MoS_2 was shown to be somewhat uniform in size and spherical in shape with an average diameter of ~5 nm. The nanowires exhibited large quantum confinement phenomena but were not photoluminescent.

There have been several attempts to synthesise DNA templated CdS nanowires by templating reaction of CdS nanoparticles on DNA. The ability of DNA to stabilise nanocrystals of CdS was first reported by Coffer et al [67]. Calf thymus DNA was initially reacted with cadmium perchlorate to dope it with Cd^{2+} ion and subsequently treated with NaS_2 to give DNA templated CdS nanowires with a zinc blende lattice structure with diameter in the range of 2.3 – 12 nm.

1.7 Mechanism and growth model of DNA templated nanowires

The detailed mechanism of formation of DNA templated nanowires are extremely important because of its relevance for applications such as interconnects in nano-electronic devices and as a transducer in gas sensors. The conductivity of nanowires are greatly improved by careful synthesis to form smooth and continuous nanostructures. In sensing application which the nanowires would be used for in this research, it would increase the sensitivity of the gas sensor by responding faster when in contact with the analyte.

The synthesis of DNA templated nanowires in solution produced nanowires that were continuous and properly coated compared with those immobilised on the surface of a particular substrate. The growth of materials on DNA template immobilised on substrates produced granular structures when observed on AFM and tends to be less conductive. To synthesize nanowires that would be conductive and act as transducer in gas sensors, it would be necessary to ensure proper coverage of the DNA to form nanowires. The mechanism and thermodynamics of the process of producing these nanowires is important for achieving the desired nanostructures. Understanding and controlling the reaction mechanism is responsible for the difference in the synthesis of our nanowires compared to those reported in literature[52,68–70].

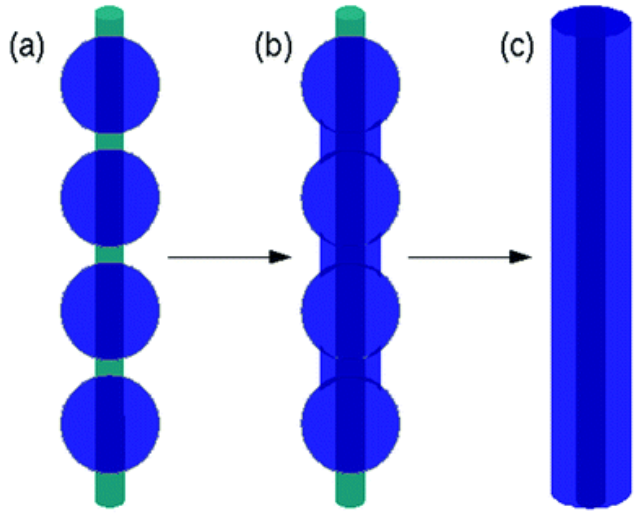

Figure 1.9 The scheme showing the evolution from bead-on-a-string structure to uniform and smooth nanowire during DNA templating process. (a) Formation of spherical nanoparticles on the DNA template by precipitation of the metal sulfides (b) the linking of the nanoparticles as more material coat the DNA template. (c) Formation of smooth and continuous nanowire with time if the reaction environment is appropriate[71].

The difference in structure between the nanowires synthesised in solution and those immobilised on the surface of substrate can be explained based on the competitive force between the line energy $\boldsymbol{\sigma}$ and the surface tension $\boldsymbol{\gamma}$ of the nanomaterial. If the state of the templating material is defined by a linear coordinate, r, which represents the radius of the thickness of the nanowire or several identical droplets, then the effect of the line energy can be better understood. The free energy of the templated material is therefore proportional to the inverse of the radius which originated from the surface

tension and also inversely proportional to the square radius of the line energy (for spheres).The line energy dominates when the volume of the templated particle per unit length (V) is very small and the lowest energy results in very smooth nanowires[69].

The free energy (G) of the system per unit length and the volume of material templated per unit length (V) can be related as;

$$\frac{G}{V} = \frac{3\gamma}{r} - \frac{3\sigma}{2\pi r^2} \tag{1.3}$$

The detailed derivation of the equation can be found in literature[69]. Further, one can determine the ratio of free energy of a “beads-on-a-string” morphology to that of a smooth nanowire:

$$\frac{G_{wire}}{G_{beads}} = \sqrt{\frac{2}{3}}\left(1 + \sqrt{\frac{V}{\pi L^2}}\right) \tag{1.4}$$

Where *L* is the length of the template. The equations (1.3 & 1.4) describe the process of formation of smooth and continuous nanowire when the preparation is carried out in solution; it indicates that one should keep the ratio of metal sulfide: DNA bases low (parameter V in equation (1.4)). Too large an amount of metal and sulfide ions results in the formation of beads/particles rather than a smooth nanowire due to competing reaction for formation of metal sulphide precipitate which is a faster process compared to self assembly.

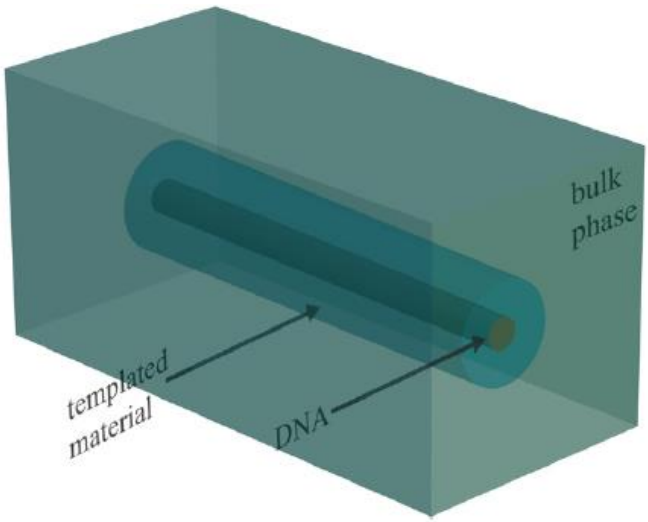

Figure 1.10 Schematic diagram showing the templated nanowires in solution surrounded by the solvent containing the material to be templated[69].

In the case where the DNA template is immobilised on a substrate before coating with the material, the theoretical model can also be used to describe the process of formation of granular structures. The adhesion of the DNA template to the substrate introduces an additional factor to the free energy of the system (~r^{-1}) and the line energy that occurs at the triple phase boundary at the edge where the substrate and the templated material is in contact[72]. The equation (1.3) above for the material in solution can be modified for the material on a substrate as;

$$\frac{G}{V} = \frac{A}{r} + \frac{3\delta}{r} - \frac{3\sigma}{2\pi r^2} \quad (1.5)$$

Where δ represent the free energy per unit length at the intersecting point of the three boundaries. The term $\frac{A}{r}$ is the surface tension of the templated material and the free energy per unit area at the contact with the substrate. This line energy modification of the equation is same as that made to Young's equation used in the theory of nanowire synthesis by the vapour-liquid-solid method[73]. This theory is based on the assumption that the templated material does not stick to the substrate, because free energy of adhesion to substrate has to be different from free energy of adhesion to template for the material to selectively bind to the template. The line energy at the three phase boundary is normally positive and therefore favours formation of contacts with circular perimeter between the material and substrate[72]. These phenomena support the formation of granular structures that prevent re-organisation to form smooth nanowires when the DNA is immobilised on substrate surface. Therefore, the nanowires used for the fabrication of the gas sensors used in this research were prepared in solution.

1.8 Alignment of DNA templated nanowires and device fabrication

Alignment of nanowires on surfaces is very important for the fabrication of nanodevices because it aids incorporation of the nanowires into the devices. Previous research has shown that nanowires were successfully aligned by electric field or flow alignment[74–76]. Huang et al have reported the alignment of single wall carbon nanotube (SWCNT) synthesised by chemical vapour deposition (CVD) to form 1D or 2D networks[77]. One of the main advantages of using DNA template for fabrication for nanodevices is it ease of synthesis, assembly, manipulations and alignment[78–82]. This method can be achievable for both in-situ preparation and surface synthesis of nanowires. Different

methods have been reported for aligning DNA and DNA templated nanostructures such as transfer printing[83], receding meniscus[84] and molecular combing[85] (nitrogen flow) methods. The transfer printing method involves depositing of DNA molecules on poly (dimethyl siloxane) (PDMS) sheet and then sucking it with pipette. This process make use of surface tension at the moving air –water interface to stretch the molecules. The stretched DNA molecules on the PDMS is then transferred by pressing it on the substrate[83] as shown in figure 1.11.

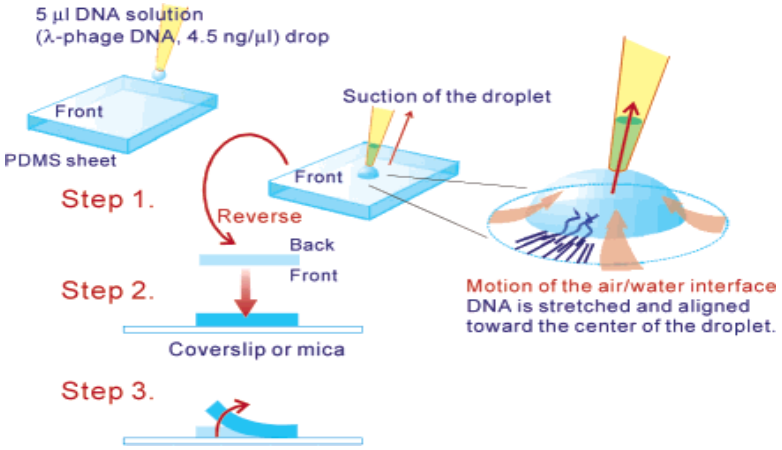

Figure 1.11 Schematic representation of transfer printed method of aligning DNA molecules[83].

One of the best methods of stretching and aligning DNA on surfaces is the molecular combing process[86]. In order to get uniform, aligned DNA templated nanowires for characterisation and device fabrication as reported in this work, a modified method of combing as reported in literature for combing lambda DNA was used[85]. A few microliters of the sample was deposited on a cleaned silicon wafer or freshly cleaved mica by drop casting. The sample was allowed to dry for a few minutes and then a stream of nitrogen gas was used to drive the solution flow in one direction. This process leads to the stretching and alignment of the DNA templated nanowires on the electrode as shown in figure 1.12.

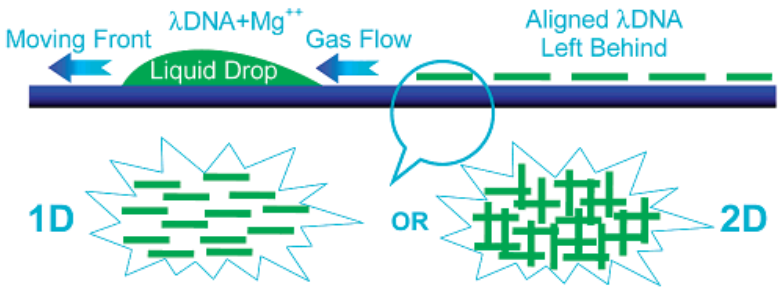

Figure 1.12 Scheme showing aligned DNA molecules on a substrate by fluid-flow-assisted molecular combing[60].

1.9 Semiconductor metal sulfides

Semi-conducting metal sulfide nanoparticles of II-IV materials have been extensively studied recently due to their interesting opto-electronic properties and their application in sensing[87]. Cadmium sulfide (CdS) is one of the most promising of the II-IV binary compound semiconductor, possessing a hexagonal wurtzite structure with a bandgap of 2.42 eV and a melting point of 1600 ^{o}C [88,89]. It can be used for visible radiation detection and also in heterojunction of solar cells as window material to increase the efficiency of solar cells as it prevents the recombination of photo-generated carriers because of its relatively wide bandgap compared to the active materials. It has also been used in light emitting diodes, electrical lasers, address decoders, photodetectors and sensors [90]. Zinc Sulfide (ZnS) is another important member of the II-IV binary compound with wide bandgap and light emitting properties[55]. The addition of dopants such as other transition metals to these chalcogenides tends to alter their properties for different applications.

1.10 Metal sulfides gas sensors

Gas sensors are devices that are able to change one or more of their physical properties when in contact with gases and thereby directly or indirectly measure the quantity of the gases. These devices are very useful because of large surface to volume ratio which makes them very sensitive to chemical processes on their surfaces and therefore can be used to measure gases at low concentrations with fast response time. Other important properties of this kind of sensors includes selectivity for different gases, low power consumption, portability and low maintenance requirement [91,92]. Studies have shown that 1-D nanostructures can be efficiently used as transducers in gas sensors using different methods of sensing mechanism such as gas ionization sensors, quartz crystal microbalances, chemiresistors, field effect transistors, optical sensors and surface acoustic wave devices. The type of material to be used, such as metals, semi-conductors or conducting polymer determine the sensing principle or mechanism to be employed [93,94].

In this research, metal sulfides are templated on double stranded DNA molecules. These synthesized semi-conducting nanowires would be utilized as conductometric or chemiresistive gas sensors either as single nanowire or nanowire network devices.

The basic principle of conductometric or chemiresistive gas sensor is the measurement of the change in conductance or resistance of this nanowires due to the absorption of an analyte gas molecules on the surface of the nanowires. The concentration of analyte gas is proportional to the change in conductance or resistance of the nanowires [92,95]. The sensitivity of this nanowires is dependent on its morphology, as smooth and continuous nanowires are more sensitive due to less potential barrier at the nanowire/nanowire junction as well as nanoparticles-depleted areas on the DNA template. The nanowires should also exhibit high surface to volume ratio to improve its sensitivity [59,94].

1.11 Electrical properties of metal sulfide nanowires

The electrical properties of semiconductor nanowires has been previous explained using different theoretical models such as Fluctuation-induced tunnelling (FIT) theory[96], Coulomb blockade effect[97], phonon assisted tunnelling theory[98,99], scaling theory[100], variable range hopping (VRH) theory[101] and space charge limited current (SCLC) theory[102]. The electrical properties of metal sulfide nanowires such as those reported here have been previously explained using the SCLC theory. This theory is quite suitable because metal sulfides nanowires have intrinsic or depleted charge carriers which makes it highly resistant to flow of current. Another reason is the increased number of traps due to reduced size of the nanowire as the material approaches the nanoscale[103]. It is used here to explain the conduction mechanism of the DNA templated metal sulfides sandwiched in the metal/ semiconductor system. The basic principle is based on the state of the junction at the nanowire-contact metal interfaces: the number of thermal free carriers are less than the number of injected charges[104–106]. Xu et al has previously used it to explain the transition from linear I-V curve of unwittingly doped GaSb nanowires at lower bias to an SCLC behaviour at large bias. This was attributed to the trap distribution energy found in the nanowires[107]. The SCLC theory I-V characteristic at low bias can be represented by the equation

$$I \propto V^{M} \tag{1.6}$$

Where the power M (≥1) depends on the trap state depth distribution under the conduction band. The magnitude of the space charge current can be minimised by the amount of traps and is also responsible for the observed shape of the I-V curves at high bias[106].

The current-voltage curve of metal sulfides generally shows a significant non-linearity at large bias due to the large contact resistance involved in the metal/semiconductor/metal system. When a semiconductor is sandwiched between two metal contacts, such as that in the typical metal/semiconductor/metal system, each interface behaves like a typical diode. The metal/semiconductor junction is generally represented with the I-V equation characteristic of a diode.

$$I = J_o \left[exp\left(\frac{eV}{K_B T}\right) - 1 \right] \quad (1.7)$$

Where I is the amount of current passing through the system is the applied voltage and J_o is the saturation current density. In the metal/semiconductor/ metal system, one of the contact is always on a reversed bias and can result in the sigmoidal I-V curves. In systems where the contact resistant (interfacial barrier) is higher than the resistance across the semiconductor nanowire, the field induced breakdown always result to very high positive curvature at large positive voltages.

Another reason why the I-V curves of metal/semiconductor/metal systems also results to non-linear curves is attributed to charge migration process in the set up as earlier suggested for thin films of semiconductors[108]. The counter ions that might be found in the nanowires due to the presence of DNA and adsorbed water molecules might also be transported alongside the electrons and gets collected at the electrode. The anions get collected at the positive terminal and the cation get collected at the negative terminal. This leads to the drop of potential across the space charge region at the metal/semiconductor electrode interfaces due to the applied voltage. This causes a sigmoidal I-V curve (negative curvature) with a linear region around very low bias with conductance related to the product of occupied and unoccupied sites density and the rate constant of electron self-exchange rate[109]. In this thesis, the I-V data generally has positive curvature $\frac{\partial^2 I}{\partial V^2} > 0$ and therefore the SCLC model is used to describe most of the data.

1.12 Mechanism of nanowire metal sulfide sensors

There is existing literature on the use of films of metal sulfide nanoparticles in gas sensing. Different mechanisms have been used to describe gas sensing in these metal sulfide nanostructures and we have employed these as our working hypotheses for the understanding for the response of DNA-templated sulfides in this thesis. The

mechanism most times are dependent on the prevailing conditions at which the reactions occur such as elevated temperature or pressure.

Two different hypotheses have been proposed for the sensing mechanism of metal sulfides resistors. The first is based on a potential barrier model used for explaining the mechanism of sensing nanoparticles thin films[110,111].This is because the biggest challenge in sensing thin film of nanoparticles is resistance to transport of charges across the inter-grain barrier. Even though this challenge is minimised by heating of the thin films at very high temperature to enable the sintering of the nanoparticles[112,113], there is a limited extent to which that can be attained. In templated nanowires, this challenge can effectively be addressed depending on the extent of templating to form smooth and continuous nanowires. This is why in the case of the DNA templated nanowires, we tried as much as possible to vary the concentration of the precursors so as to achieve smooth and conductive nanowires. This lowers the potential barrier significantly and improves it sensitivity to analytes. The schematic illustration of the sensing mechanism of DNA templated CdS nanowire is shown in figure 1.13.

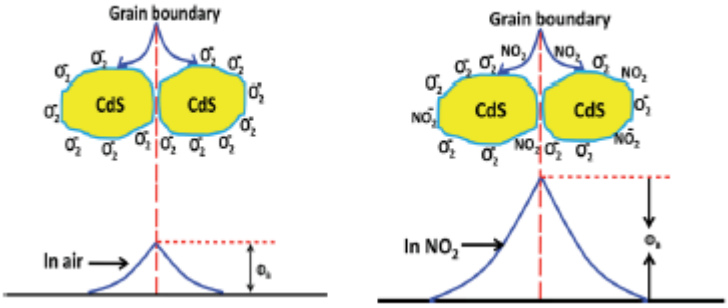

Figure 1.13 Proposed sensing mechanism of CdS nanomaterial based on inter-grain potential barrier changes[111].

The adsorption of the analyte (NO_2) in the example of figure 1.13 may alter the potential barrier experienced by an electron (or hole) moving from one particle to the next. This will be most significant for molecules with strong dipoles that can exert a larger electric field at the grain boundary.

The second mechanism is based on whether the analyte is either an oxidising or reducing vapour/gas. This can be explained based on the principle of increase or decrease in charge carrier density as the case might be accordingly. This results to lower conductance in the presence of the analyte compared to pure air as in case of

oxidizing gases/vapour or higher conductance as in case of reducing gases/vapour. This mechanism is what determines the selectivity of variuos analytes on a particular transducer. A scheme showing the mechanism of semiconductor nanowire in the presence of an analyte is shown in figure 1.14.

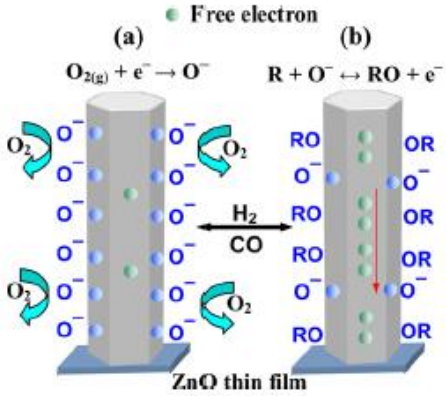

Figure 1.14 Schematic illustration of the mechanism of gas sensing using ZnO nanowire (a) in air (b) exposed to reducing gas (CO or H_2)[114].

In the case of the metal sulfide nanowire gas sensors used for sensing VOCs in this research, there is increase in conductivity in the presence of the VOCs because of their reducing nature. The concept is simply injection of charge carriers into the sulfide conductor. It should be noted that this mechanism often requires higher temperatures than the first because thermal activation of the reaction of the analyte is required in order to allow oxidation/reduction. In a later chapter we propose a variant on this mechanism which may be applicable at ambient temperatures.

1.13 Carbon nanotubes

The study of carbon nanotubes over the years has increased tremendously due to its fascinating optical, thermal, mechanical and electrical properties[115–119]. There are basically two structural types of carbon nanotubes that can have high structural perfections. Single walled nanotubes which consist of single graphite sheet perfectly wrapped to form a cylindrical tube and multi-walled carbon nanotube which contains an array of graphite sheets wrapped to form nest like rings[117]. The two types of carbon nanotubes are structurally similar and each can either be metallic or semiconducting depending on the direction the sheets are rolled to form the nanotubes. The graphite

sheet plane direction and nanotube diameter are obtained as pair of integer (n, m) that indicates the type of nanotube. The graphene sheet can be rolled up in various ways to produce different types of carbon nanotubes. The type of nanotube produce is defined by the chiral vector (C_h) as shown in figure 1.15 (b). The chiral vector (C_h) which shows the pointing from the first atom towards the second one is determined by the two integers (n, m) called chiral indices and is represented by the equation;

$$C_h = na_1 + na_2 \tag{1.1}$$

Where a_1 and a_2 are the vector lattice formed by the graphene sheets. The nanotube is either arm chair (n=m), zigzag (n=0 or m=0) or chiral (any other n or m) depending on the appearance of belt of carbon bonds around the diameter of the nanotube. All the arm chair nanotubes are metallic, others with n-m=3k, where k is not a zero integer are semiconductors with small band gap while all the rest are semiconductors too with their bandgaps inversely dependent on their diameter[120].

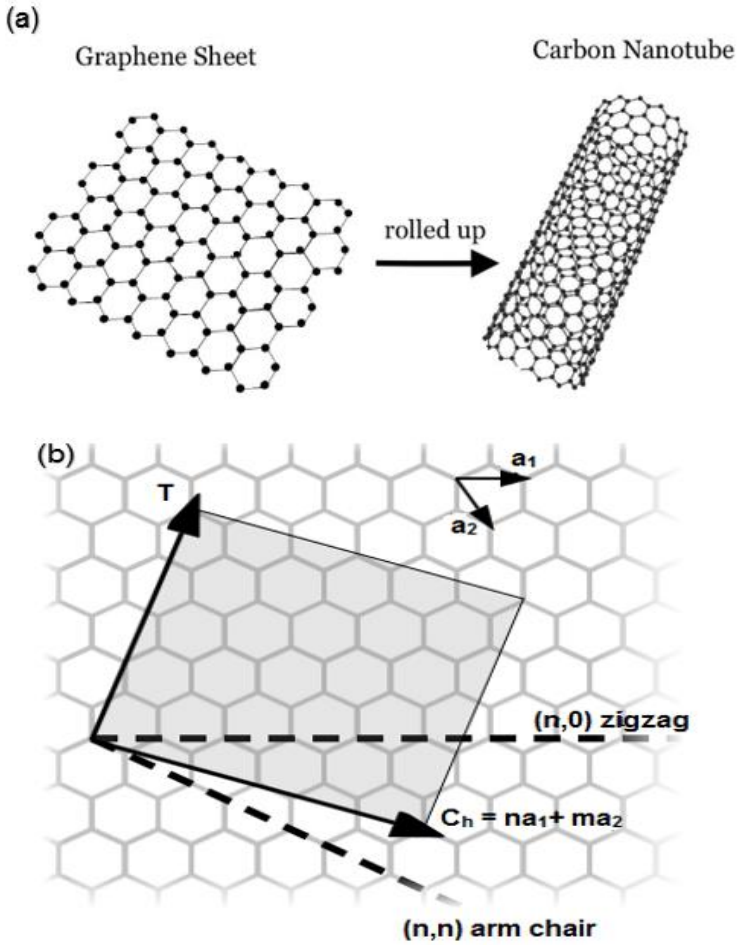

Figure 1.15 Schematic showing (a) how graphene is rolled up to form carbon nanotube (b) diagram of 2D graphene sheet showing the vector lattices.

Carbon nanotubes are usually made through laser ablation of carbon, carbon arc discharge or chemical vapour deposition[121]. Most of these known methods for synthesising carbon nanotubes result in nanotubes with high concentration of impurities especially for the SWCNT. The impurities can be removed through acid treatment which in turn causes the degradation of the nanotube length, introduce other impurities and increase the cost of production. All known synthetic routes results in the production of mixtures of various metallic and semiconducting nanotubes. The metallic nanotubes can be destroyed by electrical heating. All these processes results in very high cost of producing SWCNT and therefore it is more economical to use the more available MWCNT[122].

The diameter of nanotubes range from ~0.4 to 3 nm for the SWCNT and 1.4 to 100 nm for MWCNT .The nanotubes with small diameter has been reported to be quite stiff and strong with high tensile strength. The properties of the nanotubes can therefore be tuned by adjusting the diameter[121,123,124].

1.14 Aims and objectives

This project is aimed at using DNA template for synthesis of 1-dimensional nanostructures of semi-conductors by templating reaction of metal sulfides on DNA strands. The project explored some metal sulfide 1-dimensional (1-D) nanostructures such as CdS and ZnS that have been previously synthesised on DNA template with the view of optimising the templating techniques so as to produce smoother and more continuous nanowires that will be suitable for sensing. Another novel binary transition metal sulfide ($CdZnS_2$) will also be explored with the hope of preparing different kind of nanowires that would be tested for its sensing performance.

Throughout the project, a range of different analytical techniques have been used in order to characterise the different nanowires prepared so as to determine their structural properties, chemical composition and electrical properties. The analytical techniques that were used for the characterisations were ultraviolet-visible (UV-Vis) spectroscopy, Fourier transform infra-red (FTIR) spectroscopy, Raman spectroscopy, fluorescence microscopy, powder X-ray diffraction (XRD), X-ray photoelectron spectroscopy (XPS), atomic force microscopy (AFM), photoluminescence and transmission electron microscopy (TEM).

This project analysed results from different methods to determine the electrical properties of the DNA templated metal sulfide nanowires. The temperature dependence of the nanowire conductance was studied using two-terminal I-V measurements which would enabled the investigation of the thermal stability and conduction mechanism of the nanowire networks. Transient current measurements were used to determine the change in conductance of the nanowire with length and applied bias and contact resistance. Impedance measurements gave another determination of the contact and nanowire resistance at low applied bias. The synthesised DNA templated nanowires were used for the fabrication of sensors by aligning on platinum on silicon micro-band electrodes via molecular combing. The sensor were used for sensing VOCs such as ethanol, acetone, chloroform and hexane. The response transient, the response and recovery times, the sensitivity and selectivity towards the VOCs, effect of temperature and flow rate on the sensitivity are studied and reported. The mechanism of sensing of the metal sulfide nanowire sensors is also discussed.

The project also involved synthesis of multi-walled carbon nanotubes (MWCNT) - DNA nanocomposites by mixing and sonication to prepare 1-D nanowires. The nanocomposite nanowires were prepared by mixing MWCNT and different DNA volumes. They were characterised using atomic force microscopy (AFM), ultraviolet-visible spectroscopy and Raman spectroscopy, Fourier transform infrared spectroscopy (FTIR) and transmission electron microscopy to study their morphology and chemical composition. The different MWCNT/DNA nanocomposites were used to fabricate gas sensors for sensing various organic vapours such as methanol, ethanol, acetone and chloroform.

CHAPTER TWO
Materials, characterisation technique and experimental methods

2.1 Introduction

This chapter describes in detail all the various reagents and materials, surface treatment of substrates, alignment of the synthesised nanowires, and the methods involved in the synthesis and characterisation of cadmium sulfide (CdS), zinc sulfide (ZnS) and cadmium doped zinc sulfide ($CdZnS_2$),) templated on lambda DNA for preparing smooth and regular nanowires that can be used for gas sensing of volatile organic compounds (VOCs) such as ethanol, acetone, hexane and chloroform. The procedures for characterisation such as AFM microscopy, Fluorescence microscopy, PL spectroscopy, UV spectroscopy, Raman spectroscopy, FTIR spectroscopy TEM, XRD and XPS would be described in this chapter. The different electrical measurement techniques used and the method of fabrication of the sensor described.

2.2 Reagents and materials

The reagents and materials used during the synthesis, substrate treatment, alignment and gas sensing experiments includes cadmium nitrate [$Cd(NO_3)_2$.4H2O], zinc nitrate [$Zn(NO_3)_2.6H_2O$], sodium sulfide (Na_2S), ethanol, methanol, chloroform, hexane, acetone and chlorotrimethylsilane. All the chemicals used were of analar grade or equivalent. The chemicals were bought from Sigma-Aldrich and used as received without any form of purification. The three different kind of DNA that were used; lambda DNA (λ-DNA, Cat no.N3011L), herring testes DNA(HR-DNA) (type XIV, sodium salt) and Calf Thymus DNA (CT-DNA) (highly polymerised, 6% sodium) were all bought from New England Biolabs (UK) Ltd and used without further treatment. The herring testes DNA and calf thymus DNA were used in characterisation techniques that requires samples in large quantities because it is less expensive. Lambda DNA is used for most of the synthesis because of the length of the DNA strands (It has an approximate length of 16.7 µm).

The multi walled carbon nanotubes (MWCNT) used was purchased from Fisher Scientific Ltd. Silicon wafer p-Si<111>diameter (100 + 0.3 mm), resistivity (0.09- 0.12 Ωcm) and dopant (boron) was purchased from Pi-KEM Ltd. The prefabricated platinum microelectrodes on silicon were bought from Windsor Scientific limited, United

Kingdom while the interdigitated platinum electrodes was made by DropSens but bought from Metrohm Ltd, United Kingdom. All solutions were prepared using Nanopure^{TM} water obtained from Barnstead Diamond ^{Tm} reverse osmosis water purification system.

2.3 Surface pre-treatment of substrate

Mica surface and silicon wafers were used as substrates on which the prepared nanowires were deposited and aligned for morphological characterisation. The mica was cut into small squares of 0.5 x 0.5 cm^2 using a small sharp laboratory knife. The mica surface was treated by simply peeling off the top layers using tape in other to expose a fresh surface. Silicon wafers of dimension 1 x 1 cm^2 were cut using the tip of a diamond pen and each was properly washed with acetone and deionised water before drying with a stream of nitrogen gas. The wafers were then plasma etched for 15 minutes at 90 watts in order to remove organic residues on it by oxidizing the surface. The surface of the silicon wafers were then chemically modified by exposing it to chlorotrimethylsilane (Me_3SiCl) for 10 minutes in a process known as vapour deposition. This leads to generation of self-assembled monolayer of trimethylsilane. The interdigitated platinum electrodes used for electrical measurements are first soaked in piranha solution (a mixture of concentrated H_2SO_4 with H_2O_2 at a ratio of 4:1) for 30 minutes, after which it is sonicated with ethanol for 15 minutes and then washed with a large amount of deionised water. It is then dry using a stream of nitrogen before use.

2.4 Alignment of the nanowires on substrate

Alignment of the λ-DNA templated CdS nanowires was done on mica (glued to an iron metal disk) by depositing 5uL of the nanowire solution on a freshly ‘’cleaved’’ mica surface. The solution was allow to dry for about 3 minutes and then nitrogen gas was blown over it to ensure that the nanowires are combed in one direction (combing is a process where DNA and DNA templated materials are stretched on substrate ensure imaging and studies of surface properties). The combing also removes excess nanowires on the surface of the mica leaving behind a small amount of the solution which is then allowed to dry, leaving behind few aligned nanostructures which are then observed under the AFM[52]. The nanowires were also aligned on cleaned and chemical

modified silicon wafer same way as described in section 3.3. The same method used for mica and silicon substrate was used for alignment of the synthesised nanostructures on the micro-fabricated platinum on glass and platinum on silicon electrode for electrical measurement as well as for the sensor fabrication.

2.5 Synthesis of λ-DNA templated metal sulfide nanowires

The synthesis of the DNA templated metal sulfides were done in solution by addition of the metal salt and the appropriate sulfide source to DNA to form the metal sulfide as previously reported[63] with slight modification to ensure the formation of smooth, continuous and conductive nanowires.

2.5.1 Synthesis of λ-DNA/CdS nanowires

The templating reaction of λ-DNA and CdS that resulted to a regular, continuous and smooth nanowires was prepared by reacting an aqueous solution of λ-DNA (30 µL, 500 ng μL^{-1}) with an aqueous solution of $Cd(NO_3)_2$ (0.4 mM, 30 µL) and thoroughly shaken and kept for about 24 hours before adding about 30 µL of 0.4 mM Na_2S solution . The solution is thoroughly mixed and then kept for twenty four (24) hours at 4℃ . Next, is the addition of 3 µL of 40 mM aqueous $Cd(NO_3)_2$, which is allowed to react for 24 hours and then followed by introduction of 3 µL of 40 mM Na_2S solution. The solution is then kept for 24 hours at 4℃ and then is ready for characterisation.

2.5.2 Synthesis of λ-DNA/$CdZnS_2$ nanowires

The λ-DNA templated $CdZnS_2$ nanowires was synthesised by reacting an aqueous solution of λ-DNA (30 µL, 500 ng μL^{-1}) with an aqueous solution of $Cd(NO_3)_2$ (0.4 mM, 30 µL) and Zn (NO_3) (0.4 mM, 30 µL) before thoroughly shaking and adding about 30 µL of 0.4 mM aqueous Na_2S the next day. It is then incubated for 24 hours at 4°C, after which an aqueous solution of $Cd(NO_3)_2$ (40 mM, 30 µL) and Zn (NO_3) (40 mM, 30 µL) is then added before further incubation at 4℃ for 24 hours. The final stage is the addition of 30 uL of 40 mM Na_2S and keeping the solution for another 24 hours before characterisation. About 2 µL of the nanowire solution is then diluted to 100 µL and centrifuged (to remove the non-templated salt) before transferring 5 µL of the supernatant on to a clean mica or silicon wafer for AFM analysis.

2.5.3 Synthesis of λ-DNA/ZnS nanowires

Synthesis of DNA templated ZnS nanowire was done by reacting 50 uL aqueous solution of Lambda DNA (500 ng/µL) with 50 uL solution of 0.4 mM $Zn(NO_3)_2$ and then stirring it for a while before keeping at 4 ^oC Overnight. A 50 uL solution of Na_2S is subsequently added to the solution, stirred and then kept for 24 hours at 4 ^oC in the fridge. The process is then repeated with a higher concentration of 40 mM for $Zn(NO_3)_2$ and Na_2S respectively with 24 hour interval in between the additions and then allowed to stay overnight before the appropriate characterisations.

2.5.4 Synthesis of DNA-coated carbon nanotubes

The MWCNT solution was prepared by mixing 0.1 mg of carbon nanotube powder with 10 mL methanol. The solution is sonicated for 1 hour to ensure complete dispersion and reduce agglomeration of the nanotubes. The nanocomposites were prepared by reacting MWCNT dispersed in methanol solution with 2 uL, 5 uL and 10 uL of lambda DNA solution respectively and sonicating for few minutes and allowing it stay overnight before characterisation. The resultant nanocomposite formed clear solution after sonication. The various nanocomposites were labelled as N1, N2 and N3 respectively. The schematic illustration of the synthesis process is shown below.

2.6 Characterisation techniques

This section describes in detail all the characterisation techniques applied to 1-D templated nanostructures. These techniques are used to determine the size, diameter and smoothness of the nanowires and their suitability to be used as transducers in the fabrication of gas sensors. There are also several analytical techniques for chemical characterisation of semiconducting 1-D DNA templated nanowires.

2.6.1 Microscopy techniques

Microscopy is one of the most vital techniques for characterizing one dimensional nanostructures because it provides important conformational and morphological information. The techniques provides images of the synthesized nanostructures and in

most cases complements other analytical methods of studying the properties of these materials. These direct imaging techniques such as fluorescence microscopy, transmission electron microscopy and atomic force microscopy provides a very convenient way of characterising a range of nanostructures in different environments.

2.6.1.1 Fluorescence microscopy

Fluorescence is an optical process that involves the relaxation of an excited electron to a lower energy orbital in an atom or molecule with the corresponding emission of a characteristic photon with wavelength larger than that of the excitation light. The emitted light has longer wavelength than absorbed light because light with shorter wavelength has higher energy and some energy is always dissipated as heat e.g. via vibrational modes. The energy change in the transition is referred to as the Stokes shift. The process showing this molecular transition can be explained using the Jablonski energy diagram presented in figure 2.1.

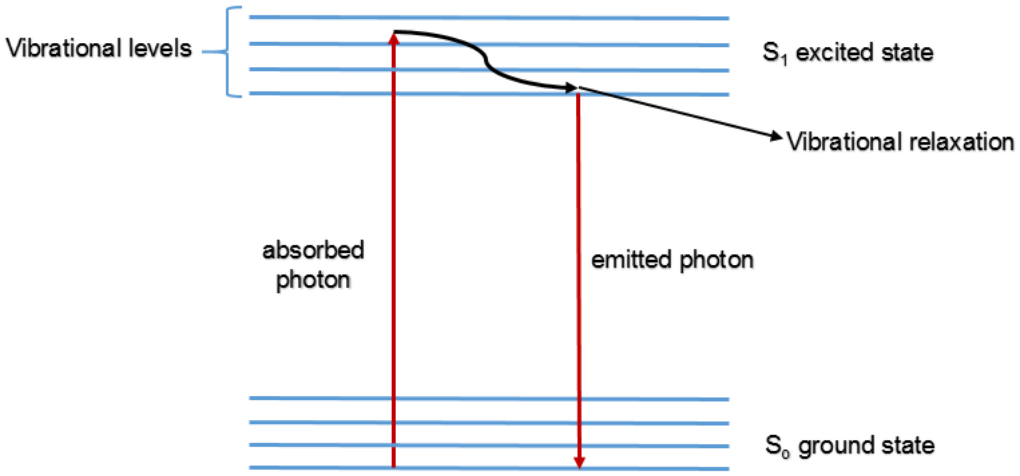

Figure 2.1 Jablonski diagram showing the changes in the electronic state of fluorescent substance during excitation and emission of photons.

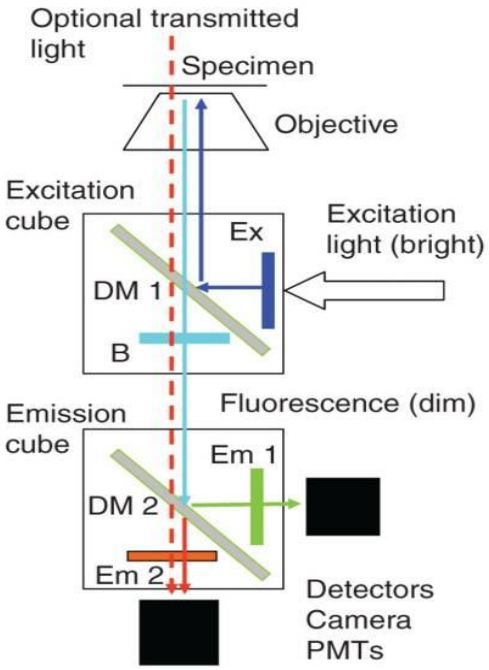

Figure 2.2 schematic representation of the basic light paths of a fluorescence microscope[125]. (Where EM1 and EM2 are emission filters while DM1 and DM2 are the dichroic mirror).

This technique would be particularly useful because it makes use of the fluorescence of the templated material since transition metal chalcogenides are used as the templating material. The technique showed a successful templating process since bare DNA does not absorb 488 nm light, nor does it emit visible fluorescence.

2.6.1.2 Atomic force microscopy

Atomic force microscopy (AFM) is the most common scanning probe microscopy used for imaging conducting, semiconducting and non-conducting surfaces[126]. It was invented in 1985 by Binning, Quate and Gerber[127]. It is one of the most powerful and versatile nanoscale microscopy techniques and is used for studying many different kinds of samples. It can generate images with minimum sample preparation at submicron scale lateral resolution and sub-nanometre vertical resolution. It can also be used to obtain different kind of surface measurement (mechanical, electrical, magnetic and thermal properties). The AFM operates by measuring the deflection of a sharp tip attached to a flexible cantilever. The deflection is measured by reflecting a laser beam off the reflective back side of the cantilever and directing it to a split photodiode position detector.

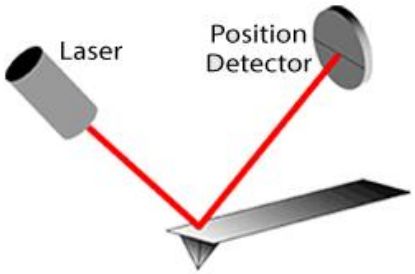

Figure 2.3 Schematic illustration showing laser light deflection off cantilever during AFM measurement[128].

The AFM cantilevers and tips used as probes are normally made from Si or Si_3N_4 with the tip radius in the range of a few nanometres. The images in AFM are acquired by measuring the lateral and vertical deflections of the cantilever between the tip and surface. If the stiffness of the cantilever is known, then the change in height of the tip is related to the force by Hooke's law.

$$F = -kz \tag{2.1}$$

Where F is the force, z is the deflection of the cantilever and k is the stiffness of the cantilever. The deflection of the cantilever is monitored by the amount of laser beam light reflecting back to detector. The different signals of the deflection are collected and processed into a topographical image of the sample surface, usually in false colour.

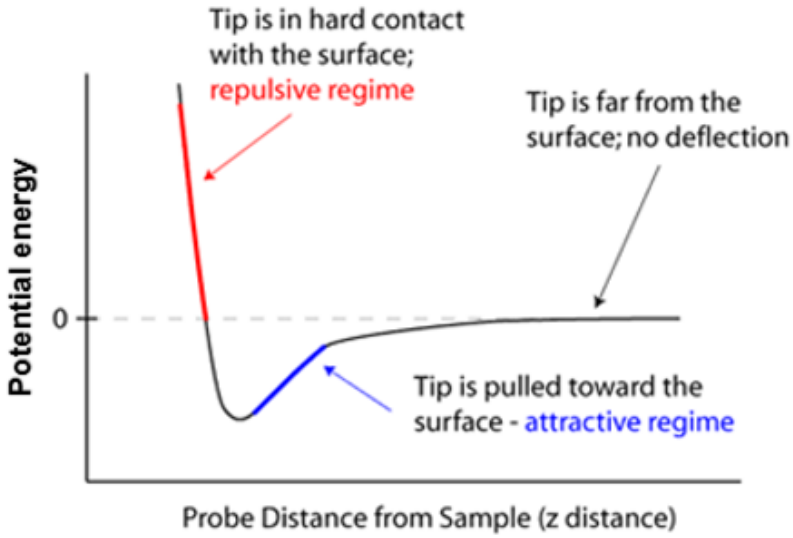

Figure 2.4 The sample- tip separation showing the attraction and repulsion forces as a function of probe distance from sample during AFM measurement.

The general scheme illustrating the different components and the working principle of an AFM is shown in figure 2.5. It consists of a piezoelectric scanner which controls image acquisition with precise control of the probe in relation to the sample surface in three dimensions. A cantilever with a tiny probe attached to it which scans across the surface when the cantilever is in motion. A split photodiode which measures the deflection of the cantilever, a laser with sets of mirrors and a z-axis feedback loop which controls the vertical movement to and from the sample, the control electronics and an attached computer system for data display and analysis. In this research, the AFM was used to acquire the morphological properties of the DNA templated nanowires and nanotubes such as diameter and height.

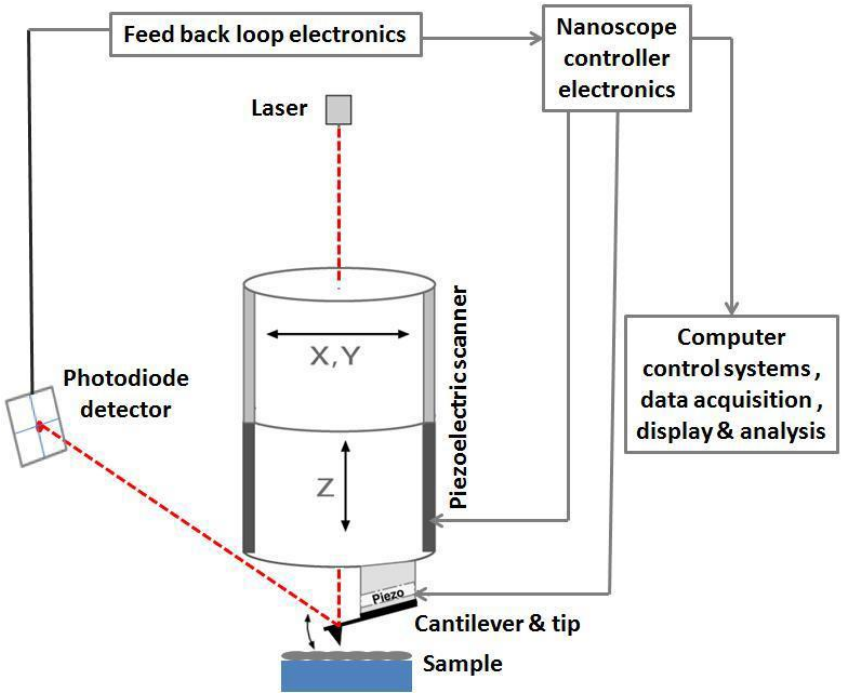

Figure 2.5 Schematic diagram of atomic force microscopy showing how topological images of nanomaterials are obtained[129].

2.6.1.3 Transmission electron microscopy

The transmission electron microscope is a vital instrument for imaging ultrathin samples of nanostructures. In transmission electron microscopy (TEM), an electron gun with accelerating voltage typically within 100 - 400 kV with high penetrating power is channelled through a sample. The electrons undergo a range of scattering processes when in contact with the sample resulting in changes in their angular distribution and energy. The regions of the sample with higher electron density scatter

the electrons more intensely and through a greater angle leading to the area appearing darker in the image[7]. The transmitted electron beam through the ultrathin sample is scattered into a non-uniform electron intensity after transmission. The non-uniform electron intensity is collected on the detector and is converted to a contrast image on the screen. The direct beam is used to form the bright field image while the diffracted beam forms the dark field images[130]. The process of the image formation using the direct beam in the bright field mode is presented in figure 2.6.

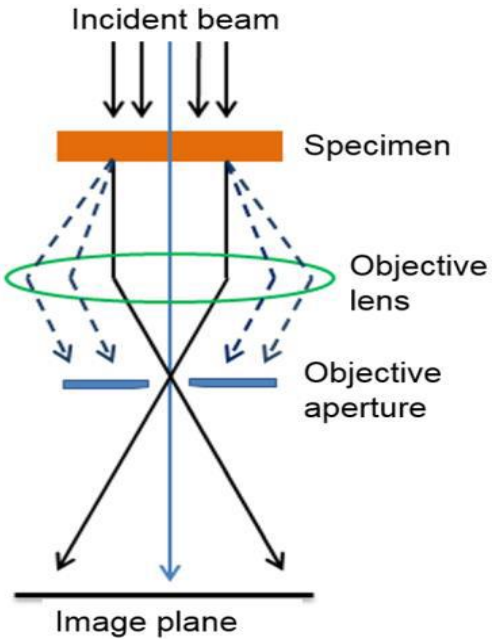

Figure 2.6 Schematic illustration showing the process of image formation in a typical TEM in bright field image mode. The scattered electrons are indicated with the dash lines.

The objective aperture blocks the scattered electrons in order to improve the contrast. The primary beam interacts with the sample and produces other secondary signals too which can be used in determining the chemical composition and other relevant properties of the sample[131]. TEM experiments are carried out in an ultra-high vacuum environment to prevent the scattering of the electrons by atmospheric gas molecules and thereby reducing the electrons passing through the sample and further to the detector. TEM was used in this research to acquire the morphology of the templated material since DNA appears ‘transparent’ under the electron microscope.

2.6.2 Spectroscopy techniques

2.6.2.1 Ultraviolet spectroscopy

UV-Vis spectroscopy is a basic characterisation technique used to investigate the electronic structure of semiconductor materials through their interaction with light. When light is incident on a material, the light is either absorbed, reflected or transmitted[132]. UV-Vis spectrometers measure the extent of this interaction, which provides information on the bandgap of semiconductor materials; this is related to the energy threshold above which absorption of light occurs. The band gaps are of great interest because they provide insight about the electrical properties of semiconductors. The UV –Vis spectra obtained in our studies are due to transitions from the valence to the conduction bands of the metal sulfides.

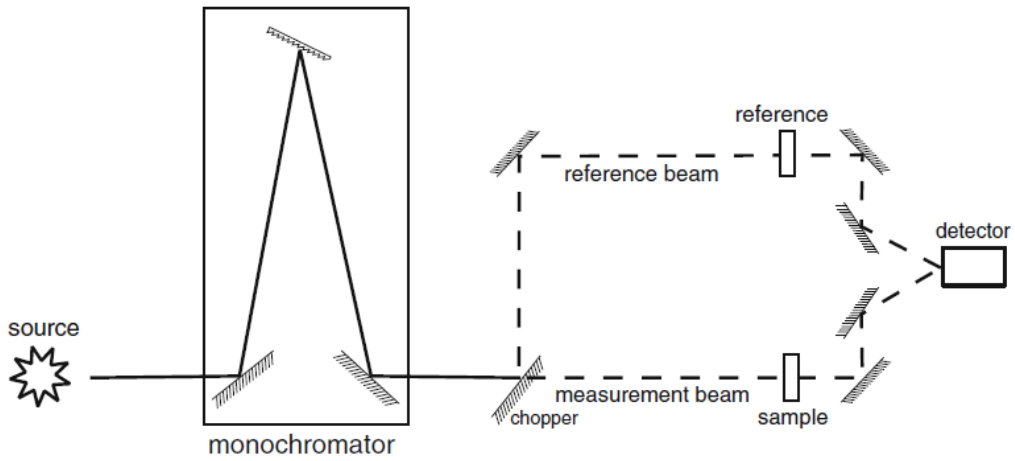

Figure 2.7 Schematic diagram showing the transmittance operation mode of a dual beam spectrophotometer[132].

2.6.2.2 Fourier transform infrared spectroscopy

Fourier transform infrared spectroscopy (FTIR) is used for determination of functional groups and can also be used to acquire information on the nature of chemical bonding of compounds[133,134]. When nanomaterials are exposed to IR radiation, they absorb radiation at certain frequencies that correspond to their vibration modes. The chemical bond in molecular materials vibrates at characteristic frequencies determined by the force constant of the bond and the atomic masses.

In the harmonic oscillator approximation:

$$f = \bar{\nu}c = \frac{1}{2\pi}\sqrt{\frac{k}{\mu}} \quad (2.2)$$

Where *k* is the force constant and μ is the reduced mass; functional groups with strong bonds and light atoms therefore have high vibration frequencies *f* and high wavenumbers $\bar{\nu}$ in the FTIR spectrum.

The IR spectrum can be collected by determining the amount of incident radiation that is absorbed at a given frequency when infrared radiation is passed through the sample[135]. Here, the vibration modes of pure DNA and the DNA-templated materials were obtained and compared to see the effect of the interactions on the vibrational bands. This gives an idea where the binding and type of bonding in the templated materials.

2.6.2.3 Raman spectroscopy

Raman Spectroscopy is a vital method used in the studies of semiconductors and semiconductor doped materials. It can be used for studies of extrinsic and intrinsic properties of semiconductors and non-metals[136]. It is usually employed to determine chemical composition, crystal orientation, crystal quality and structure, optical interaction, interface and surface chemistry, strain and dopant concentration[137].

In Raman spectroscopy, scattering of the incident photon and emission of scattered photon off the molecule occurs with transfer of energy between the molecule and the photon-this is called inelastic scattering or Raman scattering. This Raman scattering is caused by the modulation of the dielectric polarisation produced during excitation of crystals with finite energy and momentum[137]. The incident photon that interacts with the molecule may be scattered elastically with same energy as the incident light (Rayleigh scattering). The photon can also interact and transfer energy to the molecular vibration bonds of the molecule and therefore result in inelastic scattering with different energy from that of the incident light[138] (Raman scattering). The process is distinct from photoluminescence in which light is absorbed and then emitted; however, the instrument has many similarities to a fluorescence spectrometer because it also involves measurement of light intensity from the sample.

The process of Raman scattering can be considered in terms of virtual excited state as shown in figure 2.8. This virtual state has less energy than the normal excited state

produced by absorption of a photon. When the photon in the virtual state is emitted, its energy is slightly different from the incident photon. The emitted photon ends up in a longer wavelength (red shift) vibrational state when the incident photon loses energy to the molecular bond vibration (Stokes scattering). When it gains energy during the transition (anti-Stokes scattering), the molecule emits a photon with lower wavelength (blue shift) than the incident wavelength. The wavenumber difference between the incident and scattered photon is referred to as the Raman shift[139]. As each molecule has its own unique bonds and vibrational modes, this process provide fingerprint information about the molecule very similar to that from FTIR absorption spectroscopy. However, because the technique typically involves visible light, which has much shorter wavelength than IR light, the excitation source can be focused to a small spot and Raman spectra can be obtained during an imaging experiment as the laser spot is scanned across the sample. The technique was used here to confirm the formation of the metal sulfide on DNA via the characteristic vibration modes for M-S.

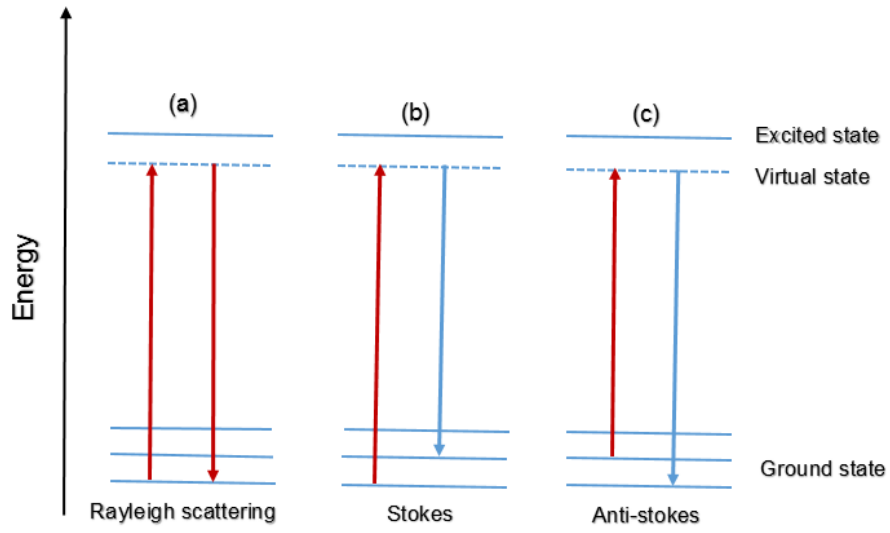

Figure 2.8 Schematic diagram showing the energy transitions involved in (a) Rayleigh scattering (b) Stokes scattering and (c) anti-Stokes scattering.

2.6.2.4 Photoluminescence

Photoluminescence is a phenomenon in which a material radiate photons when they absorb light. It is a very useful technique for studying nanomaterials because it reveals many important intrinsic properties of the material. It can be used in the studies of templated nanowires because it reveals optical and electronic properties of the nanowires such as quantum confinement, radiative efficiency, band edge emission and

trap states[140,141]. It was used to obtain the band edge emission and trap state luminescence of the templated metal sulfides.

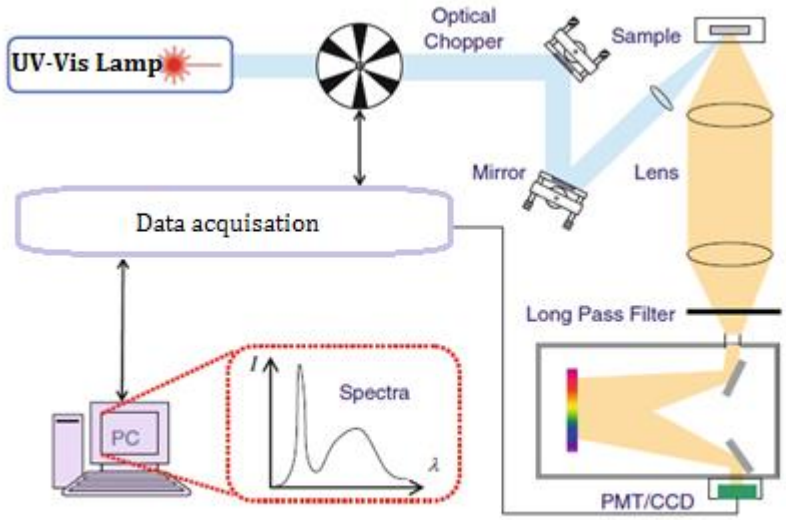

Figure 2.9 The schematic illustration of Photolumiscence measurement experimental set-up[142].

2.6.2.5 X-ray diffraction

XRD is a powerful method extensively used in the study of crystal structure, stresses and defects in nanomaterials. The wavelength of X-rays used are on the atomic scale and therefore can be used to probe the structure of nanomaterials. The intensity data obtained from XRD studies can provide accurate and qualitative information about the arrangement of atoms at interfaces which leads to determining atomic spacing and strain states[143]. The method is non-destructive and non-contact and therefore can be applied to different kind of samples. An X-ray diffractogram provides detailed information about the crystallite size, phase composition, crystallographic orientation and lattice strain. The process identify specimen components by searching and marching with previous obtained data in the database. It therefore serve as a fingerprint for identification of pure sample substances[143].

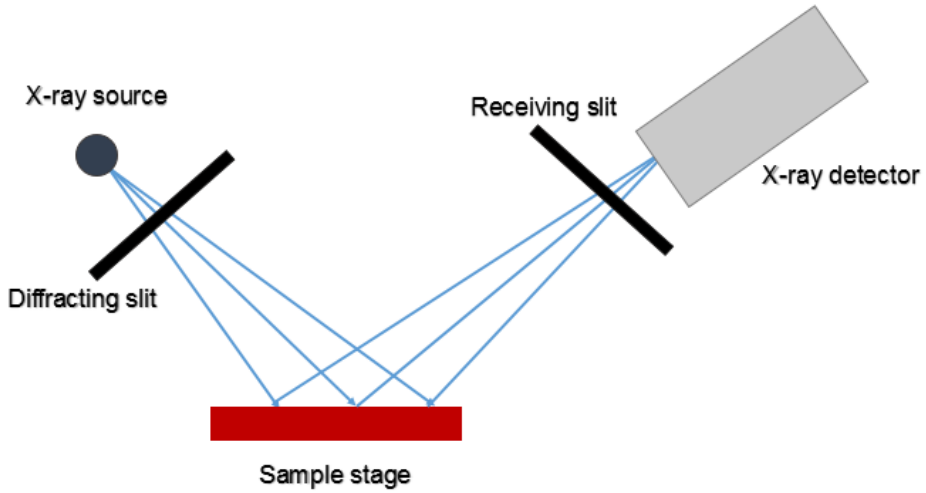

Figure 2.10 The basic component of an X-ray diffractometer.

An X-ray diffractometer usually consist of four basic component such as X-ray source, sample stage, optical slits and X-ray detector. In XRD, the data is acquired by diffracting a beam of X-ray with a wavelength ranging from 0.07 nm to 0.2 nm on a crystalline sample according to Braggs law;

$$\lambda = 2dsin\theta \tag{2.3}$$

Where λ is the wavelength of the X-ray, d is the inter-planar distance. The diffracted beam intensity is measured as a function of diffraction angle (2θ) and sample orientation. The intensity of the diffracted signal are usually plotted against the diffraction angle 2θ. A series of peaks at well-defined values of 2θ appears where the path length difference between beams diffracted from the 1st, 2nd etc atomic layers are in-phase. For a crystal of infinite extent, the destructive interference between beams scattered at angles other than those given by equation (2.3) is complete and the peaks are sharp. However, for finite crystals, there is some contribution of neighbouring angles to the scattered intensity and the peaks appear broad. The line broadening from the plot can be used to determine the average crystallite size of the nanomaterial using the Scherer formula.

$$\text{Scherrer } (D) = \frac{K\lambda}{\beta Cos\theta} \tag{2.4}$$

Where K ~ 0.94 is the Scherer constant, λ is the wavelength of the X-rays, β is the full width at half maximum (FWHM) height of the diffraction peak and θ is the diffraction angle. The crystal structure and crystallite size of the synthesised metal sulfides nanowires were determined using powder X-ray diffraction.

2.6.2.6 X-ray photoelectron spectroscopy

XPS is an essential analytical technique that is used to acquire information about the surface composition and electronic state of different samples[144]. The surface of the sample is irradiated with X-ray source which leads to absorption of radiation. The molecule/atom that absorbed radiation undergoes ionisation and emission of electrons which are then analysed. Different X-ray sources such as AlKα (1486.6 eV) and MgKα (1253.6 eV) with different wavelengths can be used to acquire the spectra. An ultraviolet energy source at 21.2 eV are sometimes used to provide information about high count rates at low energy region which contains information about the valence band[145].

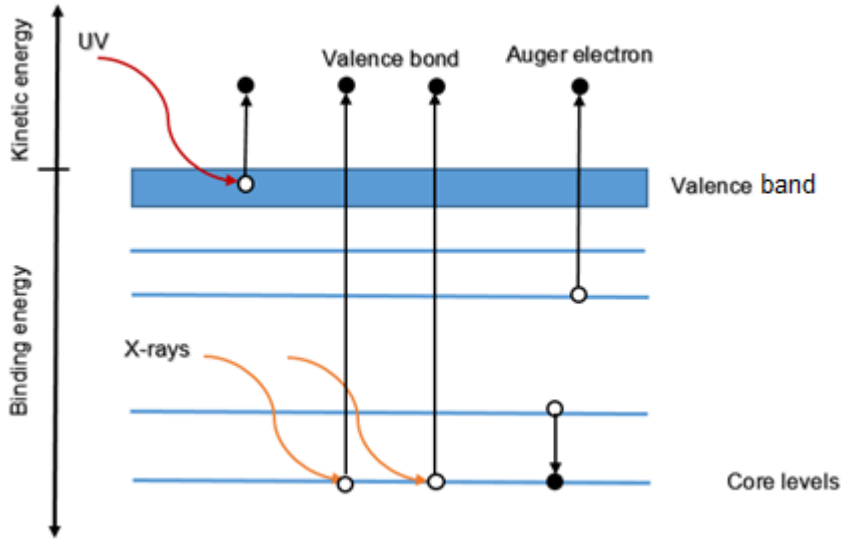

Figure 2.11 An illustration of how X-ray radiation causes an emission of photoelectrons.

The irradiation of a specimen with X-ray photons of energy hv causes the emission of electrons from atoms on the surface region. The photons with higher energy penetrates deeper into the sample surface and causes the emission of electrons from the inner atomic energy levels with binding energy BE. The emitted electrons from the inner energy level is called photoelectrons[146]. The generated photoelectron have kinetic energy KE. An example of emitted photoelectron due to incident photon from X-ray is shown in figure 2.12. The XPS spectrometer only detects photoelectrons originating close to the surface because, although the radiation penetrates a few micrometres, only those electrons within a few nm of the surface escape without undergoing inelastic

collisions[147]. The kinetic energy of the emitted photoelectrons can be obtained and the binding energy of the electrons calculated with the simple equation;

$$KE = hv - BE + \varphi \tag{2.5}$$

Where hv the energy of the X-ray source and φ is the work function (the minimum amount of energy required to remove an electron completely from the inside of a solid to its surface) and BE is the binding energy of the electron. A typical XPS spectrophotometer comprises of three basic components. An X-ray source, an electron energy analyser and a high vacuum environment. A scheme showing the key component of an XPS spectrophotometer is shown in figure 2.12. An XPS spectrum shows characteristic peaks of binding energy values that corresponds to elements found on the surface of the specimen been analysed. This helps in identification of component element in samples. It was used in this research to prove the formation of metal sulfides on the DNA template and also provide information about oxidation state.

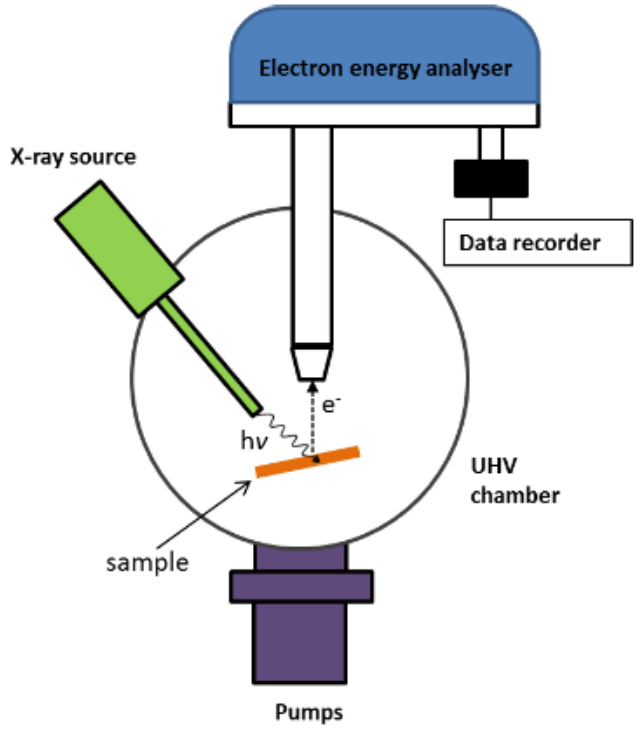

Figure 2.12 The key components of an X-ray photoelectron spectrophotometer[148].

2.6.3 Electrical measurements

The electrical properties of the synthesised nanowires were studied using two terminal I-V measurements, Impedance spectroscopy and transient current measurements.

These investigation provide information on the bulk resistance of the nanowires and the electrode/nanowire contacts.

The electrical properties of the prepared DNA templated metal sulfide nanowires was first determined by carrying out two terminal current-voltage (I-V) measurement of the nanowires using the probe station. They I-V measurement were carried out using a Cascade Micro-tech probe station and the readings collected using a Hewlett Packard Agilent Technologies B1500A Semiconductor Device Analyzer driven by an Agilent Easy EXPERT software. Impedance spectroscopy can be used to effectively determine the resistance of a two terminal device as well as ascertain the various contribution of the contact resistance between the two electrodes and the nanowire resistance. It can also be an important characterisation technique for determining the electrical properties such as conductivity and electron transfer mechanism of nanomaterials. The impedance measurement of the aligned sample was carried out with a PalmSens^3 potentiostat (PalmSens Compact Electrochemical interfaces, Houten Netherlands). The transient current measurement was also carried out to determine the conductivity of the synthesized nanowire by measuring the change in conductance of the nanowire with length. The method was also used to determine the separate contribution of contact resistance and the nanowire resistance to the overall resistance of the two terminal device. The transient current of the device was measured by connecting it to the PalmSen^3 potentiostat via the crocodile clips. The detailed working principle and the mathematical derivations of the electrical measurement procedure are explained in chapter 5.

2.7 Experimental methods for the metal sulphide templated DNA nanowires.

2.7.1 Atomic force microscopy

The solutions for AFM analysis were synthesised as stated above in section 3.5. The samples were prepared by depositing and aligning 5 uL solution of the λ-DNA templated metal sulfide nanowires synthesised on a freshly cleaved mica surface or functionalised silicon wafer. The detailed procedure for depositing and aligning the nanowires on the substrate surface is described in section 3.4. The AFM data of the surface topography were acquired using the ScanAsyst® imaging mode of the Nanoscope Multimode VIII system (Bruker Daltonics Inc., Manning Park Billerica, MA,

USA) in air using silicon nitride probe cantilever (Bruker Daltonics Inc., Manning Park Billerica, MA, USA) with a spring constant of 0.4 N/m and a resonance frequency of 150 kHz. The AFM Data analysis was carried out using Nanoscope analysis software version 1.50 (Bruker Daltonics Inc.,).

2.7.2 Fluorescence microscopy

Fluorescence images of the λ-DNA templated nanowires were obtained by dropping 5 uL of the sample solutions on a cleaned and functionalised silicon wafers and allowing it to dry at room temperature in the laminar flow fume hood. The images were captured using an epifluorescence Axioplan 2 microscope (Zeiss) with an AxioVision Viewer 3 software. The samples were excited using a Hg lamp light passing through a band pass filter of 300-400 nm with a maximum transmittance of 65% at λ= 365 nm. For better images of the single strand nanowires, the magnification x40 was used.

2.7.3 Photoluminescence

The sample for photoluminescence measurement was prepared same way as stated above in section 3.5 but further diluted to obtain a higher volume. The photoluminescence spectra of the synthesised DNA templated nanowires were measured using a Shimadzu RF-6000 Spectro Fluorophotometer using a UV quartz cuvette (20 uL) with a path length of 10 x 2 mm and the system was controlled using Lab Solutions RF software.

2.7.4 Raman spectroscopy

Raman spectra of the λ-DNA templated CdS nanowires were obtained on the same solution synthesised for AFM analysis. The sample was prepared by depositing 5 uL of the sample solutions on a functionalised (see section 3.3) silicon wafers (because of its high hydrophobicity which aids in the molecular combing of the nanowires) and allowing it to dry at room temperature under the fume cupboard to prevent contamination. A CRM 200 confocal Raman microscope (Witec GmBH, Ulm, Germany) that is equipped with a cooler CCD detector, a Raman edge filter to reduce elastic scattering of light and diode laser (λ= 488 nm) as source of excitation light were used to obtain the Raman spectra.

2.7.5 Ultraviolet-Visible spectroscopy

The sample for UV-Vis absorption measurement was prepared same way as that used for AFM studies but since larger volume of solution was required, higher volume of the various reagent were used during sample preparation. The solution was further diluted in tenfold so as to reduce the absorption intensity. The UV-Vis spectra were obtained by using a Varian Cary-100 Bio UV-Vis spectrometer. The spectra were recorded in the range of 250-700 nm at a data interval of 0.5 nm. Deionised water was used as the background solvent since all samples were in aqueous state.

2.7.6 Transmission electron microscopy

The sample used for TEM was same as that synthesised in section 3.3 above. The sample was prepared for the TEM analysis by dropping 2 uL of the synthesised sample solution on a holey coated copper grid and allowing the solvent to slowly evaporate at room temperature, leaving behind aligned nanowires for imaging. The TEM images were obtained using a Philips CM-100 TEM operating at an accelerating voltage of 100 kV.

2.7.7 Fourier transform infrared spectroscopy

The sample of λ-DNA templated nanowires that were used for FTIR characterisation was same as the solution synthesised for AFM analysis. About 20 ml of the synthesised solution was deposited on a functionalised silicon wafer substrate and allowed to dry for about 4 hours in the fume hood. In order to have enough material for obtaining a good spectrum, the process was repeated thrice.

The FTIR Spectra were recorded in the range of 400 cm^{-1} to 4000 cm^{-1} with about 32 scans (collected and averaged) by using a Shimadzu IRAffinity-1S Fourier Transform Infrared Spectrophotometer operating at 4 cm^{-1} spectral resolution and with a DTGS detector system. A plasma etched clean silicon wafer was used as the background.

2.7.8 Powder X-ray diffraction (XRD)

In order to have enough sample for X-ray Diffraction data collection, the concentration and volume of the reagent used was increased significantly so as to get enough precipitate for powder XRD. Samples for XRD were prepared by mixing an aqueous solution of Herring DNA (1 mg mL^{-1}, 10 mL) and metal salt (0.5M, 10 mL) and then stirring the reaction mixture and allowing it to rest for about 3 hours before adding Na_2S (0.5M, 10 mL). The formation of precipitate was indicated by a yellow colour. The reaction mixture was then stirred and left to stand overnight at room temperature to allow the formation and settling of the precipitate formed to the bottom of the vials. The supernatant was carefully decanted and the yellow precipitate collected over Buchner funnel. The precipitate was then washed severally with deionised water and ethanol and dried in air. PANalytical X'pert Pro diffractomer equipped with a Cu $K\alpha_1$ radiation source (λ = 1.54 x 10^{-10} m) was used to obtain the powder X-ray diffraction data.

2.7.9 X-ray photoelectron spectroscopy

The sample that where use for AFM studies was also used for XPS characterisation. In the case of XPS studies, the sample was not diluted because a chuck of about 10 um in height was required to obtain significant signal. The solution of about 80 uL was deposited on a plasma etched silicon with high hydrophobicity (to enable sufficient sticking of the sample to the silicon wafer) in series of about 20 uL for about four times to obtain a sufficient chunk of material in the middle of the silicon wafer for effective signal acquisition.

The X-ray photoemission spectra of the various DNA templated nanowires samples were recorded using a monochromic Al Kα X-ray excitation source of a Thermo scientific K-Alpha X-ray photoelectron Spectrometer with a 30-400 µm in 5 µm steps variable spot size. The photoelectrons were recorded using the multichannel detector after filtration with the hemispherical analyser. A dual beam charge neutralisation gun was used for compensating of the charging surface and acquisition was obtained at a take-off angle of 90°. The calibration of the binding energies obtained was done using hydrocarbon C1s peak at 284.1 eV as the reference. The Casa XPS software (www.casaxps.com) was used for peak fitting of the data obtained.

2.7.10 Electrical measurement

The electrical measurement of the templated nanowires were determine using two terminal I-V measurement with probe station, ac impedance measurement and transient current measurement. The detailed descriptions of the methods are discussed below.

2.7.10.1 Two terminal I-V measurement

The electrical measurement of synthesized nanowires was done using two different kind of electrodes. A prefabricated platinum microelectrodes on silicon which consisted of four individually distinct micro-bands electrodes that were formed by patterning a high graded platinum films on an insulating silicon substrate via microelectronic technology. The four (4) micro-bands are separated by a width of 10 µm and the length of the micro-bands is 2 µm. This electrodes where bought from Windsor Scientific limited, United Kingdom. The second type of electrodes that was also used were interdigitated platinum electrodes (IDEs) which are made up of two interdigitated electrodes with two connection tracks of platinum micro-fingers on a glass substrate. It is very suitable for working with very low amount of sample and quite easy to use as well. The two kind that was bought has micro- fingers separated by 5 µm and 10 µm respectively with the former particularly suitable for electrical measurement of nanowires with short length.

The samples were prepared by aligning 2 uL of the synthesised DNA templated nanowires across the gaps between the platinum micro-electrodes on the various substrates by molecular combing. The electrical measurements were carried out using the two types of electrodes described above on a Cascade Micro-tech probe station and the readings collected using a Hewlett Packard Agilent Technologies B1500A Semiconductor Device Analyzer driven by an Agilent Easy EXPERT software. In each of the measurements, the current was obtained in steps of 0.2 V for an applied voltage range of -2 V to 2 V. All the readings were obtained at room temperature in the dark in nitrogen except for measurement of current at different temperatures. The different temperatures were obtained by connecting the probe station to an ESQEC ETC-200L thermal chuck.

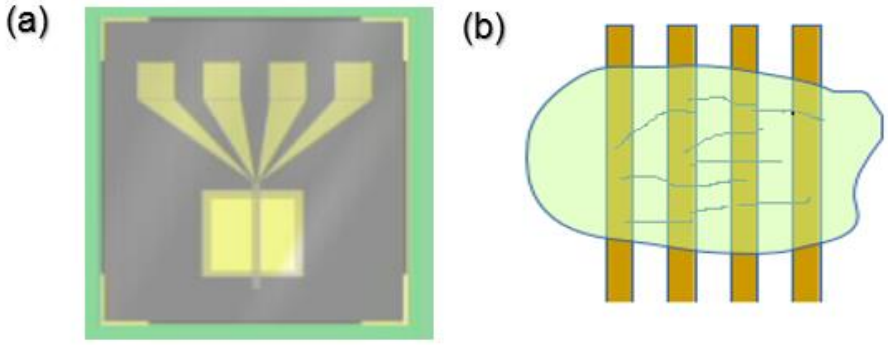

Figure 2.13 (a) Image of the micro-band chip used for electrical measurement (b) image of the micro-band fingers where the nanowires are deposited.

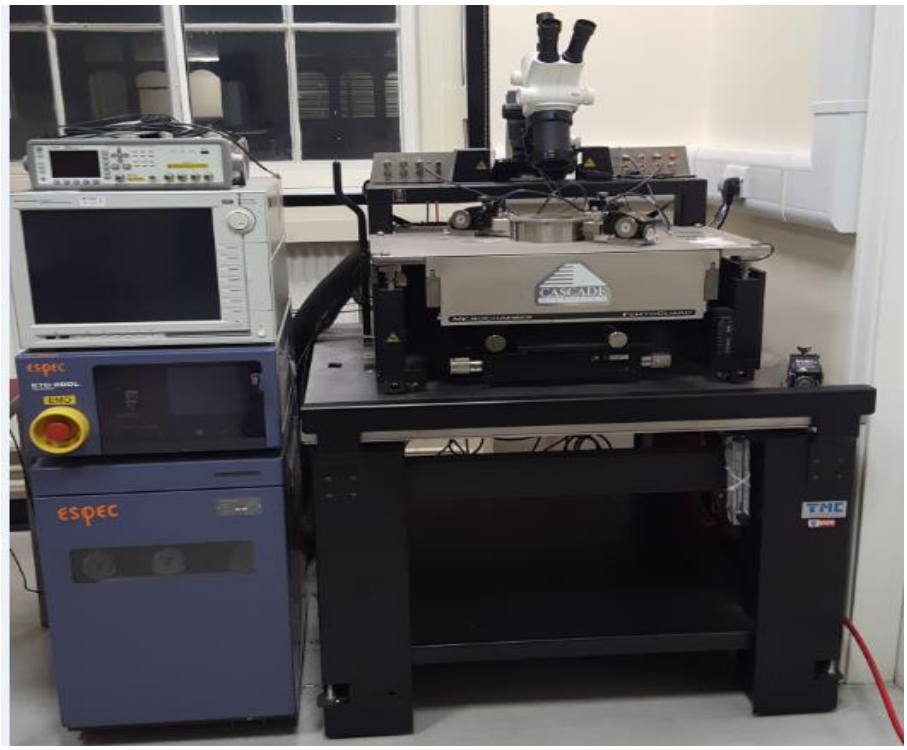

Figure 2.14 Photograph showing Hewlett Packard Agilent Technologies B1500A Semiconductor Device Analyzer attached with an ESQEC ETC-200L thermal chuck used for the I-V measurement at different temperature.

2.7.10.2 Impedance Measurement

The sample of the nanowire was carefully aligned on the electrode by drop casting and combed with the tip of the pipette and dried in air under the fume hood. A total of 3 µL of the sample was deposited on the electrode by dropping 1 µL at a time. This was done to avoid spreading of the sample beyond the electrode and to ensure the concentration of the sample on the electrode.

The impedance measurement of the aligned sample was carried out with a PalmSens^3 potentiostat (PalmSens Compact Electrochemical interfaces, Houten Netherlands). The electrode which was connected with wires was contacted to the potentiostat using crocodile clips. The wires were four and the distance between it was 20 µm. The change in conductance with distance was measured by contacting two wires at a time corresponding to 20, 40 and 60 µm. The measurement was obtained using the PSTrace 4.8 software using the impedance spectroscopy technique. The data was obtained as Nyquist plot with an applied ac voltage amplitude of 0.2 V. This was done at a frequency range of 0.1- 10000 Hz with a minimum acquisition time of 3 s and maximum equilibration time of 2 s.

2.7.10.3 Transient Current Measurement

The sample used for the transient measurement was prepared same way as that for EIS as described in Section 3.6.10.2. The transient current of the device was measured by connecting it to the PalmSen^3 potentiostat via the crocodile clips. The collection of data was done using the multistep amperometric technique of the PSTrace 4.8 software. The measurement was obtained at time interval of 0.1s. The data was collected as a function of distance for the three electrode separations 20, 40 and 60 µm. The collected data was in the form of current against time plot which was obtained at different voltage. It was then analysed to obtain the total resistance at the different voltages and plotted as a function of distance. The nanowire resistance per unit length was obtained from the slope of the plot while the contact resistance from the intercept.

The total resistance of the nanowire can be determined according to figure 2.15 where E is the applied potential, R_b is the contact resistance, i_{ss}, R_c is contact resistance is transient time and τ is the lifetime.

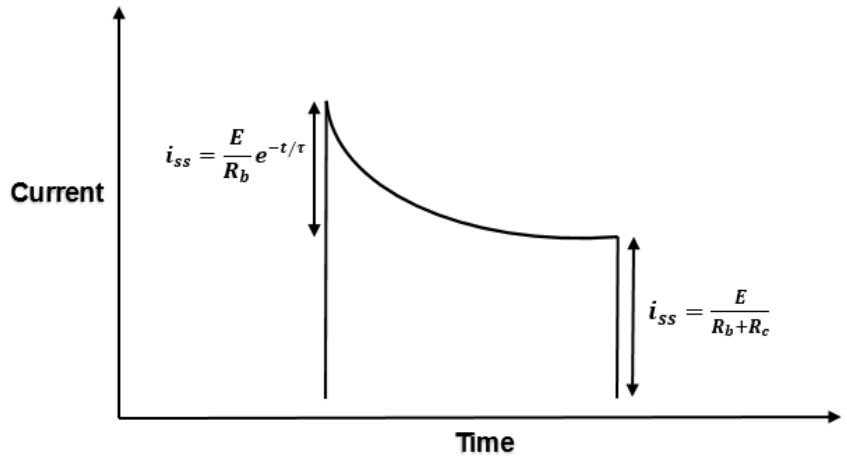

Figure 2.15 An illustration of how to calculate the total resistance of the templated nanowire device from transient current measurement.

2.8 Fabrication of the gas sensor

The sample for gas sensing was carefully aligned on the micro fabricated electrode by drop casting. In order to have sufficient sample for good response, about 2 uL of the sample was carefully combed on the electrode and allowed to dry in air under the fume hood and the process is repeated thrice so as to have a thick film of aligned nanowires on the platinum electrode. The dry sample on the electrode is then inserted into a glass cell and then connected to the mass flow controller (MFC) gas sensing system. An optical image of the nanowire network film on the electrode and how it is inserted in glass cell has been shown in figure 2.16.

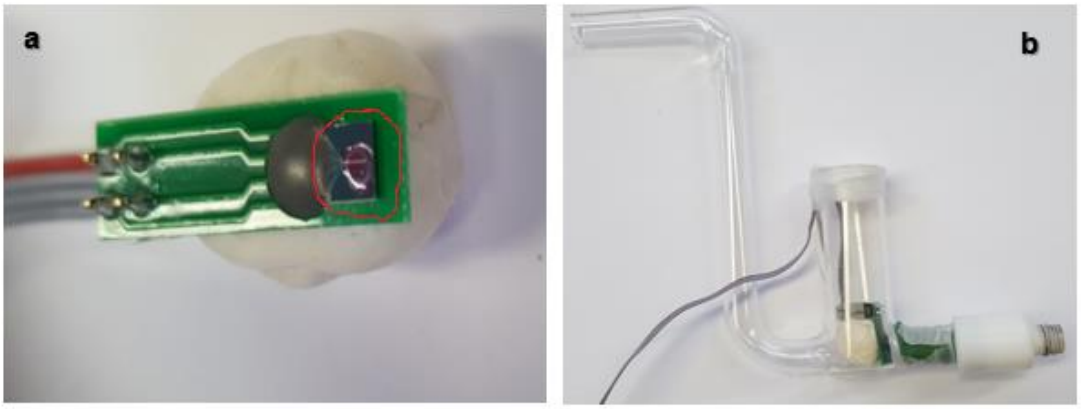

Figure 2.16 A photograph image of (a) the fabricated gas sensor showing the electrodes on which are aligned DNA templated nanowires (red circle) (b) the sensor device in a glass cell ready to be connected to the gas sensing set-up.

2.9 Gas sensing flow system

The schematic representation of the gas sensing set up showing all the components has be presented in figure 2.17. The gas sensing set up consist of a gas bottle which contains the zero air (BOC limited) that is use as background and for generating the organic vapour through bubbling. Zero air is pure synthetic air made by mixing nitrogen and oxygen in 4:1 ratio and contains very low levels of impurities than ambient air (hydrocarbon <0.1 vpm; CO_2 <1 vpm; H_2O <2 vpm and NO_x < 0.1 vpm) .The two mass flow controllers (Brooks 5850S) which are operated using the Brooks 0260 smart interface and software are used for controlling the amount of the analyte channelled to the sensor. The dreschel bottle which is connected to one of the MFC contains the organic solvent to be vaporised for sensing. The gas cell is the point where the sensor chip is placed during the gas sensing measurement. The gas cell is normally immersed in a water bath during gas sensing at different temperatures. The potentiostat provides a dc bias voltage between the two neighbouring micro-bands and measures the change in the conductance when the organic vapour is in contact with the sensor which records the current change as a function of time on the computer.

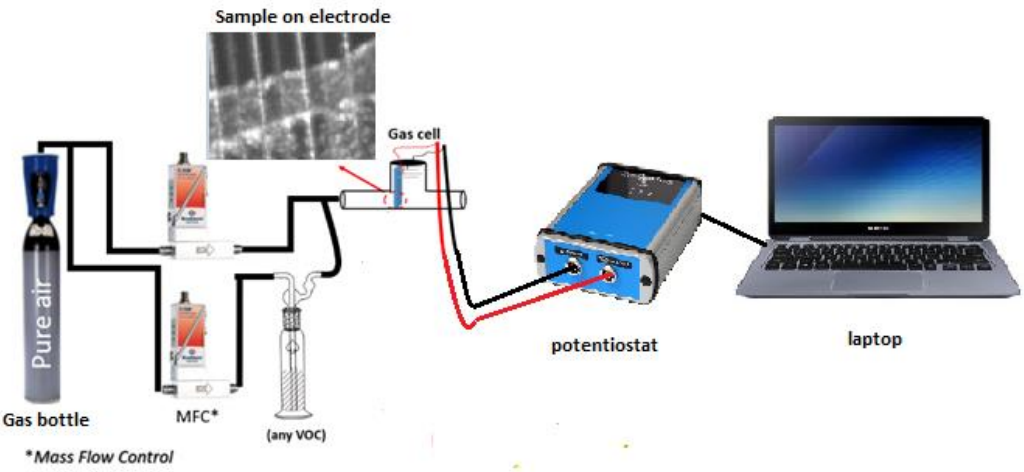

Figure 2.17 Showing the set up for the gas sensing of the volatile organic vapour using the fabricated nanowire gas from the templated metal sulfides.

2.10 Gas sensing process

The gas mixing and transport to the gas sensor is monitored and controlled using BROOKS SMART interface software on a laptop. Zero air was used as the background for stabilisation and equilibration of the response. The data from the various analyte

were obtained by passing zero air through the analyte connect to the system via a dreschel bottle to generate vapour which was channelled to the electrode. The gas concentration is controlled using separate MFCs to control the flow rates of the zero air and zero air passing through dreschel bottle to saturate the air with the organic vapour of interest (ethanol, acetone, chloroform and hexane). These two streams are mixed before been channelled through the glass cell containing the sensing device under test.

The partial pressure of the analyte P, in the gas stream is given by the mixing ratio:

$$P = p^* \frac{V_v}{V_v + V_{air}} \quad (2.6)$$

Where p^* is the saturated vapour pressure of the analyte at the temperature of the dreschel bottle, V_v and V_{air} are the gas flow rates (mL min^{-1}) of the ethanol saturated air and the zero air.

The response is seen as a change in the current with time when the gas is on and off. The temperature of the dreschel bottle is measured and used to calculate the saturated vapour pressure of the various analyte as showing in chapter 2.2.5.

The conventional definition of the sensitivity of a gas sensor is normally expressed a $S = \frac{R_g - R_a}{R_a}$ where R_g and R_a stands for the resistance of the sensor in the presence of the organic vapour and in dry air respectively[149].The sensitivity (S) of our room temperature nanowire sensor is expressed in terms of the change in current.

$$\text{Sensitivity (S)} = \frac{I_v - I_a}{I_a} \quad (2.7)$$

Where I_a and I_v are the current in the presence of zero air and the organic vapour.

2.11 Gas sensing at different temperatures

The response of the sensor with temperature is done by inserting the glass cell inside a water bath. The temperature of the bath is adjusted accordingly and allowed to equilibrate to the set temperature. The temperature around the sensor is monitored by using a K-type thermocouple connected via an A/D interface (TC-08 Pico technology Ltd) to a laptop and operated using Picolog software (Pico-technology Ltd).

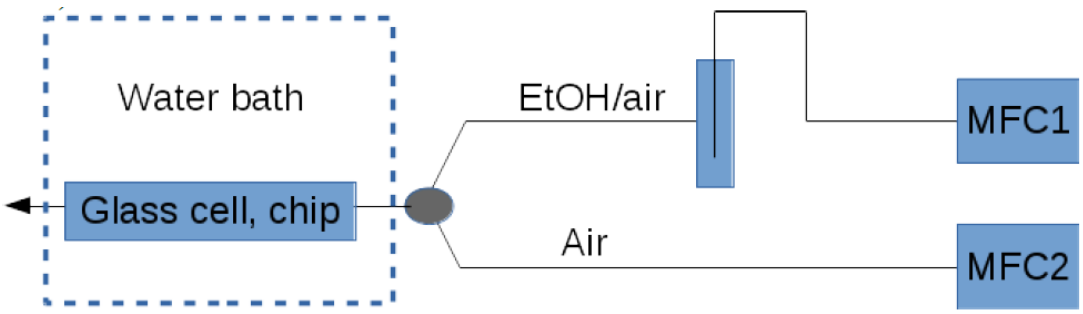

Figure 2.18 Schematic illustration of the gas flow system used for testing the sensing device at different temperature.

2.12 Experimental methods for MWCNT/DNA nanocomposite

In order to determine the effective interaction of multiwall carbon nanotube with DNA to form composite and not just mere mixtures, the synthesized MWCT and DNA nanocomposite were characterized by atomic force microscopy (AFM), ultraviolet-visible spectroscopy and Raman spectroscopy, Fourier transform infrared spectroscopy (FTIR) and transmission electron microscopy. The procedure for each of the characterisation method is presented below. This research on MWCNT and MWCNT/DNA nanocomposites were done in collaborations with Dr. Shams Ali.

2.12.1 UV-Vis spectroscopy

The Uv-Vis spectra was obtained using thermo scientific ™ NanoDrop 2000 spectrophotometer by dropping 1 uL of the sample on the metal plate. The spectrum was record in the range of 200 nm to 750nm.

2.12.2 AFM studies

Atomic force microscopy images were obtained by using a ScanAsyst-in-Air mode of a Multimode VIII AFM coupled with a Nanoscope V controller (Bruker) and an ‘‘E’’ scanner. Nanoscope software version 9.1 was used to acquire the images. A silicon nitride cantilevers (ScanAsyst, Bruker) was used as the tips for imaging. The cantilevers has a spring constant of 0.7 Nm^{-1} and a resonance frequency of 150 kHz with a nominal tip radius of about 2 nm. The acoustic and vibrational noise of the microscope was reduced by placing it on an acoustic enclosure/isolation table. Image analysis were done with Nanoscope analysis software (version 1.5).

2.12.3 Raman spectroscopy:

Raman spectra were obtained using a confocal microscope (CRM200 model, Ulm, Germany). The excitation was done at a wavelength of 488 nm using a diode laser of 60 mW output power. The microscope is fitted with a Raman edge filter to reduce elastic scattering of the transmitted light. Light dispersion was done with the 600 mm^{-1} grating and sample detection with a Peltier-cooled CCD detector.

2.12.4 FTIR spectroscopy

An IRAffinity-1S Fourier transform infrared spectrophotometer (Shimadzu) operating at 8 cm^{-1} spectral resolution and equipped with a DLATGS detector was used to record the spectrum in the range of 400 to 4000 cm^{-1}. About 32 scans were collected and averaged. About 5uL of the sample was used to obtain the spectra.

2.12.5 TEM studies

The sample was prepared for the TEM analysis by dropping 2 uL of the synthesized sample solution on a holey coated copper grid and allowing the solvent to slowly evaporate at room temperature, leaving behind aligned nanowires for imaging. The TEM images were obtained using a Philips CM-100 TEM operating at an accelerating voltage of 100 kV.

2.12.6 Electrical Measurement

The MWCNT/DNA nanocomposite was deposited onto the Pt-on-glass IDEs by drop casting and carefully combed using the tip of pipette. The IDEs were then kept in the laminar air fume hood at room temperature to facilitate drying of the solution. Conductivity measurements were done on a Cascade Micro-tech probe Station and the readings collected using a Hewlett Packard Agilent Technologies B1500A Semiconductor Device Analyzer driven by an Agilent Easy EXPERT software. The sample was kept in the probe station chamber under nitrogen for 30 minutes before collecting the data. All the reading were obtained in room temperature except during conductivity measurement against temperature which was obtained by connecting the probe station to an ESQEC ETC-200L thermal chuck (Japan).

2.13 Gas sensor fabrication and sensing system for MWCNT/DNA

The gas sensor was fabricated by drop casting 2 uL of the MWCNT/DNA samples as films on platinum micro-band on silicon substrate electrode. The samples were ultra-sonicated to ensure even dispersion before drop-casting on the electrode since MWCNT easily aggregate in solution. The drop casted sample was kept in the fume hood to dry under ambient condition to get rid of the solvent. The sensor was then inserted into a glass cell and connected to the sensing system as shown in figure 2.19.

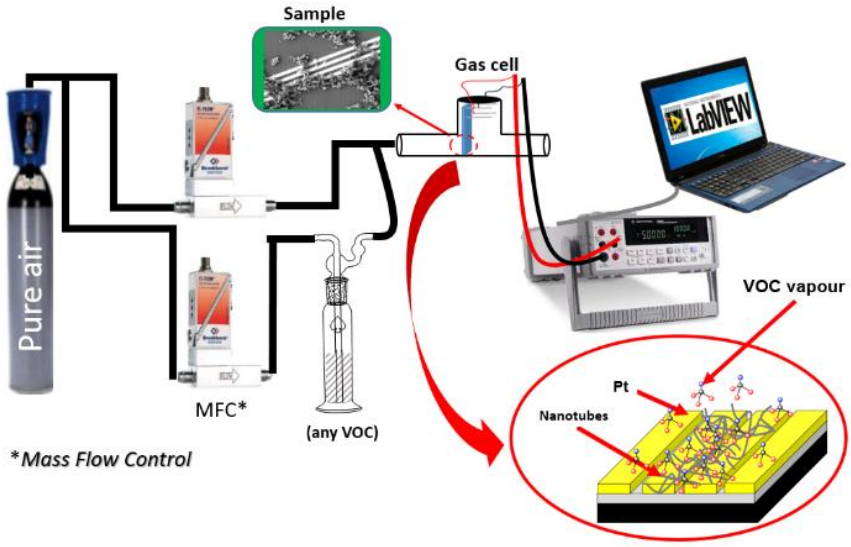

Figure 2.19 A block diagram of the sensing system used to assess the response of DNA-CNT nanocomposites to various volatile organic compounds (VOCs) in the gas phase.

The sensing system consist of the gas bottle containing zero air (It is a mixture of 80% pure nitrogen and 20% pure oxygen with very low water and hydrocarbon impurity levels) that supplies the zero air and the air for generating the vapour. The flow of the gas is controlled using the two MFC which control the concentration of the vapour sent to the gas sensor. The analyte are kept in the Dreschel bottles and connected to the sensing system. The analyte vapour was generated by bubbling air through the analyte in the Dreschel bottle. The VOCs vapour channelled to the sensor and the sensing measurement evaluated.

2.14 Measurement of sensing properties of MWCNT/DNA

All the MWCNT/DNA based gas sensor devices prepared with different ratio of MWCNT and DNA were studied for their gas sensing properties by determining the change in resistance of the fabricated sensor when exposed to zero air and to various analyte. The measurement was done using Agilent 34401A digital multi-meter that was interfaced with a LabVIEW software to monitor the change in resistance. The temperature of the dreschel bottle used for holding the various analyte was monitored using a thermocouple. The response of the analyte was evaluated by measuring the sensitivity. The sensitivity of the sensor can be defined as

$$S = \frac{R_{gas} - R_{air}}{R_{air}} \tag{2.8}$$

Where R_{gas} was the resistance of the device when exposed to the analyte and R_{air} is the resistance in the presence of zero air. The sensitivity is a measure of the performance of the sensor, with higher sensitivity indicating a measurable signal even when the concentration of the analyte is low. The resistance of the zero air was used as control for the measurement. In this research the flow of dry air was fix at 125 mL min^{-1} for all the tests while various amount of the VOCs vapour such as 125, 250, 375 and 500 mL min^{-1} flow rate was selected for different measurements.

2.15 Conclusion

This Chapter has described in detail the various methods that was used in the synthesis of the different DNA templated nanowire in solution. The experimental technique for morphological, chemical and optical characterisation of the nanowires was also presented. It also highlighted the different methods for measuring the electrical properties of the synthesised samples. The methods of fabrication of the sensor with the synthesised nanowires, the gas sensing set up, the procedure for gas sensing at room and at different temperature were also explained in details. The result from the experimental procedure described here is presented in the following chapters. The various characterisation techniques used in the studies to prove the synthesis of 1D DNA-templated nanowires has also been discussed. The basic working principles and the instrumentation including schematic diagrams of these techniques were presented and explained in detail.

CHAPTER THREE
Synthesis and characterization of DNA templated CdS, $CdZnS_2$ and ZnS nanowires

3.1 Introduction

Metal sulfide semiconductors have been attracting interest for application as gas sensors for different analytes. Even though many papers have reported the use of metal oxides as transducer for gas sensors[149–152], few have reported on the use of metal sulfides as gas sensors. The few published papers that reported metal sulfide gas sensors do not provide in-depth studies of their sensing properties and mechanism[153,154]. The metal oxides have been proven to show fast response and recovery times, good sensitivity and cost effectiveness[110,155]. However, they still have some major draw backs such as poor selectivity and instability in their response[156,157]. They also requires very high temperatures (typically 300^{o}C or higher) to support chemical reactions on their surfaces[158]. Therefore, there is a need to investigate a new set of materials that can remedy some of the draw backs. Previous studies on metal sulfides have shown that the sulfides have the potential to address these challenges. They require lower temperatures to activate reactions on their surfaces and show lower band gaps compared to their counterpart metal oxides[158]. Moreover, the mechanism of conduction of the metal sulfides are supposed to be different due to the absence of oxygen in their crystal lattice and therefore they may be less prone to drifting of the signal as a result of diffusion of oxygen vacancies[158]. This could prove to be the reason for increased selectivity and stability as reported in literatures[159,160]. Hence, the focus of these research is on metal sulfides as conductometric gas sensors for sensing volatile organic compounds.

Another reason why nanomaterial requires higher temperature for gas sensing is because of the high resistance that occurs at the particle- particle junction during the transport of electrons across different particles[161]. The fewer the particle barriers, the less the resistance and presumably the higher the sensitivity. Previous studies have tried to overcome the challenge by heating the material at extreme high temperatures to improve the sintering of materials at the junctions. This requires very high temperature which is provided in the form of heating element in gas sensors and thereby making it quite expensive and not robust enough for different applications. In this research, we have adopted the method of templating of metal sulfides on DNA strand to form continuous and conductive nanowires which was earlier reported by our

research group and few other groups[63,162]. The method is quite simple and easy for preparing large scale nanowires for sensing applications. The conductive nature of these nanowires would be exploited for use as transducer for making room temperature gas sensor without heating elements. This chapter therefore discusses the results of synthesis, alignment and characterisation using microscopy and spectroscopic methods for morphological, chemical and optical properties of the metal sulfide nanowires.

3.2 Results and discussion

3.2.1 Synthesis of the λ-DNA templated nanowires

Previous attempts by other researchers to synthesise DNA templated nanowires of organic, inorganic and metals carried out on a pre-immobilised support surface such as mica and silicon wafers have been reported to generate nanowires that looks like ‘’beads on a string’’ and do not show a regular particle size distribution[50,163]. Therefore, the templating reaction in solution which have proven to be a more effective way of DNA nanowire synthesis have been adopted to enhance the preparation of smooth and regular DNA templated nanowires.

DNA molecules are generally known to coordinate with metal cations by interacting with the phosphate groups on the DNA backbone and the nitrogen atoms of the nucleobases [50,64].This process takes place during the addition of the appropriate metal salt which leads to binding of the metal cation on DNA. For preparation of the metal sulfides as reported in this report, this was followed by addition of sodium sulfide which is responsible for the precipitation of the appropriate metal sulfide on DNA.

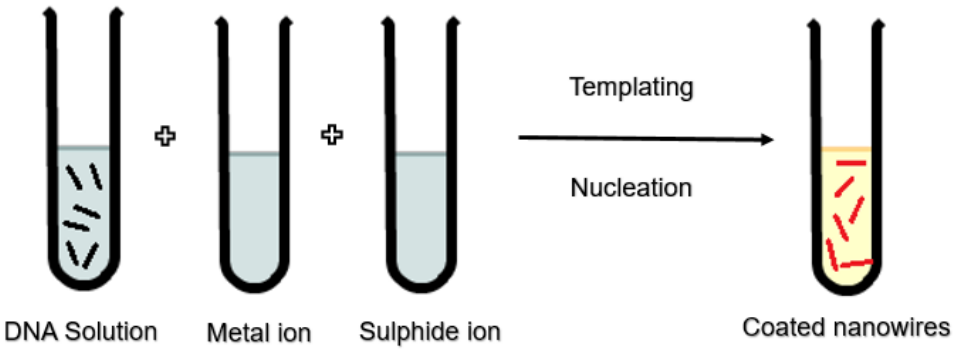

Figure 3.1 Diagrammatic representation of the DNA templating synthesis process of the metal sulfide in solution.

Earlier attempts to prepare smooth and continuous DNA templated nanowires of metal sulfides showed that the concentration of the reagents used has a very important role to play on the morphology of the nanowires produced. Higher concentration of the reagents resulted to formation of clustered DNA templated metal sulfide nanostructures as shown here in CdS network (figure 3.2a). This can be attributed to the coordination of the metal chalcogenides to the DNA resulting to an effective charge neutralisation of the poly-anionic phosphodiester backbone of the DNA which causes a significant reduction in the electrostatic repulsion forces between the DNA strands. This phenomena has been earlier reported in DNA templated metal nanowires[72,164–167] binary semiconductors[58,64,65,168] and polymers[54,163,169–171]. This process can also be seen in metal sulfide semiconducting materials as illustrated in figure 3.2 a.

Attempt to use very low concentration of the reagents to avoid the aggregation of the DNA during synthesis of nanowires lead to preparation of irregular wires with very low coating of the DNA strand. This can be attributed to having insufficient material in solution to completely coat the DNA template. In other to prepare a well templated DNA nanowires, the concentration of the precursor metal salt should neither be too concentrated nor diluted so as to ensure effective self-assembly to form conductive nanostructures[72,172,173]. In order to synthesize smooth and continuous templated DNA nanowires, it was also established that the reaction has to be in two stages and sufficient time should be allowed during addition of the precursors[140]. This is because self-assembly growth processes that result in smooth nanostructures takes place very slowly. Having a concentrated precursor in the presence of many competing binding site speed up the reaction and leads to irregular nanostructures. The addition of both reagents at the same time also leads to formation of CdS nanoparticles which are not templated on the DNA because of higher affinity of metal ion to bind with sulfide ion to form nanoparticles. This has been shown in figure 3.2b which shows aggregation of nanowires from attempt to prepare λ-DNA templated $CdZnS_2$ without the 24 hour incubation period and without the two stage process. This involves adding all the reagents at same time without allowing the metal cation to bind to the DNA template before adding the sulfide ion salt.

The best way of synthesising continuous and smooth nanowires therefore involves two stages. The first stage involves using very low concentration of the reagents (0.4 mM) and allowing it to interact with the DNA for about 24 hours, which is then followed by addition of the high concentration of reagent (40 mM). For the binary metal

chalcogenide, the two metal salts are added at the same time and then followed by the incubation period.

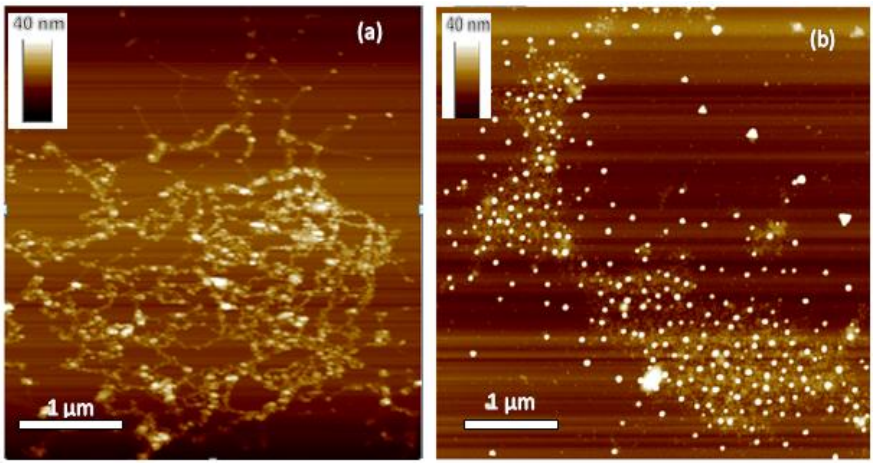

Figure 3.2 AFM Images of CdS and $CdZnS_2$ nanowires in solution. (a) CdS nanowires prepared at very high concentration of the reagents showing a dense network of nanowires with ''beads-on the rope'' structures. (b) $CdZnS_2$ nanowires prepared without the 24 hour incubation period showing aggregation of the DNA strands with un-templated salts.

3.2.2 Atomic Force Microscopy

AFM studies was carried out on the λ-DNA templated CdS, $CdZnS_2$ and ZnS nanowires synthesised to determine the morphology and size distribution. The nanowires were aligned on the surface of either fresh peeled mica or cleaned silicon wafer by molecular combing before imaging. Even though the theoretical height of DNA is about 2 nm[58,72] as measured from crystallographic data of the double helix, measurement using cantilever in tapping mode gives lower heights due to molecule/substrate and tip/substrate interaction[174]. Previous measurement using silicon probe tip shows bare DNA with approximate heights of 1 nm[60,64,175]. The effective control of some of the reaction conditions has resulted in the synthesis of smooth and continuous nanowires. In order to show the difference in height between DNA and DNA templated nanowire, a line profile was drawn across an untemplated DNA and CdS templated DNA nanowire as shown in Figure 3.3.

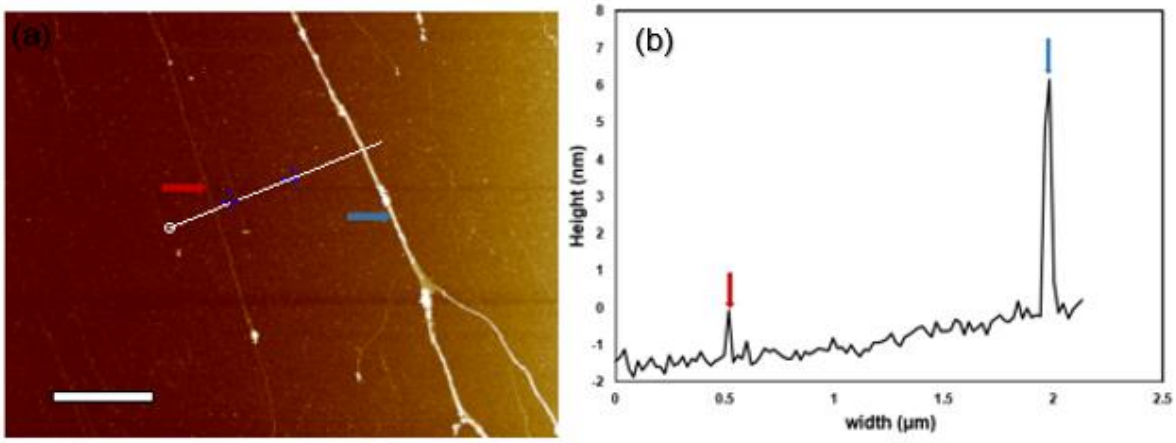

Figure 3.3 AFM image of CdS@DNA (a) showing a single strand of untemplated DNA (red arrow) and templated (blue arrow) nanowire. (b) A line profile showing the difference in height between DNA and DNA templated nanowire. Scale bar = 1µm and grayscale (height) = 10 nm.

It can be seen that there is change in height from 1.5 nm for DNA to about 6 nm for DNA templated nanowire (figure 3.3). This shows that the metal sulfides did template and grow on the DNA strand to form nanowires. In order to image a single nanowire, the surface of the silicon wafer was modified by treating with chlorotrimethylsilane (Me_3SiCl) for about few minutes in order to increase the hydrophobicity. This process reduces the amount of nanowires that would adhere to the surface. The modification of the silicon had made it possible to image a single nanowire as shown in figure 3.4. The size distribution of the nanowires were also determined and presented in figure 3.4.

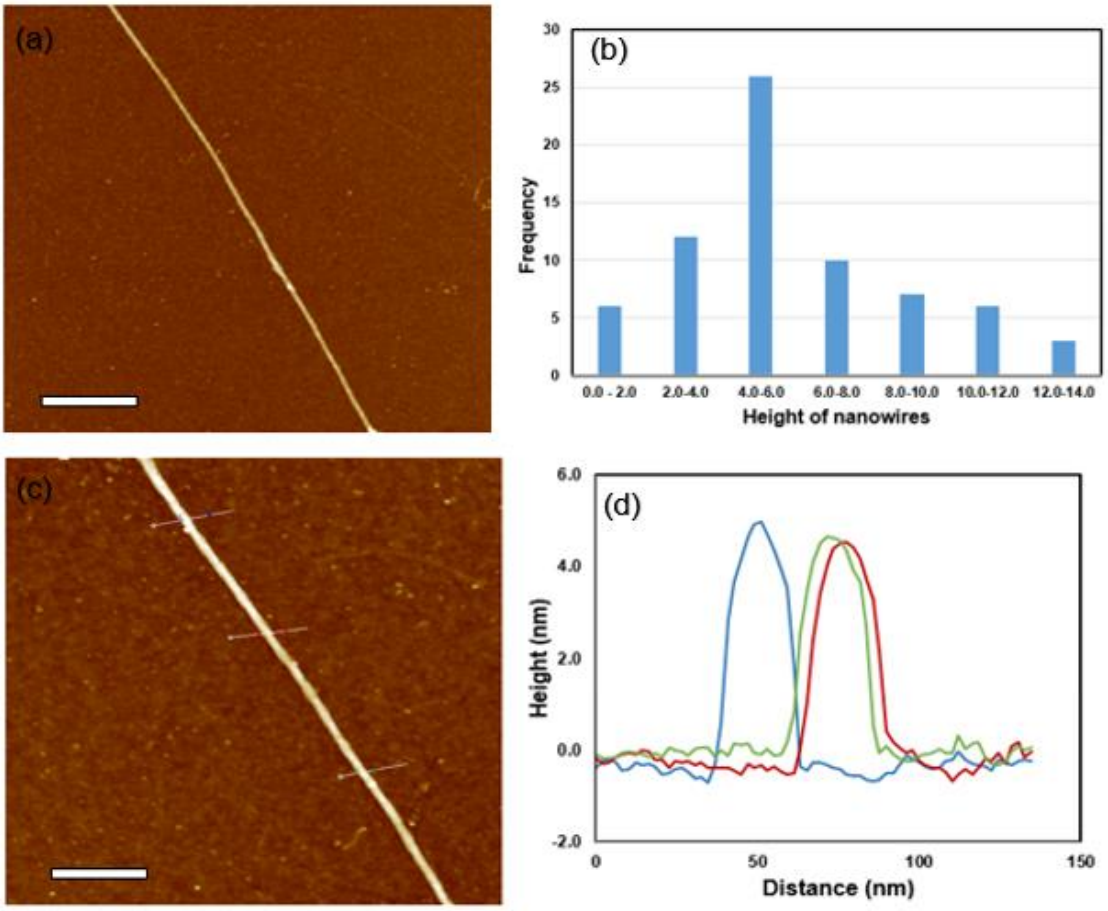

Figure 3.4 AFM images of DNA templated CdS nanowires (a) Showing a smooth and continuous nanowire (Scale bar = 1µm and grayscale (height) = 10 nm. (b) A histogram showing height distribution of 70 DNA templated CdS nanowires obtained by AFM line profile measurement. (c) Lines drawn at different point to showing how smooth the nanowires are across the length (Scale = 1µm and grayscale (height) =14 nm. (d) A plot of the line profile in (c).

The observation of a single strand of the nanowire has shown that the nanowires are quite uniform and continues as shown in figure 3.4. In order to determine the uniformity of the nucleation, a line profile was drawn at different point on the nanowire. The line profile shows that the nanowires are generally uniform along a given nanowire as show in Figure 3.4 (d). A line profile drawn on a network of different nanowires showed that the sample is a mixture of untemplated DNA and templated nanowires with modal height of 4- 6 nm. The synthesis shows that most of the DNA are templated when the right amount of concentration (40 mM) of the metal salts are added. This can be seen by the low amount of untemplated DNA as shown in the histogram shown in figure 3.4 (b).

A line profile of $CdZnS_2$/DNA is shown in Figure 4.5. The height of this example is about 8 nm.

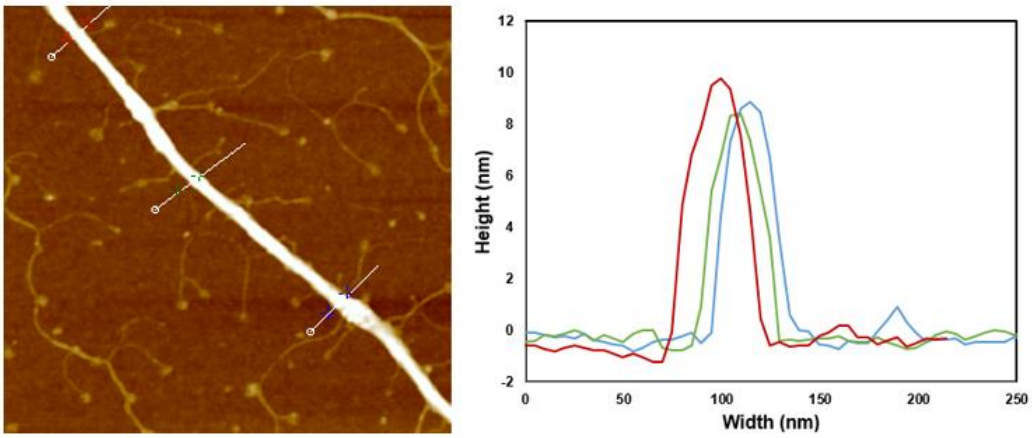

Figure 3.5 AFM images of DNA templated $CdZnS_2$ nanowires showing a smooth and continuous nanowire and the associated cross section (Scale bar = 1µm and grayscale (height) = 10 nm.

Even though the nanowires looks very smooth as shown by the diagonal line profile, a straight line drawn along the nanowire shows that the top of the nanowires is quite rough as shown in figure 3.6. This rough top of the nanowires would particularly be important for the application of these nanowires for gas sensing. This is because gases stick better on rough surfaces and therefore would increase the sensitivity of these nanowires to the different analyte it would be used for sensing.

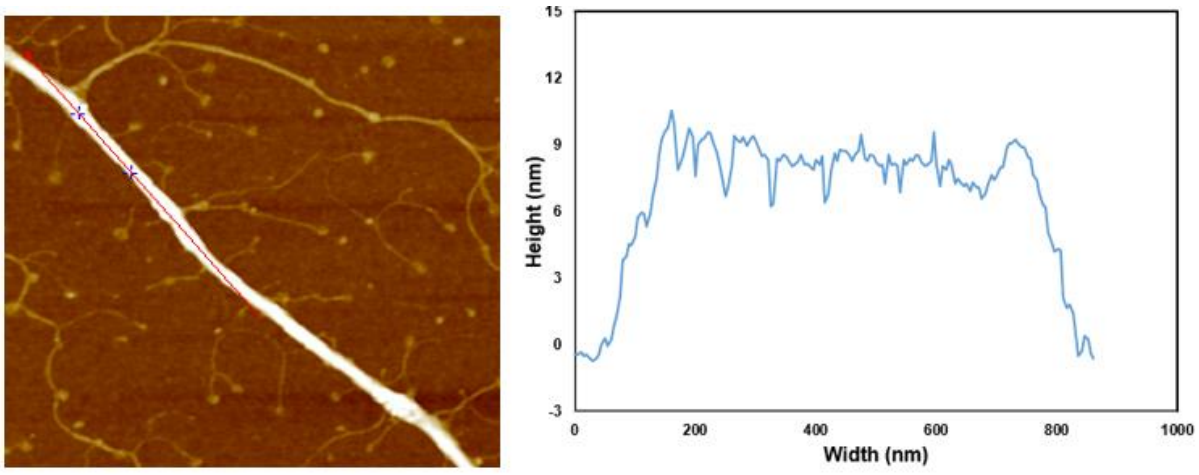

Figure 3. 6 AFM images of DNA templated $CdZnS_2$ nanowires showing a rough top but continuous nanowire as indicated with the cross section (Scale bar = 1µm and grayscale (height) = 10 nm).

A line profile of about hundred nanowires to determine the uniformity of the $CdZnS_2$ shows the same modal height range of 4-6 nm but with more nanowires within this range. The histogram has also shown higher number of nanowire above the modal range as compare with that of CdS/DNA. The sample also show less uncoated DNA strands.

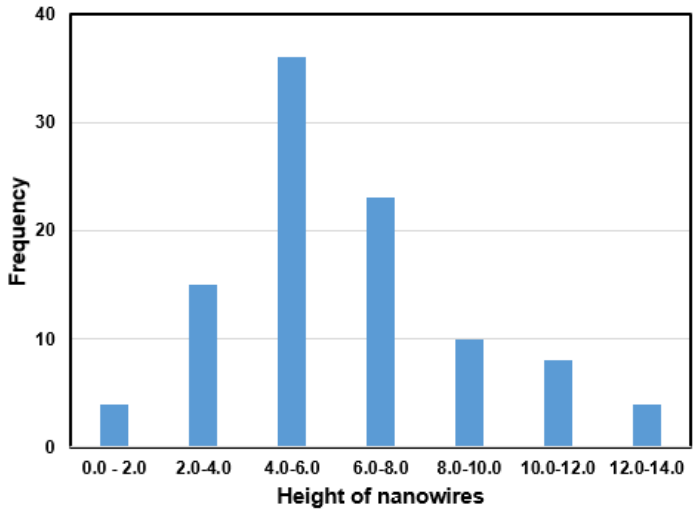

Figure 3.7 A histogram showing height distribution of 100 DNA templated $CdZnS_2$ nanowires obtained by AFM line profile measurement.

Prior to the alignment of the nanowires on the substrate, the sample of the prepared nanowire is subjected to pre-treatment so as to get rid of the untemplated salt and most of the bare DNA. The sample is first of all diluted to minimise the amount of nanowire per volume and reduce the amount to be deposited. The diluted solution is the centrifuged at 6000 rpm for 3 minute so as to separate the templated nanowires from dissolved salt. The sample to be aligned is obtained from the middle of the Eppendorf tube with the use of a pipette.

3.2.3 Fluorescence Microscopy

Fluorescence image of λ-DNA templated CdS and $CdZnS_2$ nanowires produced in solution was simply obtained by using the epifluorescence microscope and the optical image obtained from the confocal microscope.

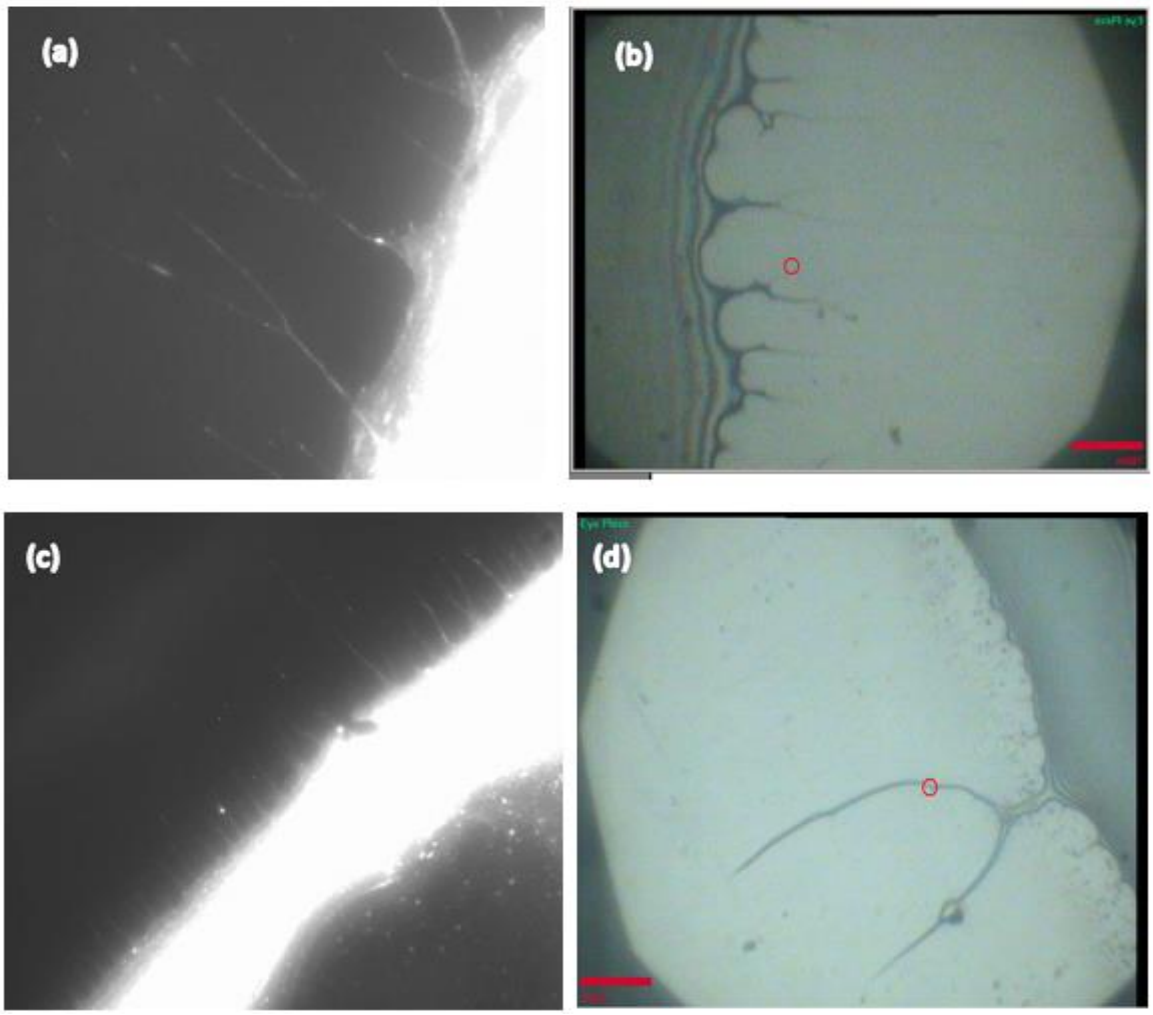

Figure 3.8 Optical Images of CdS and $CdZnS_2$ Nanowires prepared in solution. (a) &(c) Optical image of CdS and $CdZnS_2$ templated on Lambda DNA showing florescence of single strands of the nanowires protruding from the dense network deposited on silicon wafer. (b) & (d) Confocal microscope images of CdS and $CdZnS_2$ templated on Lambda DNA showing single nanowires extending from the bulk.

The image shows a bright emission from the dense network of nanowires and single nanowires can also be seen as tiny extensions from the dense mass. Figure 3.8a shows the fluorescence image of CdS/DNA nanowires on silicon wafer. The broad bright area in the image shows the large mass of CdS/DNA nanowires deposited on a hydrophobic silicon surface. The solution of CdS/DNA nanowire solution was drop-casted on a functionalised square piece of silicon wafer and allowed to dry by air. As the solution dries, the edges of the solution on silicon wafer recedes, leaving behind single strands of CdS/DNA nanowires as seen beside the bright mass in figure 3.8a. This can be seen as a way of molecular combing whereby the surface forces alongside with solution movement during drying causes DNA strands to stretch[84]. It is a very common phenomenon in DNA that is well understood. Previous research has shown

that nanowires produced from organic materials also exhibits this phenomenon [49,54,163]. This research has also shown that templated metal sulfide nanowires can also be combed in the same way as DNA.

The measurement of fluorescence of the solution of templating reactions of metal sulfides on lambda DNA facilitates the visualization of single strands of templated DNA nanowires in solution since DNA in solution does not fluoresce. Figure 3.8 (b) & (d) shows confocal microscope optical image of CdS and $CdZnS_2$ templated on lambda DNA showing single strands of the nanowires protruding from the dense network deposited on silicon wafer. These single nanowires protruding from the lump can serve as contact point for measuring the conductance of this DNA nanowires during electrical measurement experiments and therefore enables the I-V characterisation of a single strand of this one dimension nanostructures produced. The same phenomenon was also observed in λ-DNA templated ZnS nanowires prepared in solution.

3.2.4 Photoluminescence

The room temperature photoluminescence (PL) of the DNA templated nanowires in solution were studied because it is an effective method for determining the nature of transitions and material defects[140]. The photoluminescence spectrum of DNA templated CdS nanowire excited at 370 nm is presented in figure 3.9. The spectrum shows two broad emission in the range of 530-630 nm. Semiconductor nanowires usually has two emissions due to excitonic and trap or defects emissions[176]. The room temperature PL can therefore provide information about the electronic structure as well as structural quality of nanowires. The first emission band with the peak centred at 546 nm (2.27eV) is due to excitonic emission of CdS nanowire near the band edge. This emission is attributed to the direct transition from the conduction to the valence band. The second band is a broad trap emission in the range of 585 to 625 nm with its maximum at 603 nm. The trap emission can be ascribed to the sulphur vacancies or extrinsic defects[4,177]. Vanalakar et al reported the synthesis of CdS nanowire with two broad emission peaks centred at ~550 nm and ~770 nm which were ascribed to excitonic and trap state luminescence[140]. Maity and Chattopadhyay also studied the room temperature photoluminescence of nanosized CdS nanowire films. The nanowires showed a broad band with its peak centred at ~567 nm (2.19 eV) which was attributed to defects/traps related transitions[176]. Room temperature synthesis of nanowires create more defects states due to the high surface to volume ratio[178]. The

value of the excitonic band gap is less than that obtained from UV-Vis spectroscopy measurement due to the Stokes' shift.

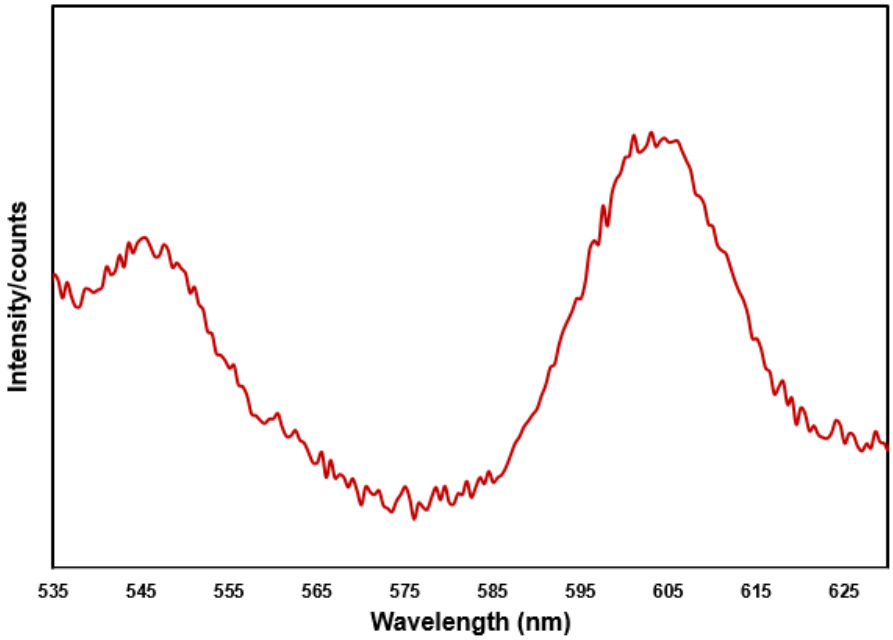

Figure 3.9 Photoluminescence spectrum of DNA templated CdS nanowire with excitation wavelength of 370 nm.

The room temperature PL of the synthesised $CdZnS_2$ was also determined in solution. The spectrum of the room temperature PL at excitation wavelength of 460 nm is presented in figure 3.10. The spectrum shows two distinct bands for the excitonic and defect transitions. The excitonic band is found at lower wavelength with the band centred at 549 nm (2.25 eV). The band centred at 695 nm is the defect or vacancy band. There is a shift in the wavelength of emission of the DNA templated $CdZnS_2$ nanowire due to the doping with zinc.

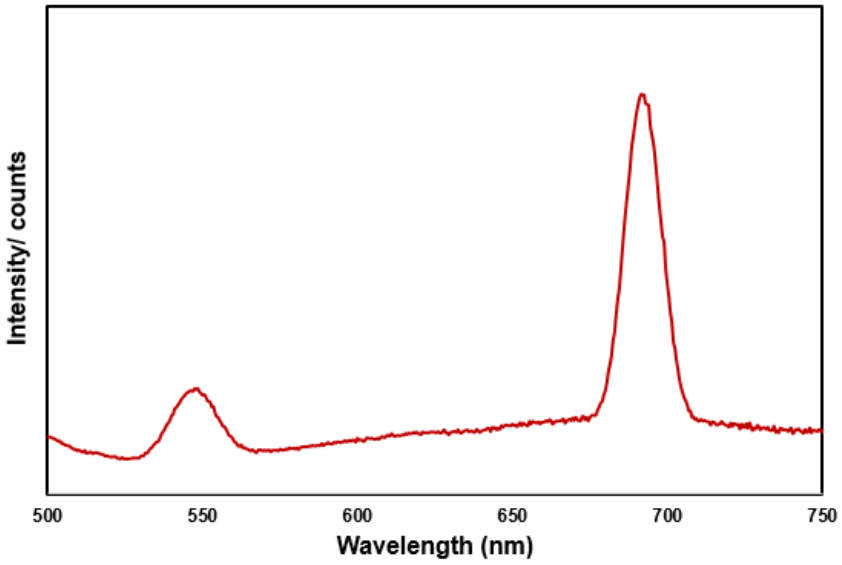

Figure 3.10 Photoluminescence spectrum of DNA templated $CdZnS_2$ nanowire with excitation wavelength of 460 nm.

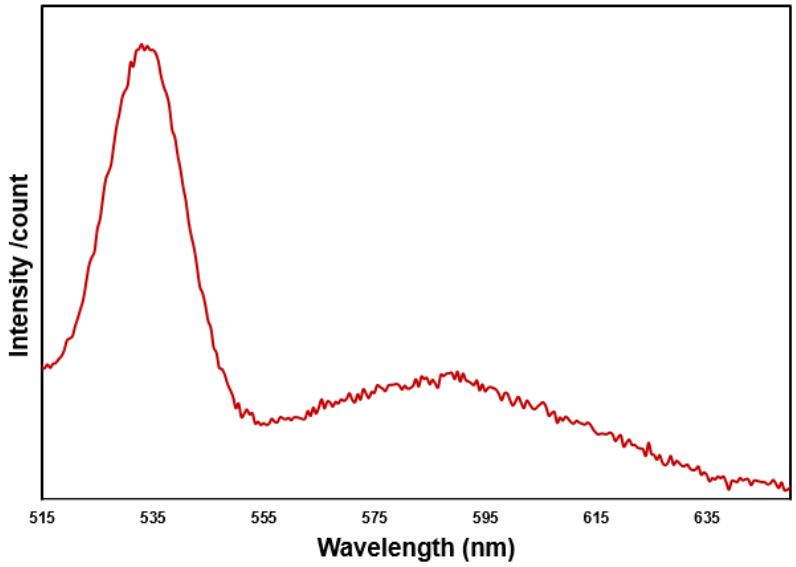

Figure 3.11 Photoluminescence spectrum of DNA templated ZnS nanowire with excitation wavelength of 450 nm.

The room temperature PL of DNA templated ZnS nanowire was also obtained in solution and the result is presented in the figure 3.11. Two distinct peaks were observed with the strong peak at 534 nm and the weak broad peak with the centre at 590 nm. These two peaks are all ascribed to defects and interstitial states. Zhang et al reported the room temperature PL of ZnS nanowire that also showed two peaks; with the high intensity peak at 415 nm and a weak broad peak at 552 nm. The peak at 415 nm was ascribed to radiative recombination of sulphur vacancies on the surface of ZnS

nanocrystals while the peak at 552 nm was attributed to vacancy states, interstitial states or self-activated centres[179].

3.2.5 Raman spectroscopy

Raman spectroscopy is a useful method for determining the purity, the crystalline nature, structural modulation and confined phonon states of nanowires[137]. Therefore the Raman scattering was used to confirm the formation of nanosized metal sulfides on the DNA template and its crystallinity. The figure 3.12 shows the room temperature Raman spectrum of DNA templated CdS nanowires excited with an argon laser of 488 nm wavelength attached with a Raman edge filter to reduce elastic scattering of light.

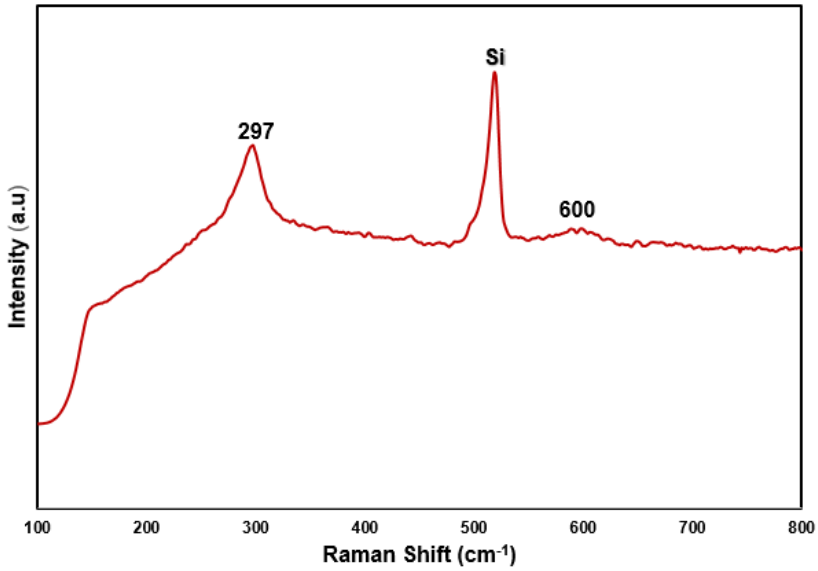

Figure 3.12 Room temperature Raman spectrum of DNA templated CdS nanowires excited with an Argon laser of 488 nm wavelength attached with a Raman edge filter to reduce elastic scattering of light.

Two fundamental Raman peaks of 297 and 600 cm^{-1} can be identified, corresponding to first and second (1LO and 2LO) longitudinal optical phonon frequency of CdS nanowires respectively. Hu et al also reported CdS nanowires prepared from vapour-liquid-solid (VLS) method that showed two Raman peaks near 302 cm^{-1} and 600cm^{-1} that was attributed to the 1LO and 2LO phonons respectively[178]. These bands are evidence of crystalline CdS of the same structure as bulk CdS.

Raman spectroscopy was also carried out to further confirm the formation of the $CdZnS_2$ on the DNA template. The Raman spectrum can be used to measure the extent of doping of semiconductors which is indicated by peak shift. The room

temperature Raman spectrum of DNA templated $CdZnS_2$ nanowires excited at 488 nm wavelength is presented in figure 3.13. The result shows two main band peak at 301 cm^{-1} and 619 cm^{-1} which corresponds to the first and second longitudinal optical (LO) phonon frequency of $CdZnS_2$. These optical phonon frequency shows a blue shift as compared to the DNA templated CdS nanowires due to the doping with zinc to produce the $CdZnS_2$ nanowires. It has also been reported in literature that doping of CdS with Zn leads to blue shift of longitudinal optical phonon frequency[180].

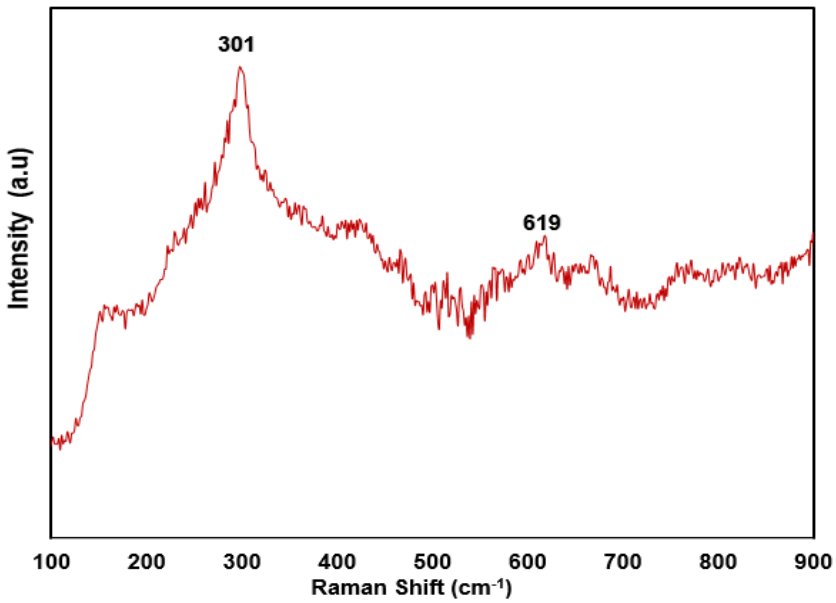

Figure 3.13 Room temperature Raman spectrum of DNA templated $CdZnS_2$ nanowires excited with an Argon laser of 488 nm wavelength attached with a Raman edge filter to reduce elastic scattering of light.

The Raman Spectrum of the DNA templated ZnS nanowire synthesised was also obtained to confirm the formation of nanostructures. The Raman spectrum shows a characteristic peak at 354 cm^{-1} which is due to the longitudinal optical phonon peak which is similar to those reported in literature[181,182].

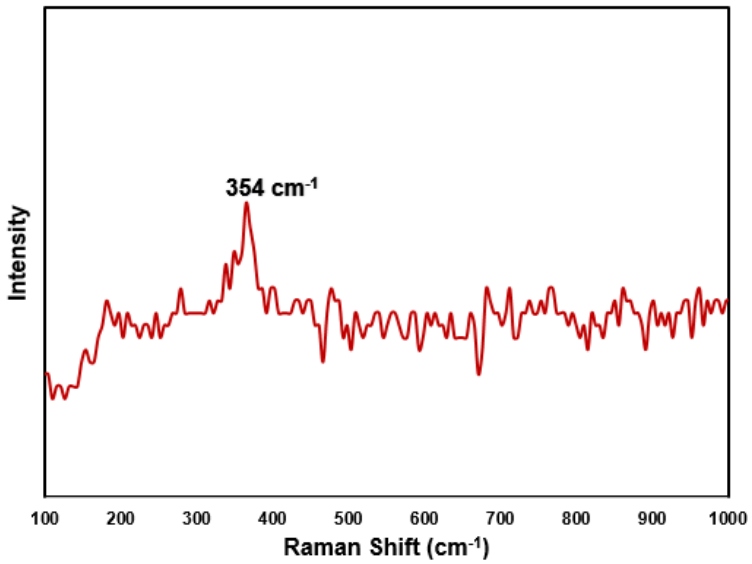

Figure 3.14 Room temperature Raman spectrum of DNA templated ZnS nanowires excited with an Argon laser of 488 nm wavelength attached with a Raman edge filter to reduce elastic scattering of light.

3.2.6 Ultraviolet-Visible Spectroscopy

The UV-Vis absorption spectroscopy is a very important method for studying the optical properties of organic-inorganic nanosized templated semiconductors[183–185]. The templating of inorganic nanomaterials on organic templates leads to a significant change in their optical properties. Figure 3.15 (a) shows the UV-Vis spectra of bare lambda DNA (blue line), CdS/DNA and CdS nanoparticles (orange line). Figure 3.15 (c) shows the UV-Vis spectra of bare lambda DNA (blue line), $CdZnS_2$ nanoparticles (orange line) and $CdZnS_2$/DNA nanowires (black line). The aqueous lambda DNA solution shows the signature nucleic acid absorption peak at 260 nm. Upon reaction with the different metal sulfides, the absorption peaks shifted and reduce in intensity.

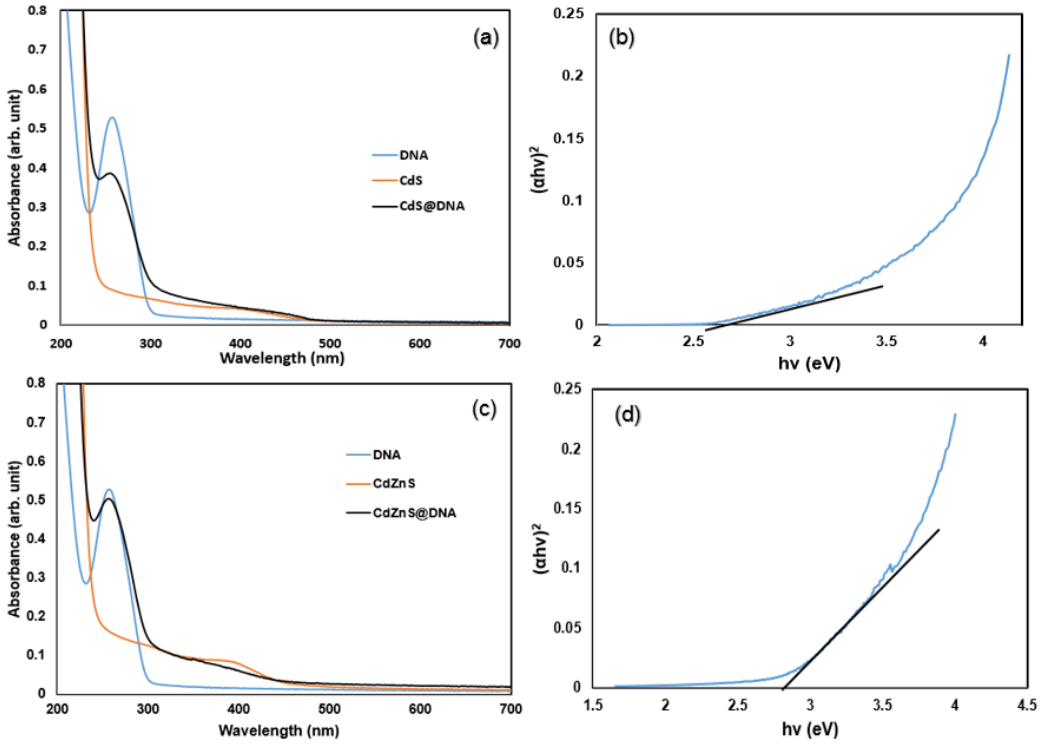

Figure 3.15 UV spectra of (a) bare lambda DNA (blue line), CdS nanoparticles (yellow line) and DNA templated CdS nanowires (black line). (c) Bare lambda DNA (blue line), $CdZnS_2$ nanoparticles (yellow line) and DNA templated $CdZnS_2$ nanowires (black line). (b) & (d) Tauc plot to obtain the band gap of DNA templated CdS nanowire.

As can be seen from figure 3.15 (a), the absorption edge of the DNA templated CdS is slightly red-shifted to about 485 nm from the 475 nm of the CdS nanoparticles in the visible light region. The red shift observed in the UV-Vis spectra is as a result of chemical interactions between the CdS nanoparticles and the DNA template leading to the formation of a bigger particle size on the DNA. This shows that there was nucleation and growth of CdS nanoparticles on DNA template in order to form the continuous and smooth nanowires synthesized. The same process is observed in the case of the $CdZnS_2$/DNA sample as well. The shift in wavelength is due to the interaction of the $CdZnS_2$ with the DNA.

One of the most important property of semiconducting materials is their bandgap, which gives the energy difference between the occupied valence band and the unoccupied conduction band[186]. As we move from bulk to nanomaterial, there is a corresponding increase in band gap as a result of increasing gap between the discrete energy levels of materials due to size quantisation. The band gap of the synthesised DNA templated CdS nanowires was determined and this would be compared to that of the bulk CdS to ascertain the size quantum effect. Figure 3.15 (b) & (d) shows the

energy band gap of the synthesised nanowires as determined from UV-Vis spectroscopy data. This was obtained by extrapolating the edge of the plot of absorbance against energy to the energy axis. The data was obtained at the steep edge of the curve of the spectrum where there was an unusual increase in energy of excitation because optical excitation of electron at the band gap is extremely efficient which give rise to an abrupt increase in absorbance at energy corresponding to the band gap. The band gap energy obtained by extrapolation from CdS/DNA spectrum is 2.58 eV and that from the $CdZnS_2$/DNA is 2.80 eV. It is above the band gap energy of bulk CdS which is 2.40 eV. The result shows that the DNA templated CdS nanowires exhibits weak but significant quantum confinement properties.

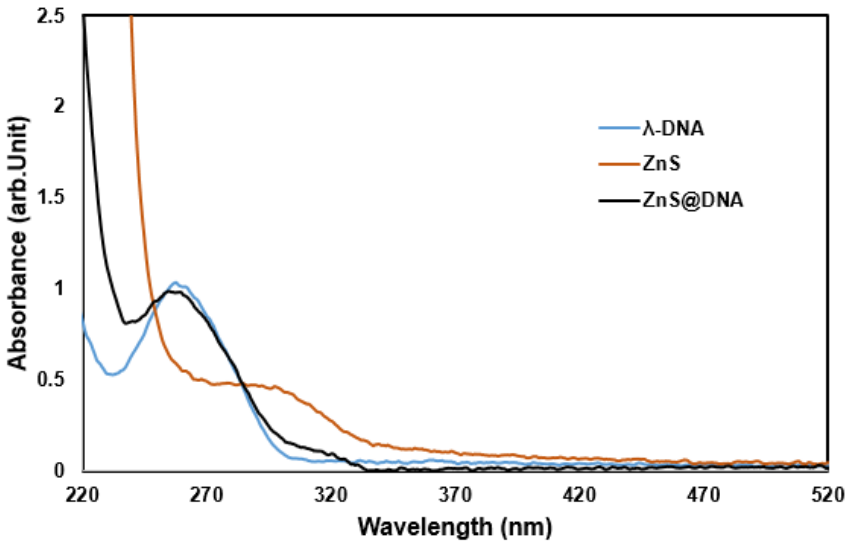

Figure 3.16 The spectrum of bare lambda DNA (blue line), ZnS nanoparticles (orange line) and DNA templated ZnS nanowires (black line) obtained using UV-VIS spectroscopy.

The absorption spectrum of the synthesised ZnS/DNA nanowires was also obtained and compared to that of bare DNA and ZnS nanoparticles as presented in figure 3.16. A slight shift in the absorbance peak of the characteristic DNA band was seen with a decrease in intensity. An appearance of a shoulder band edge emission with the maximum peak at 320 nm signifies the interaction of the ZnS with DNA to form nanowires. The band gap of the ZnS/DNA was calculated to be 3.87 eV which is higher than that reported in literature for bulk, probably due to the effect of quantum confinement in the nanowire.

3.2.7 Transmission Electron Microscopy

In order to also prove the synthesis of one dimensional nanowire of DNA templated CdS nanowire, TEM image of the synthesised sample on holey carbon grid was obtained. Figure 3.17 shows the DNA templated CdS nanowire at low and high magnification respectively. As can be seen in the images, tiny strands of the 1D nanowires showing the templating of the metal sulfide on the DNA. Bare DNA is transparent in transmission electron microscope due to the low atomic number of its constituent atoms.

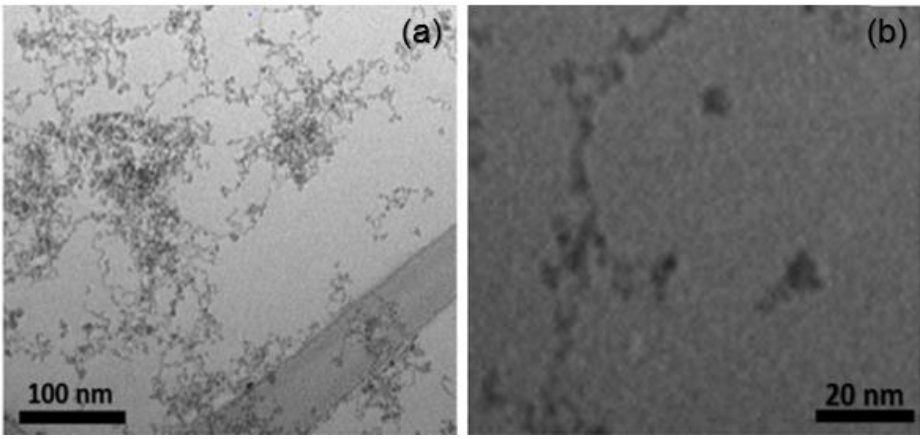

Figure 3.17 Transmission electron microscopy (TEM) image of DNA templated CdS nanowires. (a) Network of the templated nanowires at low magnification. (b) A single templated nanowire at high magnification.

TEM was also done on the DNA templated $CdZnS_2$ nanowires to ascertain the interaction of $CdZnS_2$ with the DNA template. The image of the templated nanowires can be seen in figure 3.18 showing templated nanoparticles as DNA is not visible under the electron microscope. Figure 3.18 (b) is a higher magnification image of the individual coiled nanowires.

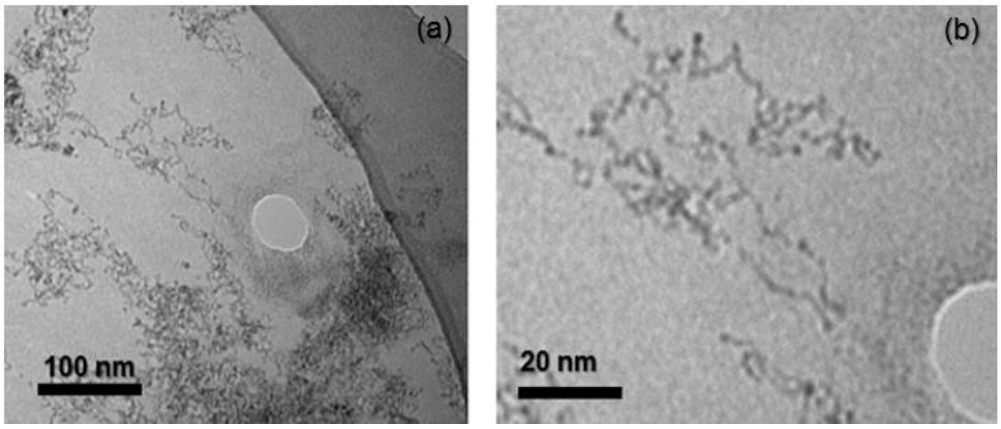

Figure 3.18 Transmission electron microscopy (TEM) image of DNA templated $CdZnS_2$ nanowires. (a) Network of the templated nanowires at low magnification. (b) The templated nanowire at high magnification.

The TEM of the templated ZnS nanowire obtained also confirmed the nucleation of the ZnS along the DNA template since the control (image of DNA) was opaque under the electron microscope. The TEM image of the ZnS/DNA nanowire is shown in figure 3.19. The figure in 3.19 (b) shows the zoomed image of the nanowire confirming the wire-like nature of it.

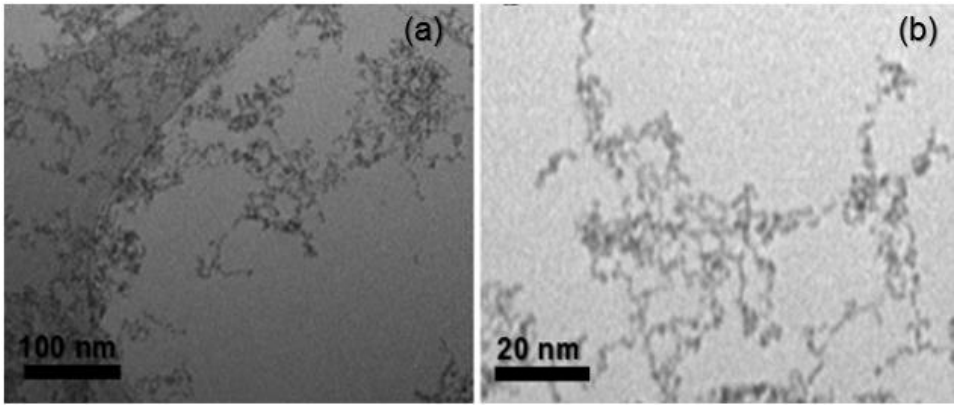

Figure 3.19 Transmission electron microscopy (TEM) image of DNA templated ZnS nanowires. (a) Network of the templated nanowires at low magnification. (b) The templated nanowire at high magnification.

3.2.8 Fourier Transform Infrared Spectroscopy

Fourier transform infrared spectroscopy (FTIR) is the most common analytical method used for determination of functional groups and can also be used to acquire information on the nature of chemical bonding of compound. The technique has been widely used previously for investigating the interaction of DNA with metals, metal oxides and metal

sulfides[187–189]. It has been used here to determine the coordination of metal sulfides to DNA after addition of metal salt to DNA and subsequent precipitation with sodium sulfide. This helps to determine the point of coordination by way of observing the areas in the spectra that are greatly influenced by this interactions. Figure 3.20 shows the FTIR spectra of bare DNA and DNA templated CdS nanowires. As can be seen in the figure, there is a significant shift in the vibrational wavelength as well as intensity of vibration between bare DNA and the DNA templated nanowire.

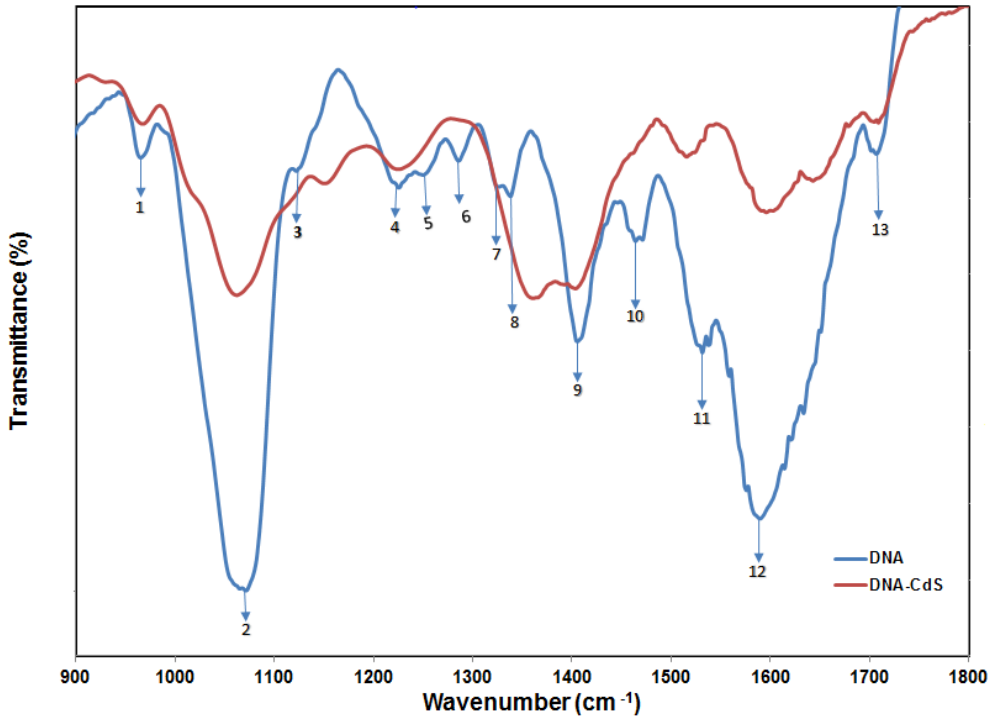

Figure 3.20 FTIR transmission spectra of bare DNA (blue line) and CdS templated DNA (red line). The spectra was collected at 4cm^{-1} and 30 scans.

The full peak assignment of the bare DNA as well as the DNA templated nanowire as supported by literature has been done and presented in table 3.1. Several sites for coordination of DNA to metal ions have been reported in [190–192].

Table 3.1 Showing the vibrational energy of (a) Lambda DNA (b) DNA templated CdS nanowire.

Peak Number	Wave Number (cm^{-1})			Assignment
	DNA	DNA/CdS	Peak Shift	
1	966	968	+2	C-C deoxyribose stretch
2	1072	1063	-9	P-O or C-O backbone stretch
3	1115 (s)	1152	+37	PO2- symmetric stretch
4	1225	1229	+4	PO2- asymmetric stretch
5	1233	-	-	C-N stretch of cytosine and guanine
6	1285	-	-	C-H /N-H deformation; C-N stretch
7	1323 (s)	-	-	C-N stretch of adenine
8	1339	1364	+25	C-N stretch of thymine, guanine and cytosine
9	1406	1404	-2	Ring vibration of cytosine and guanine
10	1464	1516	+52	In plane vibration of guanine and cytosine
11	1532 (s)	1518	-14	In plane vibration of Adenine
12	1589	1597	+8	C=O stretch of cytosine and thymine; In plane vibration of thymine
13	1707	1709	+2	C=O stretch of guanine and thymine, N-H thymine

As shown in figure 3.20, the FT-IR region of 800 cm^{-1} to 1000 cm^{-1} in the spectrum is mostly associated with the deoxyribose region on the DNA. The peak at 966 cm^{-1} of our pure DNA sample is shifted to 968 cm^{-1} for the DNA templated CdS nanowires, which shows a clear indication of CdS nanoparticles interaction with the deoxyribose sugar moiety of the DNA strands.

The high intensity peak and other relevant peaks found within the 1250 cm^{-1} to 1000 cm^{-1} are mainly due to the vibration of the sugar-phosphate group in DNA. The peak at 1072 cm^{-1} is due to the stretching vibrations of the P-O or C-O-C bond in the DNA but have shifted to lower wavenumber of 1063 cm^{-1} due to co-ordination with CdS in the DNA templated CdS nanowires. The peak at 1115 cm^{-1} is for symmetric stretching of the phosphate group of DNA which has shifted to 1152 cm^{-1} in the DNA templated CdS nanowires. The asymmetric stretching of the phosphate group of the DNA is shifted from 1225 cm^{-1} to 1229 cm^{-1} compared to that of DNA templated CdS

nanowires. The significant change of vibrational band in these region is an indication of strong binding of the metal sulfide to the phosphate moiety of the DNA.

The vibrational peaks in the region of 1250 cm^{-1} to 1500 cm^{-1} are due to sugar- base vibrations. The peaks observed at 1339 cm^{-1} and 1464 cm^{-1} can be attributed to the coupled C-N stretches of thymine/cytosine/guanine and in-plane vibration of cytosine/guanine respectively. These vibrational peaks has shifted to 1364 cm^{-1} and 1516 cm^{-1} respectively in the templated nanowire. The vibrational bands in the region of 1500 – 1800 cm^{-1} are due to in plane vibration of the double bonded moieties of the bases. The band which appeared as a shoulder at 1532 cm^{-1} due to in plane vibration of adenine has decreased to 1516 cm^{-1} as a distinct peak. The band at 1589 cm^{-1} is due to C=O stretch of cytosine and thymine as well as in plane vibration of thymine but have shifted to 1597 cm^{-1}. The band at 1707 cm^{-1} is attributed to the C=O stretch of guanine and thymine and also the N-H stretch of thymine but have shifted to 1709 cm^{-1} in the templated nanowire.

FTIR spectroscopy was also used to investigate the interaction as well as the binding sites of the $CdZnS_2$ on the DNA template. The different functional groups in DNA can offer different sites for both the Cd and Zn ion to selectively bind with the DNA. The figure 3.21 compares the FTIR spectrum of bare Lambda DNA and $CdZnS_2$@DNA. The peak assignment were done in accordance with that report in different literetures[190,193–195].

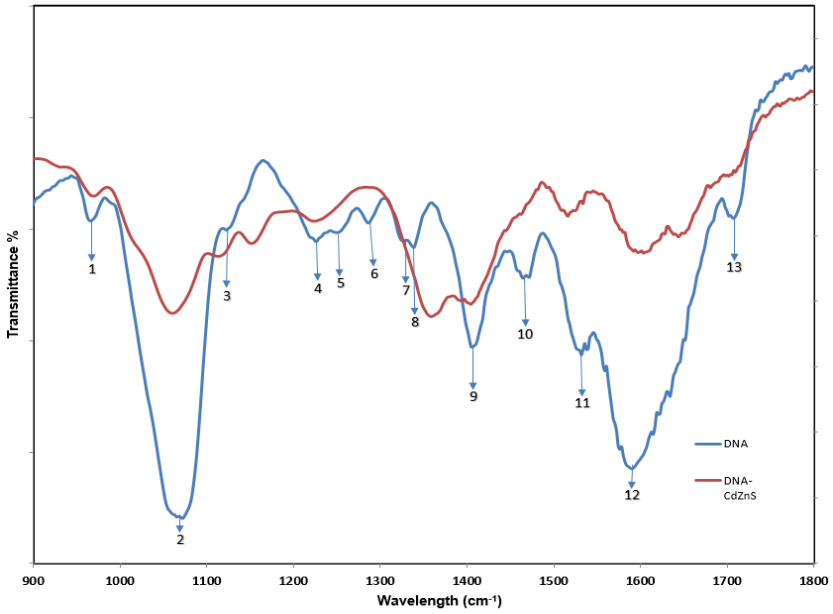

Figure 3.21 FTIR transmission spectra of bare DNA (blue line) and $CdZnS_2$ templated DNA (red line). The spectra was collected at 4cm^{-1} and 30 scans.

The vibrational peak at 966 is due to the C-C peak for deoxyribose stretch. The C-C stretch of the DNA is shifted from 966 cm^{-1} to 970 cm^{-1} in the templated nanowire. Absorptions in the range of 1000 cm^{-1} to 1250 cm^{-1} regions are caused by sugar-phosphate vibrations. It can be observed that there is a significant change in the intensity and position of some of the characteristic peaks in the spectra showing reasonable interaction between the $CdZnS_2$ with the sugar phosphate moiety of the DNA. The P-O/C-O stretch, the PO^{2-} symmetric stretch and the PO^{2-} asymmetric stretch at 1072 cm^{-1}, 1123 cm^{-1} and 1227 cm^{-1} are shifted to 1063 cm^{-1}, 1115 cm^{-1} and 1153 cm^{-1} respectively for the nanowire.

The stretches in the regions of 1250-1800 cm^{-1} are caused by base-sugar vibrations. There is appreciable distortion in the position and intensity of the stretches around these frequencies as well. The C-N stretch of cytosine and guanine at 1252 cm^{-1} is shifted to 1225 cm^{-1} frequency while C-N stretch of the thymine, guanine and cytosine at 1339 cm^{-1} is shifted to 1360 cm^{-1}. The in plane vibration of guanine and cytosine has been shifted by 52 cm^{-1} as compared with bare DNA. The carbonyl stretch of cytosine and thymine as well as guanine and thymine have been shifted from 1589 cm^{-1} and 1707 cm^{-1} to 1607 cm^{-1} and 1643 cm^{-1} respectively. It can be observed from the spectra that there was a significant distortion in vibration band in the range of 900-1800 cm^{-1}

which suggest that there was a significant binding of the $CdZnS_2$ to the DNA and that the samples were not simple mixture of both.

Table 3.2 Showing the vibrational energy of (a) Lambda DNA (b) DNA templated $CdZnS_2$ nanowire.

Peak	Wave Number (cm^{-1})			Assignment
	DNA	DNA/$CdZnS_2$	Peak Shift	
1	966	970	+4	C-C deoxyribose stretch
2	1072	1063	-9	P-O or C-O backbone stretch
3	1123 (s)	1115	-8.	PO^{2-} symmetric stretch
4	1227	1153	-74	PO^{2-} asymmetric stretch
5	1252	1225	-27	C-N stretch of cytosine and guanine
6	1287	-	-	C-H /N-H deformation; C-N stretch
7	1323 (s)	-	-	C-N stretch of adenine
8	1339	1360	+21	C-N stretch of thymine, guanine and cytosine
9	1406	1406	0	Ring vibration of cytosine and guanine
10	1464	1516	+52	In plane vibration of guanine and cytosine
11	1532 (s)	-	-	In plane vibration of Adenine
12	1589	1607	+18	C=O stretch of cytosine and thymine; In plane vibration of thymine
13	1707.0	1643	+64	C=O stretch of guanine and thymine, N-H thymine

In order to ascertain the interaction of ZnS with the Lambda DNA template as well as the point of coordination, FTIR spectrum of the DNA templated ZnS nanowire was also collected. A general overview of the spectra shows a significant change in the spectrum of the nanowire as compared to the bare λ-DNA. The FTIR spectra of DNA templated ZnS nanowire and bare DNA obtained at $4cm^{-1}$ resolution is presented in figure 3.22.

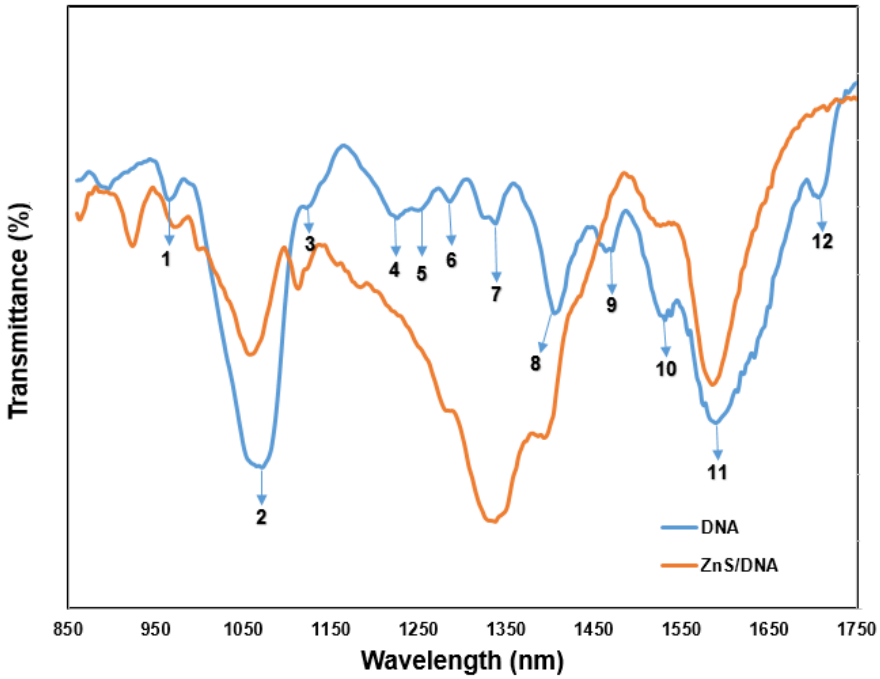

Figure 3.22 FTIR transmission spectra of bare DNA (blue line) and ZnS templated DNA (red line). The spectra was collected at 4cm^{-1} and 30 scans.

The characteristic peaks of the bare DNA strand can still be seen in the spectrum of the DNA templated ZnS nanowires. The peaks have shown significant changes in intensities and positions due to coordination with the DNA. The shift in position of the peaks have been shown in table 3.3. The characteristic DNA vibrational peaks in the table were identified and assigned in accordance with those reported in different literatures[190,195].

The C-C deoxyribose stretch of the bare DNA has significantly reduced in intensity and shifted to higher frequency from 959 cm^{-1} to 974 cm^{-1}. The backbone P-O or C-O vibration at 1072 cm^{-1}, the PO^{2-} symmetric stretch and the PO^{2-} asymmetric vibration at 1117 cm^{-1} and 1225 cm^{-1} respectively have shown a shift of 11, 9 and 39 cm^{-1} respectively in their frequencies. The shoulder vibration at 1250 cm^{-1} due to C-N stretch of cytosine and guanine has disappeared in the templated DNA/ZnS nanowire. These changes in the region of 1000 - 1250 cm^{-1} in the spectrum of DNA/ZnS nanowires are ascribed to the interaction of ZnS with the phosphodiester backbone of DNA.

Table 3.3 Showing the vibrational energy of (a) Lambda DNA (b) DNA templated ZnS nanowire.

Peak	Wave Number (cm^{-1})			Assignment
	DNA	DNA/ZnS	Peak Shift	
1	959	974	+15	C-C deoxyribose stretch
2	1072	1061	-11	P-O or C-O backbone stretch
3	1117 (s)	1113	-9	PO^{2-} symmetric stretch
4	1225	1186	-39	PO^{2-} asymmetric stretch
5	1250	-	-	C-N stretch of cytosine and guanine
6	1287	1285 (s)	-2	C-H /N-H deformation; C-N stretch
7	1339	1339	0	C-N stretch of thymine, guanine and cytosine
8	1406	1395 (s)	-11	Ring vibration of cytosine and guanine
9	1472	1435	-35	In plane vibration of guanine and cytosine
10	1531	1525 (s)	-6	In plane vibration of Adenine
11	1589	1585	-5	C=O stretch of cytosine and thymine; In plane vibration of thymine
12	1707	-	-	C=O stretch of guanine and thymine, N-H thymine

The C-N vibration of cytosine and guanine at 1287 cm^{-1} has been shifted to 1285 cm^{-1}. The ring vibration of guanine and cytosine as well as the in plane vibration of guanine and cytosine has shifted from 1406 cm^{-1} and 1472 cm^{-1} to lower frequencies at 1395 cm^{-1} and 1435 cm^{-1} respectively. The in plane vibration of adenine has shifted from 1531 cm^{-1} to 1525 cm^{-1} while the carbonyl stretch of cytosine and thymine has shifted from 1589 to 1585 cm^{-1}. The carbonyl shift of thymine and guanine observed at 1707 cm^{-1} is no longer visible. The changes in the region of 1250 – 1800 cm^{-1} are due to nucleobase vibrations.

3.2.9 Powder X-ray Diffraction

The powder XRD studies was conducted to confirm the formation and purity of the synthesized metal sulfides since other product such as CdO and ZnO are also possible in aqueous media. It can also be used to determine the crystal structure and crystallite size of the templated nanoparticles. The powder XRD pattern of the synthesised DNA

templated CdS nanowires shows four strong peaks due to reflections from the (111), (220) (311) and (331) planes of the templated CdS at angles (2θ) of 26.70º, 44.05º , 53.25º and 73.06º respectively for a cubic CdS crystal lattice. This correlates well with the international centre for diffraction data in the JCPDS Card (PDF file No 04-006-3897).

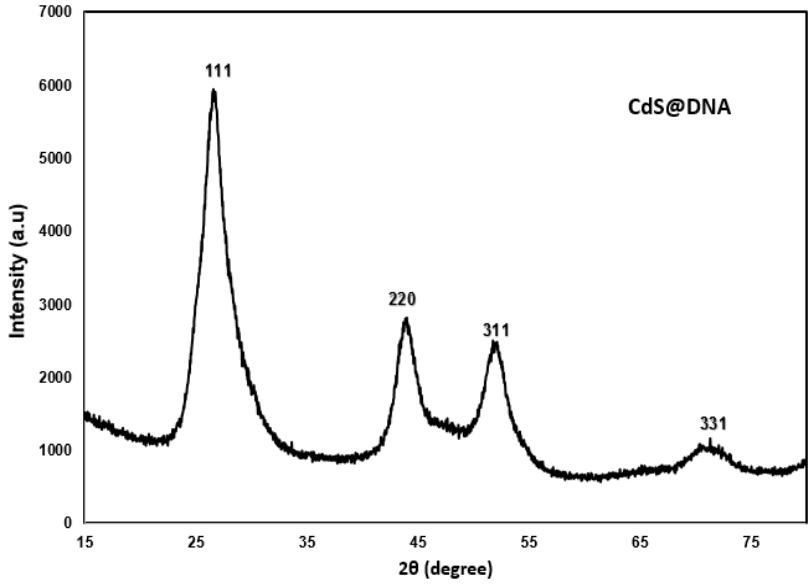

Figure 3.23 XRD of CdS@DNA nanowires prepared in solution.

The average crystallite size of the CdS nanoparticles templated on the DNA strand to form a smooth and continuous 1-dimensional nanowires were calculated from the full width at half maximum (FWHM) of the most intense XRD peak (111) using Scherer equation

$$Scherer\ (D) = \frac{\mathrm{K}\,\lambda}{\beta\ \mathrm{Cos}\ \theta} \qquad (4.1)$$

Where D is the average crystallite size of the nanowire, β is the width of the peak in radians at full width half maximum (FWHM), K is a constant with a value of 0.94, λ is the wavelength of the Cu $K\alpha_1$ radiation source ($\lambda = 1.54 \times 10^{-10}$ m) and θ is the diffraction angle of the main XRD peak (111). The XRD showed that the synthesised nanowires has cubic Zinc blende structure with an average crystallite size of about 3 nm. Comparing this to the AFM studies which showed an average height of about 7- 8 nm proved that the nanowires are about twice the thickness of the crystallite.

XRD was also obtained to further support the formation of $CdZnS_2$ on DNA. The XRD pattern showed 2θ peaks at 27.6 º, 45 º, 53 º and 72.3 º which corresponds to the

(111), (220), (311) and (331) planes of cubic zinc blende structure of $CdZnS_2$ in the JCPDS card (PDF #04-018-5512). The crystallite size of the nanoparticles of $CdZnS_2$ templated on the DNA to form the nanowires were also determined using Scherer's equation to be about 2.5 nm.

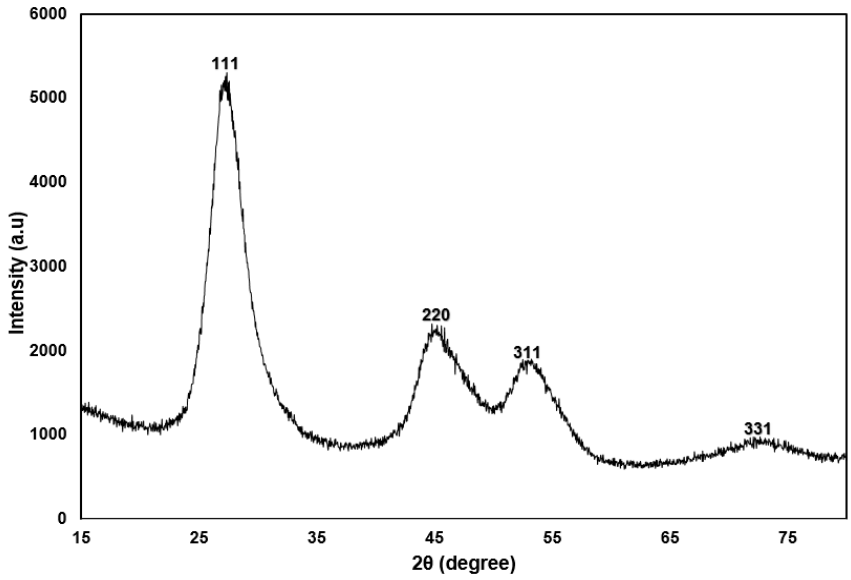

Figure 3.24 XRD Pattern of DNA templated $CdZnS_2$ nanowires prepared in solution.

The crystal structure of DNA templated ZnS nanowires was also characterized by powder X-ray diffraction (XRD). The XRD characteristic spectrum of the synthesised DNA templated nanowires was collected in the 2θ range of 10–80º and presented in figure 3.25. The intense diffraction peaks for the nanostructures appeared at 2θ= 28.7º, 48.1º, 56.9º, 70.3º and 77.5º which can be attributed to the (111), (220), (311), (400) and (331) crystallographic planes respectively. The intense diffraction peaks of the synthesised nanostructure can clearly be attributed to the cubic wurtzite structure of ZnS according to the JCPDS card (PDF-01-077-8756). The crystallite size of the nanoparticles templated on the DNA to form the nanowire as determined from Scherer equation was also about 3 nm.

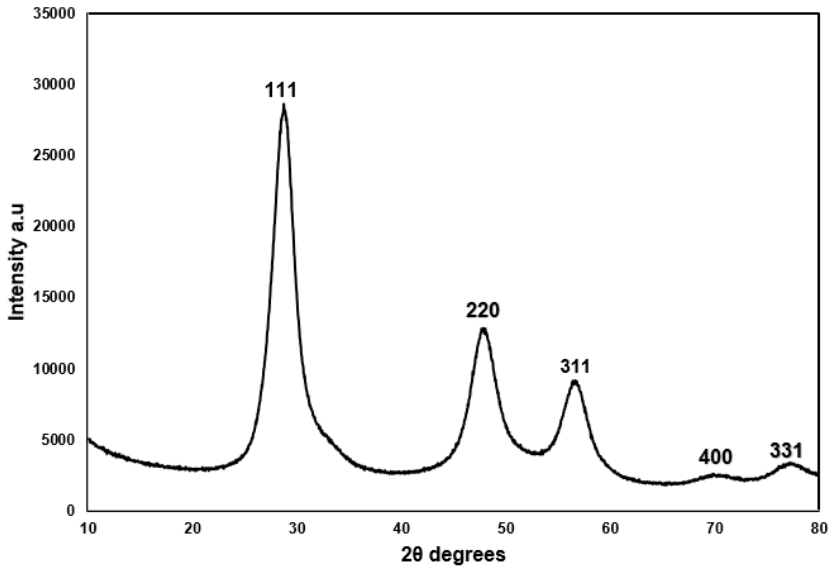

Figure 3.25 The XRD pattern of DNA templated ZnS nanowires synthesised at room temperature.

All the XRD pattern of the DNA templated nanowires have shown an intense peak at (111), which shows a preferential growth along that direction. The broad nature of the peaks shows the nanosized nature of the crystals.

3.2.10 X-ray Photoelectron Spectroscopy

To analyse the elemental composition of the synthesised DNA templated CdS, $CdZnS_2$ and ZnS nanowires, the X-ray photoelectron spectroscopy of the samples were carried out. XPS is surface chemical analysis technique that provide information about the surface composition of materials[196]. It would be used here to determine the chemical state of the synthesised nanostructure surface. Figure 3.26 below shows the XPS survey of DNA templated CdS nanowires. The survey indicated the presence of C, N, O and P which are present as a result of the DNA. The Na is from the Na_2S while the Cl is from the buffer solution in which the DNA is extracted while the Si is from the substrate.

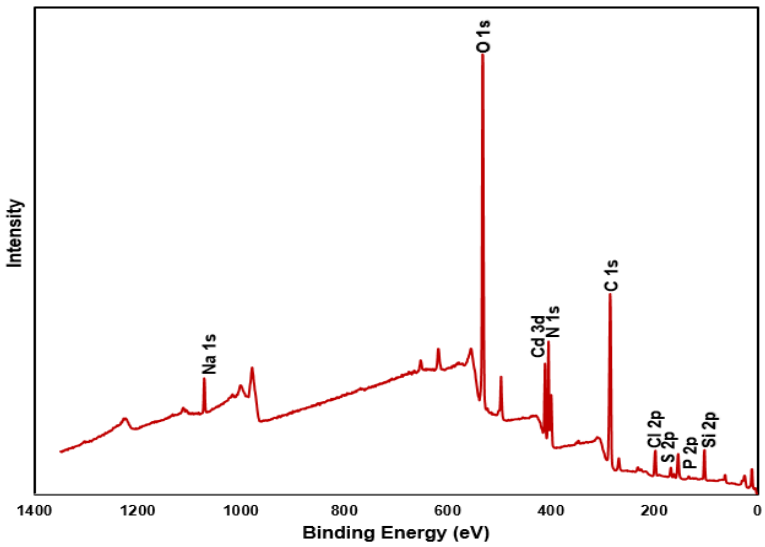

Figure 3.26 XPS survey spectrum of DNA templated CdS nanowire.

The N1s spectrum of CdS/DNA nanowires was further resolved into different components as shown in figure 3.27. It can be observed that there are two major peaks which indicate separate nitrogen environment in the spectrum. The peak at higher binding energy is attributed to the N atom from the unreacted cadmium nitrate salt. The peak at the lower binding energy can be further resolved into two peaks. The first peak at 399.8 eV is attributed to neutral atoms of nitrogen while the peak at 401.5 eV is ascribed to nitrogen atoms of pyrimidine ring of the DNA templated nanowire. Lee et al in his previous research also reported two peaks at 398.8 eV and 400.6 eV in the N1s spectrum of pure DNA on gold surface for neutral nitrogen and the nitrogen of pyrimidine of DNA respectively. The reported peaks for pure DNA are less than that of the templated DNA which shows that there was a significant interaction between the DNA and CdS to form the nanowires.

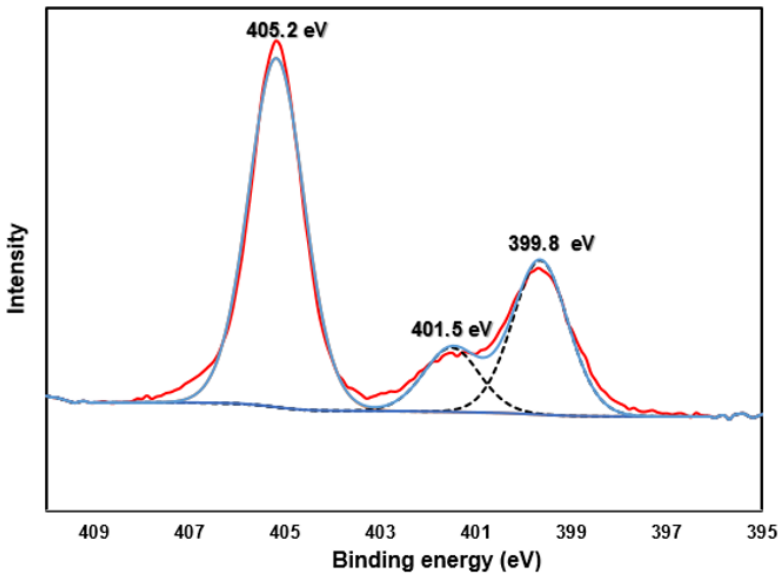

Figure 3.27 High resolution XPS spectrum of N1s region of DNA templated CdS/DNA nanowire.

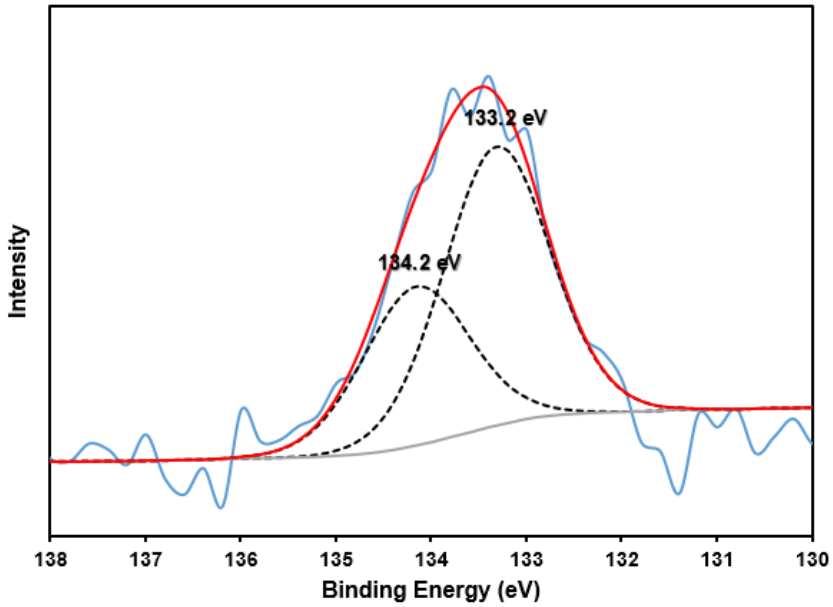

Figure 3.28 High resolution XPS spectrum of P 2p region of DNA templated CdS/DNA nanowire.

The presence of DNA in the nanowire was also confirmed by analysis of the high resolution spectrum of P 2p as shown in figure 3.28. The P 2p spectrum of the templated CdS/DNA was further resolved into two different components with their sub peaks centred at 133.2 eV and 134.2 eV due to spin-orbit coupling with a 2:1 intensity ratio as expected for the multiplicity. The peaks are assigned to the P $2p_{3/2}$ and P $2p_{1/2}$ binding energy of phosphorus of the phosphate group of DNA. These reported values are quite similar to those reported in literature[135].

The high resolution XPS core level spectra for the Cd 3d region of the synthesised nanowire was obtained and presented in figure 3.29. The binding energies observed at 405.2 eV and 411.9 eV corresponds to the characteristic photoelectron peaks of Cd $3d_{5/2}$ and Cd $3d_{3/2}$ core level of cadmium sulfide. These values are in good agreement with those reported in literature[140,197].

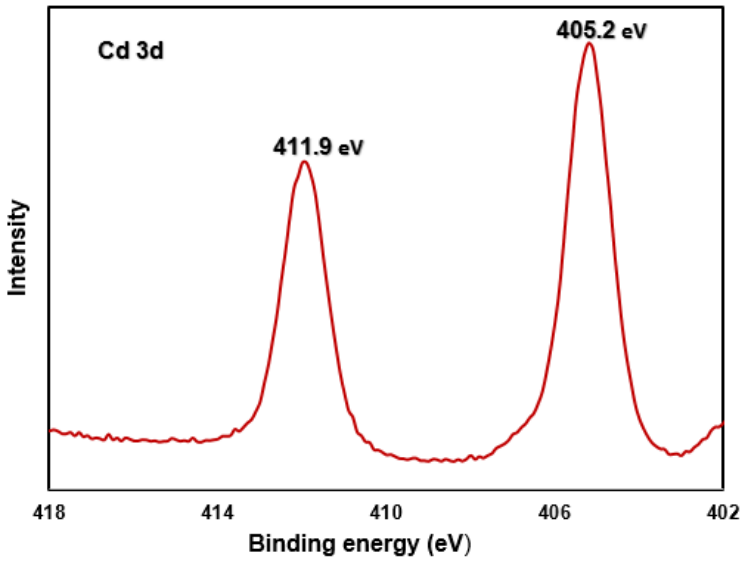

Figure 3.29 High resolution spectrum of Cd 3d region of DNA templated CdS nanowire.

The high resolution XPS peaks of S 2p can be observed at 162.0 eV. The peak can be further resolved into a doublet peak at 161.8 eV and 163.0 eV corresponding to the S $2p_{3/2}$ and S $2p_{1/2}$ core level photoelectron peaks of CdS with an intensity ratio of 2:1 and a binding energy difference of 1.2 eV.

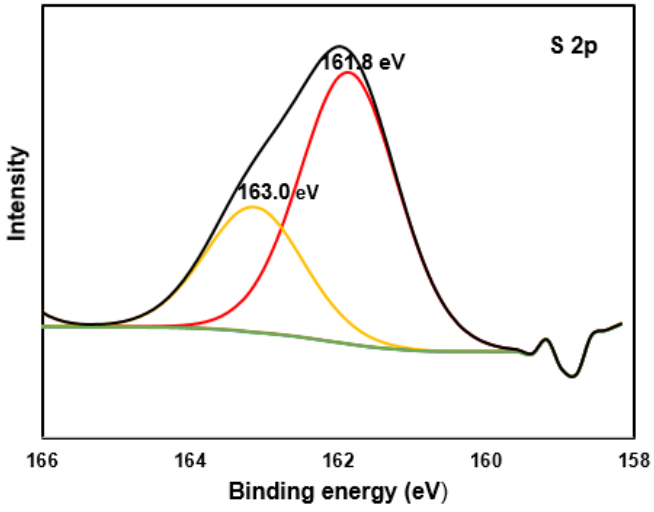

Figure 3.30 High resolution spectrum of S 2p region of DNA templated CdS nanowire.

The peak position for Cd $3d_{5/2}$ at 405.2 eV and that at 161.8 eV for S $2p_{3/2}$ corresponds to the literature reported value for the compound CdS[198,199].

The XPS survey of the DNA templated $CdZnS_2$ nanowire was also studied so as to determine the surface composition. The XPS survey of DNA templated $CdZnS_2$ nanowire have been shown in figure 3.31. The survey shows the presence of the characteristic peak of the elements C, N, O and P from the DNA as well as the Cd, Zn and S from the metal salt solution. This confirms the templating of this metals sulfide on the DNA. The presence of the three chemical elements observed for ternary system shows the formation of the ternary alloy nanowire.

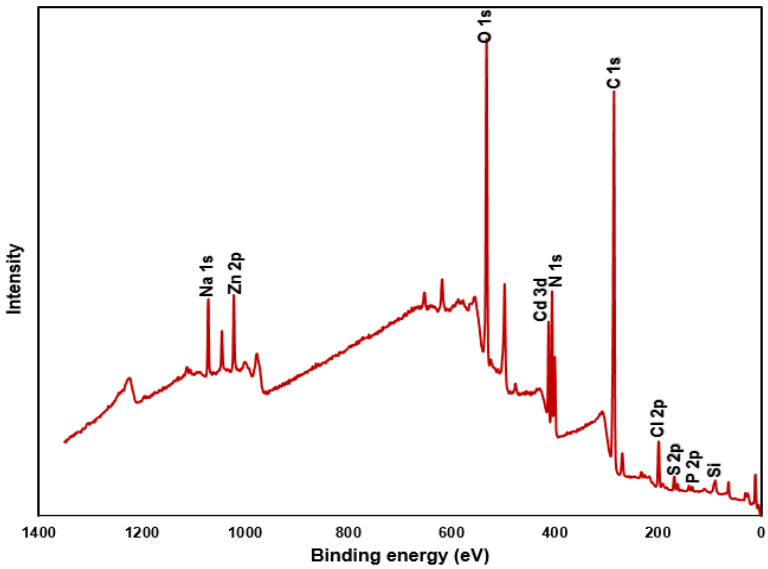

Figure 3.31 XPS survey spectrum of DNA templated $CdZnS_2$ nanowire.

The high resolution XPS core level spectra for the Cd 3d, Zn 2p and S 2p region of the synthesised nanowire was further resolved into their component peaks. The binding energies observed at 405.2 and 411.9 eV corresponds to the characteristic photoelectron peaks of Cd $3d_{5/2}$ and Cd $3d_{3/2}$ core level transition associated with CdS. The separation in the binding energy of the two photoelectron peak is 6. 7 eV which is in agreement with those in literatures[147,200,201]. The peaks at 1021.7 eV and 1044.8 eV are attributed to the Zn $2p_{1/2}$ and Zn $2p_{3/2}$ binding energy of Zn^{2+} respectively. The binding energy difference between the component peaks is approximately 23.0 eV which corresponds to previous research results[147,201–203].

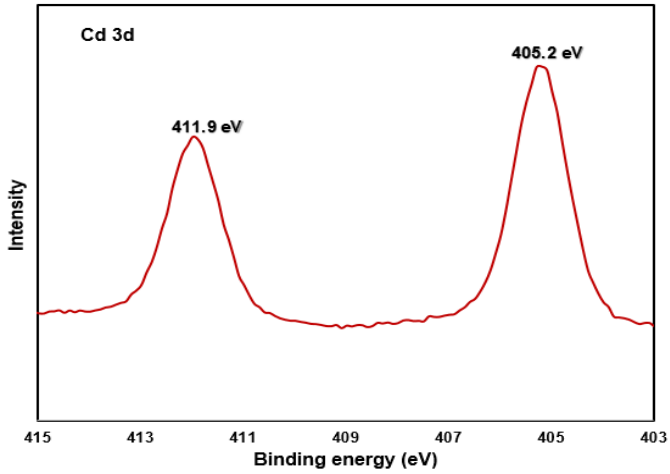

Figure 3.32 High resolution XPS spectrum of Cd 3d region of DNA templated $CdZnS_2$ nanowire.

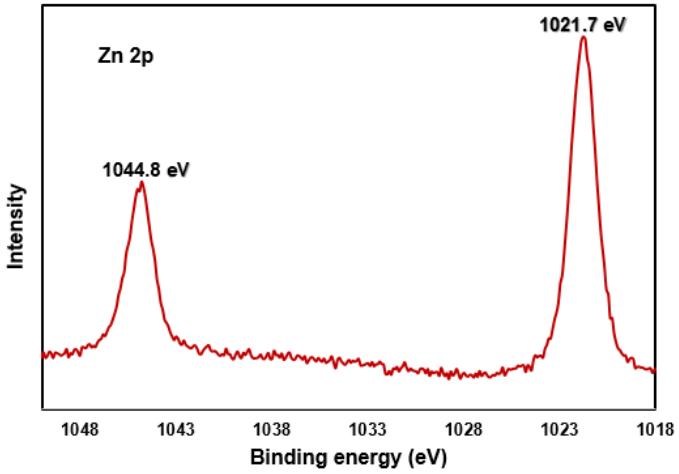

Figure 3.33 High resolution XPS spectrum of Zn 2p region of DNA templated $CdZnS_2$ nanowire.

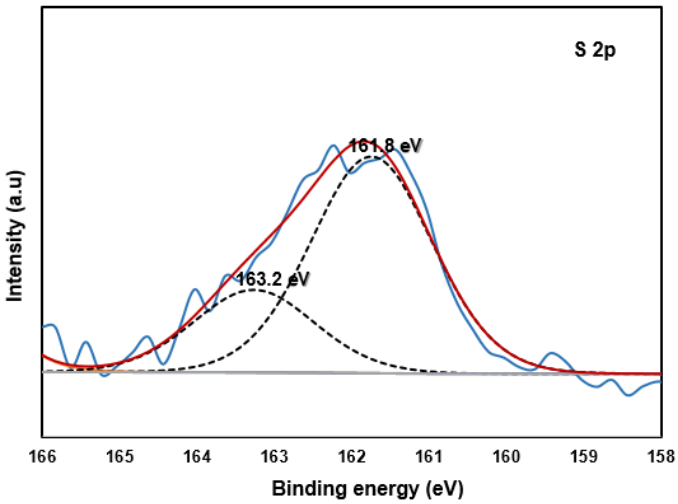

Figure 3.34 High resolution XPS spectrum of S 2p region of DNA templated $CdZnS_2$ nanowire.

The further resolution of XPS core level spectra for the Zn 2p region of the synthesised ZnS nanowire was obtained and presented in figure 3.35. The binding energies seen at 1021.7 eV and 1044.9 eV is attributed to the characteristic photoelectron peaks of Zn $2p_{1/2}$ and Zn $2p_{3/2}$ core level of Zinc sulfide. The spin orbit binding energy of the peaks are separated by 22.3 eV[204]. The high resolution XPS peak of S 2p can be further resolved into a doublet peak at 161.8 eV and 163.0 eV corresponding to the S $2p_{3/2}$ and S $2p_{1/2}$ core level photoelectron peaks of ZnS.

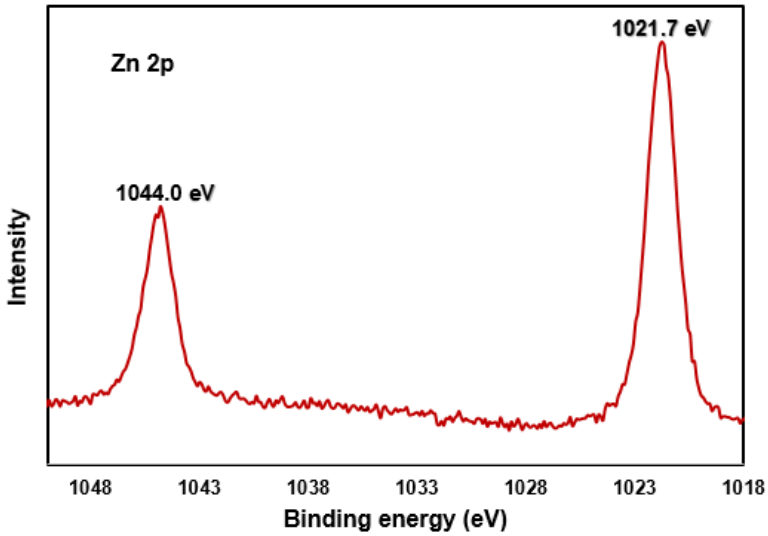

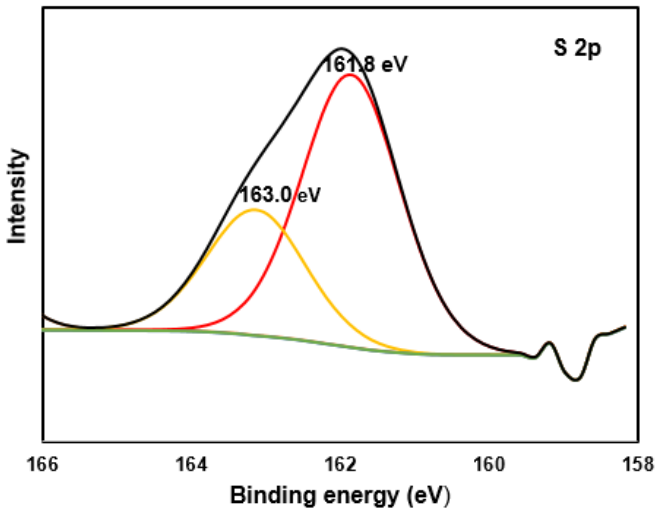

Figure 3.35 High resolution XPS spectrum of (a) Zn 2p region (b) S 2p region of DNA templated ZnS nanowire.

3.3 Conclusion

DNA templated CdS, $CdZnS_2$ and ZnS were synthesized in solution to form smooth and continuous nanowires. In other to synthesize smooth and continuous templated DNA nanowires, it was also established that the reaction has to be in two stages and sufficient time should be allowed during addition of the precursors. AFM studies was carried out on the λ-DNA templated CdS, $CdZnS_2$ and ZnS nanowires synthesised to determine the morphology and size distribution. The templated nanowires were found to have height distribution of 4-8 nm. The optical images shows a bright emission from the dense network of nanowires and single nanowires can also be seen as tiny extensions from the dense mass. The nanowires were photoluminescent with Raman peaks that shows size quantisation. The UV-Vis spectra indicted peaks for the DNA as well as the metal sulfides and the FTIR spectra demonstrated shift between the bare DNA and the nanowires which can be ascribed to the reaction of the metal sulfides with the DNA. The TEM images showed tiny strands of the 1D nanowires showing the templating of the metal sulfide on the DNA .The crystallite size and crystal structure of the nanowires were determine via XRD and it showed that a smaller size compared to the AFM image. This can be ascribed to the height being more than one particle size. This phenomenon has also been previously reported in the synthesis of other nanomaterials[57]. The corresponding elemental composition determined from the surface XPS spectroscopy showed the presence of the various elements accordingly indicating the formation of the binary and ternary metal alloys on the DNA template.

CHAPTER FOUR

Electrical measurement and gas sensing using λ-DNA templated CdS, $CdZnS_2$ and ZnS nanowires

4.1 Introduction

This chapter analyses the different methods that were used to determine the electrical properties of the DNA templated metal sulfide nanowires that were synthesised in solution. The three methods that were used to determine the electrical properties of these nanowires are two terminal I-V measurement, transient current measurement and impedance spectroscopy. The two terminal I-V measurement was used to measure the current of carefully aligned nanowire networks on a microfabricated electrode. The temperature dependence of the nanowire conductance was also studied using this method so as to investigate the thermal stability and conduction mechanism of the nanowire networks. The transient current measurement was used to determine the change in conductance of the nanowire with length and along with the impedance measurement used to determine the contact and nanowire resistance. The synthesised DNA templated nanowires were used for the fabrication of sensors by aligning on platinum on silicon electrodes via molecular combing. The sensor was used for sensing VOCs such as ethanol, acetone, chloroform and hexane. The response transient, the response and recovery times, the sensitivity and selectivity towards the VOCs, effect of temperature and flow rate on the sensitivity were studied and reported here. The mechanism of sensing of the metal sulfide nanowire sensors were also discussed.

4.2 Results and discussion

4.2.1 Electrical properties of DNA templated nanowires.

The electrical properties of networks of DNA templated nanowires were studied using two terminal probe station measurements, impedance spectroscopy and transient current measurements. These measurements facilitated an understanding of the conduction mechanism and an assessment of the contact resistances.

4.2.1.1 Two terminal probe station measurement

The electrical properties of the prepared DNA templated metal sulfide nanowires were determined by carrying out two terminal current-voltage (I-V) measurement of the nanowires using a probe station. The measurement of I-V properties of the nanowires was very important because it provided evidence on the conduction mechanism of the templated nanowires. The synthesized nanowires were drop-cast on the micro-fabricated electrodes and aligned via molecular combing by blowing nitrogen across the device in the direction perpendicular to the electrodes. Figure 4.1(a) showed network of CdS/DNA nanowires prepared in aqueous solution and deposited on platinum micro-band electrodes fabricated on a silicon chip. Figure 4.1a shows the fluorescence image of the nanowire film drop casted on a microfabricated electrode to bridge the gap between the platinum micro-band fingers. Figure 4.1b shows the network of the aligned nanowire when viewed under AFM. It is difficult to align a single nanowire across the electrode gap of 10 μm and hence the network of nanowires is a more practically relevant situation. The four platinum electrode track can be seen running from top to bottom while the deposited nanowires is crossing from left to right. The pre-fabricated micro-electrode with aligned sample was then inserted into the chamber of the probe station and contacted with two needles from different sides of the electrode pads and readings of current and voltage obtained.

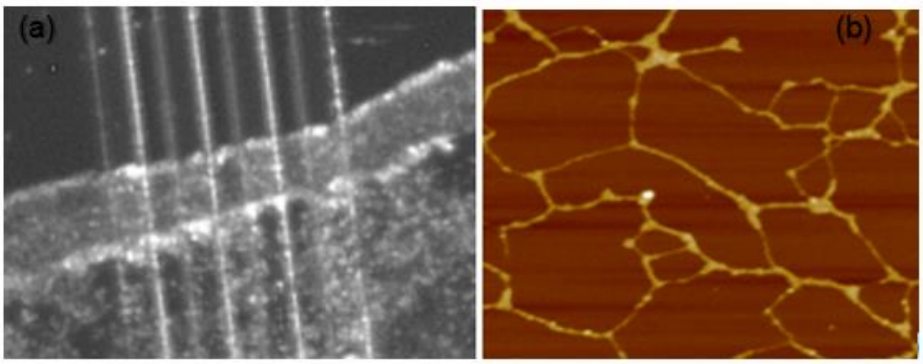

Figure 4.1 Network of CdS/DNA nanowire prepared in aqueous solution and deposited on platinum micro-band electrodes fabricated on a Si/SiO2 chip (a) The CdS/DNA nanowire network on the electrode showing florescence with excitation light from a mercury lamp passed through a 300 – 400 nm band pass filter. (b) AFM image of the CdS/DNA nanowires aligned on the electrode in the inter-electrode gap.

Attempts to determine the conductivity of a single nanowire were not successful due to the difficulty involved in trying to align a single nanowire in between an electrode

with a gap of 10 µm. The experiment is difficult because of the small size of the nanowire and the possibility of small gaps along the nanowire due to uneven coating of the nanowire with the metal sulfide. The AFM profile analysis showed that the nanowires have a modal height of about 4-7 nm and there is slight difference in the height along the length of the nanowire (see figure 3.4). Therefore, all the I-V measurement performed were on a networks of nanowires because such networks are tolerant of small numbers of gaps or breaks and ultimately, more useful as sensing devices than single nanowires. Figure 4.1 shows how nanowire film was aligned on the electrode and the structure of the network as observed under the AFM. The plotted I-V curve of the DNA templated CdS/DNA and $CdZnS_2$/DNA nanowires are shown in Figure 4.2 while that of ZnS/DNA can be found in Appendix A.

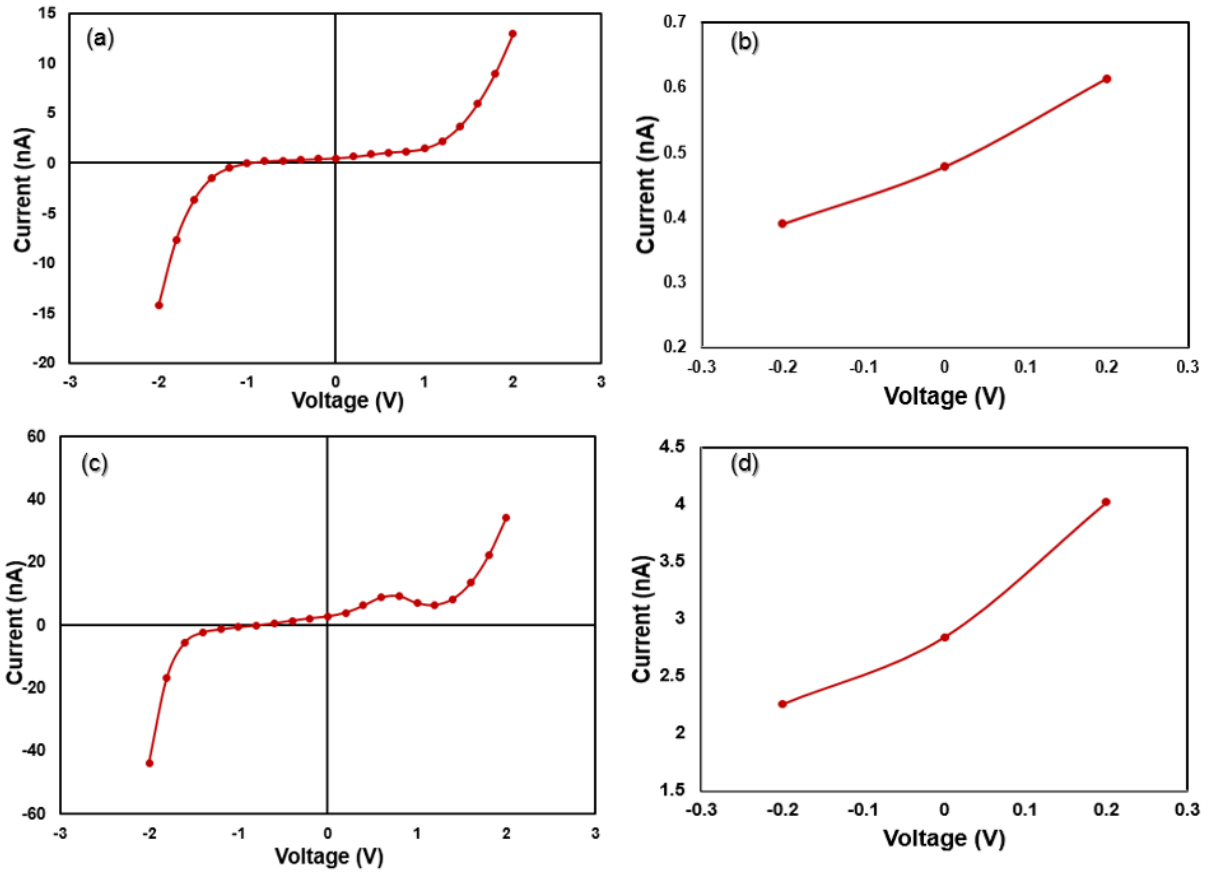

Figure 4.2 Electrical measurement (I-V curve) of DNA templated nanowire network prepared in aqueous solution and aligned on platinum on silicon microfabricated electrode. (a) & (c) CdS/DNA and CdZnS2/DNA Plot showing space charge limited current. (b) & (d) Low voltage I-V plot of CdS/DNA and $CdZnS_2$/DNA.

The devices studied have the structure M/S/M where M indicates a metal and S a semiconductor. An M/S interface have the I-V characteristic of a diode represented

with the Shockley diode equation (4.1) which is used to explain the non-linear nature of the plots.

$$\frac{i}{i_o} = e^{-\frac{eV}{K_B T}} - 1 \qquad (4.1)$$

Where *V* is the applied potential and i_o is a constant. In reverse bias, V<0, the current is nearly independent of potential, $i = -i_o$, but in forward bias, V>0, the current rises exponentially. However, the two interfaces, M/S and S/M in the present devices are opposed and at least one must be reverse-biased, therefore a diode-like characteristic is not expected. At small applied potentials, $eV < k_B T$, the characteristic is linear as can be seen by a Taylor expansion of equation (5.1). At higher applied biases, a different model is required.

The plots in figure 4.2 show a non-linear characteristic which can be attributed to different types of conduction mechanism. The non-linear I-V properties of semiconducting nanowires are normally studied and analysed using the theory of space charge limited current (SCLC) conduction[103,106] (an explanation is found in chapter 1.11) . The theory is suitable for explaining the conduction mechanism of metal sulfide sandwiched between two metal electrodes due to the high resistance of the semiconductor either as result of it being intrinsic or because of depletion charge carriers[103]. This theory predicts that the current can be represented by the equation:

$$I \; \alpha \; V^n \qquad (4.2)$$

Where V = voltage, I = current and n = the slope of a plot of log I vs log V.

Figure 4.3 shows two different slopes for the low and high applied voltages within the applied bias. The slope at low voltage (less than 1V) determined from ln I vs ln V is n~1 while that in the high voltage (greater than 1V) is n~2. The low voltage section showed an approximately ohmic conduction. This has been ascribed to a carrier density higher than the injected charge carrier density at such a low voltage[205]. The conduction at higher voltage has a slope of n~2 which clearly indicates a space charge limited conduction mechanism. The change in the slope of the plot as the voltage is increased is due to the high transient density of space charge carriers in the conduction band due to injection from the electrodes. The most important factors responsible for this kind of conduction mechanism are charge traps and surface defects[106].

The slope from the ohmic portion at small bias voltage correlate to a resistance of 1.6 GΩ and 5.63 GΩ for CdS/DNA and $CdZnS_2$/DNA nanowires respectively. This result is two order higher than that reported in literature[63]. This might be due to the different kind of electrode (Au/Si) used in addition to other factors such as concentration, crystallinity and amount of material[206]. The large resistance of semiconductors sandwiched between electrodes to form metal/semiconductor/metal interface is partly due to contact resistance which is present in all two terminal devices and is investigated later in this thesis.

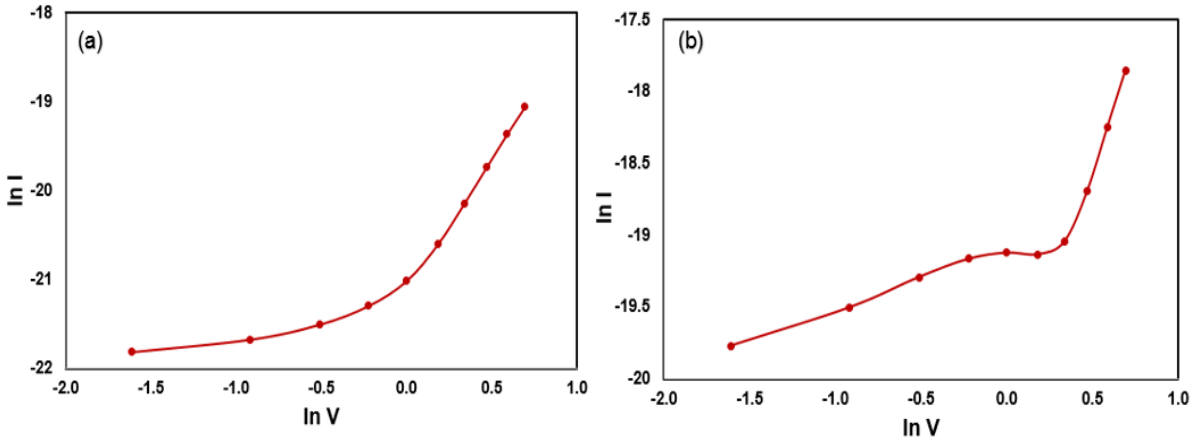

Figure 4.3 Showing two different slopes for the low and high applied voltages within the applied bias for (a) CdS/DNA (b) $CdZnS_2$/DNA.

The direct measurement of the I-V properties of the nanowires aligned on the electrode can also be extremely useful for investigating the temperature dependence of conduction. The mechanism of conduction of nanomaterials used for making nanoscale devices are important because it shows how the devices will response to the varying atmospheric temperature or the temperature of the environment they can be put to use. The combed nanowire on the electrode are first dried in air and then under nitrogen. The measurement at room temperature were obtained and then different temperatures were obtained by connecting the probe station to an ESQEC ETC-200L thermal chuck. Even though lambda DNA normally comes in length of ~16 μm[207], it is actually difficult to have nanowires of up to 10 μm when fully templated. This might be due to coiling of DNA in the presence of metal salts. It is also useful to study the properties of the network of nanowires because the two terminal sensing device that the samples are to be used for works better with a network of nanowire due to increased surface area. Nanowire network devices are also known to be more robust

than single nanowire devices because one break in the single nanowire device destroys it. Figure 4.4 shows the I-V curves of the CdS/DNA and $CdZnS_2$/DNA nanowire network at different temperatures over a temperature range of 283 to 363 K.

The curves of I-V measurements at the various temperatures showed a non-linear trend especially at high voltages. The I-V characteristic of many 1-D nanostructures and their conduction mechanism have been explained previously using different theoretical models[96–98,101,102,208]. It is difficult to be certain of the best description of the non-linear behaviour of these 1-D nanostructures due to complexities in structure[209]. The simple SCLC conduction model was able to explain qualitatively the conduction of these nanowires due to high resistance attributed to depleted charge carriers[103].

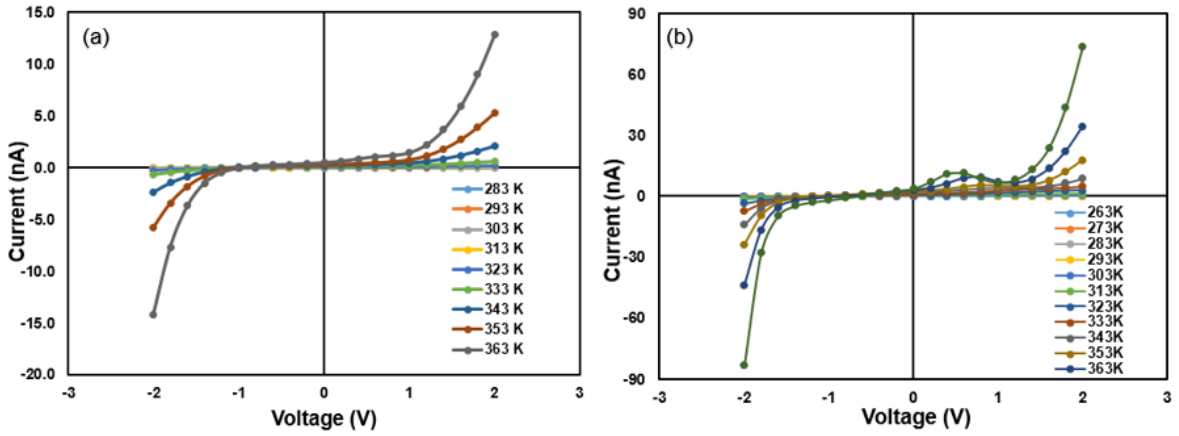

Figure 4.4 Shows the I-V curves of (a) CdS/DNA and (b) $CdZnS_2$/DNA nanowire network aligned on a platinum on silicon microfabricated electrode at different temperatures over a temperature range of 283 to 363 K.

Even though the I-V curves were generally non-ohmic in nature, at very low voltage the dependence of the current to voltage was fairly linear. The conductance of the nanowires at different temperature was therefore extracted from the slopes of the linear portion of the curves. The plot of conductance of CdS/DNA nanowire aligned on micro electrodes at different temperature is presented in figure 4.5. The plot shows a general increase in conductance of the nanowire with increasing temperature .Figure 4.5(b) & (d) showed the conductance against temperature at temperatures below 340 K. The increase in conductance with temperature was gradual and consistent at temperatures below 340 K. However, at temperatures above 340 K, there was significant change in the conductance with temperature and this might be due to change in mechanism of conduction. The change in mechanism could be as a result of fusion of the ‘’nanogaps’’

between the templated materials as a result of sintering or increase in the kinetic energy of the electrons and hence reduced coulomb blockade[97]. The temperature dependence of these nanowires like any other semiconductor is also governed by trap distribution. An increase in temperature leads to increased number of space charges in the conduction band[106].

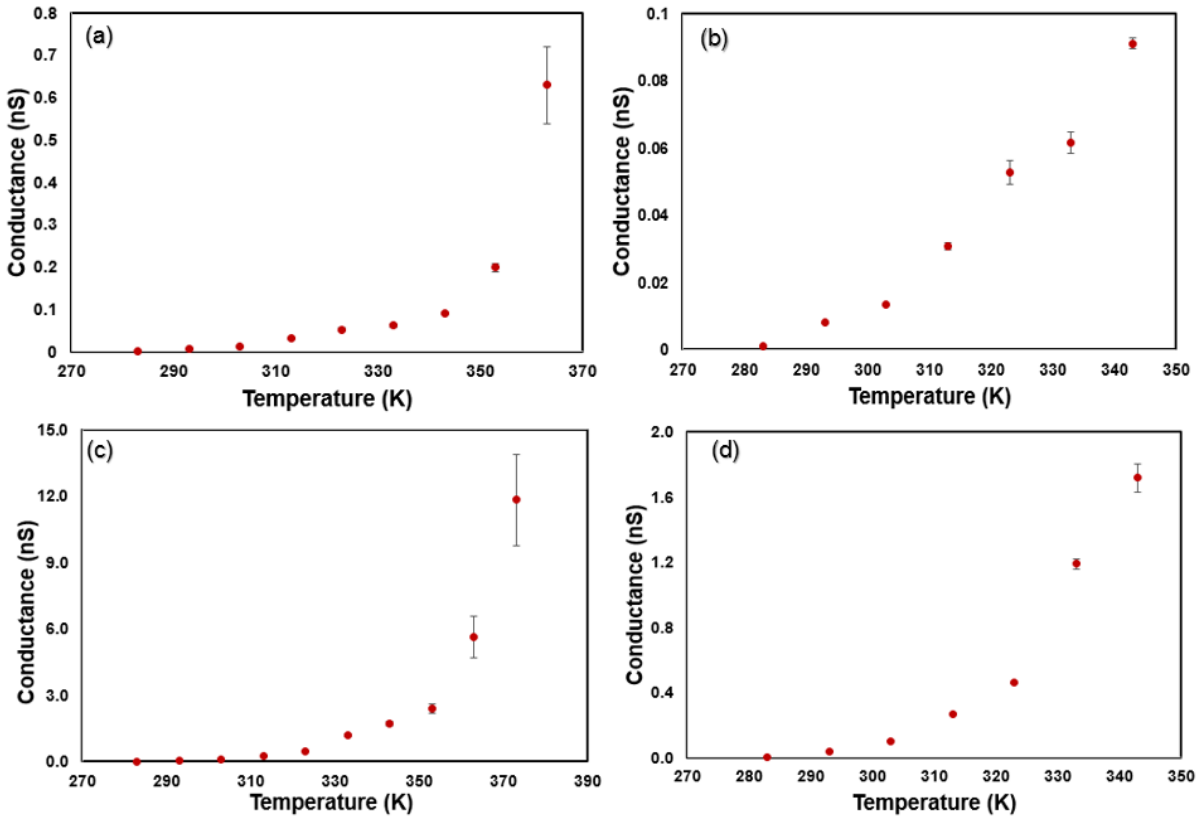

Figure 4.5 The plot of conductance of CdS/DNA and $CdZnS_2$/DNA (a & c) nanowire aligned on a platinum on silicon microfabricated electrode at different temperature. (b & d) Conductance of the nanowires at low temperatures showing a more gradual response.

The different temperature I-V measurement was also used to extract the activation energy barrier for a temperature range of 283K to 363K at an applied voltage of 0.2 V. This was done by extracting the conductance from the slope at low bias from the temperature range between 283K and 363K. The conductance obtained from the slope of the curves (at low voltage) at different temperature was fitted into the Arrhenius model equation [$InG = InG_o - \left(\frac{To}{T}\right)^D$], by plotting InG against $\frac{1}{T}$. The plot showed a fairly straight line confirming an Arrhenius like behavior (D~1). The slope of this plot was used to extract the activation energy barrier as previously done in literature[210–212]. The activation energy was calculated by extracting the slope of the plots (-To) in figure

4.6 and multiplying it to -R (universal gas constant) since the plot is showing Arrhenius behaviour with D~1.The activation barrier energy of the CdS/DNA and $CdZnS_2$/DNA nanowire network were calculated to be 57.4 kJ mol^{-1} (0.60 eV) and 68.4 kJ mol^{-1} (0.71 eV) respectively. These values are roughly consistent with a Schottky barrier at the Pt/NW interface.

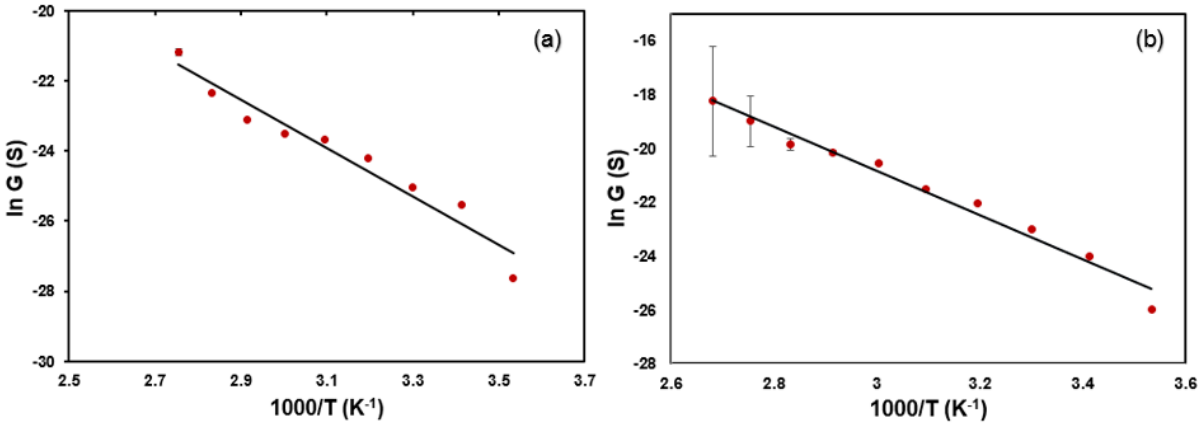

Figure 4.6 Arrhenius plot of the conductance of (a) CdS/DNA and (b) $CdZnS_2$/DNA nanowire aligned on platinum microelectrode.

4.2.1.2 Impedance measurement

Impedance measurements were performed to determine the electrical properties of the DNA templated metal sulfide nanowires and to assess the contribution of contact resistance to the devices. Impedance is an important method that can be used to determine the contact and bulk resistances separately. Devices were prepared for impedance spectra by carefully aligning the DNA templated nanowires between the platinum micro-band fingers by molecular combing and allowing to dry in air to bridge the gap on the electrodes. The contact resistance and nanowire resistance of the device was determined by analysing the curve of the impedance spectrum. First, the theory of impedance spectroscopy is reviewed and then the equivalent circuit used to analyse the data is described.

The impedance Z of a simple resistor is given by Ohm's law; where E is the applied potential and i the current passing through the system is equal to resistance R.

$$Z = \frac{E}{i} = R \tag{4.3}$$

The concept of impedance is a generalization of resistance that applies also to capacitive circuit elements. The amount of electric charge Q, transported in such a circuit is given by

$$Q = CE \tag{4.4}$$

Where C is the capacitance of the circuit and E the applied potential. Differentiating equation (4.4) and substituting $\frac{\delta Q}{\delta t} = i$, we have;

$$i = C\frac{\delta E}{\delta t} \tag{4.5}$$

Given that the applied ac potential of a capacitor is given as $E = E_0 e^{j\omega t}$, then $\frac{\delta E}{\delta t} = j\omega E_0 e^{j\omega t} = j\omega E$ and substituting in equation (4.5) allows the determination of the ratio E/i for a capacitor;

$$i = j\omega CE \text{ Or } Z = \frac{E}{i} = \frac{1}{j\omega C} = -\frac{j}{\omega C} \tag{4.6}$$

Where E_0 is amplitude and E is the potential at time t, ω the radial frequency $j = \sqrt{-1}$ and $e^{j\omega t} = \cos\omega t + \sin\omega t$

In the impedance measurement experiment, an ac potential $E = E_0 \sin\omega t$ was applied and the resulting alternating current which comprised sine and cosine components was measured. The results of impedance measurement was reported in the form of $Z = \mathrm{Z'} - \mathrm{jZ''}$ where $\mathrm{Z'}$ and $\mathrm{Z''}$ are known as the real and imaginary part of the impedance. A pure resistor has only a real part $Z = \mathrm{Z'}$ as shown in equation (4.3) while a pure capacitor has only the imaginary part $Z'' = \frac{1}{\omega C}$ as shown in equation (4.6). The total impedance was then calculated by combining the components according to same rules as for normal resistors. Impedances in series were added while the reciprocals of impedances in parallel were also added. The equivalent circuit for the two terminal device can be represented as shown in figure 4.7.

If we assume that the impedance for the interface on the left is Z_{int}, then the contact resistance (R_c) and the interfacial capacitance C are in parallel combination representing the fact that high frequency currents will pass mainly through the capacitance, but at low frequencies the current will pass mainly through the contact resistance;

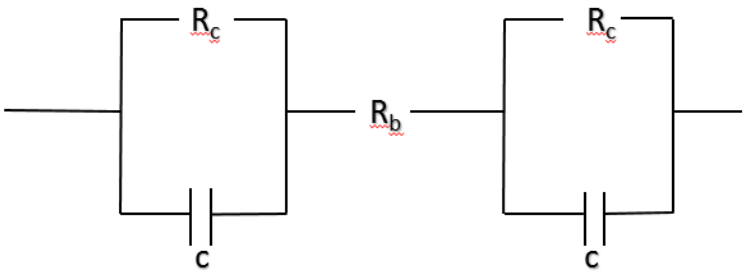

Figure 4.7 Equivalent circuit of the Pt/NW/Pt device showing parallel combination of contact resistors (R_c) and impedance (C) in series with the bulk nanowire resistance (R_b).

$$\frac{1}{Z_{int}} = \frac{1}{R_c} + j\omega C = \frac{1+j\omega CR_c}{R_c} \tag{4.7}$$

Equation (4.7) was inverted, then we had:

$$Z_{int} = \frac{R_c}{1+j\omega CR_c} \tag{4.8}$$

Since the instrument plotted the data for real and imaginary parts, then the equation was written in the form of $Z = Z' - jZ''$. The next thing done was to multiply equation (4.8) by $1 = \frac{1-j\omega CR_c}{1-j\omega CR_c}$ and keeping in mind that j^2=−1. We have,

$$Z_{int} = \frac{R_c(1-j\omega CR_c)}{1+\omega^2 C^2 {R_c}^2} \tag{4.9}$$

The total impedance for the equivalent circuit as shown in the figure 4.7 was achieved by multiplying Z_{int} by 2 so as to account for the right hand interface and the nanowire resistance was added because it was in series with the interfaces.

$$Z_{int} = R_b + \frac{2R_c}{1+\omega^2 C^2 {R_c}^2} - j\frac{2\omega C{R_c}^2}{1+\omega^2 C^2 {R_c}^2} \tag{4.10}$$

Comparing equation (4.10) to the equation form $Z = Z' - jZ''$, we can clearly see that;

$$Z' = R_b + \frac{2R_c}{1+\omega^2 C^2 {R_c}^2} \text{ and } Z'' = \frac{2\omega C{R_c}^2}{1+\omega^2 C^2 {R_c}^2}$$

The instrument measured and plotted Z'' on the y-axis and Z' on the x-axis with different point for different values of the frequency in Hz. Scheme 4.1 shows a typical Nyquist plot showing how contact and nanowire resistance was extracted.

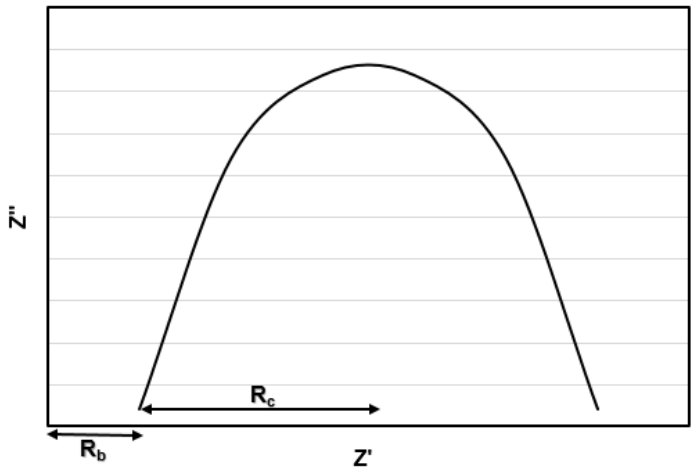

Scheme 4.1 A typical Nyquist plot showing how contact and nanowire resistance can be calculated. Note: R_c contact resistance and $R_b$nanowire resistance.

It can be observed from equation (4.10) that as $\omega CR_c \rightarrow 0$ or $\omega CR_c \rightarrow \infty$, the imaginary impedance $Z'' \rightarrow 0$. The real part of the impedance became $Z' = R_b + 2R_c$ as $\omega CR_c \rightarrow \infty$ and $Z' = R_b$ as $\omega CR_c \rightarrow 0$.

From the scheme, it was deduce that R_b is the axis intercept at high frequency while R_c is the radius of the semi-circle. The capacitance C can also be determined using the fact that the maximum of $Z''$is at $\omega CR_c = 1$. Figure 4.8 shows the impedance spectrum of the different DNA templated metal sulfide nanowires aligned on micro-fabricated platinum on silicon electrodes.

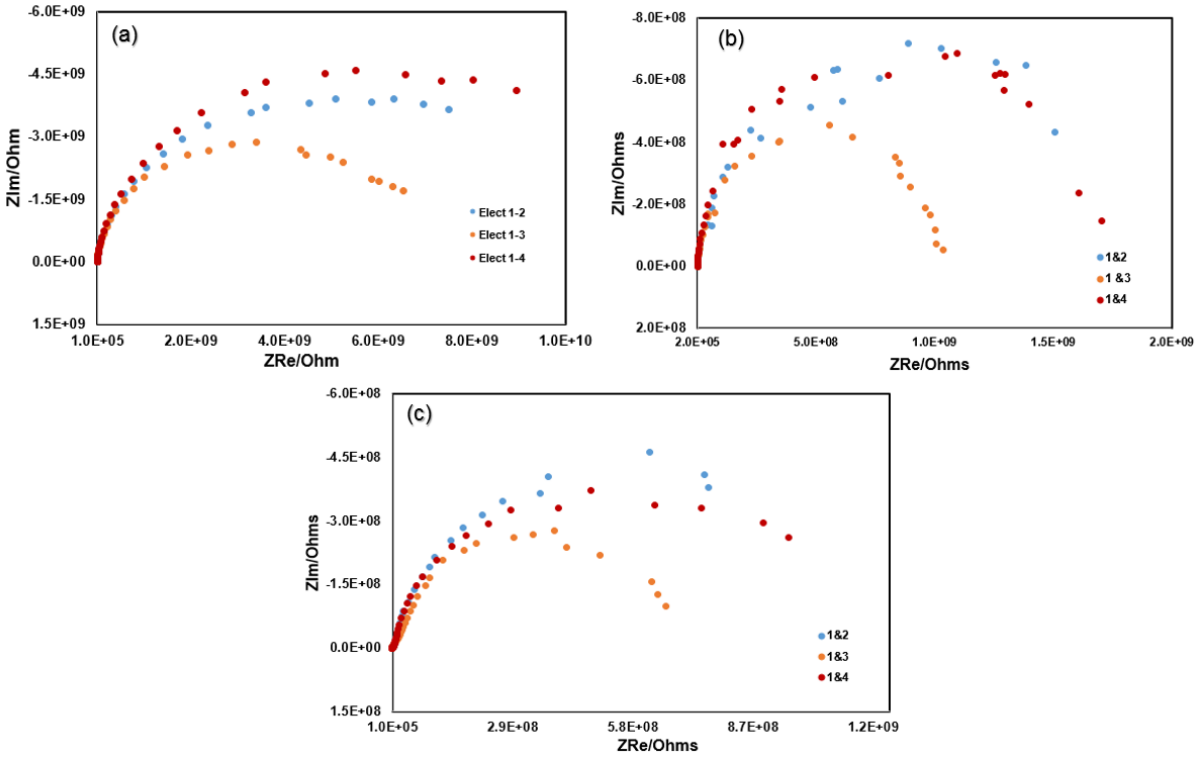

Figure 4.8 Shows the impedance spectrum of DNA templated (a) CdS/DNA (b) $CdZnS_2$/DNA (c) ZnS/DNA nanowires aligned on micro-fabricated platinum on silicon electrodes.

From the Figure 4.8 above, the nanowire resistance was obtained by extrapolating the left hand side of the semicircle to the x-axis. It is clear immediately from the figures that the contact resistance dominates the impedance of these devices because the real axis intercept at high frequency is negligible compared to the radius of the semicircle. The summary of the nanowire and contact resistance for the different type of metal sulfide synthesized at various electrode separations is shown in table 4.1. The separation was achieved by contacting electrodes 1&2, 1&3 and 1&4 which corresponds to 20 µm, 40 µm and 60 µm respectively because the separation between the electrodes is 20 µm as measured from the centre of each electrode (image of the electrode is shown in figure 4.9).

Table 4.1 Summary of the nanowire and contact resistance for the different type of metal sulfide synthesized at various electrode separations.

	Nanowire resistance (R_b) (Ω)			Contact resistance (R_c) (Ω)		
Electrode spacing	**20 µm**	**40 µm**	**60 µm**	**20 µm**	**40 µm**	**60 µm**
CdS/DNA	1.91 E05	2.41 E05	2.46 E05	3.76 E09	3.27 E09	4.48 E09
CdZnS/DNA	3.44 E05	4.72 E05	5.02 E05	7.55 E08	5.20 E08	8.55 E08
ZnS/DNA	1.55 E05	2.08 E05	2.06E05	3.82 E08	3.30 E08	4.78 E08

The results showed that there is a general increase in nanowire bulk resistance with increase in separation of the electrodes, as expected although some deviations from expected behaviour was also seen in few cases. The deviation might be due to uneven distribution of the nanowires across the electrode or the variation in coating along the nanowires. A resistance anomaly in 1D nanowires has also been reported in previous research, where there is reduction in the nanowire resistance with increase in length[213–215]. This was attributed to the presence of high density electron accumulation layer on the surface of the nanowires[216]. The results also indicated a high contact resistance compared with the nanowire resistance. The total resistance for all the synthesized nanowires fall within the same range with just a slight difference. The result was based on the assumption that same amount of nanowires are deposited per drop and the alignment are uniform for all the fabricated devices. This might not necessary be true as same devices fabricated at different times even with same batch of sample shows slight difference in the contact resistance and nanowire resistance.

4.2.1.3 Transient current measurement

The transient current measurement was also carried out to determine the conductivity of the synthesized nanowire by measuring the change in conductance of the nanowire with length. The method can also be used to determine the separate contribution of contact resistance and the nanowire resistance to the overall resistance of the two terminal device. The data obtained is similar to that from impedance, except that it is restricted to small amplitude applied voltage biases.

The current-time transient for the two terminal devices were determined by coating the platinum micro-band electrode with the DNA templated nanowires (NWs). This was done by carefully aligning the DNA templated nanowires between the platinum micro-band fingers by molecular combing to make the device.

The two contact electrode device was represented as Pt/NWs/Pt where / indicates the junction between the platinum (Pt) micro-band electrodes on the silicon chip and the network of nanowire film. When potential E was applied between the two electrodes, current flow from one platinum electrode through the network and then back to the other Pt electrode. Two kinds of current are observed during the process. The first type was the current that involves electron transport from the metal into the nanowire network and flowing through the nanowire film and then out through the other metal electrode. The size of the current was dependent on the applied potential and the three resistances; the resistance of the nanowire film between the two electrodes (R_b) and the two contact resistance between the Pt/Nws and Nws/Pt interface. The interface resistance was represented as R_c and is based on the assumption that the two interfaces are symmetrical and have same contact resistance.

The second type of current that can flow through the device was due to accumulated charges at or near the Pt/NW and NW/Pt interfaces on either side of the electrode and doesn't necessarily involve electrons flowing through the whole device, crossing from the metal into the nanowire and flowing in the film. This type of current is referred to as charging current or capacitive current. The current only flows through the device in response to applied voltage while the ions/electron adjust their positions. The amount of electric charge Q that is transported during the process is proportional to the applied voltage *E*.

$$Q = CE \tag{4.11}$$

Where C is the proportionality constant called capacitance. It indicates the amount of charge that accumulated at the interface at a given applied voltage. Figure 4.9 shows the electrical equivalent circuit of the Pt/NW/Pt device.

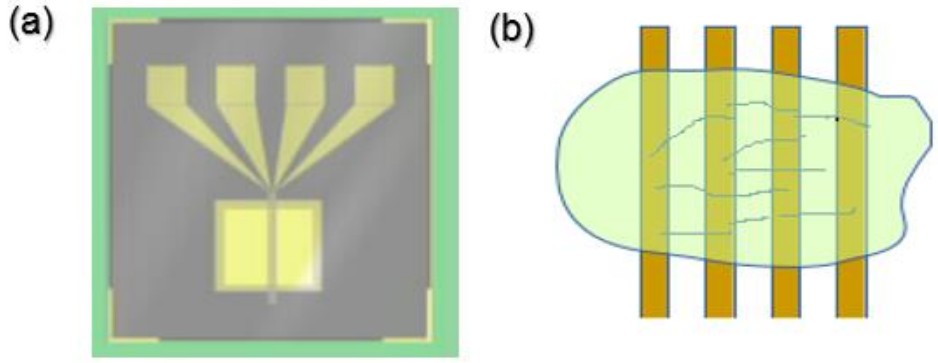

Figure 4.9 (a) Shows the electrode used for electrical measurements. (b) Image showing how the nanowires were aligned on the micro-fabricated platinum on silicon electrode. The electrode part were the nanowires are deposited (yellow square) consist of four platinum 'micro-fingers' (width 10 μm, length 2 mm).

The current flowing through the nanowire film and the Pt/NW interface (resistor, R) was proportional to the applied potential (Ohm's law) at low potential. The current that flow with change in the applied potential from 0 to E was calculated using Ohm's law because current is expressed as the rate of change of charge $\frac{\delta Q}{\delta t}$. The total potential, E, applied across the whole set up was divided between the capacitance at the Pt/Nw (E_C) interface and the NW film. This can be written as

$$E = E_c + E_R \tag{4.12}$$

Applying equation (4.11) for the potential across the capacitor, E_C and Ohm's law for the potential across the NW, E_R we get:

$$E = \frac{Q}{C} + iR_b \tag{4.13}$$

Differentiating with respect to time t, we get

$$\frac{\delta E}{\delta t} = \frac{i_c}{C} + R_b \frac{\delta i}{\delta t} = 0 \tag{4.14}$$

Where i_c is the current passing through the capacitor and E is a constant. i is the total current passing through the circuit but is not equal to i_c because some current passes through the contact resistance R_c and the rest through the capacitor (i_c). Note that the value of R_c considered here is the combined value for the two interfaces, assumed identical. The amount of current passing through the contact resistance was expressed using Ohm's law as the potential across the capacitor divided by the contact resistance. The total current was then expressed as

$$i = \frac{E_c}{R_c} + i_c = \frac{Q}{R_c C} + i_c \tag{4.15}$$

But substituting equation (4.11) into equation (4.15), we get

$$i = \frac{E - iR_b}{R_c} + i_c \tag{4.16}$$

Eliminating i_c between equations (4.14) and (4.16), we obtain an equation relating only the measured (i) and the control (E) variables:

$$R_b C \frac{\delta i}{\delta t} + i\left(1 + \frac{R_b}{R_c}\right) = \frac{E}{R_c} \tag{4.17}$$

Solving and rearranging equation (4.17), we get;

$$i = \frac{E}{R_b}\frac{R_c}{R_b + R_c} e^{-t/\tau} + \frac{E}{R_b + R_c} \tag{4.18}$$

$$\tau^{-1} = \frac{1}{C}\left(\frac{1}{R_b} + \frac{1}{R_c}\right) \tag{4.19}$$

At $t = 0$, no current flows through the contact resistance (equivalent to the high frequency limit of the impedance experiment) and $R_b = E/i$, the nanowire resistance. The steady state current (i_{ss}) is achieved when $t/\tau \rightarrow \infty$, the equation then reduced to Ohm's law with the resistance equal to sum of nanowire and contact resistance.

$$i_{ss} = \frac{E}{R_b + R_c} \tag{4.20}$$

The values of $R_b and\ R_c$ was determined separately by varying R_b while keeping the R_c constant. In our case, R_b was varied by increasing the distance between the electrodes because resistance varies linearly with distance. This was achieved by contacting electrodes 1&2, 1&3 and 1&4 which corresponds to 20 µm, 40 µm and 60 µm respectively because the separation between the electrodes is 20 µm as measured from the centre of each electrode.

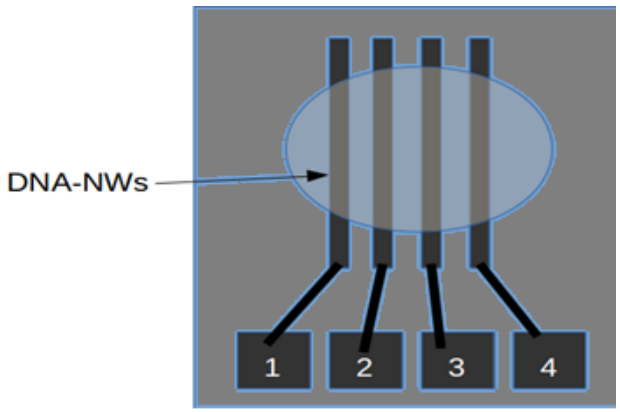

Figure 4.10 The chip showing the electrode contact pads.

Using the equations above, the transient current of CdS/DNA templated nanowire was measured at different voltages and the result presented in table 4.2. The results were obtained by applying a potential between the electrodes connected to the computer via a potentiostat and measuring the transient current with time using PS trace (4.8) software. The transient current and the steady state current increases with increasing voltage. The total resistance decreases with increasing voltage. The nanowire resistance and the contact resistance were also calculated and presented as shown in table 4.2. The nanowire resistance were higher than the contact resistance at lower voltage while the converse is the case at higher voltage. Note that the difference between the nanowire resistances obtained in this measurement and those obtained by impedance (table 4.1) are due to the difference in applied voltages: the impedance measurement employs much smaller applied biases in the linear region of the I-V characteristics of figure 4.2, whereas the transient current measurements used applied voltages >1 V in the non-linear region of figure 4.2.

Table 4.2 Transient current measurement data for CdS/DNA templated nanowire measured at different voltages.

D/µm	I_{tot}/nA	I_{ss}/nA	I_{trans}/ nA	E/V	$R_{i\text{-}v}$/GΩ	R_b/GΩ	R_c/ GΩ
20	6.3	0.2	6.1	1	5.0	0.16	2.42
	14.8	3.5	11.3	2	0.57	0.14	0.22
	33.6	15.8	17.8	3	0.19	0.09	0.05
	45.9	24.3	21.6	4	0.17	0.07	0.04
	54.0	30.7	23.3	5	0.16	0.09	0.04
40	3.1	0.5	2.6	1	2.0	0.32	0.84
	7.8	2.3	5.5	2	0.87	0.14	0.31
	13.4	6.7	6.7	3	0.45	0.22	0.11
	22.8	12.5	10.3	4	0.32	0.18	0.07
	30.5	19.8	10.7	5	0.25	0.16	0.04
60	2.5	0.8	1.7	1	1.25	0.40	0.43
	5.4	2.4	3.0	2	0.83	0.37	0.23
	10.1	5.3	4.8	3	0.57	0.30	0.14
	14.2	10.7	3.5	4	0.37	0.28	0.05
	23.1	17.4	5.7	5	0.29	0.22	0.04

Note: Where (R_{I-V} =R_b +2R_c), R_b (nanowire resistance) and R_c (contact resistance).

Using the calculated total resistance R_{I-V} reported in table 4.2 and plotting it against electrode separation (d), the resistance per unit length can be calculated. The plot of the transient current with time at different voltages at steady state against the electrode separation is presented in figure 4.11. The size of this current is dependent on the applied potential and three resistances; the resistance of the DNA templated nanowire films between the electrodes R_b and the contact resistance which is located at the Pt/NW interface and NW/Pt interface R_c. Based on the assumption that the interfaces are symmetrical and that the amount of material aligned on both interface are same, then the contact resistance at both interfaces are same.

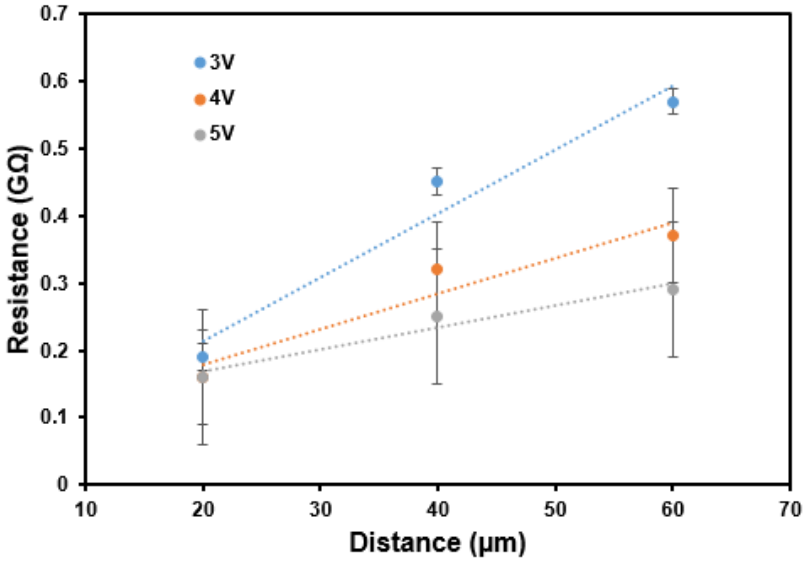

Figure 4.11 The plot of total resistance at different voltages at steady state of the CdS/DNA nanowire aligned on platinum on silicon microfabricated electrode.

At steady state, the contact and nanowire resistance are related to the current by equation (4.20). The plot was roughly a straight line which was then extrapolated to the zero separation to give the intercept on the y-axis which is the contact resistance (R_c). The average contact resistance at 3V, 4V and 5V are 23.3 MΩ, 73.3 MΩ and 103 MΩ respectively. The slope of the straight lines at the different voltages gives the average nanowire network resistance R_b per unit length. The resistance per unit length obtained for the DNA templated nanowire at 3V, 4V and 5V are 9.5 MΩ cm^{-1}, 5.3 MΩ cm^{-1} and 3.3 MΩ cm^{-1} respectively.

The results for transient current of $CdZnS_2$/DNA templated nanowire measured at different voltages obtained by applying a potential between the electrodes connected to the computer via a potentiostat and measurement done using PS trace (4.8) software is presented in table 4.3. The current tunnelling through the nanowire network from left to right across the electrode was increasing with increased voltage. The total resistance of the device decreased with increasing voltage. The nanowire resistance and the contact resistance were also calculated at steady state and presented in table 5.3. Both the nanowire and contact resistance also decreased with increasing voltage.

Table 4.3 Transient current measurement data for DNA/CdZnS2 templated nanowires at different voltages.

D/μm	I_{tot}/nA	I_{ss}/nA	I_{trans}/ nA	E/V	R_{i-v}/GΩ	R_b/GΩ	R_c/ GΩ
20	2.6	0.1	2.5	1	10.0	0.39	4.81
	6.3	0.5	5.8	2	4.0	0.32	1.84
	10.6	2.9	7.7	3	1.03	0.28	0.38
	20.0	9.2	10.8	4	0.44	0.20	0.12
	31.8	17.9	13.9	5	0.28	0.16	0.06
40	2.0	0.1	1.9	1	10.0	0.50	4.75
	3.9	0.6	3.3	2	3.33	0.51	1.41
	9.3	3.6	5.7	3	0.83	0.32	0.26
	17.1	7.9	9.2	4	0.51	0.23	0.14
	24.3	12.3	12.0	5	0.41	0.21	0.10
60	2.2	0.1	2.1	1	10.0	0.46	4.77
	5.6	0.5	5.1	2	4.00	0.36	1.82
	9.7	2.5	7.2	3	1.20	0.31	0.45
	13.1	6.0	7.1	4	0.67	0.30	0.18
	18.5	10.2	8.3	5	4.90	0.27	0.11

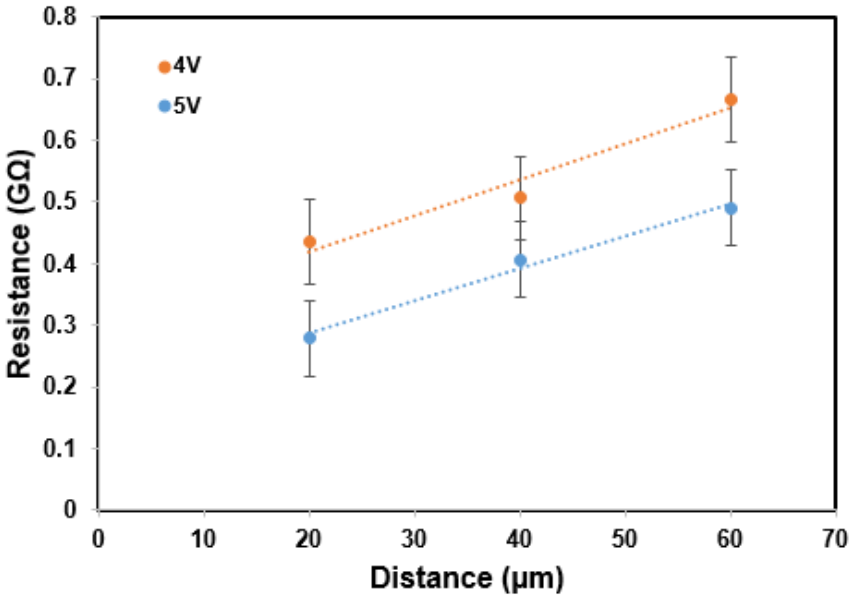

Figure 4.12 The plot of total resistance at different voltages at steady state of the $CdZnS_2$/DNA nanowire aligned on platinum on silicon microfabricated electrode.

The average contact resistance at 4V and 5V were calculated by extrapolating the plot to y-axis to be 304 MΩ and 181 MΩ respectively. The average nanowire resistance

per unit length determined from the slope of the plot is 5.8 MΩ cm^{-1} and 5.3 MΩ cm^{-1} for 4V and 5V respectively.

The transient current results for ZnS/DNA templated nanowire measured at different voltages were also obtained presented in table 4.4. As the voltage was increased, the current passing through nanowires was increasing and the resultant total resistance of the nanowires decreased. The nanowire and contact resistance were separately calculated as shown in table 4.4 and it showed that the contact resistance was predominantly higher than the nanowire resistance.

Table 4.4 Transient current measurement data for DNA/ZnS templated nanowires at different voltages.

D/μm	I_{tot}/nA	I_{ss}/μA	I_{trans}/μA	E/V	R_{i-v}/GΩ	R_b/GΩ	R_c/GΩ
20	1.8	0.5	1.3	1	2.00	0.56	0.72
	9.4	2.2	7.2	2	0.91	0.21	0.35
	118.4	60.9	57.5	3	0.05	0.03	0.02
	333.6	174.6	159.0	4	0.02	0.01	0.01
	607.4	307.3	300.1	5	0.02	0.01	0.01
40	1.9	1.3	0.6	1	0.77	0.52	0.12
	4.4	3.1	1.3	2	0.65	0.50	0.10
	11.2	5.8	5.4	3	0.52	0.30	0.13
	36.5	9.7	26.8	4	0.41	0.11	0.15
	59.9	12.6	47.3	5	0.40	0.08	0.16
60	3.0	0.8	2.2	1	1.25	0.33	0.46
	12.9	2.7	10.2	2	0.74	0.15	0.29
	115.1	48.6	66.5	3	0.06	0.03	0.02
	321.3	153.1	168.2	4	0.03	0.11	0.01
	574.2	248.6	325.6	5	0.02	0.08	0.01

4.2.2 Sensing results

The synthesised DNA templated nanowires was aligned on a micro-fabricated platinum on silicon electrode by molecular combing to determine their response to different volatile organic compounds (VOCs). The response of the fabricated sensor was determined by passing the various analyte over the sensor by use of mass flow controller (MFC) controlled by a Brooks Smart Interface (model 0260, Brookes) and a computer. The response was measured as change in conductance between zero air

and the various gaseous analytes. In order to ensure that the zero air serves effectively as background with uniform current throughout the experiment, zero air was passed over the electrode for about 15 minutes to ensure that the sample on the electrode stabilised. This was done in order to reduce the large change in current of zero air at the beginning of the experiment due to presence of atmospheric air. The line for the change in current becomes fairly smooth when the sample has equilibrated and stabilised as shown in figure 4.13.

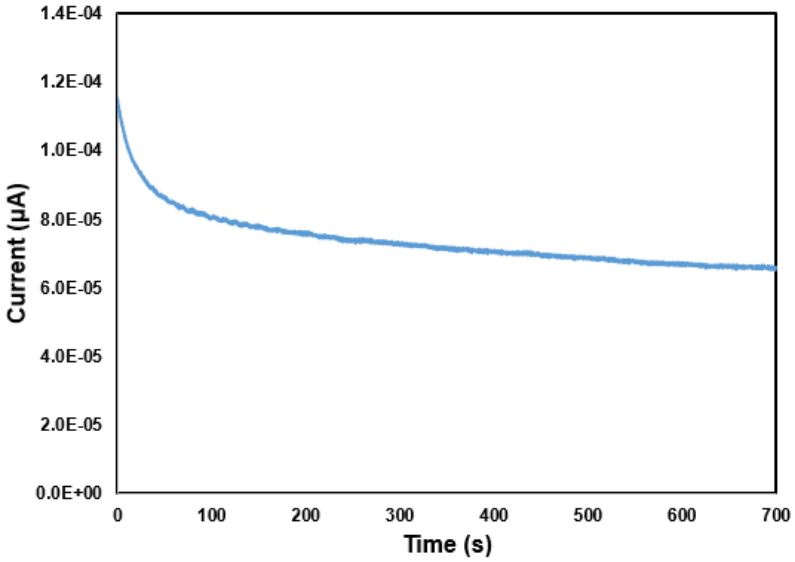

Figure 4.13 Plot showing the equilibration and stabilisation curve of zero air over the DNA templated metal sulfide nanowire sensors.

4.2.2.1 Response transient of CdS/DNA Nanowire

The transient response curve for three cycle of different organic vapour exposed to CdS/DNA and $CdZnS_2$/DNA nanowire sensor were studied. The exposure was done at fixed voltage of 5V at organic vapour concentration of 1.3 mM (calculation of the organic vapour concentration percent is shown in appendix C). The transient response curve was obtained by passing Zero air over the aligned nanowire on the electrode for some time to attain stability in the response before passing the organic vapour. The various organic vapours were then passed over the nanowire sensor so as to obtain the response before passing the zero air again. The process was repeated all over again to obtain as much as three cycles. The response is reported as the fractional change in current upon exposure to the analyte:

$$Response = \frac{i - i_o}{i_o} \tag{4.21}$$

Ethanol vapour showed the highest response and therefore the response transient has been presented in figure 4.14. The templated nanowire gas sensor showed a consistent reversible response to ethanol vapour with a maximum response of about 139% and 1000% to CdS/DNA and $CdZnS_2$/DNA respectively. The maximum response of ethanol vapour to ZnS/DNA was found to be 47% (appendix C). The $CdZnS_2$/DNA sensor has shown an enhanced response compared to those of CdS/DNA and ZnS/DNA. The high response of the nanowire sensors to ethanol vapour with reversible properties indicates that the templated nanowires has a potential to make a good gas sensor in practical application.

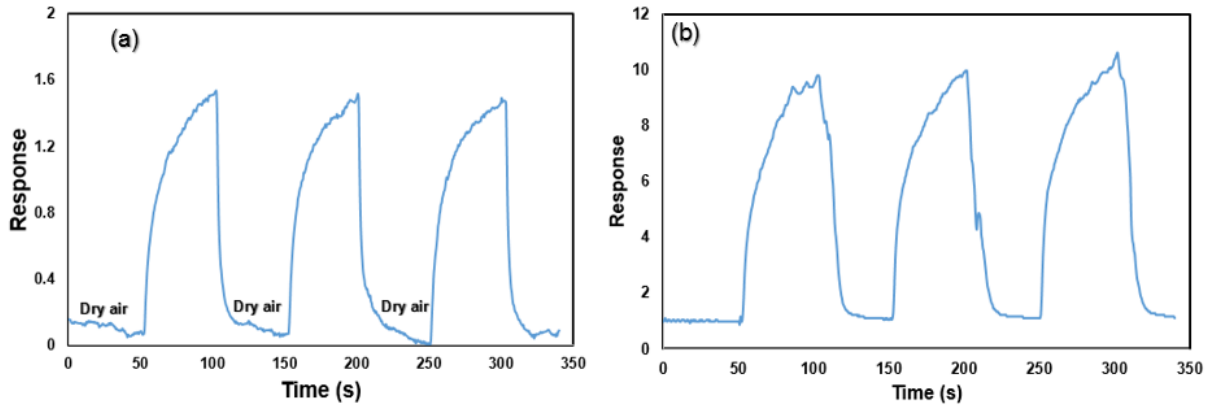

Figure 4.14 Response transient curve of (a) CdS/DNA (b) $CdZnS_2$/DNA micro-electrode fabricated nanowire sensor with ethanol vapour at room temperature at constant concentration of 1.3 mM.

The transient response curve was also used to determine the response and recovery time of the CdS/DNA, $CdZnS_2$/DNA and ZnS/DNA nanowire gas sensor. The response time which is the time required for the current response of the templated nanowire to attain at least 90% of the maximum saturation point of the sensor on exposure to the ethanol vapour. The recovery time is the time required for the current response of the templated nanowire sensor to decrease to at least 10% of the initial maximum response of the gas sensor. The response and recovery times of the templated nanowire gas sensors were calculated using the equations response time = time for the current to reach 90% of maximum and recovery time = time for current to recover within 10% of background. The response and recovery time were determined to be 35 s and 10 s for CdS/DNA, 30 s and 15 s for $CdZnS_2$/DNA and 120 s and 40 s for ZnS/DNA (appendix C). The DNA templated metal sulfide nanowire gas sensor showed a generally good response and recovery time especially for room temperature

gas sensing. The $CdZnS_2$/DNA sensor has shown an enhanced response and recovery time compared to those of CdS/DNA and ZnS/DNA. The reason for such enhanced response has been explained based on the difference in the potential barrier formed at the NW-NW junction and the depletion layer region (see scheme 5.2) of the different metal sulfides[217]. Detail of the response mechanism of the different nanowires were explained in section 5.2.4.

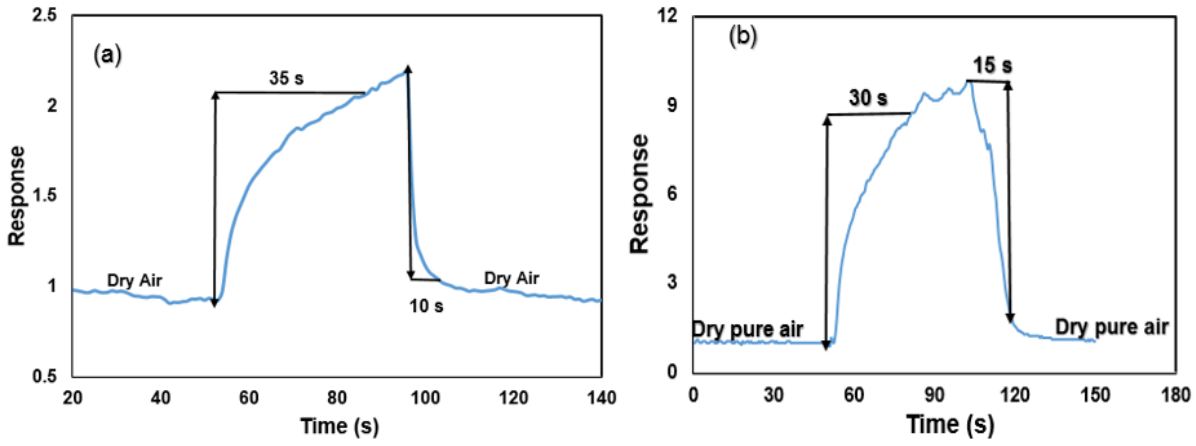

Figure 4.15 Response time and recovery time of (a) DNA templated CdS (b) $CdZnS_2$/DNA microelectrode fabricated nanowire sensor with ethanol Vapour at room temperature.

4.2.2.2 Sensitivity of the DNA templated nanowires

The sensitivity of the CdS/DNA, $CdZnS_2$/DNA and ZnS/DNA templated nanowires against various volatile organic compounds (VOCs) were studied in the laboratory using a two probe conductance measurement set-up. VOCs such as ethanol, acetone, hexane and chloroform were used at different mole ratios to determine the sensitivity and selectivity of the device. Figure 4.17 and 4.19 show the dynamic response and recovery curves of the microfabricated CdS/DNA and $CdZnS_2$/DNA sensors respectively towards different concentrations of ethanol.

The amount of analyte channelled to the sensor were obtained by mixing different volumes of the organic vapour with zero air. The zero air was used for generating the vapour and as carrier for the vapour. The mixing of zero air and the generated vapour from the dreschel bottle leads to reduction in the partial pressure of the resulting mixture of the saturated vapour of the VOCs. The equation below was used in calculating the partial pressure of the organic vapour in the mixture.

$$p = P^*.\frac{V_v}{V_v+V_{air}} \quad (4.22)$$

Where p = partial pressure of the organic vapour in the mixture, P^*= saturated vapour pressure of the organic vapour in question as obtained from AIST database at the laboratory temperature. V_v= volume of the organic vapour in the mixture while V_{air} = volume of the zero air in the mixture. The equation above can be used to calculate the exact partial pressure of the organic vapour getting to the sensor from the flow rate of the zero air and that from the dreschel bottle.

The result shows a good sensing response of these nanowires to the measured analyte. The response at fixed volume of zero air increased with increasing mixing ratio of the vapour (p/P*) from 0.5 to 0.83 due to more organic vapour adsorbing. These results suggest that CdS/DNA nanowire showed good sensing performance and good reversibility to the various concentration of the VOCs vapour. The fast response and good sensitivity of the sensors might be due to the 1D structures of the DNA templated nanowires which showed high length-to-diameter and surface-to-volume ratio[218,219]. 1D nanostructures has also been reported to show good response because it facilitate the migration of gas molecules around their interaction region[220]. The sensitivity of the synthesized DNA templated nanowires were expressed in terms of the current of the sensor in air (I_a) and in the presence of ethanol vapour (I_g) using the equation (4.23).

$$S = \frac{\Delta I}{I_a} = \frac{I_g - I_a}{I_a} \quad (4.23)$$

The correlation between the sensitivity of the CdS/DNA nanowire towards ethanol, chloroform, acetone and hexane at different concentration is presented in figure 4.21. The amount of analyte in the mixing ratio was converted to concentration using the ideal gas equation as shown in the appendix C. Different sensing response were exhibited for the various VOCs at the given concentrations. Even though the saturated vapour pressure of these gases are different at the measured temperatures given rise to different concentrations, ethanol has showed the highest response even at lower concentration compared to the other VOCs.

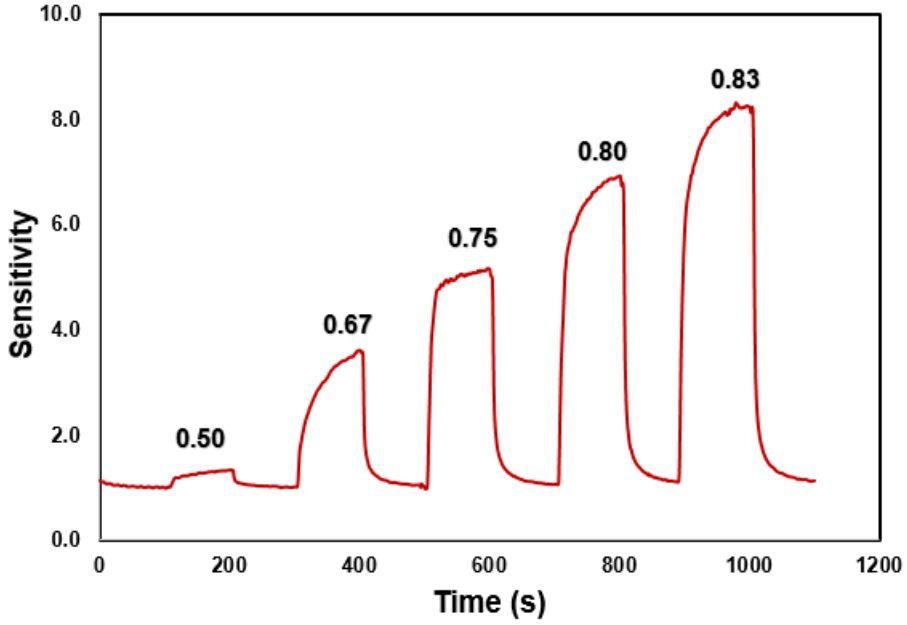

Figure 4.16 A dynamic curve of sensitivity against time plot of ethanol on the microfabricated CdS/DNA nanowire gas sensor at different partial pressures (p/P*). Note; P* is the saturated vapour pressure.

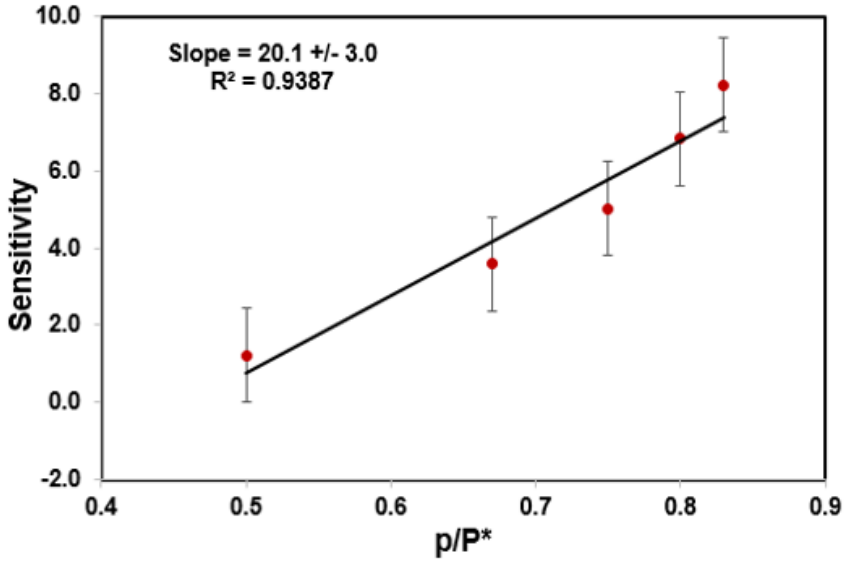

Figure 4.17 Shows the change in the sensitivity of ethanol on CdS/DNA nanowire gas sensor at different partial pressures.

The doping of the CdS/DNA with Zn has shown improved sensitivity of the nanowire sensor. This might be due to increase in carrier content and enhanced oxygen absorption process in the nanowire[217]. High response of CdS nanowire sensor was previously reported due to enhancement of oxygen absorption process ascribed to doping with Zn[217,221]. The dynamic curve of sensitivity against time plot of ethanol on

the microfabricated $CdZnS_2$/DNA nanowire gas sensor at different mole ratio was obtained and presented in figure 4.18.

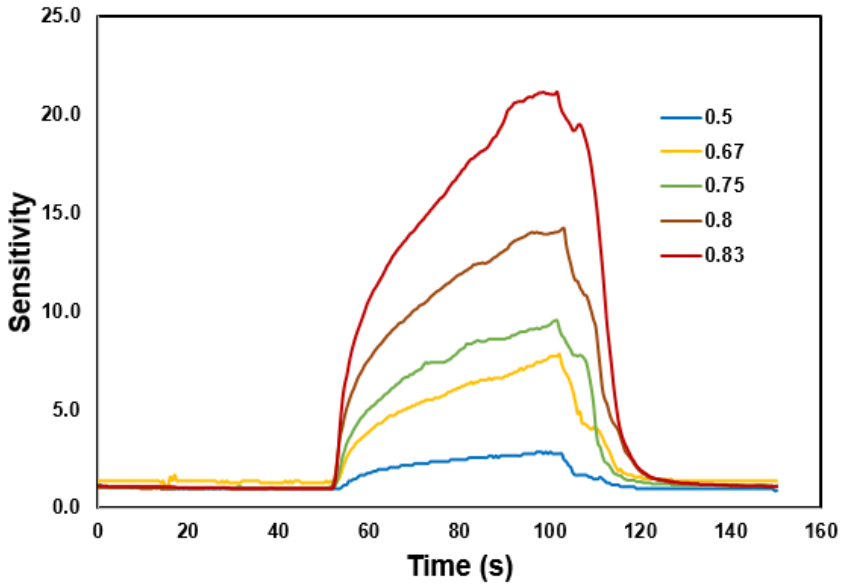

Figure 4.18 A dynamic curve of sensitivity against time plot of ethanol on the microfabricated $CdZnS_2$/DNA nanowire gas sensor at different partial pressures.

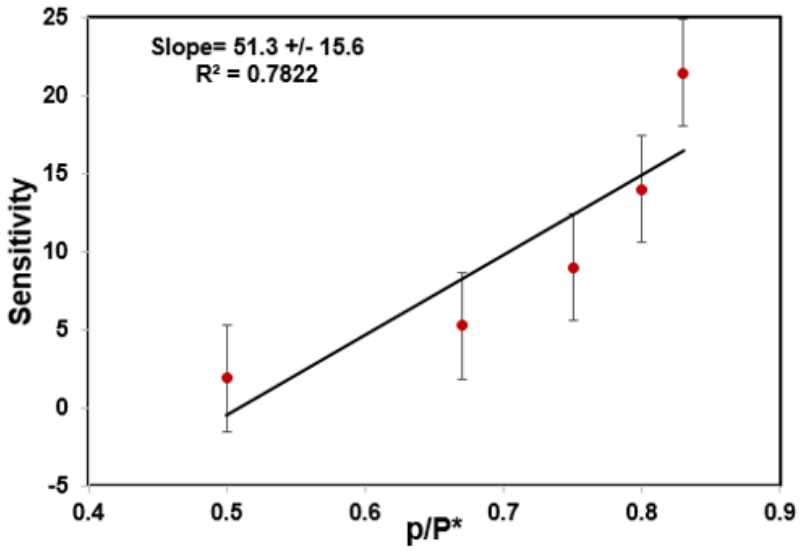

Figure 4.19 Shows the change in the sensitivity of ethanol on $CdZnS_2$/DNA nanowire gas sensor at different partial pressures.

A plot of sensitivity against mole ratio was done in order to determine the relationship between sensitivity of ethanol with changing mole ratio. Figures 5.17 and 4.19 showed the change in sensitivity of ethanol on CdS/DNA and $CdZnS_2$/DNA nanowire gas sensor at different mole ratio. The plot showed a gradual increase in sensitivity with

increasing mole ratio. This implies that as the concentration of the analyte increase, the sensitivity increases as well.

The sensitivity of the different VOCs (ethanol, chloroform, acetone and hexane) were plotted against concentration in order to show which analyte exhibited better performance. Figure 4.20 showed sensitivity against concentration of ethanol, chloroform acetone and hexane on the microfabricated CdS/DNA nanowire sensor. It can be seen from the figure that ethanol showed higher response than any of the analyte, followed by chloroform, acetone and hexane. Figure 4.20 showed sensitivity against concentration of ethanol, chloroform, acetone and hexane on the microfabricated $CdZnS_2$/DNA nanowire sensor. The $CdZnS_2$/DNA nanowire also showed higher response to ethanol as compared with the other VOCs. The doping also enhanced the response of acetone making it show a larger response than chloroform as seen in the case of CdS/DNA. The difference in the sensitivity for the room temperature sensing with DNA templated metal sulfide nanowires to the different VOCs studied might be due to their difference in dielectric constant and dipole moment[222]. Table 4.5 shows the dielectric constant and dipole moment of the various analytes tested.

Table 4.5 Dielectric constant and dipole moment of the various analyte tested[223].

Analyte	Dielectric constant	Dipole moment
Ethanol	24.3	1.68
Acetone	20.7	2.88
Chloroform	4.81	1.04
Hexane	2.02	-

The higher response of ethanol might be due to the presence of the OH group which makes it form hydrogen bond with the metal sulfide[224]. The higher dielectric constant of ethanol also makes it more reactive towards the ionized oxygen species on the nanowire surface and thereby inducing higher variation in conductivity of the nanowires due to change in carrier density[222]. The higher ability of an organic molecule to react with oxygen specie has also been reported to facilitate a higher response of nanowires to VOCs[225]. The sensitivity of ZnS/DNA nanowire was not discussed in detailed here because it showed very low sensitivity to ethanol and acetone but none to chloroform and hexane at the concentration used for the experiment.

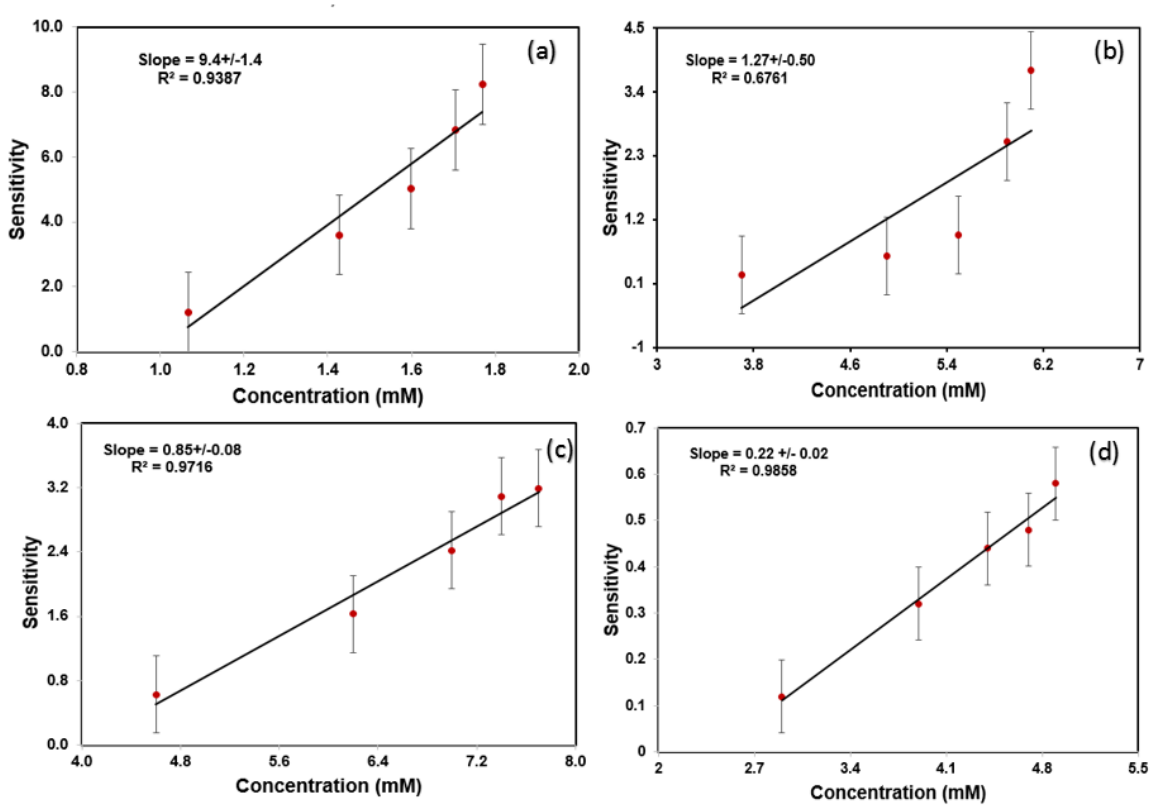

Figure 4.20 Sensitivity against concentration of (a) ethanol (b) chloroform (c) acetone (d) hexane on the microfabricated CdS/DNA nanowire sensor.

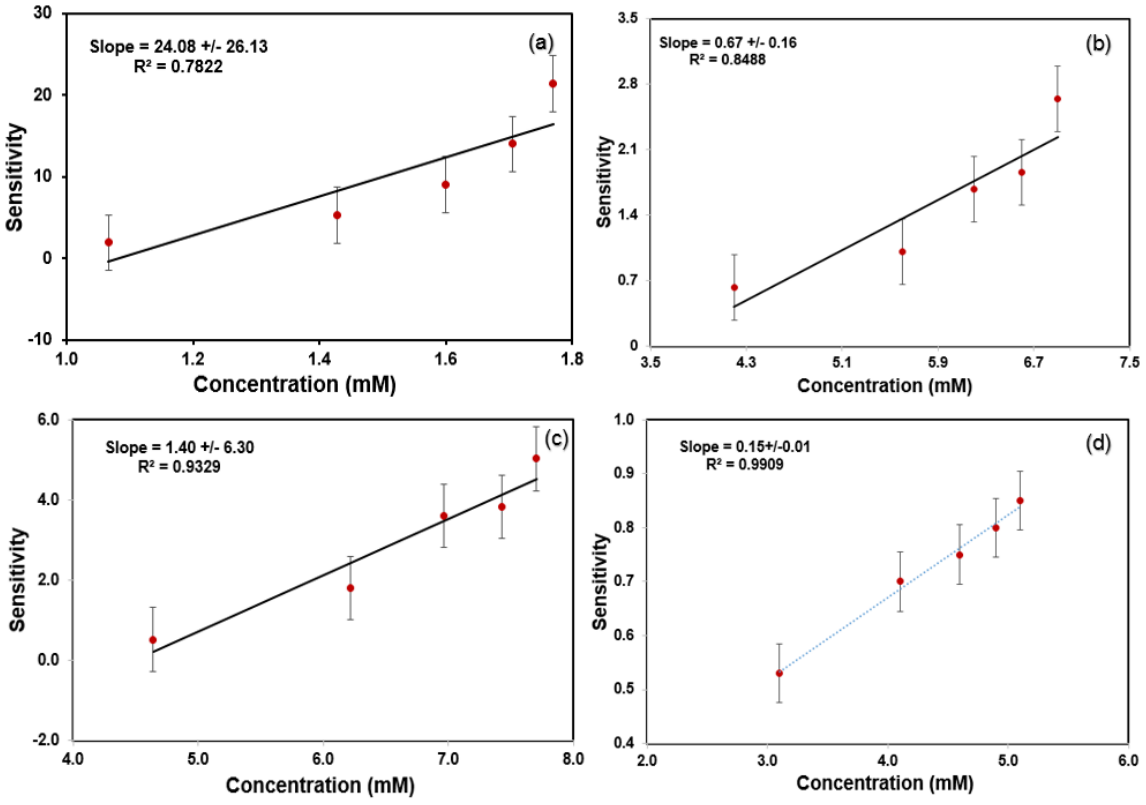

Figure 4.21 Sensitivity against concentration of (a) ethanol (b) chloroform (c) acetone (d) hexane on the microfabricated $CdZnS_2$/DNA nanowire sensor.

In order to determine the type of interaction between the DNA templated metal sulfide nanowires with the different VOCs, we plotted the slope of sensitivity of the nanowires vs concentration against the dielectric constant of the analytes. Figure 4.22 shows the graph of slope of sensitivity of the nanowires vs concentration against the dielectric constant of the analytes of CdS/DNA and $CdZnS_2$/DNA.

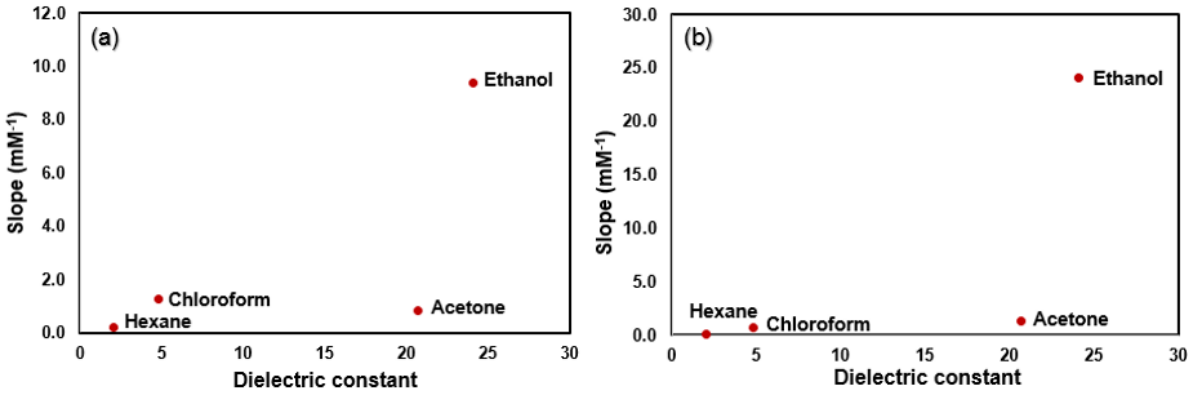

Figure 4.22 Shows the graph of slope of sensitivity of the nanowires vs concentration against the dielectric constant of the analytes of (a) CdS/DNA and (b) $CdZnS_2$/DNA.

The absence of an obvious trend with dielectric constant suggests that the interaction of the analyte with the nanowire is some kind of specific chemical interaction rather than a simple electrostatic one. The high response of CdS/DNA and $CdZnS_2$/DNA nanowire gas sensor to ethanol vapour also indicates a special kind of interaction of the hydroxyl group in the ethanol with the metal sulfides.

The effect of change in flow rate on the response of the CdS/DNA and $CdZnS_2$/DNA nanowire sensor was also studied by increasing the amount of zero air and analyte in the ratio of 1:1 but keeping the partial pressure constant. The plot of sensitivity of the nanowire sensors against total flow rate of ethanol vapour at constant partial pressure is presented in figure 4.23 and 4.24. Figure 4.23 and 4.24 show that the devices respond to flow rate as well as partial pressure of the analyte. In these experiments the analyte: air ratio is fixed and therefore the partial pressure of the analyte is fixed. However it is clear that increasing flow rate causes a small decrease in device response. This is likely to be a local cooling effect as the higher flow rate causes the nanowires to cool by increasing the rate at which adsorbed gas molecules are removed – an endothermic process.

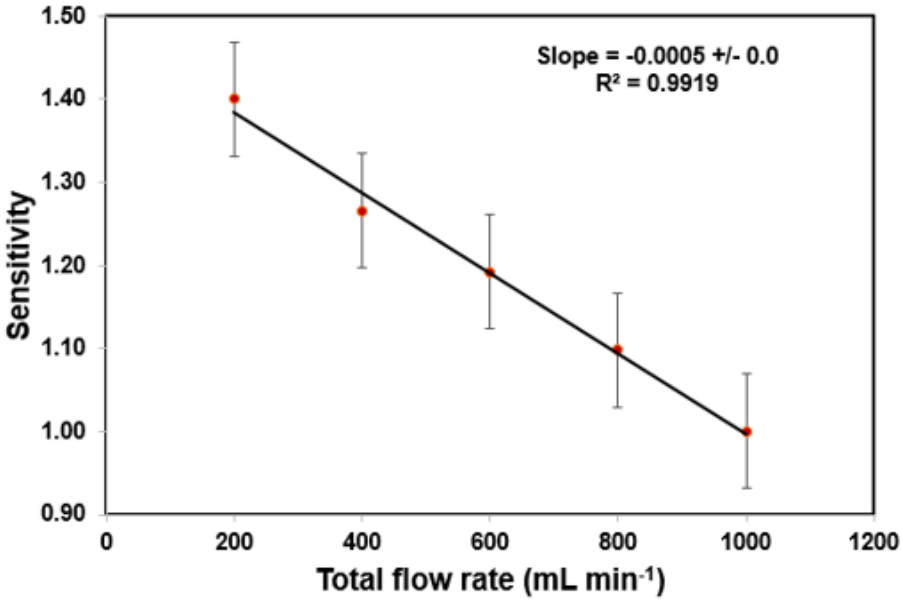

Figure 4.23 The plot of sensitivity of CdS/DNA nanowire sensor against total flow rate of ethanol vapour at constant partial pressure of 3.09 kPa at room temperature (21^{o}C).

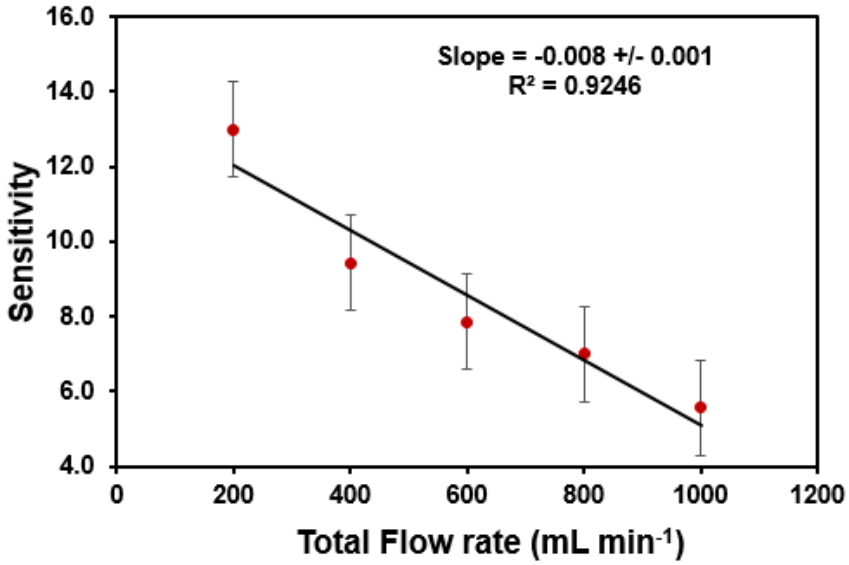

Figure 4.24 The plot of sensitivity of $CdZnS_2$/DNA nanowire sensor against total flow rate of ethanol vapour at constant partial pressure of 2.58 kPa at room temperature (18 ^{o}C).

4.2.2.3 Effect of temperature on the gas sensors

The effect of change in temperature on the sensitivity of the device is particularly important because it gives an idea how the device will respond to the varying temperatures. For a device to have practical application, it has to withstand different temperatures[226]. In addition it allows some deduction to be made about the nature of

the sensing mechanism. The temperature response of the synthesised metal sulfides nanowire sensors at different temperatures has been studied and presented here. The temperature dependence was studied at the temperatures 293, 298, 303, 308 to 313K. Figure 4.25 showed the sensitivity of the CdS/DNA sensor as a function of temperature. It can be seen that the response of the sensor decreased with increasing temperature from ~18.84 at 293 K to ~0.03 313K. The sensitivity of the $CdZnS_2$/DNA at different temperature was also obtained and presented in figure 4.26. The response was also observed to be decreasing with increasing temperature. The significant jump in the sensitivity between 293 and 298 K might be due to change in sensing mechanism.

We propose that the sensing mechanism is due to an adsorption process[114]. Given that the device operates at room temperature, it is unlikely that the mechanism is based on direct injection of electrons from the analyte to the conduction band of the semiconductor as in metal oxide sensors [6,11] . Oxygen molecules can adsorb at the semiconductor surface in air; these will act as traps for electrons in the conduction band that approach the semiconductor surface. Since most metal sulfides prepared by precipitation reactions are n-type materials, the presence of such electron traps reduces the conductivity. Analyte molecules which preferentially adsorb can displace oxygen and release additional charge carriers into the conduction band. However, a small change in temperature can lead to a large change in response. This response becomes less as the temperature increases because the amount of adsorbed ethanol on the surface of the nanowire decreases at the elevated temperature as long as the adsorption is an exothermic process. Simple adsorption of a gas at a solid will always be exothermic, but an exchange of one species for a second may be either exothermic or endothermic overall. Below we develop a simple model based on the assumption of an exothermic process.

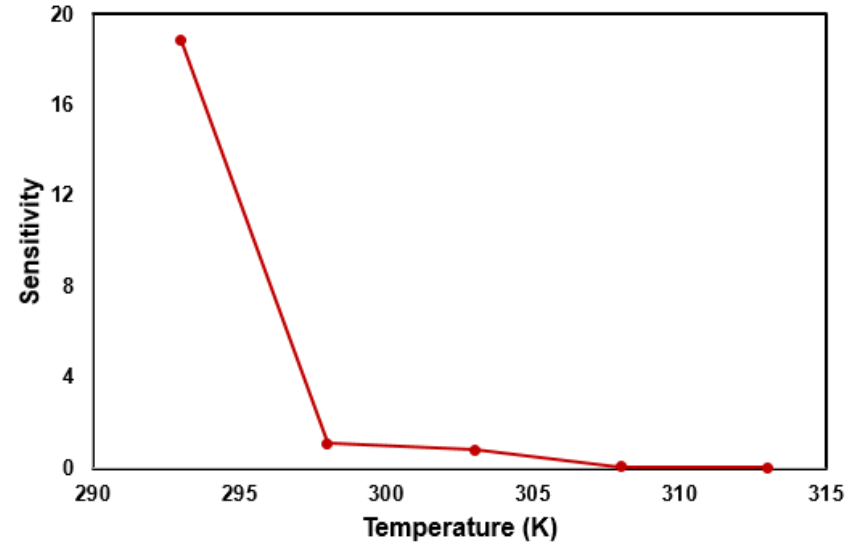

Figure 4.25 shows the sensitivity of the CdS/DNA sensor as a function of temperature at constant concentration of ethanol vapour.

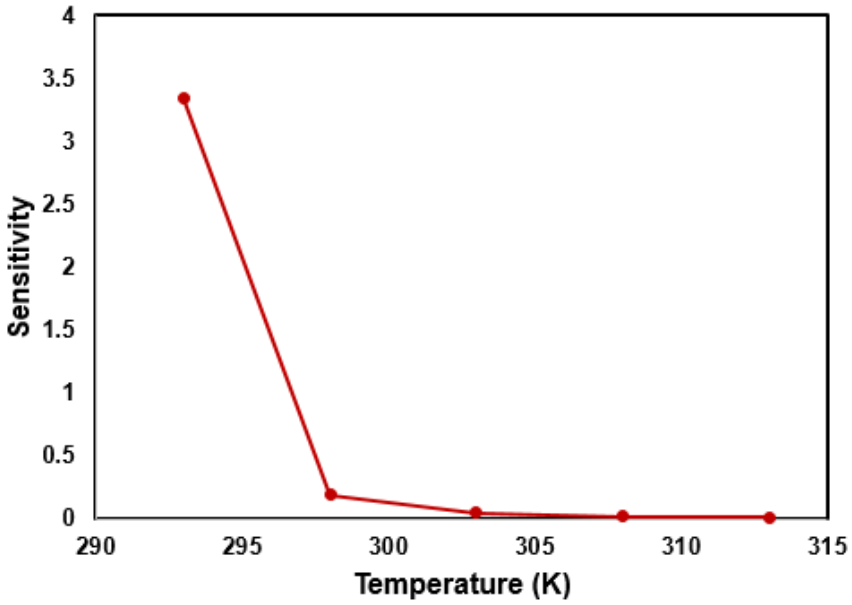

Figure 4.26 The sensitivity of the $CdZnS_2$/DNA nanowire sensor as a function of temperature at constant concentration of ethanol vapour.

The standard enthalpy change of the adsorption process of ethanol on the metal sulfide nanowire conductance based sensor has been explained using a simple model. This model used the Van't Hoff equation to explain the temperature dependence of adsorption of the VOCs on the conductance of the templated nanowires and the Langmuir isotherm to compare the amount of the adsorbed gas to the signal.

During the experiment, the change in the conductance of the templated nanowire sensors when in contact with the VOCs were measured. The measured current was

then normalised and reported as a fractional change in conductance, S, because different devices can have different background conductance, I_a, due to variations in synthesis of the material, the extent of templating of the material, the electrode configuration, the amount of material deposited on the electrode[228]. This process makes it possible to compare data acquired from different devices. The conductance change after exposure of the device to ethanol vapour, ΔI,was then calculated and the normalised signal of the vapour was determined using the equation

$$S = \frac{\Delta I}{I_a} = \frac{I_g - I_a}{I_a} \tag{4.24}$$

Where I_a is the current in the device when exposure to Zero air (background) and I_g is the change in current after exposure to the analyte for long enough that the current reaches steady state.

The signal of the interaction of ethanol vapour with the sensor was then processed. This was done based on two assumptions. First, that only gas molecules which adsorb on the sensor can affect the current and second, that the signal is proportional to the amount adsorbed per unit area, Γ. This can be represented mathematically as;

$$S = \alpha\Gamma \tag{4.25}$$

Where α is a constant of proportionality and Γ is the surface concentration or surface excess with SI unit of mol m^{-2}. The quantity Γ was then related to the parameters that were controlled during experiment such as the partial pressure p of the ethanol vapour. This was done by making assumptions about how gases adsorbs on surfaces. In this case, we used the simplest adsorption model, the Langmuir isotherm. This model is based on three main assumptions (i) that all the sites available for adsorption on the surface are identical (ii) adsorption of gas molecule at a particular site has no influence on the prospect of another gas molecule adsorbing at a neighbouring site (iii) molecules can only adsorb on the surface to form a single molecular layer (monolayer) and stops at maximum surface coverage Γ_m. The surface coverage Γ and the partial pressure p of the ethanol vapour is related via equilibrium constant K for the adsorption process by the Langmuir isotherm.

$$\frac{\Gamma}{\Gamma m} = \frac{Kp}{1+Kp} \tag{4.26}$$

Where *p* is the partial pressure (measured in bar). The amount of gas molecules adsorbed increased with increasing pressure and Γ increases until K*p*>>1 as $\Gamma \rightarrow \Gamma m$. At extreme high pressure, the signal would stop changing because all the available

sites have been fully occupied. The relevant regime for sensing is at low pressures (K*p*<<1) because $\Gamma \sim \mathrm{Kp}\Gamma\mathrm{m}$ and the gas adsorbs to a different extent with change in pressure. For the condition K*p*<<1, substituting equation (4.26) into equation (4.25) ,we got;

$$S = \alpha\Gamma = \alpha Kp\ \Gamma\mathrm{m} \tag{5.27}$$

The next thing was to consider the temperature dependence of the parameters in equation (4.27). The proportionality constant α was not dependent on temperature and $\Gamma\mathrm{m}$ which is the monolayer surface concentration was also not dependent on temperature because it was controlled by the maximum amount of molecules attached per unit surface area. The partial pressure p was independent of the temperature because the total pressure of the gas during the experiment was always the atmospheric pressure (open system) and was controlled by the temperature of the Dreschel bottle. The partial pressure of the analyte was derived by multiplying the total pressure by the mole fraction of the analyte according to Dalton's law. The vapour pressure in the Dreschel bottle controls the mole fraction which was normally done at room temperature. Therefore only the equilibrium constant K that was dependent on the temperature. The equilibrium constant of reactions are strongly dependent on temperature[229,230]. According to Le Chatelier's principle, equilibrium constants shift with temperature because equilibrium of reactions adjust if heat is added or withdrawn from reactions by increasing or decreasing temperature. The relationship between the equilibrium constant and temperature is represented mathematically by the Van't Hoff equation:

$$\frac{\delta InK}{\delta 1/T} = -\frac{\Delta H^{\theta}}{R} \tag{4.28}$$

Where ΔH^{θ} is the standard enthalpy change during adsorption of gas molecules on the substrate at standard conditions (1 bar). Since K was the only temperature dependent factor in equation (5.27), change in equilibrium constant is same as change in sensitivity S. Therefore, we can combine equation (5.27) and (5.28) as;

$$\frac{\delta InS}{\delta 1/T} = -\frac{\Delta H^{\theta}}{R} \tag{4.29}$$

Therefore $In\ S$ against $1/T$ (T in units of Kelvin) was plotted and present in figure 4. 27 and figure 4.28 for CdS/DNA and $CdZnS_2$/DNA respectively. The data points was fitted

with the line of regression and the slope of the line was determined and was equal to $-\frac{\Delta H^{\theta}}{R}$ where R= 8.314 J $K^{-1}mol^{-1}$ (universal gas constant).

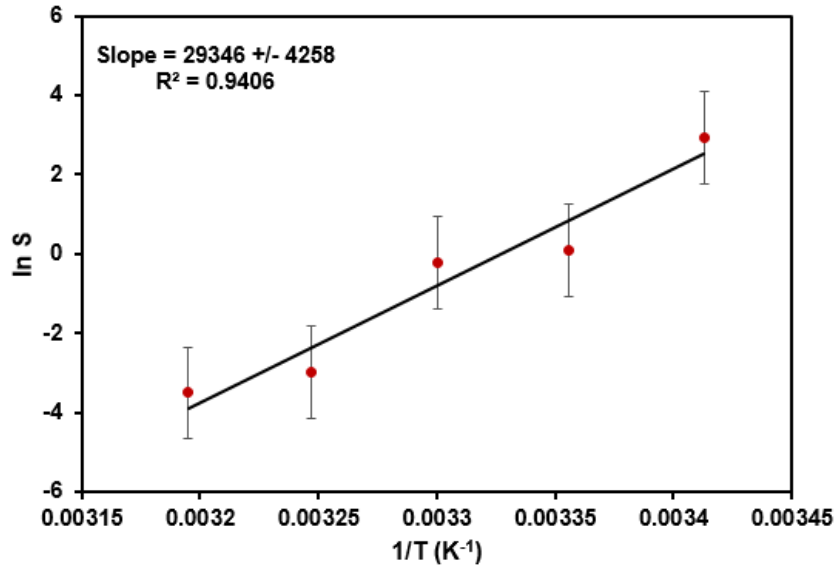

Figure 4.27 The plot of ln S vs 1/T for ethanol on the CdS/DNA nanowire sensor.

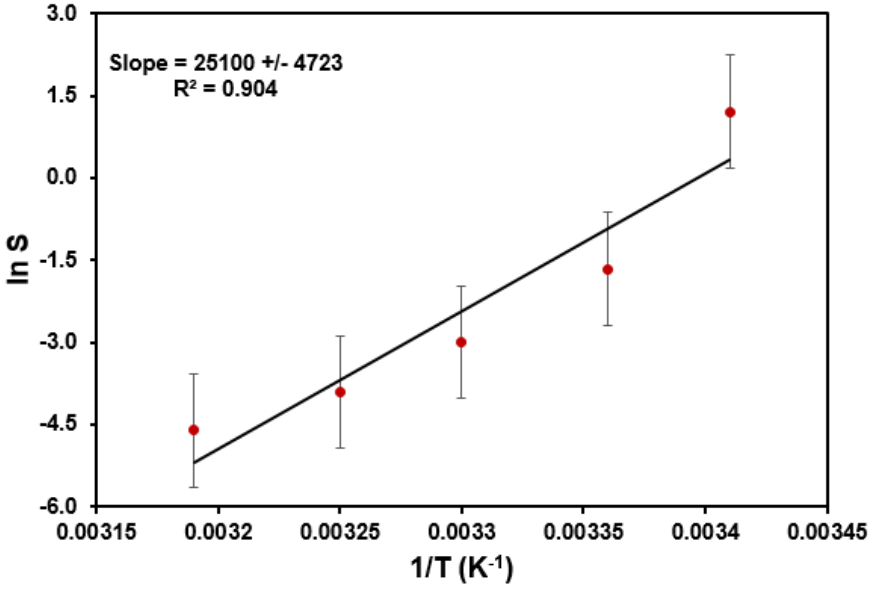

Figure 4.28 The plot of ln S vs 1/T for ethanol on the $CdZnS_2$/DNA nanowire sensor.

The enthalpy of the adsorption process was calculated by multiplying the slope with the universal gas constant. The calculated enthalpy of adsorption (ΔH^{θ}) for ethanol on the CdS/DNA and $CdZnS_2$/DNA nanowire sensors were -244 ± 35 kJ mol^{-1} and -208 ± 39 kJ mol^{-1} respectively. The processes were exothermic reactions because ΔH^{θ} was negative. It therefore indicates an adsorption process. The reason was that adsorption always results in decrease in entropy of the system as the gas molecules lose their freedom of movement upon adsorption. If instead, it were proposed that the current

change was due to a chemical reaction involving injection of charge into the semiconductor, the signal would be more likely described by a kinetic equation such as Arrhenius law which gives a rate proportional to $exp(-E/RT)$ and the signal would increase with increased temperature. Finally, the large magnitudes of ΔH^{θ} are also consistent with the proposed adsorption-displacement mechanism.

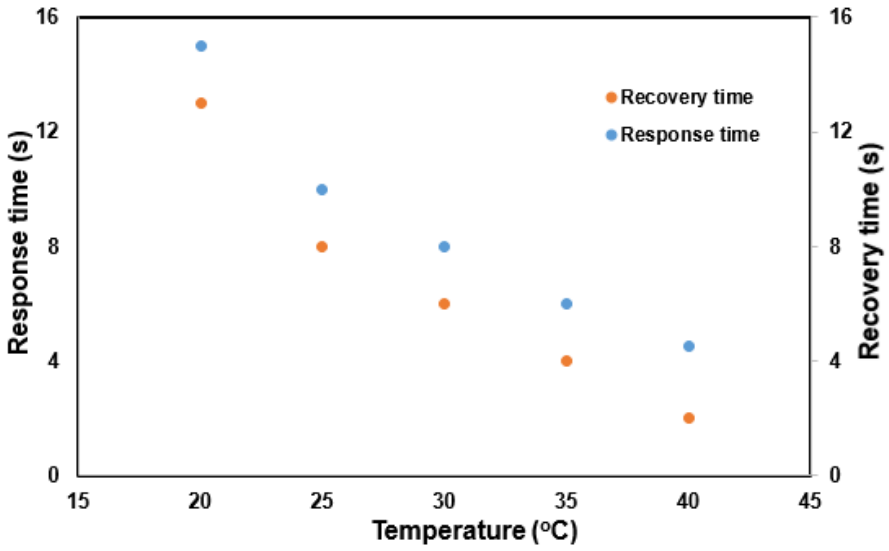

Figure 4.29 The response and recovery time of the CdS/DNA nanowire sensor as a function of temperature at constant concentration of ethanol vapour.

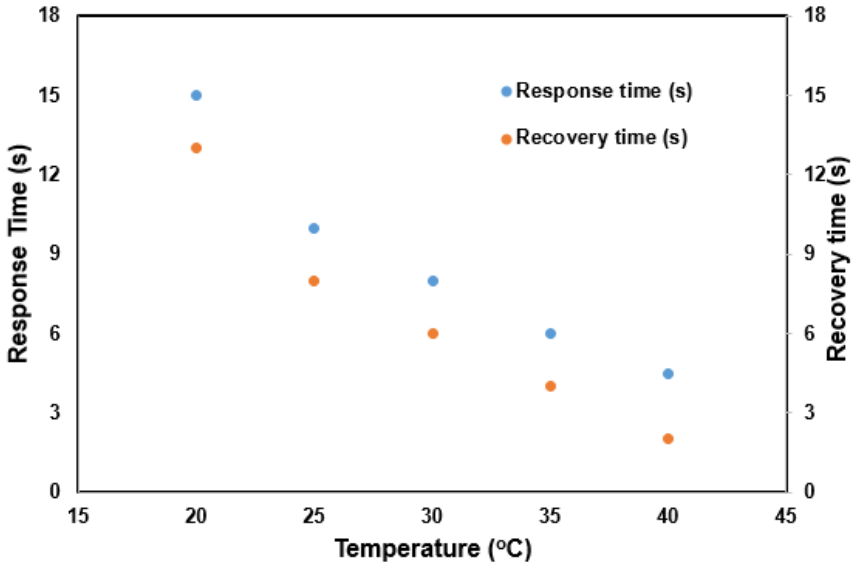

Figure 4.30 The response and recovery time of the $CdZnS_2$/DNA nanowire sensor as a function of temperature at constant concentration of ethanol vapour.

The response and recovery time of the CdS/DNA and $CdZnS_2$/DNA nanowire sensor was determined and plotted against temperature to show the effect of elevated temperature on these nanowire gas sensors as presented in figure 4.29 and 4.30. It was observed that both the response and recovery time of both nanowire sensor decrease with temperature. The faster response time might be due to faster replacement of oxygen by ethanol i.e a kinetic effect. The easier desorption of the attached ethanol molecules on the nanowires at elevated temperature is likely also a kinetic effect and it clearly follows a similar temperature dependence.

4.2.2.4 Sensing mechanism of DNA templated metal sulfide nanowire sensor

Different mechanisms have been used to describe gas sensing using one dimensional metal sulfide nanostructures. The mechanism most times are dependent on the prevailing conditions at which the reactions occur such as elevated temperature or pressure. However, the basic sensing principle of any conductometric based metal sulfide gas sensor is the change of the relative conductance of the device when exposed to different analyte[114,231]. In general, the modulation is attributed to charge transfer between the transducer (sensing element) and the analyte due to adsorption-desorption process[227,232,233]. In order to make a very good sensor, it is therefore advantageous to make a device that can give a higher relative change in conductance when in contact with analyte. Hence, the need to synthesise properly coated DNA templated 1D metal sulfide nanowires with large surface to volume ratio.

The mechanism of sensing in metal sulfides is slightly different from that of metal oxides due to different catalytic process involved as a result of absence of oxygen in the crystal lattice of metal sulfides[158]. The exposure of the metal sulfide nanowires under normal atmospheric condition can lead to adsorption of oxygen from ambient air on its surface. This lead to formation of different oxygen species such as O^- O^{2-} and O_2^- as a result of capturing electrons from the conduction band of the metal sulfides leading to generation of potential barrier at the NW-NW junctions and depletion region at the nanowire surface[217]. The formation of the oxygen species involves the conversion of the adsorbed oxygen to superoxide by abstracting electron from the conduction band of the metal sulfides. The capturing of another electron leads to the dissociation of the superoxide to form the other oxygen species as shown in the mechanism[234].

$$O_2(gas) \rightarrow O_2(ads) \quad (1)$$

$$O_2(ads) + e^- \rightarrow {O_2}^-(ads) \quad (2)$$

$${O_2}^-(ads) + e^- \rightarrow 2O^-(ads) \quad (3)$$

$$O^-(ads) + e^- \rightarrow O^{2-}(ads) \quad (4)$$

The trapping of electron causes reduction in the electron density on the nanowire surfaces and causes depletion layer[235]. The generated depletion regions on the nanowire result in formation of small size nanowires that are thinner than the usual original size due to a modified potential well ascribed to confined carriers[221]. The oxygen species generated due to adsorption of oxygen also block the electron flow across the nanowire intersection due to the increased induced potential well which reduce electron tunnelling[221]. It is worth noting that in the present experiments, the temperature is quite low (< 50^{o}C) and therefore steps 3 & 4 in the reaction scheme are less plausible because they would require the breaking of the strong O-O bond in molecular oxygen. It has been reported that at room temperature, majority of the pre-adsorbed oxygen species are O^{2-} from DFT results[222].

The scheme showing the depletion layer caused is shown in scheme 5.2 (a),where φ is the potential energy barrier at the crossing of the wires, EVB is the valence band maximum and ECB is the conduction band minimum. The size of the depletion layer differs for CdS/DNA, $CdZnS_2$/DNA and ZnS/DNA. This was also responsible for the difference in the sensitivity of the templated nanowires to the various VOCs. It has been reported that in n-type nanostructures, the width of the surface depletion is inversely proportional to the square root of electron concentration[221]. The low conductance of the nanowires in air is as a result of formation of space charge areas on the nanowire surface and potential energy barriers at the NW-NW intersections[111].

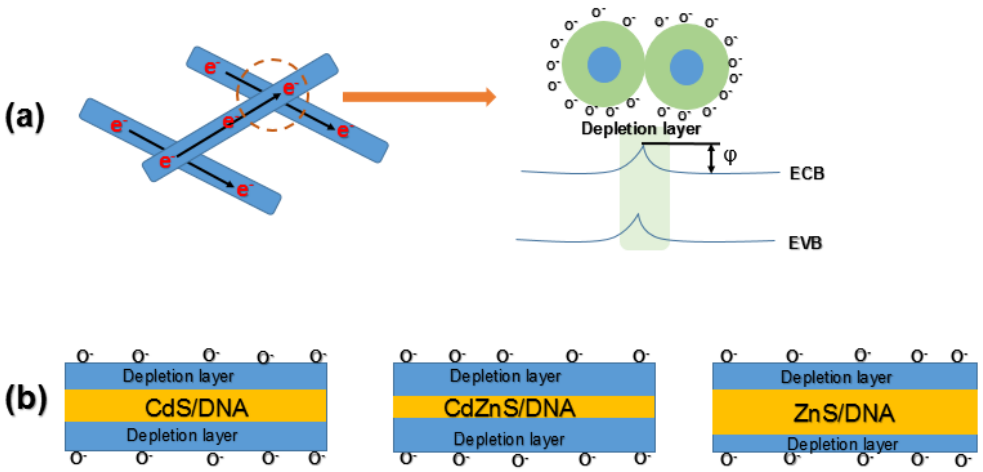

Scheme 4. 2 Mechanism causing conductance change in a metal sulfide based gas sensor (a) the effect of the absorbed oxygen species on the tunnelling of electron across the nanowire network. (b) The variation of the depletion layer in the CdS/DNA, $CdZnS_2$/DNA and ZnS/DNA nanowires.

The second step involves interaction of the adsorbed oxygen species with the analyte. When a reducing gas or organic vapours such as ethanol, chloroform, hexane and acetone come in contact with the CdS/DNA, $CdZnS_2$/DNA and ZnS/DNA nanowire network, it leads to increase in the carrier concentration by releasing the trap electrons into the conduction band and hence increasing the conductivities of the nanowire sensors. Among the formed oxygen ion species, the O- act as the best chemical oxidation centre for the catalytic oxidation of gases for easy detection[221]. The reaction for catalytic oxidation of ethanol molecules on the surface of the nanowires is shown.

$$CH_3CH_2OH + 6O^- \rightarrow 2CO_2 + 3H_2O + 6e^- \qquad (5)$$

The equation for acetone is represented as

$$CH_3COCH_3 + 8O^- \rightarrow 2CO_2 + 3H_2O + 8e^- \qquad (6)$$

However, the oxidation of these VOC can only occur at very high temperature because the formation of the various oxygen species are temperature dependent. The O^{2-} is dominant at temperature above 300^{o}C, O^- is prevalent at temperature range of 130-300 ^{o}C while the O^{2-} is the species present at temperatures below 130 ^{o}C[236]. The absorb specie O^{2-} present was less reactive and therefore unlikely to catalyse the oxidation reaction. Previous studies has ascribed the sensitivity of these nanowire at room temperature to the high surface to volume ratio, the small grain size and the morphology of the nanowire sensors[237,238].

The mechanism in this case can be explained based on the interaction or displacement of the surface adsorbed molecular oxygen by the analyte and thereby releasing the trapped electrons into the conduction band of the metal sulfides. The interaction between molecules and the nanowire surfaces is actually caused by chemical hybridisation of their molecular orbitals or physical van der Waal interactions[235].

For example, ethanol interact with the absorbed oxygen and transfer charge to the nanowires by physically adsorbing on the nanowire surface. This occur due to reduction of the potential barrier energy and the space charge region which increases the conductance of the nanowire network. This occurs because ethanol is a reducing gas and therefore can inject electrons by interaction with nanowire gas sensors. This process has been summarized in scheme 4.3. The introduction of the zero air from the gas bottle as illustrated in scheme 4.3 leads to reduced conductance due to the trapping of electrons. The introduction of the ethanol gas leads to interaction and displacement of the adsorbed oxygen species. This leads to injection of more carrier into the nanowire and therefore the increase in the conductivity as shown in the response transient of the nanowires as shown in figure 4.14. As the flow of the ethanol gas is stopped, the reverse reaction (shown in scheme 4.3) is triggered and the conductance drop drastic as a result of oxygen displacing the adsorbed ethanol gas.

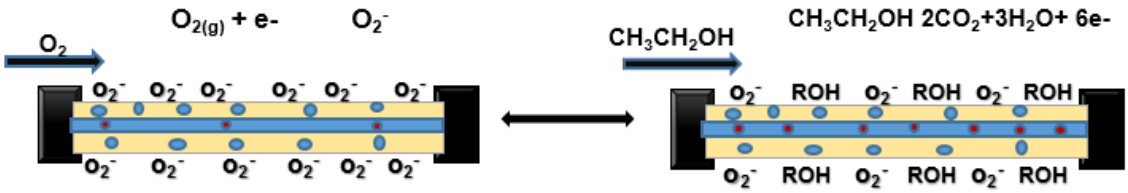

Scheme 4.3 Schematic illustration showing the adsorbed oxygen species on the nanowire surface (left side) and the displacement of the adsorbed oxygen by ethanol gas (right side).

The same mechanism of sensing is observed for hexane, acetone and chloroform because all are reducing gases/vapour. However, the sensitivity for the range of analyte is different due to difference in LUMO energies and polarity of the analyte[222,239].

4.2.2.5 Selectivity of DNA templated CdS Nanowires

The gas sensing selectivity is another important parameter used here to evaluate the sensing ability of the DNA templated metal sulfide nanowire sensor to show it

applicability in practical use. This property shows that when the sensor is exposed to multi-component analyte environment, it can precisely detect the target molecules[217]. The selectivity of the DNA templated metal sulfides nanowires against various volatile organic vapours were studied in the laboratory using a two probe conductance measurement set-up. Various VOCs such as ethanol, acetone, hexane and chloroform were used at a fixed mole ratio (0.83) to determine their selectivity. The bar chart showing the selectivity of CdS/DNA nanowires to different volatile organic vapours at room temperature is shown in figure 4.31. It can be seen from the Figure 4.31 that the nanowire sensor showed different responses to the various VOCs. Ethanol vapour has exhibited the best response towards the templated CdS/DNA nanowire sensor compared to all the other vapours at room temperature. This was as a result of the different gases/VOCs having different energies of reaction on the surface of nanostructures[111] such as the metal sulfides.

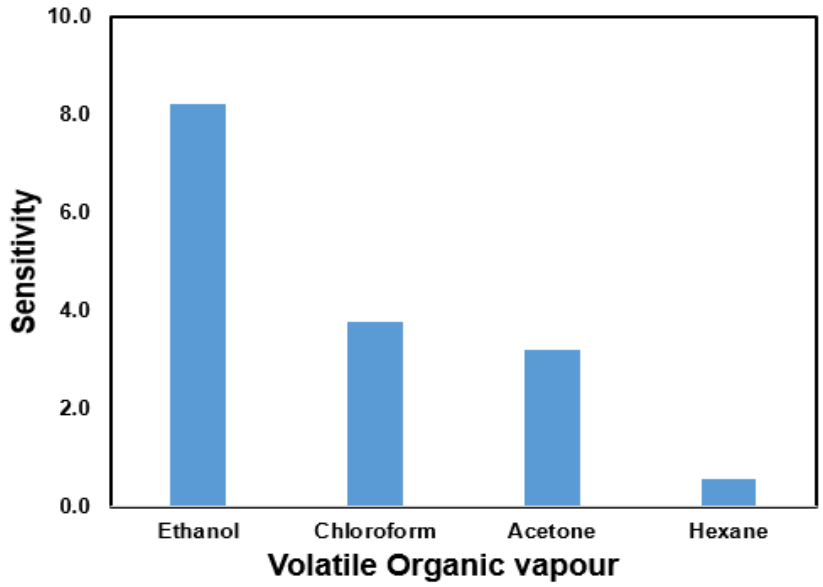

Figure 4.31 Selectivity of DNA templated CdS Nanowires to different volatile organic vapours at room temperature.

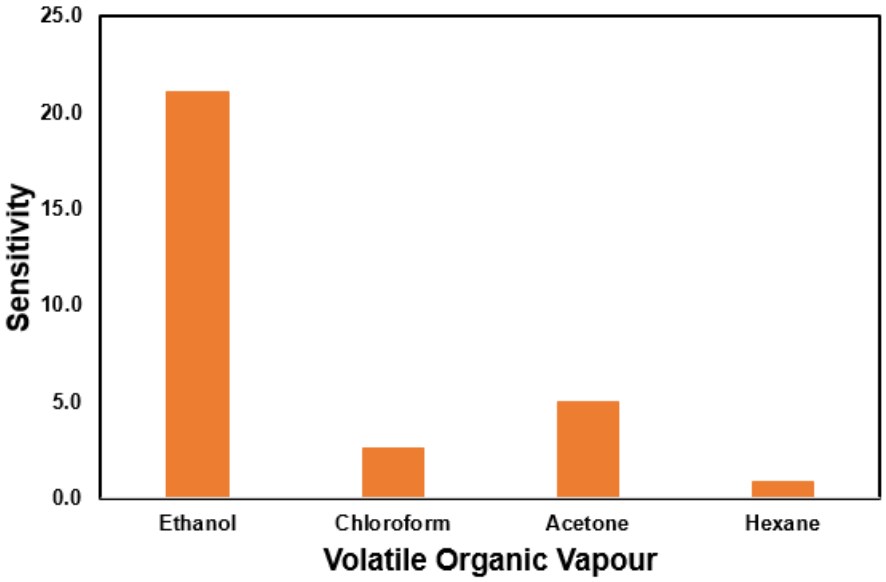

Figure 4.32 Selectivity of DNA templated $CdZnS_2$ Nanowires to different volatile organic vapours at room temperature.

The bar chart showing the selectivity of $CdZnS_2$/DNA nanowires to different volatile organic vapours at room temperature is shown in figure 4.32. The sensor showed highest response to ethanol. However, it showed better response to acetone than chloroform unlike the undoped CdS/DNA. This was caused by the doping with Zn ion which caused better depletion layer and also lowered the surface energy reaction towards acetone.

The selectivity coefficient (K) of ethanol vapour towards the nanowire sensor compared with other analyte is defined as[111],

$$K = \frac{S_{ethanol}}{S_X} \tag{4.30}$$

Where, $S_{ethanol}$ and S_X are the sensitivities of the sensor towards ethanol vapour and other vapours. The calculated selectivity coefficient values for CdS/DNA and $CdZnS_2$/DNA is presented in table 4.6. Higher value of K means the nanowire sensor has better tendency to differentiate the ethanol vapour among the mixture of other VOCs.

Table 4.6 K values of the nanowire sensor of CdS/DNA and $CdZnS_2$/DNA towards ethanol vapour.

Test vapour	Chloroform	Acetone	Hexane
CdS/DNA	2.2	2.6	14.2
$CdZnS_2$/DNA	8.0	4.2	24.8

It can be clearly observed that the sensor produced from the nanowires showed different selectivity to the different reducing gases/vapour which can be attributed to different basis of interaction between the VOCs and the nanowire network. This may be ascribed to the difference in the LUMO energies of these analyte. The difference in response of a gas sensor to different VOCs has been reported in literature and attributed to the distinctions in their orbital energies[239]. For instance, It has been report in literature that ethanol has lower LUMO energy of 0.12572 eV while acetone has 0.20525 eV and therefore it has higher tendency to transfer electron than acetone[239]. The lower the LUMO, the easier it is to transfer electrons and hence the higher sensitivity of ethanol than acetone. The selectivity coefficient of the ZnS/DNA nanowire for ethanol compared to other VOCs were quite negligible and therefore not discussed in detailed.

4.3 Conclusion

The electrical properties of the DNA templated metal sulfide nanowires were determined using two terminal probe station measurement, impedance measurement and transient current measurement. The I-V plot determined from the two terminal measurement showed a fairly ohmic conduction at low voltage and space charge limited conduction at higher voltage. The conductance extracted from the plot was in nanoSiemen range. The temperature dependence measurement showed an increasing conductivity with temperature. These nanowires temperature dependence measurement like any other semi-conductor is attributed to trap distribution caused by higher space charge in conduction band with increasing temperature[106]. It also showed Arrhenius like behaviour of the zero bias conductance with the extracted activation energy large enough to be typical of Schottky barriers at the metal/ nanowire interface.

The impedance measurement of the nanowire gave a curve from which the nanowire resistance and the contact resistance were extracted. The contact resistance of the nanowire device was higher than the nanowire resistance. The total resistance of the nanowire device determined from the impedance was also in nanometre range. The nanowire resistance and the contact resistance were also extracted from the transient current measurement at different voltages. The resistance per unit length of the nanowire where then calculated from plotting total resistance against nanowire length. The total resistance were also found to be in nanoSiemen range. Even though the total resistance from impedance and transient current measurement are within same nanometre range, the nanowire resistance is lower in the impedance measurement than in transient current measurement. The transient current measurement also showed that change in voltage plays a more dominant role in contact resistance than in nanowire resistance.

The synthesised CdS/DNA, $CdZnS_2$/DNA and ZnS/DNA nanowire was aligned on platinum on silicon electrodes to make gas sensors. The sensor were used for sensing VOCs such as ethanol, acetone, chloroform and hexane. The DNA templated metal sulfide nanowire gas sensor showed a generally fast response and recovery time especially for room temperature gas sensing. The $CdZnS_2$/DNA sensor has shown an enhanced response and recovery time compared to those of CdS/DNA and ZnS/DNA. The reason for such enhanced response has been explained based on the difference in the potential barrier formed at the NW-NW junction and the space charge region of the different metal sulfides[217].The effect of temperature on the gas sensor showed that the sensitivity decreased with increasing temperature. This was attributed to the increasing temperature favouring desorption process over adsorption. The enthalpy (ΔH) was calculated from the plot of In S against 1/T and it showed an exothermic reaction process. The enthalpy value for the $CdZnS_2$/DNA nanowire sensor was lower than that of CdS/DNA which supported the higher sensitivity of the $CdZnS_2$/DNA nanowire sensor. The sensors showed faster response and recovery time with increasing temperature. The mechanism of the sensing was explained based on simple adsorption and desorption of the adsorbed surface oxygen when in contact with the VOCs and thereby releasing the trapped electrons into the conduction band of the metal sulfides. The selectivity studies of the nanowire sensors showed different selectivity to the various reducing gases/vapour which can be attributed to different basis of interaction between the VOCs and the nanowire network. This was attributed

to difference in LUMO energies and polarity of the analyte[222,239]. The high response of the nanowire sensors to the VOCs especially ethanol vapour with reversible properties indicates that the templated nanowires has potential to make good gas sensor with practical application.

CHAPTER FIVE

Synthesis, Characterisation, Electrical and Sensing Behaviour of DNA-Coated Carbon Nanotubes

5.1 Introduction

Carbon nanotubes fabricated as chemical field effect transistors shows room temperature sensitivity as gas sensors due to gas molecule charge transfer leading to drastic change in the electrical conductivity of semiconducting carbon nanotubes. However, carbon nanotubes exhibit low solubility in all kind of solvents due to their axial geometry and van der Waal interactions which causes aggregation and bundling of the material[240]. Recent reports in literature has shown that dispersion of carbon nanotubes in different polymers [241] or solvents can result to significant increase in their sensitivity to gases and facilitate it incorporation into devices. It is therefore important to find a medium that support effective dispersion and controlled deposition of this material in devices.

DNA has shown excellent potential in the dispersion and separation of CNTs. This dispersion is attributed to the possible interaction of DNA and CNT via covalent bonding and weak van der Waal interactions[240]. DNA has a robust chemical structure with well-defined polymeric sequence that enables it to bind to different material to form complex structures. It has a net negatively charged structure that can coordinate with complementary charge materials to form strong bond[242]. It has semi-flexible properties and the length can be in micrometre even though the diameter is in nanoscale[243]. This make it possible for it to selectively bind and coil on the carbon nanotubes. These DNA/ carbon nanotubes have found application in high efficiency dye sensitised solar cell [244], as biosensor[245] and gas sensors[241]. Here, the multi-walled carbon nanotubes (MWCNT) - deoxyribonucleic acid (DNA) nanocomposite were synthesised in solution by mixing multi-walled carbon nanotubes with different volumes (2 uL, 5 uL and 10 uL) of lambda DNA in solution. The nanocomposite was characterised using different techniques to study its morphology and chemical composition. MWCNT/DNA nanocomposite was used to fabricate gas sensor using different MWCNT/DNA ratios for sensing different organic vapours such as methanol, ethanol, acetone and chloroform.

5.2 Results and discussion

5.2.1 Synthesis of DNA/MWCNT Nanocomposites

MWCNT which comes in form of a black powder was dispersed in methanol to form a solution by adding the powder to methanol and sonicating. The MWCNT/DNA nanocomposite was formed by adding the solution to different volume of DNA solution and sonicating. The solution turns colourless after sonicating, suggesting the solubility of the nanotube/DNA composite in the solvent. The schematic representation of the synthesis has been presented in figure 5.1. Molecular modelling has provided explanation for this solubility of MWCNT in DNA by suggesting that the DNA binds to the MWCNT via π-stacking which results in the wrapping of the DNA around the surface of the nanotubes[246]. The wrapping of the DNA around the MWCNT makes it soluble in polar solvent because the DNA backbone becomes available for solvation, this in turn reduces the surface tension associated with nanotubes in polar solvents. The sonication process is very important because it generate a strong hydrodynamic shear force that create space between the compact nanotube bundles, which allows the direct binding of DNA to the MWCNT surface via dispersion forces[246]. This results to stable emulsion of MWCNT/DNA nanocomposite.

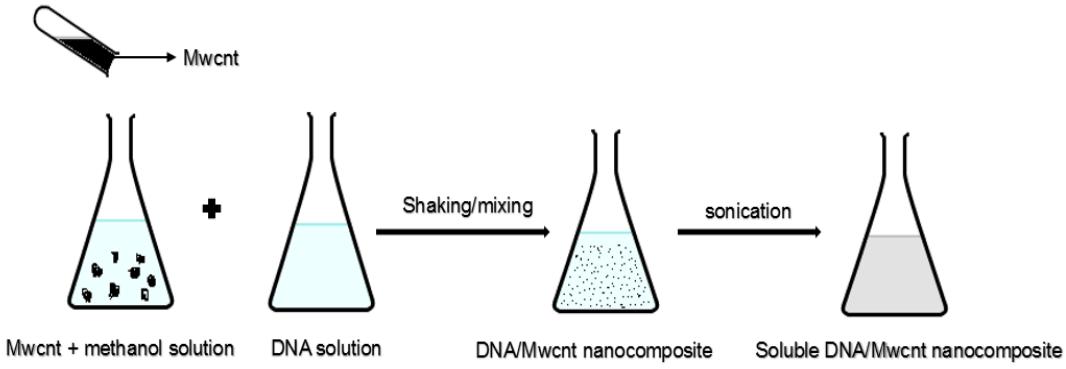

Figure 5.1 Schematic diagram showing the synthesis of DNA/MWCNT nanocomposite in solution.

5.2.2 UV-Vis spectroscopy

The UV-Vis spectra of the MWCNT/DNA nanocomposites were obtained to prove the binding of MWCNT with DNA and the result is presented in figure 5.2. The characteristic DNA absorption band 260 nm is clearly visible but upon coordination with the MWCNT, there is slight shift in the peak. The intensity of absorption of the DNA

peak has decrease in the MWCNT/DNA nanocomposite. The decrease in the absorption intensity is due to the binding and wrapping of DNA around MWCNT through π-π stacking during sonication[246,247]. The peak at about 260 nm in figure 3 is typical of the π-π * transitions in the DNA bases and provides evidence of the presence of DNA in the composite.

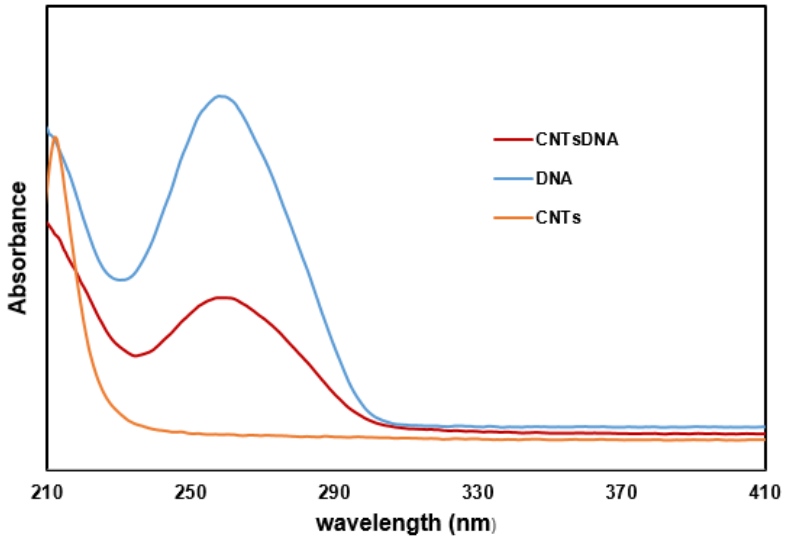

Figure 5.2 UV-Vis absorption spectra of MWCNT/DNA nanocomposites showing shift in peak due to interaction of DNA and carbon nanotubes.

5.2.3 Atomic force microscopy

The bare CNT and CNT/DNA nanocomposites were characterised using AFM to determine the effect of mixing DNA with carbon nanotube as well as mixing volume. The AFM images has shown that the DNA adheres and forms a coating on the CNTs. This was due to the increase in the diameter as well as the agglomeration of the nanocomposite as shown in the AFM images shown in figure 5.3 below. The histogram showing change in the diameter of the nanotube is shown in figure 5.4. Most of the carbon nanotubes have heights of less than 15 nm on average, but after coating the average height increased to a modal range of 15 – 30 nm. After the binding, the MWCNT diameter increased due to the sticking and wrapping of the DNA round the nanotubes. Increasing the amount of the DNA did not lead to any significant increase in the diameter but instead lead to increase in amount of DNA that bind to MWCNT. The detail understanding of how the DNA stick to the nanotubes can be seen in the TEM images in section 5.2.6.

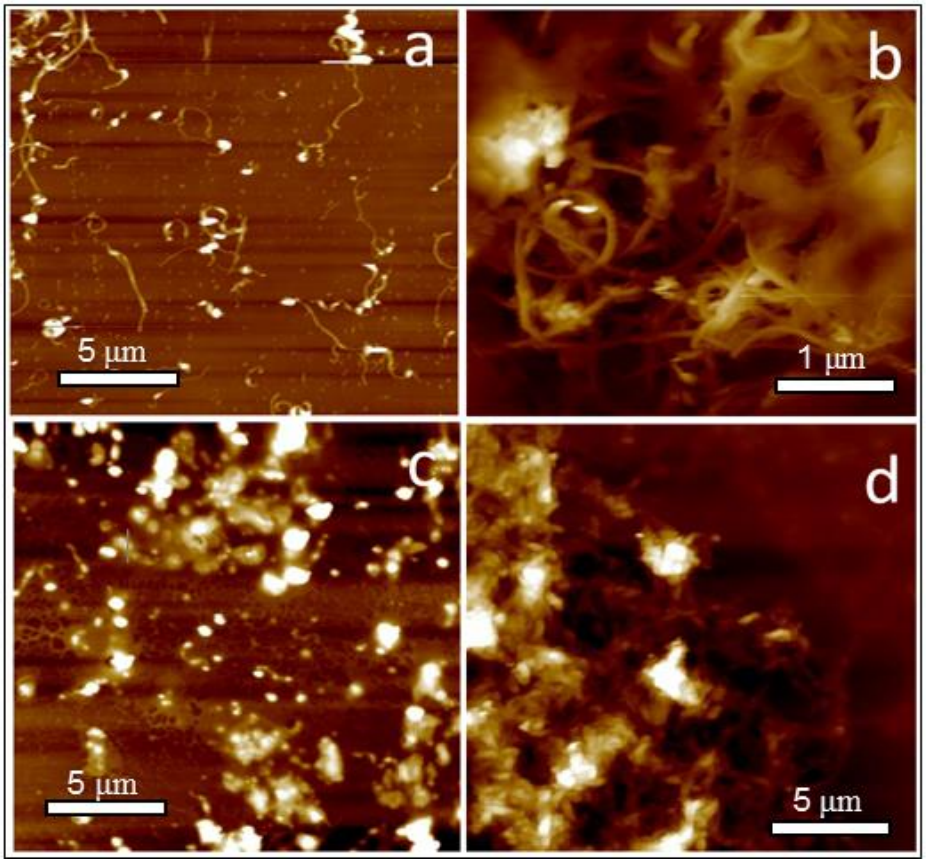

Figure 5.3 Showing AFM images of a) bare MWCNTs (grayscale = 50 nm) (b) MWCNTs/DNA (50:2) uL, (c) MWCNTs/DNA (50:5) uL and (d) MWCNTs/DNA (50:10) uL mixing ratios.(grayscale for b, c & d = 200 nm).

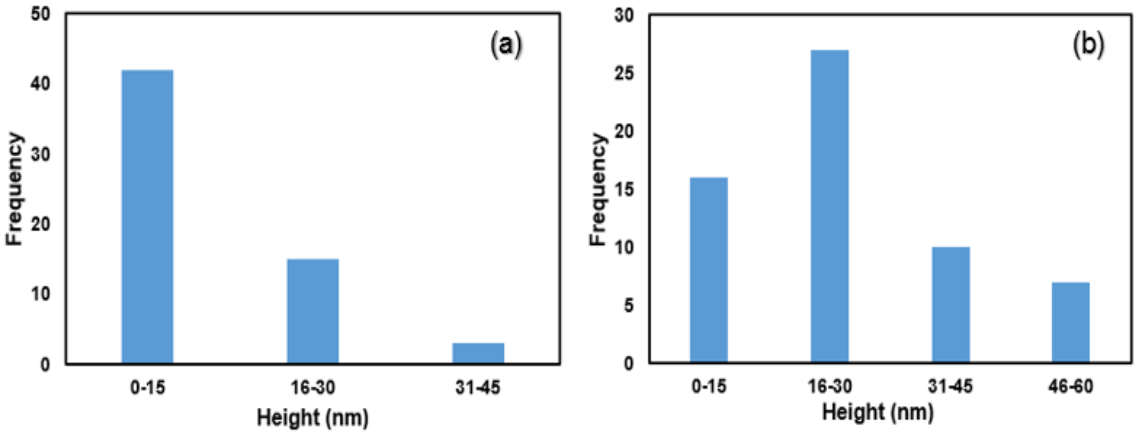

Figure 5.4 Histogram showing the change in height of the MWCNT templated with DNA (a) MWCNT and (b) MWCNT/DNA nanocomposites.

5.2.4 Raman spectroscopy

Raman spectroscopy can be used to monitor the change in composition and structure of MWCNT and MWCNT hybrids[248]. It has been used previously for extensive studies of semiconducting and metallic carbon nanotubes[249–252]. It was therefore used in this research for the studies of the adsorption of DNA to MWCNT. The Raman spectra of bare DNA, MWCNT and MWCNT/DNA nanocomposite were obtained to observe the effect of the interaction between the MWCNT with DNA. The Raman spectra of the samples are presented in figure 5.5.The Raman spectra of the MWCNT exhibited two characteristic peaks around 1380 cm^{-1} for the D-band and 1612 cm^{-1} for the G-band[253]. The D-band is usually attributed to the sp^3 defect sites that normally occur at the MWCNT side walls or amorphous carbon. The G-band is ascribed to the well-arranged ordered structure that is related to sp^2 carbon atoms in the side walls of graphene[248].

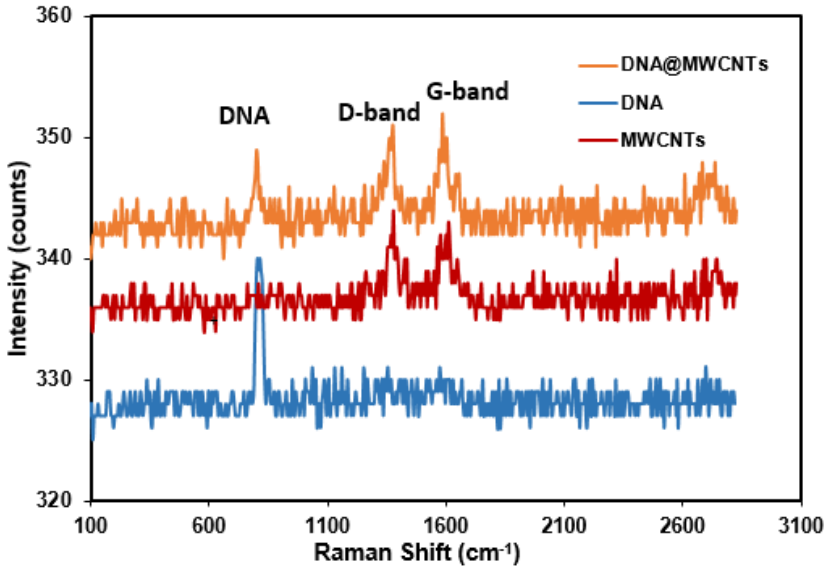

Figure 5.5 Raman spectra of (a) bare DNA (b) MWCNT and (c) MWCNT/DNA nanocomposite. The spectra have been offset on the vertical axis for clarity of presentation. The background detector signal (dark value) is about 325 counts.

When the DNA molecules adsorbed on the MWCNT surfaces, a specific vibrational peak appeared around 805 cm^{-1} which was absent for the MWCNT without DNA. This peak has been observed in the spectra of bare DNA at 815 cm^{-1} and is attributed to the sugar phosphate backbone of the DNA moiety[254]. The Raman peaks for both the D-band and G-band of the MWCNT/DNA nanocomposite has decreased to 1370 cm^{-1} and 1584 cm^{-1} respectively. Other research on MWCNT nanocomposites has also

reported a decrease in the Raman bands[255]. The appearance of this peaks and the shift in the MWCNT/DNA nanocomposite suggest the absorption of DNA on the MWCNT surface.

5.2.5 FTIR spectroscopy

FTIR measurement were obtained to provide more evidence on the binding of DNA to the MWCNT. FTIR measurements have been previously used for the characterisation of carbon nanotube composites bounded by other materials[256–258]. Figure 5.6 shows the FTIR Spectra of MWCNT, Bare DNA and MWCNT/DNA nanocomposite film. It is evident from the figure that reacting DNA with MWCNT has resulted to slight change in the IR spectra.

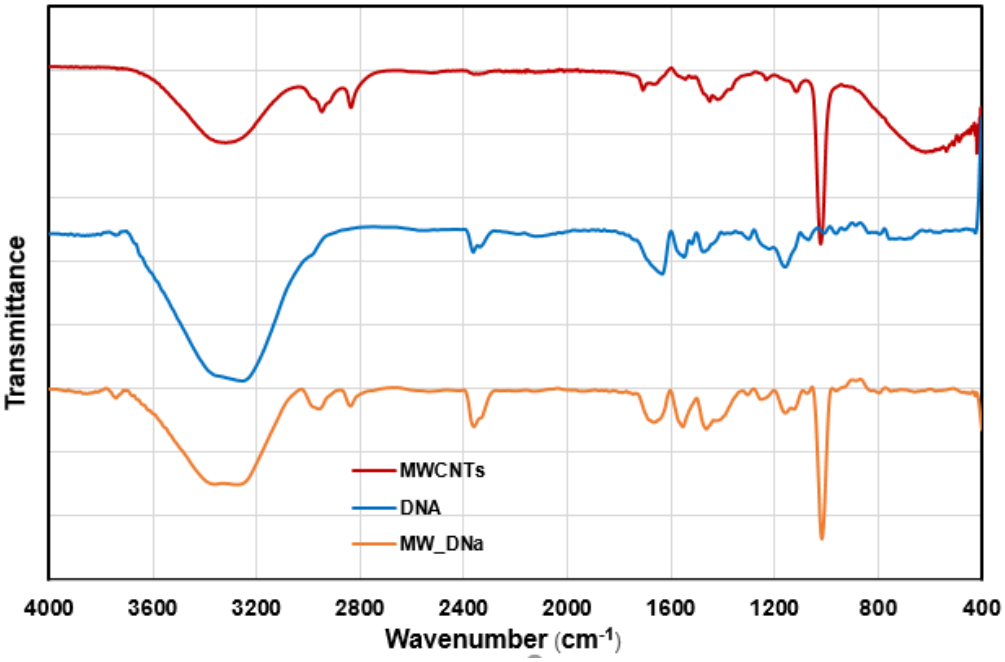

Figure 5.6 FTIR spectra of MWCNT, bare DNA and MWCNT/DNA nanocomposite film.

The modes at 1155 cm^{-1} and 1294 cm^{-1} are ascribed to PO_2^- symmetric stretching and PO_2^- asymmetric stretching respectively. The vibrational band at 1465 cm^{-1} and 1545 cm^{-1} are ascribed to the C=N and C=C stretches associated with the guanine and thymine rings. The vibrational peak obtained at 1645 cm^{-1} is attributed to the carbonyl band of the carbonyl group in thymine and guanine bases. The appearance of intense peak at 3305 cm^{-1} is due to the stretching vibration of OH groups in the DNA.

The MWCNT has been reported to exhibit several infrared active peaks within the frequency range of 800cm^{-1} to 4000 cm^{-1} in bundles of CNT with same diameter and chirality. The vibrational peak at 1010 cm^{-1} and 1705 cm^{-1} have been reported in all CNT irrespective of their diameter and chirality[259]. The peaks reported in this work is at 1010 cm^{-1}, 1113 cm^{-1}, 1447 cm^{-1} and 1705 cm^{-1} are due to mixture of the arm chair and zigzag nanotubes[260]. The intense peak at 3305 cm^{-1} is due to the stretching vibration of OH groups in the solvent (methanol).

The spectra of the MWCNT/DNA has shown deviation from that of bare DNA and MWCNT as shown in the figure 5.6. The shift in the vibrational band in the range of 1100 – 1450 cm^{-1} is attributed to the phosphate vibrational frequencies. The shift in this region is quite significant because of the geometry of the molecule. This has been attributed to the attachment of the negative phosphate ion to the slightly positive ends of the CNTs [261–263]. The shift in the vibrational band in the range of 1450 – 1800 cm^{-1} is ascribed to the in plane DNA vibrational frequencies. It has been reported that DNA is capable of interacting with the side wall of the CNTs through van dar Waal interactions via its pi electrons which has been reflected in the peak shift in the frequencies[264].

5.2.6 TEM studies

TEM has been used here to determine the point of binding and wrapping of DNA round MWCNT as reported in literature. Figure 5.7 shows the TEM images of the MWCNT bound on DNA to form MWCNT/DNA nanocomposite. It can be seen that the DNA selectively binds to the MWCNT as evidence in the figure 5.7 (a). The diameter of the nanotube at the point of binding was determined from TEM to be 12.41 ± 0.95 nm.

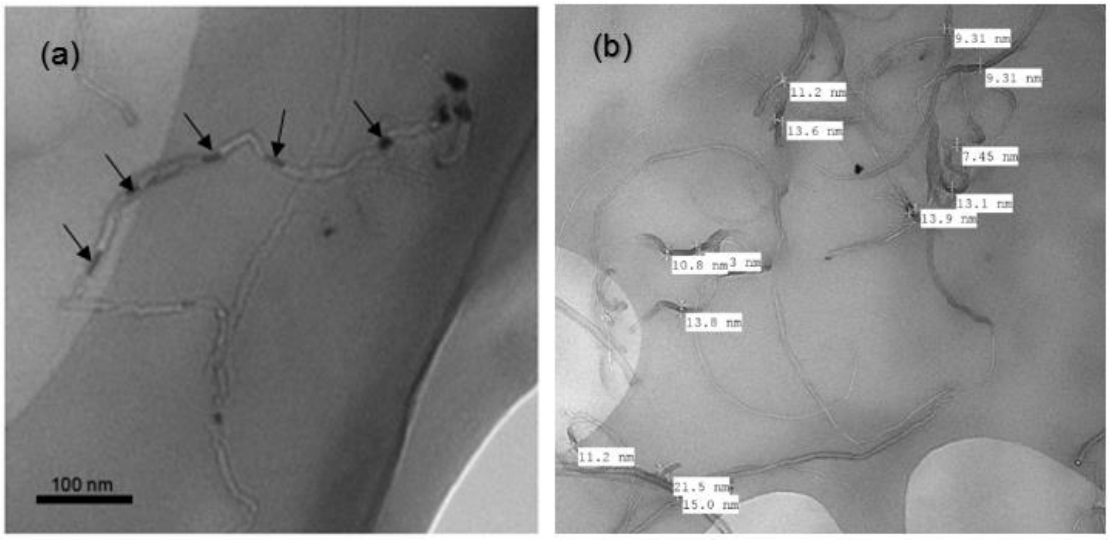

Figure 5.7 TEM image of MWCNT/DNA nanocomposite showing the attached DNA strands (a) DNA selective bind to the MWCNT (b) the diameter of the nanotube around the binding points.

The tendency of DNA to bind with the MWCNT through the π-orbitals of the nucleobases and the graphene-like surface of the CNT in order to reduce the repulsive interaction by overlap is responsible for stacking of the DNA and MWCNT. The stacking of DNA and MWCNT is different from that seen for regular AB base stacking seen in graphene. This can be ascribed to the heterogenous electronic structure exhibited by the five and six membered rings of the DNA nucleobases due to the presence of both carbon and nitrogen in the architecture of the bases. The existence of different side chains such as O, CH_3 and NH_2 on the nucleobases can also be responsible for the deviation seen on the perfect AB stacking of the MWCNT[265,266].

Theoretical studies of the binding energy of the nucleic acid bases and the MWCNTobtained by variation of the asymptotic limit between the MWCNT surface and the bases both in the base molecule plane and the nanotube perpendicular axis is taken as the energy of the equilibrium state. This has shown that the guanine base bind more strongly and efficiently to the nanotube surface than any of the other bases. The calculated polarity of the base pair which is caused by the presence of the aromatic rings, lone pair of electrons on the oxygen and nitrogen atom that results in the uneven distribution of electronic charge is responsible for selective binding of the bases as well[267].This might be responsible for the selective binding of the DNA to certain area of the MWCNT as evidence in the TEM image.

5.2.7 Electrical characterisation

The electrical properties of the bare MWCNT and the various DNA/MWCNT nanocomposites were determined using the two point probe station. This method was used to acquire quantitative information about the electrical properties of the MWCNT/DNA nanocomposites by fabrication of a two terminal device. The device was fabricated by drop casting 2 uL of the samples containing the nanocomposite nanotubes on the microfabricated Pt microelectrodes (with 20 µm gap). The sample was aligned by molecular combing[60,85] and allowed to dry leaving behind a dense network of the samples. The electrical measurement of the bare MWCNT and DNA/MWCNT nanocomposite at different ratio is presented in figure 5.8.

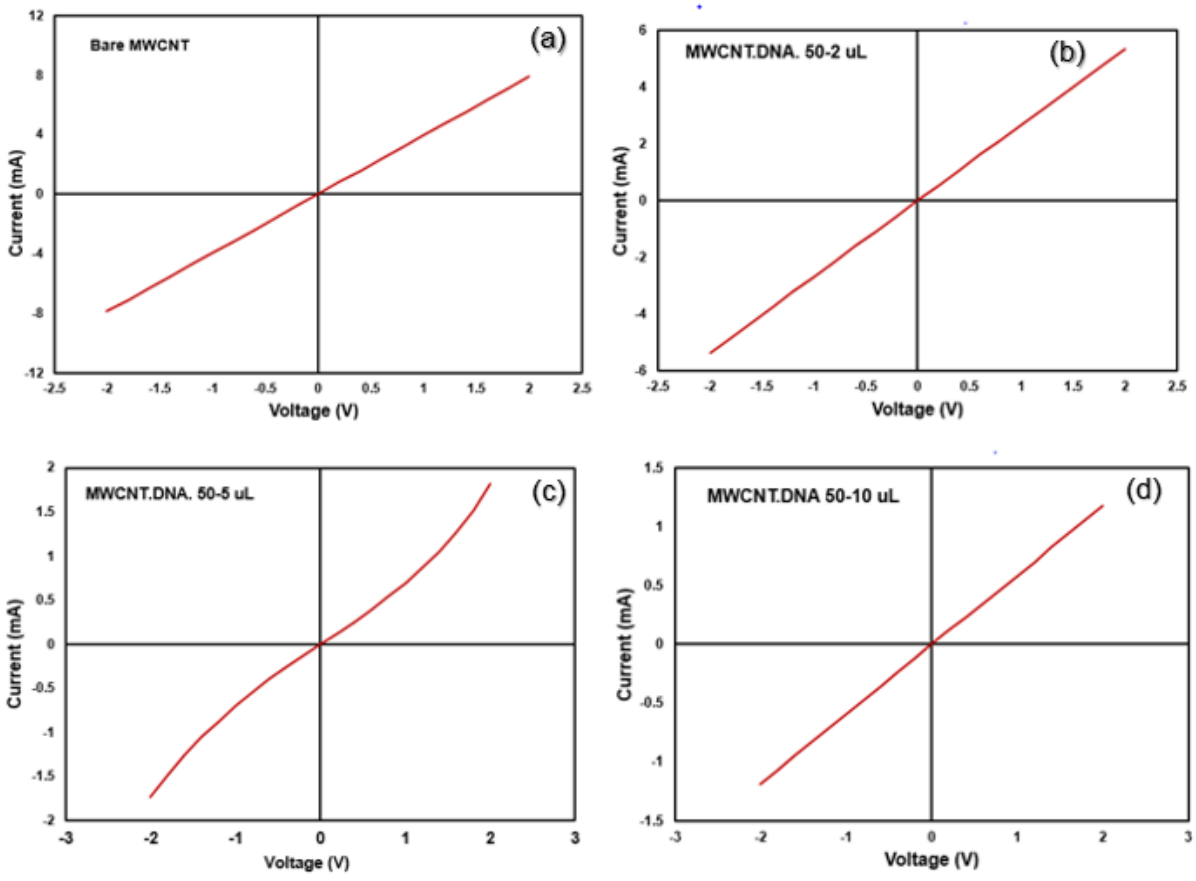

Figure 5.8 The current – voltage plot of (a) bare DNA and MWCNT. DNA nanocomposite (b) 50-2 uL (c) 50-5 uL (d) 50-10 uL.

The plots showed a generally ohmic behaviour with a little hysteresis in some cases. The current decreases, as the amount of DNA solution increases and it is clear that DNA: CNT nanocomposites was always less conductive than pure CNTs and that the differential conductance at zero bias decreases monotonically with DNA: CNT ratio.

The conductivity values of the DNA/MWCNT mixtures was determined from the gradient of the I-V plots. The conductance of the bare MWCNT and the different mixtures N1, N2 and N3 were 3.94 x 10^{-3} S, 2.64 x 10^{-3} S, 0.79 x 10^{-3} S and 0.59 x 10^{-3} S respectively. Increasing the amount of DNA reduces the conductance of the composite; we suggest this is because the insulating DNA molecules slightly separate the CNTs at junctions between CNTs, leading to lower hopping rate between CNTs and an increased resistance.

The different temperature I-V studies were also performed for the two terminal devices to determine the detailed conduction mechanism of the nanocomposites. Temperature-dependent I-V studies showed that the films of CNTs conductance decreases with temperature (in a metal-like manner) as reported in literature. However the different DNA/MWCNT nanocomposites mixtures showed a more semiconducting-like behaviour with increasing temperature. The plot of the bare MWCNT and the different mixture ratio of DNA/MWCNT at different temperature is presented in figure 5.9.

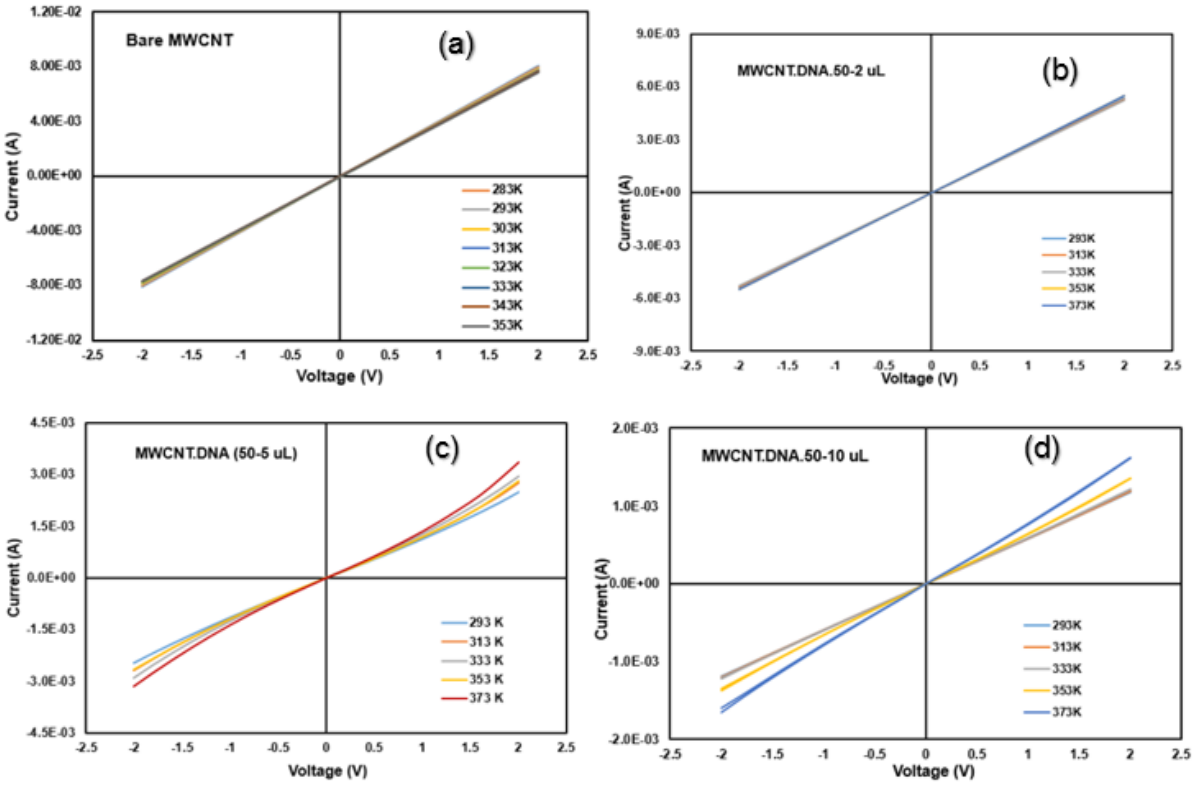

Figure 5.9 The temperature dependence current – voltage plot of (a) bare DNA and MWCNT/ DNA nanocomposite (b) 50-2 uL (c) 50-5 uL (d) 50-10 uL.

The mixture at different ratio showed complex behaviour sometimes with conductance increasing with temperature in some circumstances. This can be interpreted in terms of tunnel-junctions between CNTs in the aligned film. In the absence of DNA, CNTs come into direct contact whenever they cross. However, when the CNTs are coated with DNA molecules, they do not directly contact each other, but are separated by a thin film of insulating material (DNA).The schematic illustration of the transport model of electron through the DNA/MWCNT nanocomposite device is presented in figure 5.10.

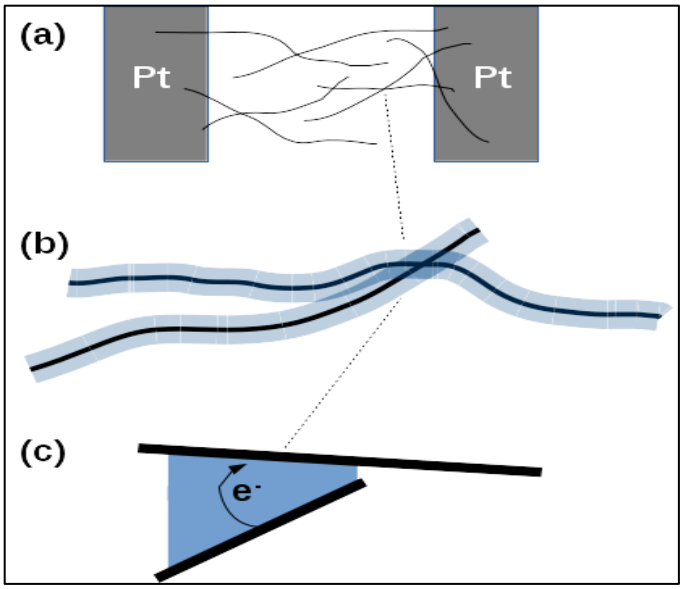

Figure 5.10 Schematic illustration of the model for transport of electrons in the DNA: CNT devices. (a) The cast film of DNA-CNTs between two metallic Pt interdigitated electrodes – electrons hop between several CNTs to cross the inter-electrode gap; (b), (c) illustrations of a single tunnelling barrier between two DNA-coated CNTs. The CNTs are drawn as solid black lines and the blue shaded area represents the insulating DNA coating that acts as a tunnelling barrier (thickness exaggerated for clarity in this diagram).

The transport of electron through this DNA/MWCNT nanocomposite would be described using the hopping model because the charge carriers are assumed to be largely localised and undergo thermally-assisted hops or tunnelling transitions between different nanotubes. The typical path followed by an electron in crossing between the Pt contact electrodes involves transport along individual CNTs, but these are generally not sufficient to cross the entire gap. The electron therefore also makes transitions between CNTs, which we expect to be an activated process, especially if the CNTs are coated with insulating DNA molecules. In general, different transitions is expected from different CNTs networks which differ in coating amount which causes difference

in hopping distance or energy barrier. This kind of scenario is referred to as variable range hopping because the different hops gives rise to a hopping range over the thermal average that is dependent on temperature.

We represent the conductance-temperature relation at the tunnel-junction between DNA-coated CNTs with a simple variable-range hopping form.

$$G_{gap} = G_0 \exp(\frac{T_0}{T})^{\beta} \quad (5.1)$$

Where β depends on the dimensionality of the system ($0 < \beta < 1$) and $T_0 = E_a/k_B$ where E_a is the activation energy and k_B is the Boltzmann constant.

We can represent the resistance of the MWCNTs themselves as a linear function of temperature.

$$G_{CNT}(l) = a + bT \quad (5.2)$$

Where *a* and *b* are proportional to the length of the CNT, *l*.

The overall conductance of the DNA: CNT composite is then modelled by equation (5.3):

$$G = G_{CNT}^{-1}(l) + G_{gap}^{-1} \quad (5.3)$$

Where $\underline{l}$ is a suitable average over the lengths of CNTs in the device. Figure 5.11 shows the least-squares fit of a regression model based on equation (5.3) to typical experimental data.

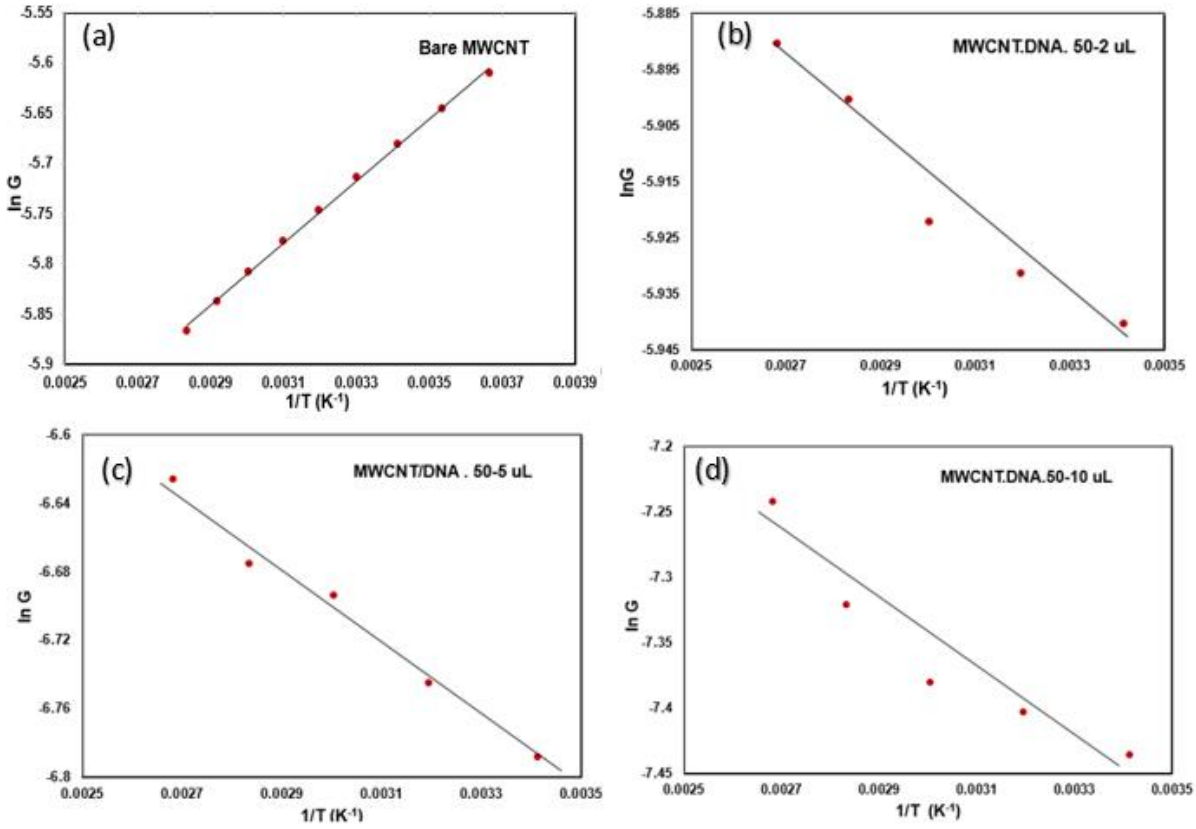

Figure 5.11 Arrhenius plot of (a) bare DNA and MWCNT. DNA nanocomposite (b) 50-2 uL (c) 50-5 uL (d) 50-10 uL.

Figure 5.11 shows the Arrhenius plot of conductance of the different mixtures of DNA/MWCNT nanocomposites. The pure CNT sample (figure 5.11a) shows a decrease of conductance with temperature – this is characteristic behaviour of metal-like conductors and is usually ascribed to an increase in the electron/hole scattering rate. In contrast, the CNT/DNA composites (figure 5.11 b-d) showed a simple Arrhenius behaviour within the measured temperature range. The activation energy (E_a) of the hopping process obtained from the Arrhenius plots shown in the figure 5.11 were 590 ± 9.0 J mol^{-1}, 1460 ± 9.0 J mol^{-1}, and 2090 ± 45.0 J mol^{-1} for the reaction ratios of 50-2 uL, 50-5 uL and 50-10 uL respectively. The result showed that the activation energy was increasing with increased DNA amount in the nanocomposite. This is consistent with our model of DNA-coated CNTs and the tunnelling barriers of figure 5.10 c.

5.2.8 Gas sensing

The gas sensing properties of the DNA/MWCNT composites to different volatile organic compounds (VOCs) in the gas phase was investigated. The DNA: CNT

composites were drop-cast onto Pt interdigitated electrodes just as for the I-V characterisation and the device was inserted in the gas stream inside a glass tube. The temperature of the device was monitored with a K-type thermocouple. The background was zero air and the analyte was zero air saturated with the VOC of interest by passage through a Dreschel bottle. Two digital mass flow controllers (DMFCs) were used to control the flow rate of the background and of the analyte. The analyte concentration was controlled by adjusting the mixing ratio of the V_{air} and V_{VOC} flows.

$$p_{VOC} = p^* \frac{V_{VOC}}{V_{VOC}+V_{air}} \tag{5.4}$$

Where p^* is the saturated vapour pressure of the VOC at the temperature of the Dreschel bottle – monitored with a second K-type thermocouple. Vapour pressure data for each analyte was obtained in the form of the Antoine equation parameters A, B, C and evaluated at the temperature of the Dreschel bottle.

$$\log_{10} p^* = A - \frac{B}{T+C} \tag{5.5}$$

Using equations (6.5) and (6.6) the analyte concentration or partial pressure p_{VOC} can be controlled as a fraction of the saturated vapour pressure. We chose a range of polar and nonpolar molecules (methanol, ethanol, acetone and chloroform) as test analyte to explore their effect on the conductance of the DNA: CNT devices.

Zero air was first channelled to the sensor device and allowed to flow through for some time to ensure equilibration and stabilisation of the DNA/MWCNT nanocomposite which is indicated by a fairly constant resistance. This was followed by different concentration of the various organics vapours. There was a change in the resistance of the organic vapours when in contact with the nanocomposites and the response is obtained as resistance against time transient curves. Figure 5.12 shows the transient response curves for different concentrations of methanol, ethanol, acetone and chloroform for DNA decorated MWCNT nanocomposites device. As shown, the gas resistance increases with increasing concentrations for all the gases even though the amount of change varies with the analyte. The change in resistance is due to the adsorbed molecules removing electrons from the surface of the carbon nanotubes[268,269].The sensor responses were quite stable and reproducible.

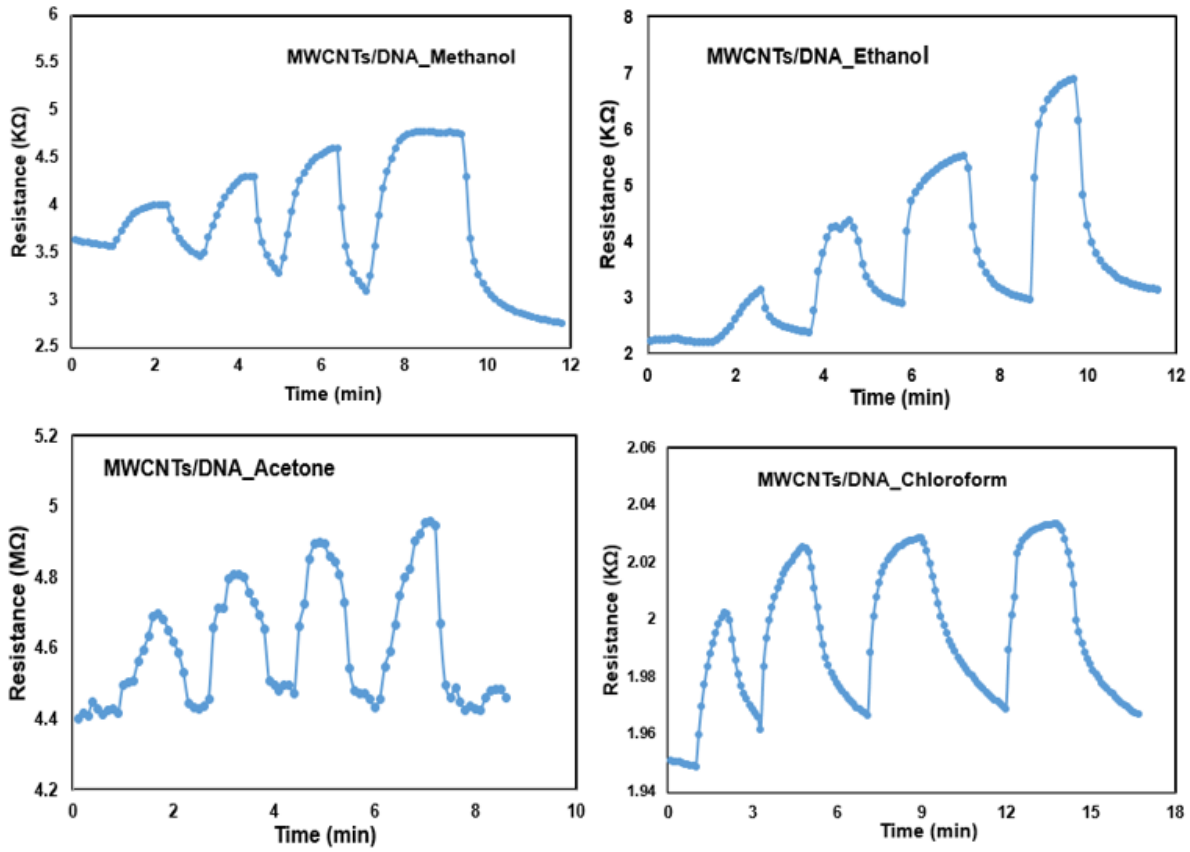

Figure 5.12 Transient response curves for different concentrations of methanol, ethanol, acetone and chloroform for DNA decorated MWCNT nanocomposites device.

The response of the VOCs was reported as normalised resistance change. The normalised resistance change is calculated using the equation (eqn.5.6):

$$S(\%) = \frac{R_v - R_a}{R_a} \tag{5.6}$$

Where R_v is the resistance of the DNA/MWCNT nanocomposite film in the presence of the vapour while R_a is the resistance of the film in zero air.

The gas flow rate of the VOCs has been reported here as the mixing fraction of the partial pressure to the saturated vapour pressure.

$$\frac{p}{p^*} = \frac{V_V}{V_V + V_a} \tag{5.7}$$

Where p is the partial pressure while p^* is the saturated vapour pressure of the VOC at the given temperature. V_a and V_v is the mixing volume of zero air and analyte volume respectively.

The response of the various VOCs at different temperature was investigated and the result reported in figure 5.13. Figure 5.13 shows the sensitivity measurement of MWCNT/DNA nanocomposite with mixture 50:2 uL at different temperatures to methanol, methanol, chloroform and acetone. The response generally decrease with increasing temperature. There was a significant change in the sensitivity of methanol and ethanol from room temperature to elevated temperatures. The change for chloroform and acetone was more gradual at elevated temperature. This might be due to the difference in the polarity of this analyte[270]. The response of the device to increased gas flow rate shows increment in sensitivity with increasing flow rate. This trend was consistent for all the different VOCs.

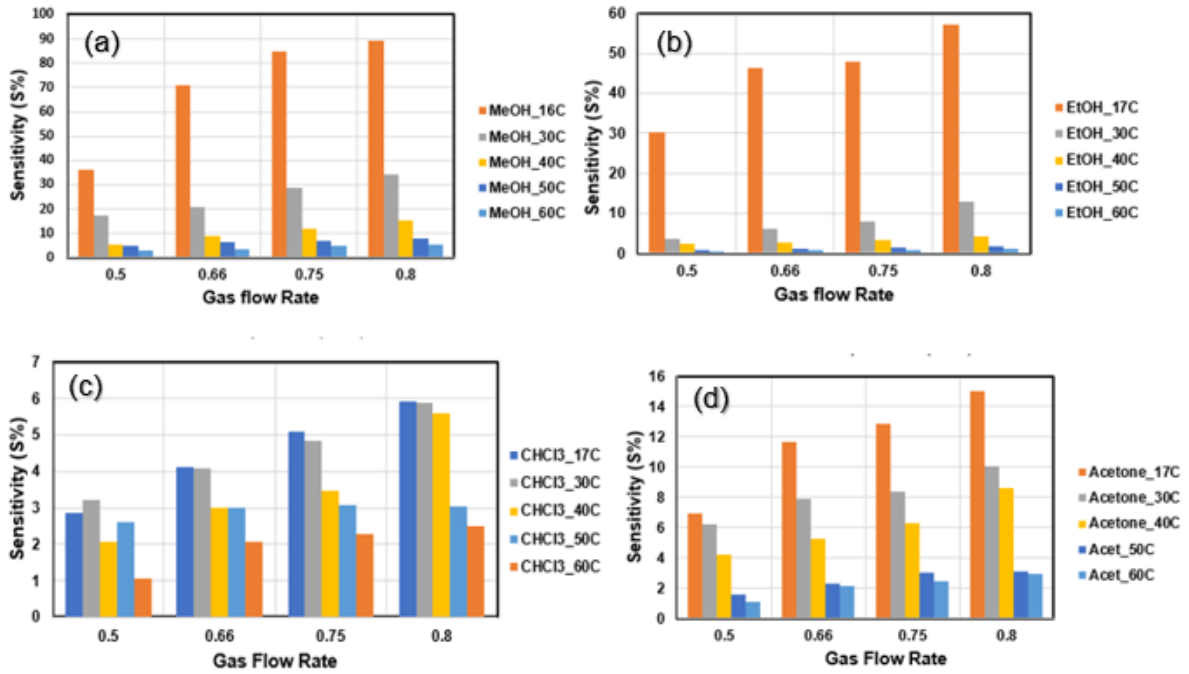

Figure 5.13 The sensitivity measurement of MWCNT/DNA nanocomposite with mixture 50:2 uL at different temperatures to (a) methanol (b) ethanol (c) chloroform (d) acetone.

As the amount of DNA is increased for the DNA/MWCNT nanocomposite, the response of the device to the VOCs also changed. Figure 5.14 shows the sensitivity of MWCNT/DNA nanocomposite with mixture 50:5 uL at different temperatures to methanol, ethanol, chloroform and acetone. The sensitivity of all the VOCs increased with increasing flow rate. Methanol showed the highest response to the VOCs by a high margin compared to the other analyte. As the temperature increases, the sensitivity of the nanocomposite film decreases for all the VOCs.

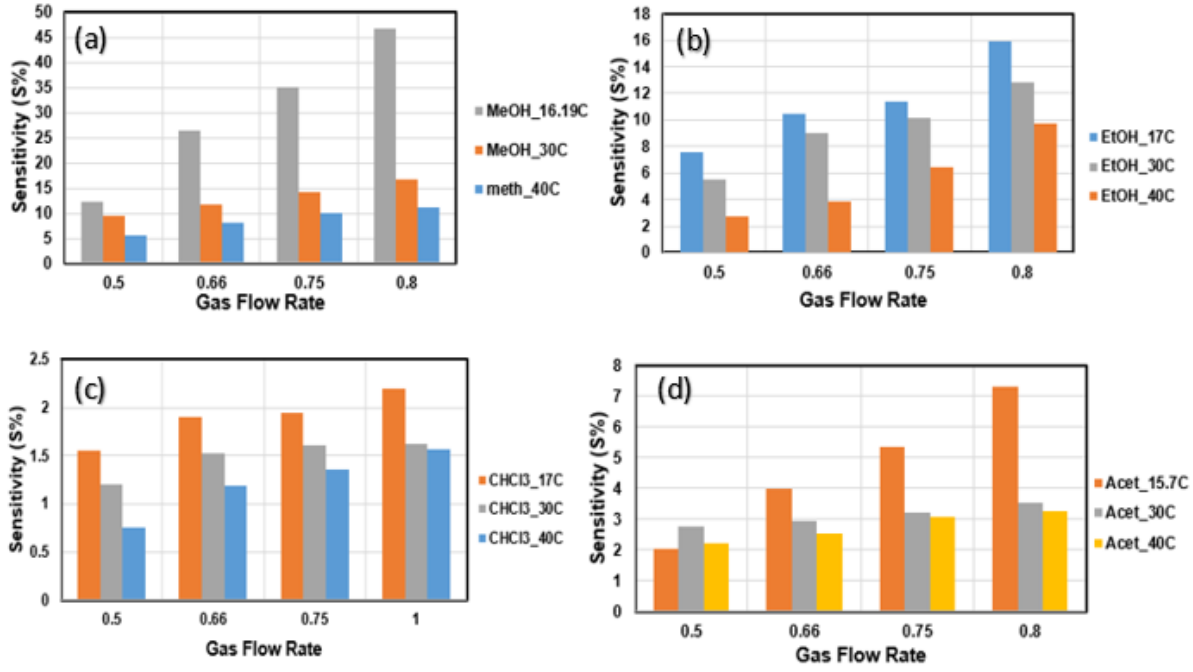

Figure 5.14 The sensitivity measurement of MWCNT/DNA nanocomposite with mixture 50:5 uL at different temperatures to (a) methanol (b) ethanol (c) chloroform (d) acetone.

Just as it was established earlier that the conductivity of the different ratio of the nanocomposites decreases with increasing amount of DNA in the film, so is the sensitivity of the device as well. This can be attributed to the increased π-π stacking of the DNA to the carbon nanotube backbone and therefore decreasing the tunnelling of electrons across the nanotubes[271–276].

The response of the various VOCs were compare with each other at different temperature and flow rate. Figure 5.15 showed the change in the sensitivity of pristine and hybrid nanotubes at different temperature with different concentrations (mixing fraction) of DNA, (a-c) bare MWCNTs, (d-f) MWCNTs/DNA (50:2) uL, (g-l) MWCNTs/DNA (50:5) uL, for methanol, ethanol, acetone and chloroform. The response of pristine MWCNT showed low response to all the VOCs even at high mixing ratios (high flow rate). Acetone showed higher response than any of the other analyte for the different temperatures for bare MWCNT. There was gradual improvement in the sensitivity of all the analyte with increasing mixing ratio (concentration) but decrease with increasing temperature. The high response of acetone to pristine CNT might be due to the high tendency of acetone to form hydrogen bond to the pristine CNT. It has been reported in literature that MWCNTs contains carboxyl and hydroxyl functional

groups which plays key role in favouring hydrogen bond formation with hydrogen accepting molecules such as acetone[277].

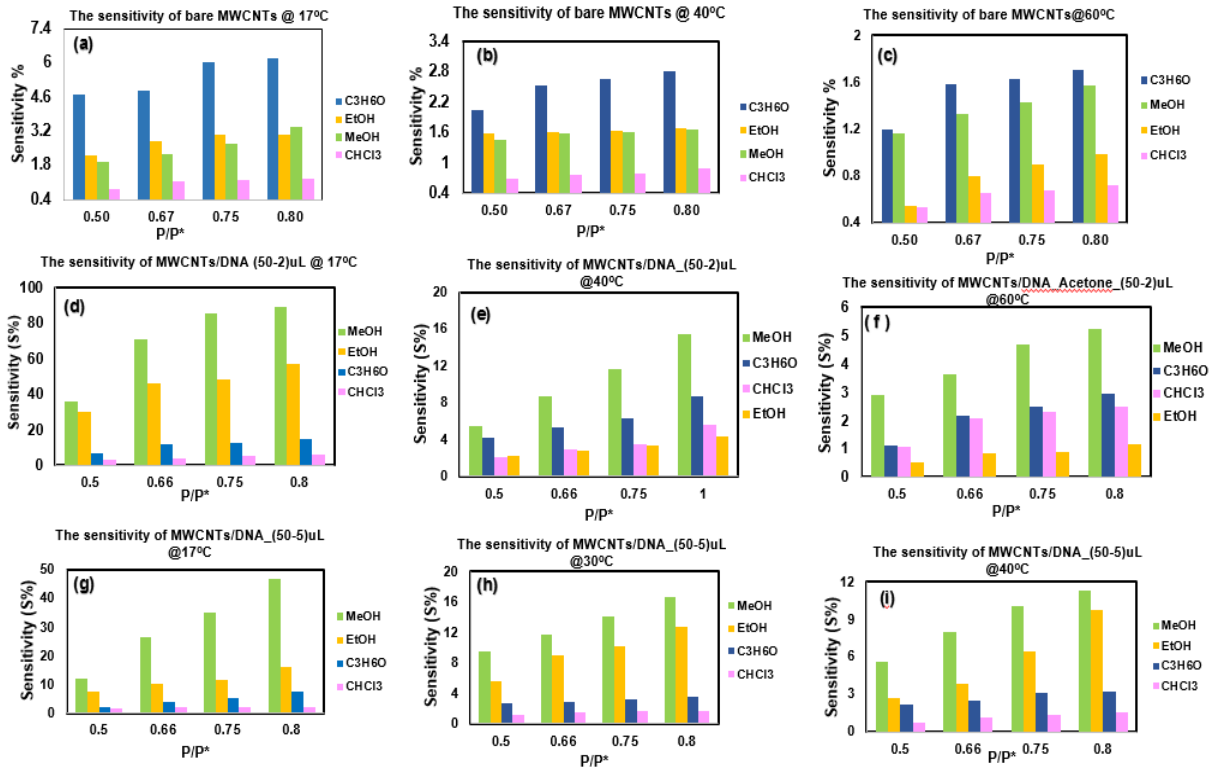

Figure 5.15 Shows the change in the sensitivity of pristine and hybrid nanotubes at different temperature with different concentrations of DNA ,(a-c) bare MWCNTs, (d-f) MWCNTs/DNA (50:2) uL, (g-i)MWCNTs/DNA (50:5) uL, for MeOH, EtOH, C_3H_6O and $CHCl_3$.

The addition of DNA solution to the MWCNT to form nanocomposite (50-2 uL) has drastically changed the sensitivity of the films. Methanol showed the highest response compared to the other VOCs and followed by ethanol. This was different from the pristine MWCNT which showed highest response to acetone. This might be attributed to the increased dispersion due to binding of the nucleobases to the MWCNT. This facilitate more binding of subsequent polar molecules to MWCNT and therefore greater responses. It has also been reported in literature that functionalisation of MWCNTs with DNA which contains hydrophilic functional groups such as amino and carboxyl groups improves the sensitivity of the MWCNT to alcohols due to dipole-dipole interactions[278].However, as the amount of DNA in the MWCNT/DNA nanocomposite is increased to 50-5 uL, the sensitivity is decreased. The use of 50- 10 uL mixing volume MWCNT/DNA nanocomposite showed little or no response to the VOCs due to

effective binding of the DNA template to the MWCNT leading to little or no tunnelling of electrons across the MWCNT networks.

The sensitivity of the MWCNT/DNA nanocomposite was seen to depend on the device temperature. The dependence was modelled using a simplified isotherm for the adsorption of the analyte on the composite and a signal proportional to the amount of adsorbed analyte. The signal (S) is given by:

$$S = \alpha\Gamma \tag{5.8}$$

Where α is the surface excess of analyte (mol m^{-2}). The adsorption isotherm may be described by the Langmuir or BET equations or more complex models, however it is sufficient for this purpose to assume that the analyte is weakly adsorbing and then the isotherm reduced to an approximately linear relation between partial pressure in the gas phase and the surface excess. In the Langmuir or BET cases where the surface coverage reaches a plateau at monolayer coverage Γ_m, the sensing response is independent of analyte pressure and not of particular interest. The linear region is.

$$\frac{\Gamma}{\Gamma_m} \simeq Kp_{VOC} \tag{5.9}$$

Γ_m is monolayer coverage, *K* is an equilibrium constant describing adsorption and p_{VOC} is the partial pressure of the analyte. The sensitivity is then given simply by substituting equation (5.9) into equation (5.8);

$$S = \alpha K p_{VOC} \Gamma_m \tag{5.10}$$

The partial pressure of the analyte is controlled by the temperature of the Dreschel bottle, not the temperature at the sensor and the gas stream is vented to a fume hood so the overall pressure is equalised with the atmosphere. Therefore the only term in equation (5.10) which is strongly temperature-dependent is *K*. Our model therefore predicts a temperature dependence for the devices analogous to the Van't Hoff equation.

$$\frac{\partial \ln S}{\partial 1/T} = -\frac{\Delta H^{\theta}}{R} \tag{5.11}$$

Where ΔH^{θ} is the standard reaction enthalpy of the adsorption process. Figure 5.16 shows the various plots of lnS against $1/T$ for devices with different DNA: CNT ratios and for different VOC analyte. The enthalpy of the adsorption was derived from the

slope of the plot and multiplied by minus the universal gas constant (R = 8.314 K^{-1} mol^{-1}).

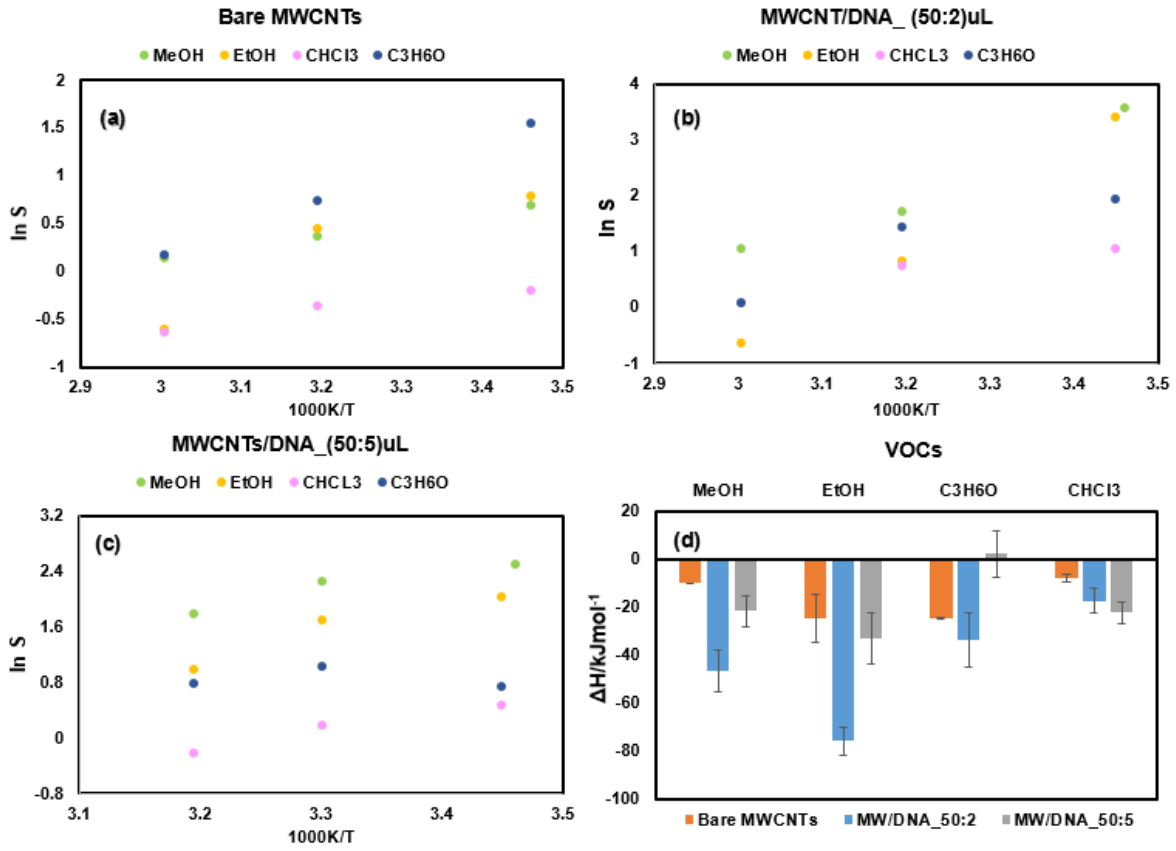

Figure 5.16 (a-d) Show the change in the sensitivity of Bare CNTs and CNTs/DNA nanocomposite at different temperatures, (d) plot of Enthalpy of Bare CNTs and CNTs/DNA nanocomposite with different volatile organic vapours.

The derived ΔH^{θ}values are collected in table 5.1 and compared against the standard enthalpies of vaporization for the VOCs. The enthalpy of adsorption was highest for acetone, followed by ethanol, methanol and chloroform. The formation of MWCNT/DNA nanocomposite with 50:2 uL mixing volume showed that the enthalpy of adsorption was highest for ethanol, followed methanol, acetone and chloroform. The MWCNT/DNA 50:5 uL mixing volume nanocomposite showed higher enthalpy of adsorption to ethanol, followed by chloroform, methanol and acetone respectively. The response of acetone showed a positive enthalpy which suggest that the process might not be adsorption. The selectivity of the carbon nanotubes to the different VOCs can be tune by varying the amount of DNA added to form the nanocomposite. In order to be certain that the process was not just condensation of the analyte on the nanocomposites, the enthalpy of adsorption was compared to standard enthalpy of vaporisation of the various organic vapours. The standard heat of vapourisation at

room temperature obtained in literature for ethanol, methanol, acetone and chloroform were 42.kJ mol^{-1} [279], 38.4 kJ mol^{-1} [280], 32.1 kJ mol^{-1} [281] and 32.5 kJ mol^{-1} [282] respectively. From table 6.1, it can be seen that the enthalpy of adsorption of the VOCs are different from the standard enthalpy of vapourisation. This confirms the interaction of the organic vapours with the carbon nanotubes and the carbon nanotube nanocomposites involve specific interactions rather than simple condensation of bulk liquid.

Table 5.1 The calculated ΔH values of the different VOCs for the bare MWCNT and MWCNT/DNA composites. Values shown are mean and standard error from the linear regression of ln S vs 1/T.

VOCs	Bare MWCNTs		MW/DNA_50:2		MW/DNA_50:5	
	ΔH (kJ mol^{-1})	error	ΔH (kJ mol^{-1})	error	ΔH (kJ mol^{-1})	error
MeOH	-9.9	0.1	-46.6	8.6	-21.5	6.33
EtOH	-24.5	10	-76	5.9	-33	10.5
C_3H_6O	-24.85	0.28	-33.6	11.6	2.47	9.8
$CHCl_3$	-7.8	1.9	-17.3	5.1	-22.3	4.4

5.3 Conclusion

Multi-walled carbon nanotubes (MWCNT) - deoxyribonucleic acid (DNA) nanocomposite were synthesised in solution by mixing multi-walled carbon nanotubes with different volumes (2 uL, 5 uL and 10 uL) of lambda DNA in solution. The nanocomposites where formed after few minutes of sonication. It was then characterised using uv-vis spectroscopy, atomic force microscopy, Raman spectroscopy, Fourier transform infrared spectroscopy and transmission electron microscopy techniques. The characterisation showed that nanocomposite was formed via π-stacking of the DNA on the carbon nanotubes leading to effective dispersion of the carbon nanotubes. MWCNT/DNA nanocomposite based gas sensor were also fabricated using different MWCNT/DNA ratios to design a resistive sensor. The gas sensor was used for sensing various volatile organic vapours (VOCs) such as methanol, ethanol, chloroform and acetone. These sensors exhibited excellent selectivity and sensitivity towards methanol vapour at room temperature even when

exposed to low concentrations. The effect of increase in temperature on the sensitivity of the various MWCNT/DNA ratio gas sensor was extensively investigated. The sensors also showed good reversibility with most of the analyte especially acetone.

CHAPTER SIX

Summary, Conclusion and Recommendations

6.1 Conclusion

In this thesis, DNA templated CdS, $CdZnS_2$ and ZnS were synthesized in solution to form smooth and continuous nanowires. It was realised that the reactions that produced somewhat smooth and continuous nanowires were dependent on factors such as concentration and incubation time. The concentration has to be appreciably low to prevent fast assembly leading to irregular templating but significant enough to enable sufficient coating of the DNA template. It was also established that the reaction has to be in two stages and sufficient time should be allowed during addition of the precursors to produce the desired nanowires. Different characterisation techniques were used to prove the formation of the DNA templated nanowires. All the techniques indicated that there was significant interaction between the metal sulfides and DNA template. The nanowires produced were also proven to be quite smooth and continuous and appropriate for deposition and alignment on electrodes to produce nanowire gas sensor. This route has not only shown that metal sulfides nanowires can be synthesised via DNA templated method but that large quantity of the nanowire can easily be prepared at prevailing laboratory conditions.

The templated nanowires were found to have height distribution of 4-8 nm. The optical images shows a bright emission from the dense network of nanowires and single nanowires can also be seen as tiny extensions from the dense mass. The nanowires were photoluminescent with Raman peaks that shows size quantization. The UV-Vis spectra indicated peaks for the DNA as well as the metal sulfides and the FTIR spectra demonstrated shift between the bare DNA and the nanowires which can be ascribed to the reaction of the metal sulfides with the DNA. The TEM images showed tiny strands of the 1D nanowires showing the templating of the metal sulfide on the DNA .The crystallite size and crystal structure of the nanowires were determine via XRD and it showed that a smaller size compared to the AFM image. This can be ascribed to the height ben more than one particle size thick which is due to nucleation of the particles. This phenomenon has also been previously reported in the synthesis of other nanomaterials. The corresponding elemental composition determined from the surface XPS spectroscopy showed the presence of the various elements accordingly indicating the formation of the binary and ternary metal alloys on the DNA template.

Electrical properties of DNA templated nanowires are very important when they are to be used as transducer in gas sensors. The electrical properties of the synthesised DNA templated metal sulfide nanowires were determine using two terminal probe station measurement, impedance measurement and transient current measurement. They I-V plot determined from the two terminal measurement showed a fairly ohmic conduction at low voltage and space charge limited conduction at higher voltage. The conductance extracted from the plot was in nanometre range. The temperature dependence measurement showed an increasing conductivity with temperature which indicated an Arrhenius-like behaviour. The nanowire resistance and the contact resistance were also extracted from the impedance spectroscopy and transient current measurement. The resistance of the nanowire gas sensor as measured from all the techniques were found to be in nanometre range. The transient current measurement also showed that change in voltage plays a more dominant role in contact resistance of the nanowire.

The synthesized nanowires were aligned on electrodes to make gas sensors. The sensor were used for sensing VOCs such as ethanol, acetone, chloroform and hexane. The DNA templated metal sulfide nanowire gas sensor showed a generally fast response and recovery time especially for room temperature gas sensing even though less than its counterpart high temperature metal sulfide sensors. The $CdZnS_2$/DNA nanowire sensor showed an enhanced response and recovery time compared to those of CdS/DNA and ZnS/DNA. The effect of temperature on the gas sensors showed that the sensitivity decreased with increasing temperature. The sensors showed faster response and recovery time with increasing temperature. The enthalpy of the adsorption process of the VOCs on the nanowire gas sensors indicated an exothermic reaction process.

The mechanism of the sensing was explained based on simple adsorption and desorption of the adsorbed surface oxygen when in contact with the VOCs and thereby releasing the trapped electrons into the conduction band of the metal sulfides. The selectivity studies of the nanowire sensors showed different selectivity to the various reducing gases/vapour which can be attributed to different basis of interaction between the VOCs and the nanowire network. The high response of the nanowire sensors to the VOCs especially ethanol vapour with reversible properties indicates that the templated nanowires has potential to make good gas sensor with practical application.

However, like other commercial available sensors, the nanowire sensors responded to a great extent to humidity.

The potential of carbon nanotubes in the sensing of VOCs was also studied and reported in this thesis. Multi-walled carbon nanotubes (MWCNT) - deoxyribonucleic acid (DNA) nanocomposite were synthesized in solution by mixing multi-walled carbon nanotubes with different volumes of lambda DNA in solution. The nanocomposites where formed after few minutes of sonication and characterised using different spectroscopic and microscopic techniques. The characterisation showed that nanocomposite was formed via π-stacking of the DNA on the carbon nanotubes leading to effective dispersion of the carbon nanotubes. MWCNT/DNA nanocomposite based gas sensor were fabricated using different MWCNT/DNA ratios to design a resistive sensor. The gas sensor was used for sensing various volatile organic vapours (VOCs) such as methanol, ethanol, chloroform and acetone. The effect of increase in temperature on the sensitivity of the various MWCNT/DNA ratio gas sensor was extensively investigated. The sensors also showed good reversibility with most of the analyte especially acetone. These sensors also showed good selectivity and sensitivity towards methanol vapour at room temperature even when exposed to low concentrations.

6.2 Recommendation

Even though this studies tried to optimize the synthesis of the nanowires as much as possible to produce smooth and continuous nanowires that are conductive, the coating was not as smooth along the DNA template as we could expect. Therefore, further experiment are require by varying other factors such as temperature, pH, precursor salts etc. to see its effect on the smoothness and conductivity of the synthesized nanowires. It would also be a good idea to carry out computational studies on templating of metal sulfides on DNA to determine the effect of different factors on the synthesis. The binding sites of metal sulfides on the DNA template can also be studied using computational studies.

The fabrication of the nanowire gas sensors were done via drop-casting of the nanowires on the microfabricated electrode, but it was quite difficult to deposit sufficient material on the small electrode spot to improve the sensitivity of the device. It is therefore recommended that formulation of ink with the synthesized nanowires and

inkjet printing as earlier reported[162] by our group be adopted for deposition of the nanowire during device fabrication. This will ensure deposition of enough material on microfabricated device and probably improve the sensitivity.

This current studies considered the application of the fabricated nanowire gas sensor to studies of low molecular weight VOCs. However, further experiment will be recommended for the studies of high molecular weight and aromatic VOCs sensing using the fabricated gas sensors. These nanowire gas sensors are also recommended to be used for the sensing of inorganic gaseous pollutants such as CO, SO_2, CO_2, NO, NO_2 and ozone to observe their responses.

Further experiments to determine the sensing mechanism of the synthesized DNA templated nanowires gas sensor to the studied VOCs is required to substantiate the mechanism proposed in this studies.

References

1 S. M. Lindsay, *Introduction to Nanoscience*, Boca Ration: Taylor & Francis group, 2008.

2 A. Zhang, G. Zheng and C. M. Lieber, *Nanowires: Building Blocks for Nanoscience and Nanotechnology*, Springer Nature, 2016.

3 B. Murty, P. Shankar, B. Raj, B. Rath and J. Murday, *Text of Nanoscience and Nanotechnology*, University Press, 2013.

4 P. M. Rorvik, T. Grande and M. A. Einarsrud, One-dimensional nanostructures of ferroelectric perovskites, *Adv. Mater.*, 2011, **23**, 4007–4034.

5 J. N. Tiwari, R. N. Tiwari and K. S. Kim, Zero-dimensional, one-dimensional, two-dimensional and three-dimensional nanostructured materials for advanced electrochemical energy devices, *Prog. Mater. Sci.*, 2012, **57**, 724–803.

6 S. Barth, F. Hernandez-Ramirez, J. D. Holmes and A. Romano-Rodriguez, Synthesis and applications of one-dimensional semiconductors, *Prog. Mater. Sci.*, 2010, **55**, 563–627.

7 R. Kelsall, I. Hamley and M. Geoghegan, *Nanoscale Science and Tecnology*, John Wiley& Sons,Ltd, Sussex,England., 2005, vol. 1.

8 M. F. Ashby, P. J. Ferreira and D. L. Schodek, *Nanomaterial, nanotechnologies and Design. An introduction to engineers and architect.*, Butterworth-Heinemann, 1st Editio., 2009.

9 S. Suresh, Semiconductor Nanomaterials, Methods and Applications: A Review, *Nanosci. Nanotechnol.*, 2013, **3**, 62–74.

10 D. L. Greenaway and G. Harbeke, *Optical properties and band structure of semiconductors*, Pergamon, 1968.

11 H. Weller and A. Eychmüller, Semiconductor Nanoclusters - Physical, Chemical, and Catalytic Aspects, *Stud. Surf. Sci. Catal.*, 1997, **103**, 5–22.

12 G. Schon and U. Simon, A fascinating new field in colloid science - small ligand-stabilized metal-clusters and possible application in microelectronics. 1 State of

the art, *Colloid Polym. Sci.*, 1995, **273**, 101–117.

13 P. Wolff, in *Electronic structures of Semiconductors. In Hannay N.B, Colombo U. Electronic materials.*, Springer, Boston, MA, 1973.

14 J. Hu, T. W. Odom and C. M. Lieber, Chemistry and physics in one dimension: Synthesis and properties of nanowires and nanotubes, *Acc. Chem. Res.*, 1999, **32**, 435–445.

15 X. Duan, J. Wang and C. M. Lieber, Synthesis and optical properties of gallium arsenide nanowires, *Appl. Phys. Lett.*, 2000, **76**, 1116–1118.

16 H. Liu, J. Kameoka, D. A. Czaplewski and H. G. Craighead, Polymeric nanowire chemical sensor, *Nano Lett.*, 2004, **4**, 671–675.

17 E. Comini, Metal oxide nanowire chemical sensors: innovation and quality of life, *Mater. Today*, 2016, **19**, 559–567.

18 D. Zappa, A. Bertuna, E. Comini, M. Molinari, N. Poli and G. Sberveglieri, Tungsten oxide nanowires chemical sensors, *Procedia Eng.*, 2014, **87**, 696–699.

19 Q. Cui, F. Gao, S. Mukherjee and Z. Gu, Joining and Interconnect formation of nanowires and carbon nanotubes for nanoelectronics and nanosystems, *Small*, 2009, **5**, 1246–1257.

20 W. H. Xu, L. Wang, Z. Guo, X. Chen, J. Liu and X. J. Huang, Copper nanowires as nanoscale interconnects: Their stability, electrical transport, and mechanical properties, *ACS Nano*, 2015, **9**, 241–250.

21 A. Roy, T. Pandey, N. Ravishankar and A. K. Singh, Single crystalline ultrathin gold nanowires: Promising nanoscale interconnects, *AIP Adv.*, , DOI:10.1063/1.4796188.

22 M. Law, J. Goldberger and P. Yang, Semiconductor Nanowires and Nanotubes, *Annu. Rev. Mater. Res.*, 2004, **34**, 83–122.

23 M. Y. Lu, L. J. Chen, W. Mai and Z. L. Wang, Tunable electric and magnetic properties of CoxZn1-xS nanowires, *Appl. Phys. Lett.*, 2008, **93**, 23–25.

24 W. Cheng, K. Tang, Y. Qi, J. Sheng and Z. Liu, One-step synthesis of

superparamagnetic monodisperse porous Fe3O4hollow and core-shell spheres, *J. Mater. Chem.*, 2010, **20**, 1799–1805.

25 J. Liu and D. Xue, Rapid and scalable route to CuS biosensors: A microwave-assisted Cu-complex transformation into CuS nanotubes for ultrasensitive nonenzymatic glucose sensor, *J. Mater. Chem.*, 2011, **21**, 223–228.

26 F. Cao, R. Liu, L. Zhou, S. Song, Y. Lei, W. Shi, F. Zhao and H. Zhang, One-pot synthesis of flowerlike Ni $_7$ S $_6$ and its application in selective hydrogenation of chloronitrobenzene, *J. Mater. Chem.*, 2010, **20**, 1078–1085.

27 X. Fang, Y. Bando, U. K. Gautam, C. Ye and D. Golberg, Inorganic semiconductor nanostructures and their field-emission applications, *J. Mater. Chem.*, 2008, **18**, 509–522.

28 D. Moore and Z. L. Wang, Growth of anisotropic one-dimensional ZnS nanostructures, *J. Mater. Chem.*, 2006, **16**, 3898–3905.

29 Z. X. Yang, N. Han, M. Fang, H. Lin, H. Y. Cheung, S. P. Yip, E. J. Wang, T. F. Hung, C. Y. Wong and J. C. Ho, Surfactant-assisted chemical vapour deposition of high-performance small-diameter GaSb nanowires, *Nat. Commun.*, 2014, **5**, 1–10.

30 a Ortiz, J. C. Alonso, M. Garcia and J. Toriz, Tin sulphide films deposited by plasma-enhanced chemical vapour deposition, *Semicond. Sci. Technol.*, 1999, **11**, 243–247.

31 L. Samad, M. Cabán-Acevedo, M. J. Shearer, K. Park, R. J. Hamers and S. Jin, Direct chemical vapor deposition synthesis of phase-pure iron pyrite (FeS<inf>2</inf>) thin films, *Chem. Mater.*, 2015, **27**, 3108–3114.

32 J. P. Ge, J. Wang, H. X. Zhang and Y. D. Li, A general atmospheric pressure chemical vapor deposition synthesis and crystallographic study of transition-metal sulfide one-dimensional nanostructures, *Chem. - A Eur. J.*, 2004, **10**, 3525–3530.

33 D. Mudusu, K. R. Nandanapalli, S. R. Dugasani, J. W. Kang, S. H. Park and C. W. Tu, Growth of single-crystalline cubic structured tin(II) sulfide (SnS) nanowires by chemical vapor deposition, *RSC Adv.*, 2017, **7**, 41452–41459.

34 B. Basnar, Y. Weizmann, Z. Cheglakov and I. Willner, Synthesis of nanowires using dip-pen nanolithography and biocatalytic inks, *Adv. Mater.*, 2006, **18**, 713–718.

35 R. . Furneaux, W. . Rigby and A. . Davidson, The formation of controlled-porosity membranes from anodically oxidized aluminium., *Nature*, 1989, **337**, 147–149.

36 C. Schönenberger, B. M. I. van der Zande, L. G. J. Fokkink, M. Henny, C. Schmid, M. Krüger, A. Bachtold, R. Huber, H. Birk and U. Staufer, Template Synthesis of Nanowires in Porous Polycarbonate Membranes: Electrochemistry and Morphology, *J. Phys. Chem. B*, 1997, **101**, 5497–5505.

37 E. Katz and I. Willner, Integrated nanoparticle-biomolecule hybrid systems: Synthesis, properties, and applications, *Angew. Chemie - Int. Ed.*, 2004, **43**, 6042–6108.

38 F. Patolsky, Y. Weizmann and I. Willner, Actin-based metallic nanowires as bio-nanotransporters, *Nat. Mater.*, 2004, **3**, 692–695.

39 Y. Huang, C. Y. Chiang, S. K. Lee, Y. Gao, E. L. Hu, J. De Yoreo and A. M. Belcher, Programmable assembly of nanoarchitectures using genetically engineered viruses, *Nano Lett.*, 2005, **5**, 1429–1434.

40 J. M. Berg, J. L. TYmoczko and L. Stryer, *Biochemistry*, W. H Freeman and Company, New York, 5Th edn., 2002.

41 J. M. Kinsella and A. Ivanisevic, DNA-templated magnetic nanowires with different compositions: Fabrication and analysis, *Langmuir*, 2007, **23**, 3886–3890.

42 R. K. and W. P. Alberts B, Johnson A, Lewis J, Raff M, *Molecular Biology of the Cell*, Garland Science, New York, 2002.

43 J. G. Duguid, V. A. Bloomfield, J. M. Benevides and G. J. J. Thomas, DNA melting investigated by differential scanning calorimetry and Raman spectroscopy, *Biophys. J.*, 1996, **71**, 3350–3360.

44 M. J. Butler, *Forensic DNA Typing: Biology and Technology behind STR Marker (London:*, Academic Press, London, 2001.

45 B. M. Ghosh A, A glossary of DNA structures from A to Z, *Acta Crystallogr D Biol Crystallogr.*, 2003, **59**, 620–626.

46 J. D. Watson and F. C. H. Crick, Molecular structure of nucleic acid. A structure for deoxyribose nucleic acid, *Nature*, 1953, **171**, 737–738.

47 M. J. Berg, J. L. Tymoczko and S. L, *Biochemistry*, W. H Freeman and Company, New York, 2012.

48 O. P. Lamba, A. H. Wang and G. J. J. Thomas, Low-frequency dynamics and Raman scattering of crystals, of B-, A-, and Z-DNA, and fibers of C-DNA., *Biopolymers*, 1989, **28**, 667–78.

49 S. Pruneanu, S. A. F. Al-Said, L. Dong, T. A. Hollis, M. A. Galindo, N. G. Wright, A. Houlton and B. R. Horrocks, Self-assembly of DNA-templated polypyrrole nanowires: Spontaneous formation of conductive nanoropes, *Adv. Funct. Mater.*, 2008, **18**, 2444–2454.

50 A. Houlton, A. R. Pike, M. Angel Galindo and B. R. Horrocks, DNA-based routes to semiconducting nanomaterials., *Chem. Commun. (Camb).*, 2009, 1797–1806.

51 A. Houlton and S. M. D. Watson, DNA-based nanowires. Towards bottom-up nanoscale electronics, *Annu. Reports Sect. 'A' (Inorganic Chem.*, 2011, **107**, 21.

52 R. M. Stoltenberg and A. T. Woolley, DNA-templated nanowire fabrication, *Biomed. Microdevices*, 2004, **6**, 105–111.

53 S. Pu, A. Zinchenko and S. Murata, Conformational behavior of DNA-templated CdS inorganic nanowire., *Nanotechnology*, 2011, **22**, 375604.

54 R. Hassanien, M. Al-Hinai, S. a. Farha Al-Said, R. Little, L. Šiller, N. G. Wright, A. Houlton and B. R. Horrocks, Preparation and characterization of conductive and photoluminescent DNA-templated polyindole nanowires, *ACS Nano*, 2010, **4**, 2149–2159.

55 Y. K. Gao, X. M. Zhao and P. G. Yin, Fabrication of ZnS nanocircles using Escherichia coli DNA as templates, *Mater. Lett.*, 2014, **131**, 112–115.

56 R. Hassanien, S. a F. Al-Said, L. Šiller, R. Little, N. G. Wright, A. Houlton and B.

R. Horrocks, O nanowires: growth morphology, spectroscopic and electrical characterization, *Nanotechnology*, 2012, **23**, 75601.

57 M. N. Al-Hinai, R. Hassanien, N. G. Wright, A. B. Horsfall, A. Houlton and B. R. Horrocks, Networks of DNA-templated palladium nanowires: structural and electrical characterisation and their use as hydrogen gas sensors, *Faraday Discuss.*, 2013, **164**, 71.

58 H. D. A. Mohamed, S. M. D. Watson, B. R. Horrocks and A. Houlton, Magnetic and conductive magnetite nanowires by DNA-templating, *Nanoscale*, 2012, **4**, 5936.

59 S. M. D. Watson, H. D. a Mohamed, B. R. Horrocks and A. Houlton, Electrically conductive magnetic nanowires using an electrochemical DNA-templating route., *Nanoscale*, 2013, **5**, 5349–59.

60 Z. Deng and C. Mao, DNA-Templated Fabrication of 1D Parallel and 2D Crossed Metallic Nanowire Arrays, *Nano Lett.*, 2003, **3**, 1545–1548.

61 T. Catherall, D. Huskisson, S. McAdams and a. Vijayaraghavan, Self-assembly of one dimensional DNA-templated structures, *J. Mater. Chem. C*, 2014, **2**, 6895–6920.

62 K. Nguyen, M. Monteverde, A. Filoramo, L. Goux-Capes, S. Lyonnais, P. Jegou, P. Viel, M. Goffman and J. P. Bourgoin, Synthesis of thin and highly conductive DNA-based palladium nanowires, *Adv. Mater.*, 2008, **20**, 1099–1104.

63 L. Dong, T. Hollis, B. a. Connolly, N. G. Wright, B. R. Horrocks and A. Houlton, DNA-templated semiconductor nanoparticle chains and wires, *Adv. Mater.*, 2007, **19**, 1748–1751.

64 W. U. Dittmer and F. C. Simmel, Chains of semiconductor nanoparticles templated on DNA, *Appl. Phys. Lett.*, 2004, **85**, 633–635.

65 L. Levina, V. Sukhovatkin, S. Musikhin, S. Cauchi, R. Nisman, D. P. Bazett-Jones and E. H. Sargent, Efficient infrared-emitting PbS quantum dots grown on DNA and stable in aqueous solution and blood plasma, *Adv. Mater.*, 2005, **17**, 1854–1857.

66 N. Goswami, A. Giri and S. K. Pal, MoS2 nanocrystals confined in a dna matrix exhibiting energy transfer, *Langmuir*, 2013, **29**, 11471–11478.

67 J. L. Coffer, S. R. Bigham, R. F. Pinizzotto and H. Yang, Characterization of quantum-confined CdS nanocrystallites stabilized by deoxyribonucleic acid (DNA), *Nanotechnology*, 1999, **3**, 69–76.

68 C. F. Monson and A. T. Woolley, DNA-Templated Construction of Copper Nanowires, *Nano Lett.*, 2003, **3**, 359–363.

69 S. M. D. Watson, A. Houlton and B. R. Horrocks, Equilibrium and non-equilibrium thermodynamics of templating reactions for the formation of nanowires, *Nanotechnology*, , DOI:10.1088/0957-4484/23/50/505603.

70 H. Kudo and M. Fujihira, DNA-templated copper nanowire fabrication by a two-step process involving electroless metallization, *IEEE Trans. Nanotechnol.*, 2006, **5**, 90–92.

71 S. M. D. Watson, A. R. Pike, J. Pate, A. Houlton and B. R. Horrocks, DNA-templated nanowires: Morphology and electrical conductivity, *Nanoscale*, 2014, **6**, 4027–4037.

72 J. Pate, F. Zamora, S. M. D. Watson, N. G. Wright, B. R. Horrocks and A. Houlton, Solution-based DNA-templating of sub-10 nm conductive copper nanowires, *J. Mater. Chem. C*, 2014, **2**, 9265–9273.

73 Y. Liu, J. Wang and X. Zhang, Accurate determination of the vapor-liquid-solid contact line tension and the viability of Young equation, *Sci. Rep.*, 2013, **3**, 1–6.

74 Y. Huang, X. Duan and Q. L. Wei C. M., Directed assembly of one-dimensional nanostructures into functional networks, *Science (80-.).*, 2001, **26**, 630–633.

75 P. A. Smith, C. D. Nordquist, T. N. Jackson, T. S. Mayer, B. R. Martin, J. Mbindyo and T. E. Mallouk, Electric-field assisted assembly and alignment of metallic nanowires, *Appl. Phys. Lett.*, 2000, **77**, 1399–1401.

76 B. Messer, J. H. Song and P. Yang, Microchannel networks for nanowire patterning [14], *J. Am. Chem. Soc.*, 2000, **122**, 10232–10233.

77 S. Huang, X. Cai and J. Liu, Growth of millimeter-long and horizontally aligned single-walled carbon nanotubes on flat substrates, *J. Am. Chem. Soc.*, 2003, **125**, 5636–5637.

78 N. C. Seeman, DNA in a material world, *Nature*, 2003, **421**, 427–431.

79 C. Mao, W. Sun, Z. Shen and N. C. Seeman, A nanomechanical device based on the B ± Z transition of DNA, *Nature*, 1999, **397**, 144–146.

80 H. Yan, X. P. Zhang, Z. Y. Shen and N. C. Seeman, A robust sequence-dependent rotary DNA nanomechanical device controlled by hybridization topology, *Nature*, 2002, **415**, 62.

81 C. Mao, T. LaBean and J. H. Reif, Logical computation using algorithmic self-assembly of DNA triple crossover molecules, *Nature*, 2000, **407**, 493–496.

82 C. Mao, W. Sun and N. C. Seeman, Designed two-dimensional DNA holliday junction arrays visualized by atomic force microscopy, *J. Am. Chem. Soc.*, 1999, **121**, 5437–5443.

83 H. Nakao, M. Gad, S. Sugiyama, K. Otobe and T. Ohtani, Transfer-printing of highly aligned DNA nanowires, *J. Am. Chem. Soc.*, 2003, **125**, 7162–7163.

84 D. Bensimon, a. Simon, V. Croquette and a. Bensimon, Stretching DNA with a Receding Meniscus: Experiments and Models, *Phys. Rev. Lett.*, 1995, **74**, 4754–4757.

85 J. Li, C. Bai, C. Wang, C. Zhu, Z. Lin, Q. Li and E. Cao, A convenient method of aligning large DNA molecules on bare mica surfaces for atomic force microscopy, *Nucleic Acids Res*, 1998, **26**, 4785–4786.

86 Z.-Q. Ouyang, J. Hu, S.-F. Chen, J.-L. Sun and M.-Q. Li, Molecular patterns by manipulating DNA molecules, *J. Vac. Sci. Technol. B*, 1997, **15**, 1385–1432.

87 N. Hullavarad, S. Hullavarad and P. Karulkar, Cadmium Sulphide (CdS) nanotechnology: synthesis and application, *J. Nanosci. Nanotechnol.*, 2008, **8**, 3272–99.

88 S. S. Li, B. J. Stanbery, C. H. Huang, C. H. Chang, Y. S. Chang and T. J.

Anderson, Effects of buffer layer processing on CIGS excess carrier lifetime:application of dual-beam optical modulation to process analysis [ofsolar cells], *Conf. Rec. Twenty Fifth IEEE Photovolt. Spec. Conf. - 1996*, 1996, 0–3.

89 C. Ferekides, D. Marinskiy and D. L. Morel, PERFORMANCE, 1997, 3–6.

90 A. S. Z. Lahewil, Y. Al-Douri, U. Hashim and N. M. Ahmed, Structural, Analysis and Optical Studies of Cadmium Sulfide Nanostructured, *Procedia Eng.*, 2013, **53**, 217–224.

91 E. Conts-de, J. Li and C. R., Latest Advances in Modified/Functionalized Carbon Nanotube- Based Gas Sensors, *Synth. Appl. Carbon Nanotub. Their Compos.*, 2013, 337–365.

92 T. Zhang, S. Mubeen, N. V Myung and M. a Deshusses, Recent progress in carbon nanotube-based gas sensors., *Nanotechnology*, 2008, **19**, 332001.

93 N. S. Ramgir, Y. Yang and M. Zacharias, Nanowire-based sensors, *Small*, 2010, **6**, 1705–1722.

94 X. Chen, C. K. Y. Wong, C. a. Yuan and G. Zhang, Nanowire-based gas sensors, *Sensors Actuators, B Chem.*, 2013, **177**, 178–195.

95 B. Ding, M. Wang, J. Yu and G. Sun, Gas sensors based on electrospun nanofibers, *Sensors*, 2009, **9**, 1609–1624.

96 A. B. Kaiser, J. G. Park, B. Kim, S. H. Lee and Y. W. Park, Polypyrrole micro-line: Current-voltage characteristics and comparison with other conducting polymers, *Curr. Appl. Phys.*, 2004, **4**, 497–500.

97 A. N. Aleshin, H. J. Lee, S. H. Jhang, H. S. Kim, K. Akagi and Y. W. Park, Coulomb-blockade transport in quasi-one-dimensional polymer nanofibers, *Phys. Rev. B - Condens. Matter Mater. Phys.*, 2005, **72**, 2–5.

98 A. Pipinys, P and Kiveris, A role of phonon-assisted tunnelling in electrical conductivity of carbon nanotube networks, *Lith. J. Phys. Tech. …*, 2008, **48**, 73–78.

99 Y. Kajikawa, K. Okamura, Y. Inoko and H. Mizuki, Analysis of temperature

dependence of electrical conductivity in degenerate n-type polycrystalline InAsP films in an energy-filtering model with potential fluctuations at grain boundaries, *J. Appl. Phys.*, , DOI:10.1063/1.4770417.

100 U. N. Nandi, S. Sircar, A. Karmakar and S. Giri, Nonlinearity exponent of ac conductivity in disordered systems, *J. Phys. Condens. Matter*, , DOI:10.1088/0953-8984/24/26/265601.

101 Y. Z. Long, M. M. Li, C. Gu, M. Wan, J. L. Duvail, Z. Liu and Z. Fan, Recent advances in synthesis, physical properties and applications of conducting polymer nanotubes and nanofibers, *Prog. Polym. Sci.*, 2011, **36**, 1415–1442.

102 G. F. Yu, W. Pan, M. Yu, W. P. Han, J. C. Zhang, H. Di Zhang and Y. Z. Long, Electrical conduction mechanism of an individual polypyrrole nanowire at low temperatures, *Nanotechnology*, , DOI:10.1088/0957-4484/26/4/045703.

103 G.-F. Yu, M. Yu, W. Pan, W.-P. Han, X. Yan, J.-C. Zhang, H.-D. Zhang and Y.-Z. Long, Electrical transport properties of an isolated CdS microrope composed of twisted nanowires, *Nanoscale Res. Lett.*, 2015, **10**, 21.

104 N. F. Mott and R. W. Gurney, *Electronic Processes in Ionic Crystals.*, Oxford University Press, Oxford, 1950.

105 S. Vaddiraju, M. K. Sunkara, a. H. Chin, C. Z. Ning, G. R. Dholakia and M. Meyyappan, Synthesis of group III antimonide nanowires, *J. Phys. Chem. C*, 2007, **111**, 7339–7347.

106 Rose A, Space-Charge-Limited Currents, *Phys. Rev.*, 1955, **97**, 1538–1544.

107 H. Uslu, E. Altindal, S. Polat, H. Bayrak and E. Bacaksiz, On the mechanism of current-transport in Cu/CdS/SnO2/In-Ga structures, *J. Alloys Compd.*, 2011, **509**, 5555–5561.

108 R. H. Terrill, J. E. Hutchison and R. W. Murray, Solid State Electron-Hopping Transport and Frozen Concentration Gradients in a Mixed Valent Viologen−Tetraethylene Oxide Copolymer, *J. Phys. Chem. B*, 1997, **101**, 1535–1542.

109 J. C. Jernigan and R. W. Murray, Consequences of restricted ion mobility in

electron transport through films of a polymeric osmium-polypyridine complex, *J. Phys. Chem.*, 1987, **91**, 2030–2032.

110 N. Yamazoe, Toward innovations of gas sensor technology, *Sensors Actuators, B Chem.*, 2005, **108**, 2–14.

111 S. T. Navale, A. T. Mane, M. A. Chougule, N. M. Shinde, J. Kim and V. B. Patil, Highly selective and sensitive CdS thin film sensors for detection of NO_2 gas, *RSC Adv.*, 2014, **4**, 44547–44554.

112 H. Chen, Y. Yu, H. L. Xin, K. A. Newton, M. E. Holtz, D. Wang, D. A. Muller, H. D. Abru??a and F. J. Disalvo, Coalescence in the thermal annealing of nanoparticles: An in situ STEM study of the growth mechanisms of ordered Pt-Fe nanoparticles in a KCl matrix, *Chem. Mater.*, 2013, **25**, 1436–1442.

113 K. Chan, B. T. Goh, S. A. Rahman, M. R. Muhamad, C. F. Dee and Z. Aspanut, Annealing effect on the structural and optical properties of embedded Au nanoparticles in silicon suboxide films, *Vacuum*, 2012, **86**, 1367–1372.

114 M. Sinha, R. Mahapatra, B. Mondal, T. Maruyama and R. Ghosh, Ultrafast and Reversible Gas-Sensing Properties of ZnO Nanowire Arrays Grown by Hydrothermal Technique, *J. Phys. Chem. C*, 2016, **120**, 3019–3025.

115 S. Subramoney, Novel Nanocarbons-Structure,Properties and Potential applications., *Adv. Mater.*, 1998, **10**, 1157–1171.

116 R. C. Haddon, Carbon nanotubes, *Acc. Chem. Res.*, 2002, **35**, 997.

117 R. H. Baughman, Carbon Nanotubes — the Route Toward, *Science (80-.).*, 2002, **297**, 787–792.

118 J. Wang, A. N. Kawde and M. Musameh, Carbon-nanotube-modified glassy carbon electrodes for amplified label-free electrochemical detection of DNA hybridization, *Analyst*, 2003, **128**, 912–916.

119 S. Berber, Y.-K. Kwon and D. Tomanek, Unusually high thermal conductivity of carbon nanotubes, *Phys. Rev. Lett.*, 2000, **84**, 4613–4616.

120 Louie S.G, in *Dresselhaus M.S., Dresselhaus G., Avouris P. (eds) Carbon*

Nanotubes. Topics in Applied Physics, vol 80., Springer, Berlin, Heidelberg, 2001.

121 R. . Ding, G. Q. Lu, Z. . Yan and M. . Wilson, Recent advances in the preparation and utilation of carbon nanotubes for hydrogen storage., *J. Nanosci. Nanotechnol.*, 2001, **1**, 7–29.

122 P. C. Collins, M. S. Arnold and P. Avouris, Engineering carbon nanotubes and nanotube circuits using electrical breakdown, *Science (80-.).*, 2001, **292**, 706–709.

123 Z. K. Tang, L. Zhang, N. Wang, X. X. Zhang, G. H. Wen, G. D. Li, J. N. Wang, C. T. Chan and P. Sheng, Supercunductivity in 4 Angstrom Single-Walled Carbon Nanotubes, *Science (80-.).*, 2001, **292**, 2462–2465.

124 E. W. Wong, P. E. Sheehan, C. M. Lieber, B. Q. Iqbal, R. Barisci, P. M. Spinks, Wallace, Mazzoldi, De Rossi D, Rinzler, Jaschinski, Roth and Kertesz, Nanobeam Mechanics: Elasticity, Strength, and Toughness of Nanorods and Nanotubes, *Science (80-.).*, 1997, **277**, 1971–1975.

125 M. J. Sanderson, I. Smith, I. Parker and M. D. Bootman, Fluorescence microscopy, *Cold Spring Harb. Protoc.*, 2014, **2014**, 1042–1065.

126 Q. Zhong, D. Inniss, K. Kjoller and V. B. Elings, Fractured polymer/silica fiber surface studied by tapping mode atomic force microscopy, *Surf. Sci.*, 1993, **290**, L688–L692.

127 G. Binnig and C. F. Quate, Atomic Force Microscope, *Phys. Rev. Lett.*, 1986, **56**, 930–933.

128 M. Flowers, How an Atomic force microscope works.

129 L.Chen, Atomic force microscope (Veeco-3100) user instruction.

130 D. B. Williams and C. B. Carter, *Transmission Electron Microscopy. A textbook for material science*, Springer, 2009.

131 M. Reza, E. Kontturi, A.-S. Jääskeläinen, T. Vuorinen and J. Ruokolainen, *BioResources*, 2015, 10, 1–32.

132 J. Soares, *Introduction to Optical Characterization of Materials.In Practical Materials Characterization*, Springer Science+Business Media, New York, 2014.

133 J. Zhang, B. Li, Q. Wang, X. Wei, W. Feng, Y. Chen, P. Huang and Z. Wang, Application of Fourier transform infrared spectroscopy with chemometrics on postmortem interval estimation based on pericardial fluids, *Sci. Rep.*, 2017, **7**, 1–8.

134 P. Singh, H. C. Andola, M. S. M. Rawat, G. J. N. Pant and V. K. Purohit, *Res. J. Med. Plants*, 2011, 5, 127–135.

135 M. N. Dole, P. A. Patel, S. D. Sawant and P. S. Shedpure, Advance applications of fourier transform infrared spectroscopy, *Int. J. Pharm. Sci. Rev. Res.*, 2011, **7**, 159–166.

136 C. S. S. R. Kumar, *Raman spectroscopy for nanomaterials characterisation.*, Springer Science+Business Media, 2012.

137 G. S. Doerk, C. Carraro and R. Maboudian, in *Raman spectroscopy for nanomaterials characterization*, Springer,Berlin,Heidelberg, 2012, vol. 9783642206, pp. 1–645.

138 S. Wachsmann-Hogiu, T. Weeks and T. Huser, Chemical analysis in vivo and in vitro by Raman spectroscopy-from single cells to humans, *Curr. Opin. Biotechnol.*, 2009, **20**, 63–73.

139 A. Folick, W. Min and M. C. Wang, Label-free imaging of lipid dynamics using Coherent Anti-stokes Raman Scattering (CARS) and Stimulated Raman Scattering (SRS) microscopy, *Curr. Opin. Genet. Dev.*, 2011, **21**, 585–590.

140 S. A. Vanalakar, V. L. Patil, P. S. Patil and J. H. Kim, Rapid synthesis of CdS nanowire mesh *via* a simplistic wet chemical route and its NO_2 gas sensing properties, *New J. Chem.*, 2018, **42**, 4232–4239.

141 D. J. Sirbuly, M. Law, H. Yan and P. Yang, Semiconductor nanowires for subwavelength photonics integration, *J. Phys. Chem. B*, 2005, **109**, 15190–15213.

142 C. Rui, D. Li, Q. Xiong and H. Sun, *Optical and Excitonic Properties of Crystalline*

ZnS Nanowires. In; UV-VIS and Photoluminescence Spectroscopy for Nanomaterials Characterization, Springer, 2013.

143 R. Sharma, D. P. Bisen, U. Shukla and B. G. Sharma, X-ray diffraction: a powerful method of characterizing nanomaterials, *Recent Res. Sci. Technol.*, 2012, **4**, 77–79.

144 A.Polini and F.Yang, *Nanofiber composites for biomedical applications.*, 2017.

145 K.Yates and R. H. West, Small area x-ray photoelectron spectroscopy, *Surf. Interface Anal.*, 1983, **5**, 217–221.

146 M. Franinović, X-ray Photoelectron Spectroscopy.

147 J. F. Moulder, W. F. Stickle, P. E. Sobol and K. D. Bomben, *Handbook of X-ray photoelectron spectroscopy: a reference book of standard spectra for identification and interpretation of XPS data*, 1992.

148 J. . Vickerman and I. Gilmore, *Surface analysis: The principle techniques*, John Wiley& Sons,Ltd, Chichester,UK., 2nd edn., 2009.

149 P. Wang, Y. Fu, B. Yu, Y. Zhao, L. Xing and X. Xue, Realizing room-temperature self-powered ethanol sensing of ZnO nanowire arrays by combining their piezoelectric, photoelectric and gas sensing characteristics, *J. Mater. Chem. A*, 2015, **3**, 3529–3535.

150 L. Hou, C. Zhang, L. Li, C. Du, X. Li, X.-F. Kang and W. Chen, CO gas sensors based on p-type CuO nanotubes and CuO nanocubes: Morphology and surface structure effects on the sensing performance, *Talanta*, 2018, **188**, 41–49.

151 L. Zhou, F. Shen, X. Tian, D. Wang, T. Zhang and W. Chen, Stable Cu2O nanocrystals grown on functionalized graphene sheets and room temperature H2S gas sensing with ultrahigh sensitivity, *Nanoscale*, 2013, **5**, 1564.

152 P. Sun, X. Zhou, C. Wang, B. Wang, X. Xu and G. Lu, One-step synthesis and gas sensing properties of hierarchical Cd-doped SnO2 nanostructures, *Sensors Actuators B Chem.*, 2014, **190**, 32–39.

153 Z. Zou, Y. Qiu, C. Xie, J. Xu, Y. Luo, C. Wang and H. Yan, CdS/TiO2

nanocomposite film and its enhanced photoelectric responses to dry air and formaldehyde induced by visible light at room temperature, *J. Alloys Compd.*, 2015, **645**, 17–23.

154 K. Xu, N. Li, D. Zeng, S. Tian, S. Zhang, D. Hu and C. Xie, Interface Bonds Determined Gas-Sensing of SnO2−SnS2 Hybrids.pdf, *ACS Appl. Mater. Interfaces*, 2015, **7**, 11359–11368.

155 H. R. Kim, A. Haensch, I. D. Kim, N. Barsan, U. Weimar and J. H. Lee, The role of NiO doping in reducing the impact of humidity on the performance of SnO2-based gas sensors: Synthesis strategies, and phenomenological and spectroscopic studies, *Adv. Funct. Mater.*, 2011, **21**, 4456–4463.

156 V. E. Bochenkov and G. B. Sergeev, *Sensitivity , Selectivity , and Stability of Gas-Sensitive Metal-Oxide Nanostructures*, 2010, vol. 3.

157 N. Barsan, D. Koziej and U. Weimar, Metal oxide-based gas sensor research: How to?, *Sensors Actuators, B Chem.*, 2007, **121**, 18–35.

158 A. Gaiardo, B. Fabbri, V. Guidi, P. Bellutti, A. Giberti, S. Gherardi, L. Vanzetti, C. Malagù and G. Zonta, Metal sulfides as sensing materials for chemoresistive gas sensors, *Sensors (Switzerland)*, , DOI:10.3390/s16030296.

159 Y. Xiong, W. Xu, D. Ding, W. Lu, L. Zhu, Z. Zhu, Y. Wang and Q. Xue, Ultra-sensitive NH3sensor based on flower-shaped SnS2nanostructures with sub-ppm detection ability, *J. Hazard. Mater.*, 2018, **341**, 159–167.

160 Z. Qin, K. Xu, H. Yue, H. Wang, J. Zhang, C. Ouyang, C. Xie and D. Zeng, Enhanced room-temperature NH3gas sensing by 2D SnS2with sulfur vacancies synthesized by chemical exfoliation, *Sensors Actuators, B Chem.*, 2018, **262**, 771–779.

161 M. R. Cássia-Santos, V. C. Sousa, M. M. Oliveira, F. R. Sensato, W. K. Bacelar, J. W. Gomes, E. Longo, E. R. Leite and J. A. Varela, Recent research developments in SnO2-based varistors, *Mater. Chem. Phys.*, 2005, **90**, 1–9.

162 R. N. Nurdillayeva, A. B. Oshido, T. A. Bamford, O. El-Zubir, A. Houlton, J. Hedley, A. R. Pike and B. R. Horrocks, Inkjet printing and electrical characterisation of DNA-templated cadmium sulphide nanowires,

Nanotechnology, , DOI:10.1088/1361-6528/aaa92f.

163 D. Liqin, T. Hollis, S. Fishwick, B. a. Connolly, N. G. Wright, B. R. Horrocks and A. Houlton, Synthesis, manipulation and conductivity of supramolecular polymer nanowires, *Chem. - A Eur. J.*, 2007, **13**, 822–828.

164 H. Yan, S. H. Park, G. Finkelstein, J. H. Reif and T. H. LaBean, DNA-templated self-assembly of protein arrays and highly conductive nanowires., *Science*, 2003, **301**, 1882–1884.

165 H. A. Becerril, R. M. Stoltenberg, D. R. Wheeler, R. C. Davis, J. N. Harb and A. T. Woolley, DNA-templated three-branched nanostructures for nanoelectronic devices, *J. Am. Chem. Soc.*, 2005, **127**, 2828–2829.

166 G. A. Burley, J. Gierlich, M. R. Mofid, H. Nir, S. Tal, Y. Eichen and T. Carell, Directed DNA metallization, *J. Am. Chem. Soc.*, 2006, **128**, 1398–1399.

167 Q. Gu and D. T. Haynie, Palladium nanoparticle-controlled growth of magnetic cobalt nanowires on DNA templates, *Mater. Lett.*, 2008, **62**, 3047–3050.

168 J. Su, F. Gao and L. Hou, DNA-templated assemblage of ZnS nanoparticle wires, *Mater. Lett.*, 2013, **92**, 206–209.

169 Y. Ma, J. Zhang, G. Zhang and H. He, Polyaniline nanowires on Si surfaces fabricated with DNA templates, *J. Am. Chem. Soc.*, 2004, **126**, 7097–7101.

170 J. Hannant, J. H. Hedley, J. Pate, A. Walli, S. A. Farha Al-Said, M. A. Galindo, B. A. Connolly, B. R. Horrocks, A. Houlton and A. R. Pike, Modification of DNA-templated conductive polymer nanowires via click chemistry., *Chem. Commun. (Camb).*, 2010, **46**, 5870–5872.

171 L. Dong, T. Hollis, S. Fishwick, B. a Connolly, N. G. Wright, B. R. Horrocks and A. Houlton, Synthesis, manipulation and conductivity of supramolecular polymer nanowires., *Chemistry*, 2007, **13**, 822–8.

172 S. M. D. Watson, A. R. Pike, J. Pate, A. Houlton and B. R. Horrocks, DNA-templated nanowires: morphology and electrical conductivity., *Nanoscale*, 2014, **6**, 4027–37.

173 L. Berti, A. Alessandrini and P. Facci, DNA-templated photoinduced silver deposition, *J. Am. Chem. Soc.*, 2005, **127**, 11216–11217.

174 H. Nakao, H. Hayashi, T. Yoshino, S. Sugiyama, K. Otobe and T. Ohtani, Development of Novel Polymer-Coated Substrates for Straightening and Fixing DNA, *Nano Lett.*, 2002, **2**, 475–479.

175 L. Cai, H. Tabata and T. Kawai, Probing electrical properties of oriented DNA by conducting atomic force microscopy, *Nanotechnology*, 2001, **12**, 211–216.

176 R. Maity and K. K. Chattopadhyay, Synthesis and optical characterization of CdS nanowires by chemical process, *J. Nanoparticles Res.*, 2006, **8**, 125–130.

177 S. R. Bigham and J. L. Coffer, Deactivation of Q-CdS photoluminescence through polynucleotide surface binding, *J Phys Chem*, 1992, **96**, 10581–10584.

178 C. H. Kuo, J. M. Wu and S. J. Lin, Room temperature-synthesized vertically aligned InSb nanowires: Electrical transport and field emission characteristics, *Nanoscale Res. Lett.*, 2013, **8**, 1–8.

179 S. Zhang, B. Yin, H. Jiang, F. Qu, A. Umar and X. Wu, Hybrid ZnO/ZnS nanoforests as the electrode materials for high performance supercapacitor application, *Dalt. Trans.*, 2015, **44**, 2409–2415.

180 A. Bakhsh, I. H. Gul, A. Maqsood, C. H. Chan, S. H. Wu and Y. C. Chang, Tailoring the structural and optical properties of CdZnS thin films by vacuum annealing, *Chalcogenide Lett.*, 2016, **13**, 443–450.

181 Y. Tang, X. Liu, C. Ma, M. Zhou, P. Huo, L. Yu, J. Pan, W. Shi and Y. Yan, Enhanced photocatalytic degradation of tetracycline antibiotics by reduced graphene oxide–CdS/ZnS heterostructure photocatalysts, *New J. Chem.*, 2015, **39**, 5150–5160.

182 O. Brafman and S. S. Mitra, Raman effect in wurtzite- and zinc-blende-type ZnS single crystals, *Phys. Rev.*, 1968, **171**, 931–934.

183 S. H. Mir, A. Nagahara, T. Thundat, P. Mokarian-tabari, H. Furukawa and A. Khosla, Review — Organic-Inorganic Hybrid Functional Materials : An Integrated Platform for Applied Technologies, *J. Electrochem. Soc.*, ,

DOI:10.1149/2.0191808jes.

184 C. Sanchez, B. Lebeau, F. Chaput and J.-P. Boilot, Optical Properties of Functional Hybrid Organic–Inorganic Nanocomposites, *Adv. Mater.*, 2003, **15**, 1969–1994.

185 R. J. Gehr and R. W. Boyd, Optical properties of nanostructured optical materials, *Chem. Mater.*, 1996, **8**, 1807–1819.

186 R. P. PAWAR, Structural and Optical Properties of Chemically Synthesized ZnS Nanoparticals, *Orient. J. Chem.*, 2013, **29**, 1139–1142.

187 G. L. Eichhorn, P. Clark and E. D. Becker, Interactions of Metal Ions with Polynucleotides and Related Compounds. VII. The Binding of Copper(II) to Nucleosides, Nucleotides, and Deoxyribonucleic Acids, *Biochemistry*, 1966, **5**, 245–253.

188 H. Arakawa, J. F. Neault and H. A. Tajmir-Riahi, Silver(I) complexes with DNA and RNA studied by fourier transform infrared spectroscopy and capillary electrophoresis, *Biophys. J.*, 2001, **81**, 1580–1587.

189 R. Hassanien, S. a F. Al-Said, L. Siller, R. Little, N. G. Wright, A. Houlton and B. R. Horrocks, Smooth and conductive DNA-templated Cu_2O nanowires: growth morphology, spectroscopic and electrical characterization., *Nanotechnology*, 2012, **23**, 75601.

190 M. Banyay, M. Sarkar and A. Graslund, A library of IR bands of nucleic acids in solution, *Biophys. Chem.*, 2003, **104**, 477–488.

191 B. Lippert, Multiplicity of metal ion binding patterns to nucleobases, *Coord. Chem. Rev.*, 2000, **200**–**202**, 487–516.

192 L. G. Marzilli and T. J. Kistenmacher, Stereoselectivity in the Binding of Transition-Metal Chelate Complexes to Nucleic Acid Constituents: Bonding and Nonbonding Effects, *Acc. Chem. Res.*, 1977, **10**, 146–152.

193 D. K. Jangir, S. Kundu and R. Mehrotra, Role of Minor Groove Width and Hydration Pattern on Amsacrine Interaction with DNA, *PLoS One*, 2013, **8**, 1–9.

194 G. Tyagi, S. Pradhan, T. Srivastava and R. Mehrotra, Nucleic acid binding properties of allicin: Spectroscopic analysis and estimation of anti-tumor potential, *Biochim. Biophys. Acta - Gen. Subj.*, 2014, **1840**, 350–356.

195 S. Agarwal, D. K. Jangir, P. Singh and R. Mehrotra, Spectroscopic analysis of the interaction of lomustine with calf thymus DNA, *J. Photochem. Photobiol. B Biol.*, 2014, **130**, 281–286.

196 E. Korin, N. Froumin and S. Cohen, *ACS Biomater. Sci. Eng.*, 2017, 3, 882–889.

197 M. Stoev and A. Katerski, XPS and XRD study of photoconductive CdS films obtained by a chemical bath deposition process, *J. Mater. Chem.*, 1996, **6**, 377.

198 V. G. Bhide, S. Salkalachen, A. C. Rastog, C. N. R. Rao and M. S. Hegde, Depth profile composition studies of thin film CdS:Cu 2 S solar cells using XPS and AES, *J. Phys. D. Appl. Phys.*, 1981, **14**, 1647–1656.

199 S. W. Gaarenstroom and N. Winograd, Initial and final state effects in the ESCA spectra of cadmium and silver oxides, *J. Chem. Phys.*, 1977, **67**, 3500–3506.

200 A. Veamatahau, B. Jiang, T. Seifert, S. Makuta, K. Latham, M. Kanehara, T. Teranishi and Y. Tachibana, Origin of surface trap states in CdS quantum dots: Relationship between size dependent photoluminescence and sulfur vacancy trap states, *Phys. Chem. Chem. Phys.*, 2015, **17**, 2850–2858.

201 M. N. Ghazzal, R. Wojcieszak, G. Raj and E. M. Gaigneaux, Study of mesoporous CdS-quantum-dot-sensitized TiO_2 films by using X-ray photoelectron spectroscopy and AFM, *Beilstein J. Nanotechnol.*, 2014, **5**, 68–76.

202 B. D. Barreca, A. Gasparotto, C. Maragno, E. Tondello and C. Sada, CVD of Nanophasic (Zn , Cd) S Thin Films : From Multi-Layers to Solid Solutions, *Chem. Vap. Depos.*, 2004, **10**, 229–236.

203 M. C. López, J. P. Espinós, D. Leinen, F. Martín, S. P. Centeno, R. Romero and J. R. Ramos-Barrado, Growth and characterization of the ZnO/ZnS bilayer obtained by chemical spray pyrolysis, *Appl. Surf. Sci.*, 2008, **255**, 2118–2124.

204 J. Wang, Y. F. Lim and G. Wei Ho, Carbon-ensemble-manipulated ZnS

heterostructures for enhanced photocatalytic H2evolution, *Nanoscale*, 2014, **6**, 9673–9680.

205 B. Vidhya, S. Velumani, J. Arenas-Alatorre, V. Sanchez Resendiz, J. A. Chavez-Carvayar, R. Asomoza and Y. Kudriavtsev, in *Program and Abstract Book - 2010 7th International Conference on Electrical Engineering, Computing Science and Automatic Control, CCE 2010*, 2010, pp. 569–573.

206 P. Kalakonda, Synthesis of silver nanowires for highly conductive and transparent films, *Nanomater. Nanotechnol.*, 2016, **6**, 1–6.

207 L. . MacHattie and C. . Thomas, DNA from Bacteriophage Lambda :Molecular Length and Conformation, *Science (80-.).*, 1964, **144**, 1142–1144.

208 U. N. Nandi, S. Sircar, A. Karmakar and S. Giri, Nonlinearity exponent of ac conductivity in disordered systems, *J. Phys. Condens. Matter*, , DOI:10.1088/0953-8984/24/26/265601.

209 E. Braun, Y. Eichen, U. Sivan and G. Ben-Yoseph, DNA-templated assembly and electrode attachment of a conducting silver wire., *Nature*, 1998, **391**, 775–8.

210 J. Appenzeller, M. Radosavljević, J. Knoch and P. Avouris, Tunneling Versus Thermionic Emission in One-Dimensional Semiconductors, *Phys. Rev. Lett.*, 2004, **92**, 4.

211 E. L. Gui, L.-J. Li, K. Zhang, Y. Xu, X. Dong, X. Ho, P. S. Lee, J. Kasim, Z. X. Shen, J. A. Rogers and Mhaisalkar, DNA Sensing by Field-Effect Transistors Based on Networks of Carbon Nanotubes, *J. Am. Chem. Soc.*, 2007, **129**, 14427–14432.

212 D. Zhang, C. Li, X. Liu, S. Han, T. Tang and C. Zhou, Doping dependent NH3 sensing of indium oxide nanowires, *Appl. Phys. Lett.*, 2003, **83**, 1845–1847.

213 R. S. Chen, T. H. Yang, H. Y. Chen, L. C. Chen, K. H. Chen, Y. J. Yang, C. H. Su and C. R. Lin, High-gain photoconductivity in semiconducting InN nanowires, *Appl. Phys. Lett.*, 2009, **95**, 2007–2010.

214 R. Calarco and M. Marso, GaN and InN nanowires grown by MBE: A

comparison, *Appl. Phys. A Mater. Sci. Process.*, 2007, **87**, 499–503.

215 C. Y. Chang, G. C. Chi, W. M. Wang, L. I. C. Chen, K. H. Chen, F. Ren and S. J. Pearton, Electrical transport properties of single GaN and InN nanowires, *J. Electron. Mater.*, 2006, **35**, 738–743.

216 A. Chaudhry and M. S. Islam, Examining the Anomalous Electrical Characteristics Observed in InN Nanowires, *J. Nanosci. Nanotechnol.*, 2008, **8**, 222–227.

217 L. Zhu, Y. Wang, D. Zhang, C. Li, D. Sun, S. Wen, Y. Chen and S. Ruan, Gas Sensors Based on Metal Sulfide $Zn_{1-x}Cd_xS$ Nanowires with Excellent Performance, *ACS Appl. Mater. Interfaces*, 2015, **7**, 20793–20800.

218 Y. Li, J. Xu, J. Chao, D. Chen, S. Ouyang, J. Ye and G. Shen, High-aspect-ratio single-crystalline porous In2O3 nanobelts with enhanced gas sensing properties, *J. Mater. Chem.*, 2011, **21**, 12852.

219 Q. Wan and T. H. Wang, Single-crystalline Sb-doped SnO2 nanowires: Synthesis and gas sensor application, *Chem. Commun.*, 2005, **1**, 3841–3843.

220 I. D. Kim, A. Rothschild, B. H. Lee, D. Y. Kim, S. M. Jo and H. L. Tuller, Ultrasensitive chemiresistors based on electrospun TiO 2 nanofibers, *Nano Lett.*, 2006, **6**, 2009–2013.

221 D. Li, J. Zhang and Q. Xiong, Surface depletion induced quantum confinement in CdS nanobelts, *ACS Nano*, 2012, **6**, 5283–5290.

222 A. A. Abokifa, K. Haddad, J. Fortner, C. S. Lo and P. Biswas, Sensing mechanism of ethanol and acetone at room temperature by SnO_2 nano-columns synthesized by aerosol routes: theoretical calculations compared to experimental results, *J. Mater. Chem. A*, 2018, **6**, 2053–2066.

223 D. L. Lide, *RC Handbook of chemistry and physics*, CRC Press, New York, 2007.

224 Z. Bai, C. Xie, M. Hu, S. Zhang and D. Zeng, Effect of humidity on the gas sensing property of the tetrapod-shaped ZnO nanopowder sensor, *Mater. Sci. Eng. B Solid-State Mater. Adv. Technol.*, 2008, **149**, 12–17.

225 W. Geng, S. Ge, X. He, S. Zhang, J. Gu, X. Lai, H. Wang and Q. Zhang, Volatile Organic Compound Gas-Sensing Properties of Bimodal Porous α-Fe 2 O 3 with Ultrahigh Sensitivity and Fast Response, *ACS Appl. Mater. Interfaces*, 2018, acsami.8b02435.

226 C. Wang, L. Yin, L. Zhang, D. Xiang and R. Gao, Metal oxide gas sensors: Sensitivity and influencing factors, *Sensors*, 2010, **10**, 2088–2106.

227 W. Li, S. Ma, Y. Li, G. Yang, Y. Mao, J. Luo, D. Gengzang, X. Xu and S. Yan, Enhanced ethanol sensing performance of hollow ZnO-SnO2core-shell nanofibers, *Sensors Actuators, B Chem.*, 2015, **211**, 392–402.

228 A. Umar and Y.-B. Hahn, Metal Oxide nanostructructures and their applications, 2010, 31–52.

229 F. H. Chapple, The Temperature Dependence of □ G ⦵ and the Equilibrium Constant , K eq ; Is There a Paradox ?, *J. Chem. Educ.*, 1998, **75**, 97301.

230 S. Z. Hassan and M. Vinjamur, Analysis of sensitivity of equilibrium constant to reaction conditions for esterification of fatty acids with alcohols, *Ind. Eng. Chem. Res.*, 2013, **52**, 1205–1215.

231 N. Singh, C. Yan, P. S. Lee and E. Comini, Sensing properties of different classes of gases based on the nanowire-electrode junction barrier modulation, *Nanoscale*, 2011, **3**, 1760.

232 S. A. Hakim, Y. Liu, G. S. Zakharova and W. Chen, Synthesis of vanadium pentoxide nanoneedles by physical vapour deposition and their highly sensitive behavior towards acetone at room temperature, *RSC Adv.*, 2015, **5**, 23489–23497.

233 S. . Yan, S. . Ma, W. . Li, X. . Xu, L.Cheng, H. . Song and X. . Liang, Synthesis of SnO2–ZnO heterostructured nanofibers for enhanced ethanol gas-sensing performance., *Sensors Actuators B Chem.*, 2015, **221**, 88–95.

234 A. Gurlo, Interplay between O2 and SnO2: Oxygen ionosorption and spectroscopic evidence for adsorbed oxygen, *ChemPhysChem*, 2006, **7**, 2041–2052.

235 M. Chitra, K. Uthayarani, N. Rajasekaran, N. Neelakandeswari, E. K. Girija, D. P. Padiyan and G. Mangamma, Enhanced ethanol gas sensing performance of zinc-tin-vanadium oxide nanocomposites at room temperature, *RSC Adv.*, 2016, **6**, 111526–111538.

236 J. C. Belmonte, J. Manzano, J. Arbiol, A. Cirera, J. Puigcorbé, A. Vilà, N. Sabaté, I. Gràcia, C. Cané and J. R. Morante, Micromachined twin gas sensor for CO and O2quantification based on catalytically modified nano-SnO2, *Sensors Actuators, B Chem.*, 2006, **114**, 881–892.

237 Y. Wang, X. Jiang and Y. Xia, A Solution-Phase, Precursor Route to Polycrystalline SnO2 Nanowires That Can Be Used for Gas Sensing under Ambient Conditions, *J. Am. Chem. Soc.*, 2003, **125**, 16176–16177.

238 Q. Zhao, Y. Gao, X. Bai, C. Wu and Y. Xie, Facile Synthesis of SnO 2 Hollow Nanospheres and Applications in Gas Sensors and Electrocatalysts, *Eur. J. Inorg. Chem.*, 2006, **2006**, 1643–1648.

239 Z. Wen and L. Tian-mo, Gas-sensing properties of SnO2-TiO2-based sensor for volatile organic compound gas and its sensing mechanism, *Phys. B Condens. Matter*, 2010, **405**, 1345–1348.

240 R. A. Zangmeister, J. E. Maslar, A. Opdahl and M. J. Tarlov, Adsorption behavior of DNA-wrapped carbon nanotubes on self-assembled monolayer surfaces, *Langmuir*, 2007, **23**, 6252–6256.

241 P. Qi, O. Vermesh, M. Grecu, A. Javey, Q. Wang, H. Dai, S. Peng and K. J. Cho, Toward large arrays of multiplex functionalized carbon nanotube sensors for highly sensitive and selective molecular detection, *Nano Lett.*, 2003, **3**, 347–351.

242 S. Kundu and H. Liang, Microwave synthesis of electrically conductive gold nanowires on DNA scaffolds, *Langmuir*, 2008, **24**, 9668–9674.

243 F. A. Aldaye, A. L. Palmer and H. F. Sleiman, Assembling materials with DNA as the guide, *Science (80-.).*, 2008, **321**, 1795–1799.

244 X. Zhang, J. Liu, S. Li, X. Tan, J. Zhang, M. Yu and M. Zhao, DNA assembled single-walled carbon nanotube nanocomposites for high efficiency dye-sensitized solar cells, *J. Mater. Chem. A*, 2013, **1**, 11070.

245 C. Staii, A. T. Johnson, M. Chen and A. Gelperin, DNA-decorated carbon nanotubes for chemical sensing, *Nano Lett.*, 2005, **5**, 1774–1778.

246 X. Zhao and J. K. Johnson, Simulation of adsorption of DNA on carbon nanotubes, *J. Am. Chem. Soc.*, 2007, **129**, 10438–10445.

247 J. H. Kim, M. Kataoka, D. Shimamoto, H. Muramatsu, Y. C. Jung, T. Tojo, T. Hayashi, Y. A. Kim, M. Endo, M. Terrones and M. S. Dresselhaus, Defect-enhanced dispersion of carbon nanotubes in DNA solutions, *ChemPhysChem*, 2009, **10**, 2414–2417.

248 S. Osswald, E. Flahaut, H. Ye and Y. Gogotsi, Elimination of D-band in Raman spectra of double-wall carbon nanotubes by oxidation, *Chem. Phys. Lett.*, 2005, **402**, 422–427.

249 M. S. Strano, S. K. Doorn, E. H. Haroz, C. Kittrell, R. H. Hauge and R. E. Smalley, Assignment of (n, m) Raman and optical features of metallic single-walled carbon nanotubes, *Nano Lett.*, 2003, **3**, 1091–1096.

250 A. M. Rao, E. Richter, S. Bandow, B. Chase, P. C. Eklund, K. A. Williams, S. Fang, K. R. Subbaswamy, M. Menon, A. Thess, R. E. Smalley, G. Dresselhaus and M. S. Dresselhaus, Carbon Nanotubes Diameter-Selective Raman Scattering from Vibrational Modes in Carbon Nanotubes, *Science (80-.).*, 2012, **187**, 187.

251 S. G. Chou, H. B. Ribeiro, E. B. Barros, A. P. Santos, D. Nezich, G. G. Samsonidze, C. Fantini, M. A. Pimenta, A. Jorio, F. P. Filho, M. S. Dresselhaus, G. Dresselhaus, R. Saito, M. Zheng, G. B. Onoa, E. D. Semke, A. K. Swan, M. S. Ünlü and B. B. Goldberg, Optical characterization of DNA-wrapped carbon nanotube hybrids, *Chem. Phys. Lett.*, 2004, **397**, 296–301.

252 J.-L. Sauvajol, E. Anglaret, S. Rols and L. Alvarez, Phonons in single wall carbon nanotube bundles, *Carbon N. Y.*, 2002, **40**, 1697–1714.

253 K. R. Moonoosawmy and P. Kruse, Ambiguity in the Characterization of Chemically Modified Single-Walled Carbon Nanotubes : A Raman and Ultraviolet - Visible - Near-Infrared Study, *Science (80-.).*, 2009, **113**, 5133–5140.

254 F. Draux, P. Jeannesson, A. Beljebbar, A. Tfayli, N. Fourre, M. Manfait, J. Sulé-

Suso and G. D. Sockalingum, Raman spectral imaging of single living cancer cells: A preliminary study, *Analyst*, 2009, **134**, 542–548.

255 M. Shoda, S. Bandow, Y. Maruyama and S. Iijima, Probing Interaction between ssDNA and Carbon Nanotubes by Raman Scattering and Electron Microscopy, *J. Phys. Chem. C*, 2009, **113**, 6033–6036.

256 D. B. Mawhinney, V. Naumenko, A. Kuznetsova, J. T. Yates, J. Liu and R. E. Smalley, Surface defect site density on single walled carbon nanotubes by titration, *Chem. Phys. Lett.*, 2000, **324**, 213–216.

257 J. L. Bahr and J. M. Tour, Covalent chemistry of single-wall carbon nanotubes, *J. Mater. Chem.*, 2002, **12**, 1952–1958.

258 A. Kuznetsova, D. B. Mawhinney, V. Naumenko, J. T. Yates, J. Liu and R. E. Smalley, Enhancement of adsorption inside of single-walled nanotubes: Opening the entry ports, *Chem. Phys. Lett.*, 2000, **321**, 292–296.

259 R. A. Jishi, L. Venkataraman, M. S. Dresselhaus and G. Dresselhaus, Symmetry properties of chiral carbon nanotubes, *Phys. Rev. B*, 1995, **51**, 11176.

260 O. P. Matyshevska, A. Y. Karlash, Y. V. Shtogun, A. Benilov, Y. Kirgizov, K. O. Gorchinskyy, E. V. Buzaneva, Y. I. Prylutskyy and P. Scharff, Self-organizing DNA/carbon nanotube molecular films, *Mater. Sci. Eng. C*, 2001, **15**, 249–252.

261 X. Guo, A. A. Gorodetsky, J. Hone, K. Jacqueline and C. Nuckolls, Conductivity of a single DNA duplex bridging a carbon nanotube gap, *Nat Nanotechnol.*, 2009, **3**, 163–167.

262 M. Guo, J. Chen, L. Nie and S. Yao, Electrostatic assembly of calf thymus DNA on multi-walled carbon nanotube modified gold electrode and its interaction with chlorpromazine hydrochloride, *Electrochim. Acta*, 2004, **49**, 2637–2643.

263 S. Roy, H. Vedala, A. D. Roy, D. Kim, M. Doud, K. Mathee, H. Shin, N. Shimamoto, V. Prasad and W. Choi, Direct Electrical Measurements on Single-Molecule Genomic DNA Using Single-Walled Carbon Nanotubes, *Nano Lett.*, 2008, **8**, 26–30.

264 Z. Guo, P. J. Sadler and S. C. Tsang, Immobilization and visualization of DNA

and proteins on carbon nanotubes, *Adv. Mater.*, 1998, **10**, 701–703.

265 M.-F. Yu, M. Dyer, J. Chen, D. Qian, W. Liu and R. Ruoff, Locked twist in multiwalled carbon-nanotube ribbons, *Phys. Rev. B*, 2001, **64**, 241403.

266 F. Tournus, S. Latil, M. I. Heggie and J.-C. Charlier, Stacking Interaction Between Carbon Nanotubes and Organic Molecules, *Phys. Rev. B*, 2005, **72**, 75431.

267 F. Seela, A. M. Jawalekar and I. M??nster, Replacement of canonical DNA nucleobases by benzotriazole and 1,2,3-triazolo[4,5-d]pyrimidine: Synthesis, fluorescence, and ambiguous base pairing, *Helv. Chim. Acta*, 2005, **88**, 751–765.

268 R. J. Chen, N. R. Franklin, J. Kong, J. Cao, T. W. Tombler, Y. Zhang and H. Dai, Molecular photodesorption from single-walled carbon nanotubes, *Appl. Phys. Lett.*, 2001, **79**, 2258–2260.

269 J. Li, Y. Lu, Q. Ye, M. Cinke, J. Han and M. Meyyappan, Carbon nanotube sensors for gas and organic vapor detection, *Nano Lett.*, 2003, **3**, 929–933.

270 J.-F. Feller, N. Gatt, B. Kumar and M. Castro, Selectivity of Chemoresistive Sensors Made of Chemically Functionalized Carbon Nanotube Random Networks for Volatile Organic Compounds (VOC), *Chemosensors*, 2014, **2**, 26–40.

271 M. P. Landry, L. Vukovic, S. Kruss, G. Bisker, A. M. Landry, S. Islam, R. Jain, K. Schulten and Strano, Comparative Dynamics and Sequence Dependence of DNA and RNA Binding to Single Walled Carbon Nanotubes., *J Phys Chem C Nanomater Interfaces*, 2015, **119**, 10048–10058.

272 Y. T. Lin, R. Singh, S. W. Kuo and F. H. Ko, Bio-inspired supramolecular chemistry provides highly concentrated dispersions of carbon nanotubes in polythiophene, *Materials (Basel).*, , DOI:10.3390/ma9060438.

273 C. Dwyer, M. Guthold, M. Falvo, S. Washburn, R. Superfine and D. Erie, DNA-functionalized single-walled carbon nanotubes, *Nanotechnology*, 2002, **13**, 601–604.

274 H. Fu, S. Xu and Y. Li, Nanohelices from planar polymer self-assembled in carbon nanotubes, *Sci. Rep.*, 2016, **6**, 1–9.

275 T. Fujigaya and N. Nakashima, Non-covalent polymer wrapping of carbon nanotubes and the role of wrapped polymers as functional dispersants, *Sci. Technol. Adv. Mater.*, , DOI:10.1088/1468-6996/16/2/024802.

276 M. E. Hughes, E. Brandin and J. A. Golovchenko, Optical absorption of DNA-carbon nanotube structures, *Nano Lett.*, 2007, **7**, 1191–1194.

277 F. Wang and T. M. Swager, Diverse chemiresistors based upon covalently modified multiwalled carbon nanotubes, *J. Am. Chem. Soc.*, 2011, **133**, 11181–11193.

278 E. Frontera, P. C. Cavallo, R. Olejnik, D. F. Acevedo, P. Slobodian, C. A. Barbero and P. Saha, Tuning the Molecular Sensitivity of Conductive Polymer Resistive Sensors by Chemical Functionalization, *Key Eng. Mater.*, 2014, **605**, 597–600.

279 M. S. Dionisio and R. M. Goncalves, The enthalpy and entropy of cavity formation in liquids and Corresponding States Principle, *Can. J. Chem.*, 1990, **68**, 1937–1949.

280 M. L. Klyueva, K. P. Mischenko and M. K. Fedorov, Vapour pressure of methanol at 5 t0 50 oC, *Zh. Prikl. Khim.*, 1960, **3**, 473–475.

281 W. A. Felsing and S. A. Durban, the Vapor Pressures, Densities, and Some Derived Quantities for Acetone, *J. Am. Chem. Soc.*, 1926, **48**, 2885–2893.

282 Boublik.T and Aim.K, Heats of vapourisation of simple non-spherical molecule compouds, *Collect. Czechoslov. Chem. Commun.*, 1972, **37**, 3513–3521.

APPENDIX A: List of symbols and abbreviations

σ	Conductivity
λ-DNA	Lambda DNA
μL	Microlitre
μm	Micrometre
μM	Micromolar
Ω	Ohm
Δθ	Phase shift
ρ	Resistivity
λ	Wavelength
ϕ	Work function
0-D	Zero-dimensional
1-D	One-dimensional
2-D	Two-dimensional
3-D	Three-dimensional
A	Adenine
AFM	Atomic Force Microscopy
AIST	Advanced industrial science technology
C	Cytosine
CB	Conduction band
CNT	Carbon nanotube
CT-DNA	Calf-thymus DNA
CVD	Chemical vapour deposition
dc	Direct current
DNA	Deoxyribonucleic acid
Eb	Binding Energy
ECD	Electrochemical deposition
EDX	Energy Dispersive X-ray
Eg	Band-gap energy
Ek	Kinetic energy
eV	Electron Volt
*f*0	Resonance frequency
FTIR	Fourier-Transform Infra-Red
FWHM	Full-width half-maximum
G	Guanine
HOMO	Highest Occupied Molecular Orbital
I-V	Current-Voltage

k	cantilever spring constant
K	Kelvin
L	Length
LUMO	Lowest Unoccupied Molecular Orbital
mg	Milligram
mL	Millilitre
mM	Millimolar
MWCNT	Multi-walled carbon nanotube
nm	Nanometre
NW	Nanowire
PDMS	Poly dimethyl siloxane sheet
Pt	Platinum
Pt/NW	Platinum/nanowire
Q-dot	Quantum dot
R	Resistance
R_b	Nanowire resistance
R_C	Resistance-Capacitance
RNA	Ribonucleic acid
S	Siemens
SCLC	Space charge limited current
SE	Secondary electron
SEM	Scanning Electron Microscopy
SPM	Scanning Probe Microscopy
SWNT	Single-walled carbon nanotube
T	Thymine
TEM	Transmission Electron Microscopy
Tm	Melting temperature
TMS	Trimethylsilane
VB	Valence band
VOCs	Volatile organic compounds
UHV	Ultra-high vacuum
XPS	X-ray Photoelectron Spectroscopy
XRD	X-ray Diffraction

APPENDIX B: I-V plot of ZnS/DNA nanowires

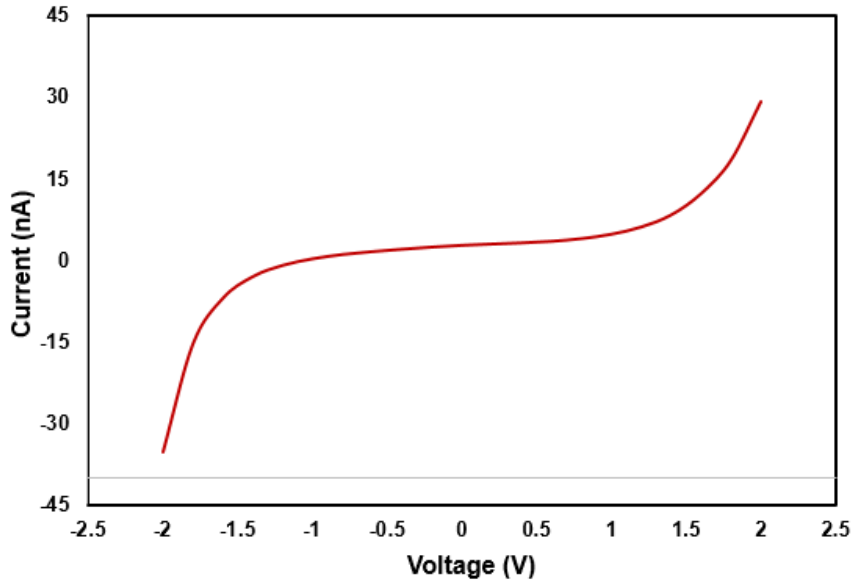

Figure 1. Electrical measurement (I-V curve) of DNA templated CdS/DNA nanowire network prepared in aqueous solution and aligned on platinum on silicon microfabricated electrode showing space charge limited current.

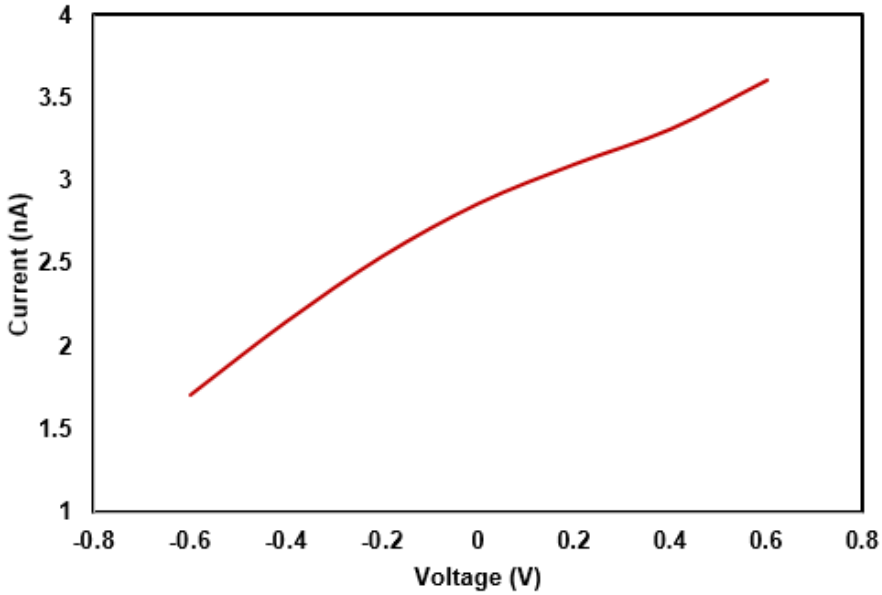

Figure 2. Low voltage I-V plot of ZnS/DNA nanowire showing fairly ohmic properties.

APPENDIX C: Response transient of ZnS/DNA nanowires.

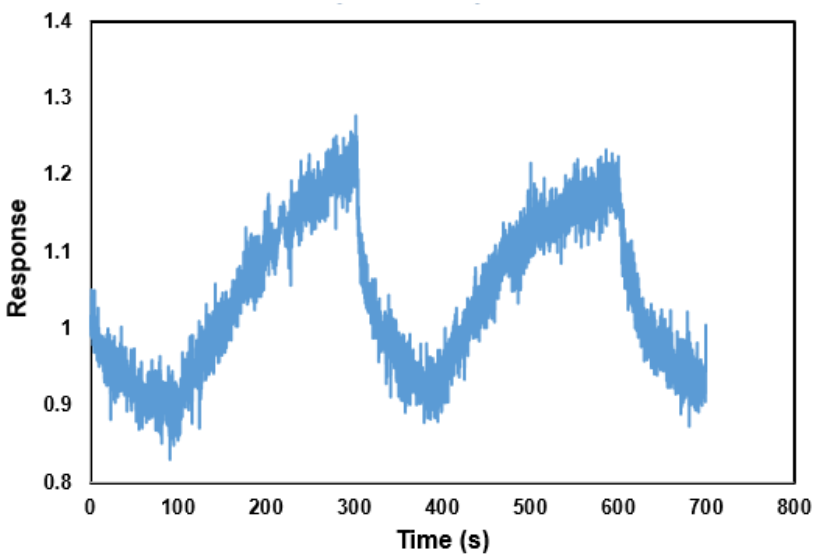

Figure 3. Response transient of ZnS/DNA nanowire to ethanol vapour.

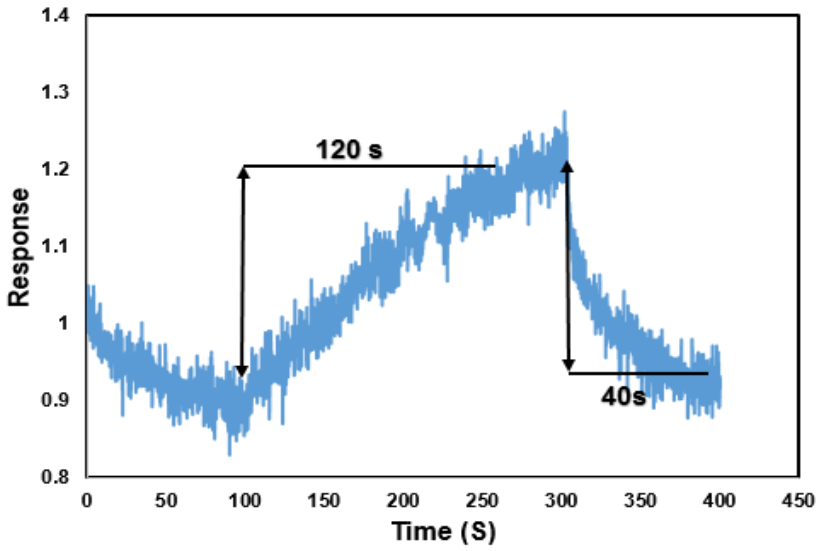

Figure 4. Response transient of ZnS/DNA nanowire to ethanol vapour showing the response and recovery time.

APPENDIX D: Conversion of partial pressure to concentration

The general gas equation is given by

$$PV = nRT \quad (1)$$

Where P= pressure of the gas (Pa), V= volume of the gas (mol/dm^{-3}), T= the temperature of the gas, n= number of moles and R= universal gas constant (JK^{-1}mol^{-1}).

Dividing both sides by V, we get;

$$P = \frac{n}{V}RT \quad (2)$$

But$C = \frac{n}{V}$, therefore

$$P = CRT \quad (3)$$

Using equation (3), we can convert partial pressure of the gas to concentration.

For example,

The gas sensing using CdS@DNA for chloroform at temperature 16oC can be done as follows;

Recall that the equation used in calculating the partial pressure of the organic vapour in the mixture (equation 5.22) is

$$p = P^*.\frac{V_v}{V_v+V_{air}} \quad (4)$$

For a constant V_{air}= 100 mL min^{-1}, and for $V_v = 100$, 200, 300, 400 and 500 mL min^{-1} respectively, the partial pressure is

Saturated vapour pressure of chloroform at 16^{o}C = 17.598 kPa (from AIST database)

1. $p_{100} = 17.589.\frac{100}{100+100}$ = 8.799 kPa

2. $p_{200} = 17.589.\frac{100}{200+100}$ = 11.791 kPa

3. $p_{300} = 17.589.\frac{100}{300+100}$ = 13.199 kPa

4. $p_{400} = 17.589. \frac{100}{400+100}$ = 14.078 kPa

5. $p_{500} = 17.589. \frac{100}{500+100}$ = 14.606 kPa

The calculated partial pressures can be converted to concentration;

R= 8.314 J K^{-1} mol^{-1}, T= (16 +273) K = 289 K, RT= 2402.75 Nm mol^{-1}.

Recall $C = \frac{P}{RT}$, from equation (3)

1. $C_{100} = \frac{8799\ Nm^{-2}}{2402.75\ Nm\ mol^{-1}}$ = 3.66 mol m^{-3}

2. $C_{200} = \frac{11791\ Nm^{-2}}{2402.75\ Nm\ mol^{-1}}$ = 4.91 mol m^{-3}

3. $C_{300} = \frac{13199\ Nm^{-2}}{2402.75\ Nm\ mol^{-1}}$ = 5.49 mol m^{-3}

4. $C_{400} = \frac{14078\ Nm^{-2}}{2402.75\ Nm\ mol^{-1}}$ = 5.86 mol m^{-3}

5. $C_{500} = \frac{14606\ Nm^{-2}}{2402.75\ Nm\ mol^{-1}}$ = 6.08 mol m^{-3}

S/No	Concentration	Mol m^{-3}	Mol dm^{-3}	mMol dm^{-3}
1	C_{100}	3.66	0.0037	3.7
2	C_{200}	4.91	0.0049	4.9
3	C_{300}	5.49	0.0055	5.5
4	C_{400}	5.86	0.0059	5.9
5	C_{500}	6.08	0.0061	6.1

NOTE: The partial pressure of the ethanol, acetone and hexane was also converted to concentration using same method. Same calculation was done for all the analyte for CdZnS@DNA and ZnS@DNA.

APPENDIX E: Published papers and conferences/seminar presentations

Published papers

(a) **AB Oshido**, BR Horrocks and A Houlton. *Gas sensing using one dimensional (1D) DNA templated cadmium sulfide nanowire*. Multidisciplinary Digital Publishing Institute Proceeding 2017, 1(8), 791.

(b) R.Nurdillayeva, **A. Oshido,** T. Bamford, O El-Zubir, A. Houlton, J Hedley, A. Pike and B Horrocks*. Inkjet printing and electrical characterisation of DNA templated Cadmium Sulfide nanowires*. Nanotechnology 2018, 29(13), 135704.

(c) Shams B Ali, **A B Oshido**, A. Houlton and B. R. Horrocks. *Electrical and sensing behaviour of DNA-coated carbon nanotubes.* (**draft**)

(d) **A B Oshido**, A. Houlton and B. R. Horrocks. *DNA-templated nanowires for sensing volatile organic compounds***.** (**draft**)

Conferences and seminar presentations

(a) 2017 -Wynne- jones research day symposium, Newcastle University, United Kingdom

(b) 2017- 5th international symposium on sensor sciences, Barcelona Spain.

(c) 2017- Nanomaterials from theory to application, University of Manchester.

(d) 2016- Nanoparticles with morphology and functional anisotropy-Faraday discussion, University of Strathclyde, Glasgow United kingdom.

(e) 2015- CHEMNANO conference (CNSN-5 2015) School of Chemistry, Newcastle University, United Kingdom.

(f) 2016- CHEMNANO conference (CNSN-6 2016) School of Chemistry, Newcastle University, United Kingdom.

(g) 2015- SCI electrochem postgrad conference, Newcastle University, United Kingdom.